Electrode performance and signal processing strategies for the discrimination of EEG alpha waves: Implications for environmental control by unconstrained subjects without training

Andrew Searle
BE. (Hons) BSc.

Department of Applied Physics
of Technology, Sydney
Australia

A thesis submitted for the degree of Doctor of Philosophy

December 2000

CERTIFICATE OF AUTHORSHIP/ORIGINALITY

I certify that this thesis has not previously been submitted for a degree nor has it been submitted as part of requirements for a degree except as fully acknowledged within the text.

I also certify that the thesis has been written by me. Any help that I have received in my research work and the preparation of the thesis itself has been acknowledged. In addition, I certify that all information sources and literature used are indicated in the thesis.

Signature of Candidate

Production Note:
Signature removed prior to publication.

ACKNOWLEDGEMENTS

I would like to acknowledge the generous support, assistance and guidance that I have received from my supervisor, Assoc. Prof. Les Kirkup, and co-supervisor Prof. Ashley Craig; their efforts through the course of this thesis have been invaluable. I would also like to thank Mr. Geoff McCredie for help in the vacuum deposition laboratory, and Dr. Paul Swift for guidance on all things optical. I would also like to thank Amanda for many years of patience and understanding.

Contents

List of Figures

List of Tables

ABSTRACT

The phenomenon of the increase in alpha EEG activity associated with eye closure has been shown to be successful for implementing environmental control for disabled persons. Studies in this thesis investigate strategies which improve the reliability, robustness, and ease of use of alpha EEG control systems. Primarily, research covers the effectiveness of alpha EEG detection algorithms (with regard to detection time and susceptibility to artifact) and the construction and use of EEG sensing electrodes.

Many new techniques for the detection of the increase of alpha EEG associated with closure are researched, developed, implemented and evaluated. All detection techniques are compared to a conventional method using a novel performance parameterisation criterion. In conjunction with the application of the same EEG data sets to all techniques, the use of the performance criteria enables a fair and quantitative comparison to be made between alpha detection methodologies. Detection techniques employed include enhanced versions of conventional methods, localisation of apparent alpha sources in the brain, and preprocessing methods (such as spatial filtering, adaptive filtering and independent component analysis). The best performance of alpha EEG detection was given by the source power alpha localisation technique, which showed statistically significant and practically important improvements in performance over conventional techniques. Additionally, this localisation technique is convenient and fast to implement.

In situations in which electrodes are intended for unsupervised use with environmental control systems, the evaluation of alternative types to the conventional wet electrodes is required, as the use of wet electrodes has several drawbacks. The performance of wet, dry and insulating electrodes is compared in this research. One aspect of the quantitative comparison of electrodes types is the measurement of contact impedance. To enable the fast and accurate measurement of impedance spectra, a new impedance spectroscopy system was developed as part of this thesis. In addition to comparison of impedance criteria, electrodes were evaluated in the presence movement-based, and electric field induced, artifacts. The electrode comparisons were carried out in a direct and quantitative manner in a controlled test environment for the first time. Results indicate that, in contrast to earlier reports, both dry and insulating electrode perform well with respect to artifact and offer a viable alternative to wet electrodes for long-term monitoring of biosignals from the surface of the skin. More improvements are required before such electrodes are suitable for EEG usage.

Chapter 1

Introduction

In the current technological age, the portrayal of physiological phenomenon in graphical or numerical form is so commonplace that it is difficult to consider undertaking any study of physiology without using the 'language of machines'. However, until the early 19th century the act of medical diagnosis was confined to observations of structural defects of the body, rather than indices of bodily functions such as circulation, temperature and respiration (Reiser 1978, p. 107). The use of scientifically gathered numerical data for diagnosis gained momentum in the mid 1800's when John Hutchinson used his spirometer to measure lung capacity and successfully diagnose some disorders. The use of transducers became widely accepted by practitioners and this new method of medical examination expanded quickly. It was only a matter of time before the rhythms of the body were transformed into electrical signals. In 1874, Richard Caton discovered electrical brain signals by probing directly on the surface of exposed brains of animals. In 1924 Hans Berger recorded the first human electrical brain activity, and called such activity the electroencephalogram (EEG). Berger went on to publish 14 papers (in German) on the subject of his life's work, all under the same title: 'On

the Electroencephalogram of Man'. Much of this thesis is concerned with the acquisition and analysis of signals generated by the human brain. It is appropriate therefore, to begin by considering the EEG in some detail.

1.1 The electroencephalogram

There are many ways in which to analyse the activity observed in the EEG. A commonly used method is to divide the EEG signals into frequency spectra. These spectral bands are denoted using Greek letters, as shown in Table 1.1.

Band identifier	Frequency range (Hz)
delta	0.5 - 3.5
theta	4 - 7.5
alpha	8 - 13
beta	13 - 30

Table 1.1: Spectral components of the EEG

Investigations in this thesis involved particular characteristics of the alpha EEG rhythm.

1.1.1 The alpha EEG rhythm

The International Federation and Society of Electroencephalography and Clinical Neurophysiology (IFSECN) defined the alpha rhythm as:

> '..a rhythm at 8-13 Hz occurring during wakefulness over the posterior regions of the head, generally with higher voltage over the occipital areas. Amplitude is variable but is mostly below in the adult. Best seen with eyes closed and under conditions

> of physical relaxation and relative mental inactivity. Blocked or attenuated by attention, especially visual, and mental effort.' (Shaw 1992)

Despite this 'standard' definition, confusion still arises in alpha EEG terminology; for some authors it is any rhythm in the posterior region regardless of form, while for others it is any 10 Hz oscillation in different parts of the brain (Basar & Schurmann 1997). A 20 Hz harmonic of the alpha EEG is described and modelled by Azizi et al. (1996). Bhattacharya et al. (2000) defined three alpha rhythms in human subjects;

- The classical posterior rhythm, mainly localised in posterior areas when eyes are closed with no visual information processing.
- The mu rhythm (or wicket rhythm), which is well-defined at the central region of the scalp, over the sensorimotor cortices. This rhythm is attenuated by movement or imagined movement, but not by eye opening.
- A third rhythm which is found over the midtemporal region, considered an alpha activity of the auditory cortex. This rhythm can only be recorded with an underlying bone defect.

The third alpha rhythm is rarely referred to. In general, the use of the term 'alpha rhythm' (or 'alpha wave') denotes posterior activity, mu-alpha activity is usually referred to simply as the mu-rhythm. For terminology in this thesis, alpha rhythm denotes the EEG activity in the range 8-13 Hz which shows an increase upon eye closure, primarily in the posterior region of the head, and which is normally detected using electrodes pressed against the scalp. Indeed, it is the observable change in alpha EEG activity between eyes open and eyes closed states that forms the basis for much of the study in this thesis.

The alpha rhythm has been the subject of a very large body of research since it was identified by Berger. Adrian & Matthews (1934) confirmed that the alpha signals were sourced in the cortex, rather than originating at the eye muscles or at other locations outside the brain. However, debate still occurred regarding whether the alpha rhythm was due to ocular muscle tremor (Lippold 1970); this idea was soon discredited (as described by Shaw (1992)). There are many theories on the neural origins of the alpha rhythm, and such theories often have their basis at a cellular level. Accordingly, these theories will not be covered here, but many articles are available on the theory and modeling of alpha EEG (for example, by Robinson et al. (1998), Azizi et al. (1996), Lopes Da Silva (1991) or Dick & Vaughn (1970)). Similarly, models for locating the 'alpha generator(s), in the brain are common, such as dipole modeling by He et al. (1989), and Wilson & Bayley (1950).

As the of the alpha EEG are routinely linked to visual activity, many studies have been devoted to exploring the relationship between vision and alpha activity. The effect of eye closure, and the resulting increase in alpha EEG amplitude is a well established phenomenon (HardIe et al. 1984). Ghiyasvand et al. (1994) suggested that partial eye closure leads to an alpha activity increase, but this claim remains unsupported. Many studies have investigated the effects of illumination on the alpha increase after eye closure (Cram et al. 1977, Bohdanecky et al. 1984.) and on alpha activity in general (Nathan & Hanley 1975). Sinusoidally varying illumination levels at frequencies in the alpha band have been shown to stabilise the alpha EEG frequency (Townsend et al. 1975). Increases in alpha activity are also observed when the eyes are rolled upwards (Mulholland & Evans 1965), leading to suggestions that the alpha increase is a result of a tendency for the eyes to defocus and relax convergence (Dewan 1967).

In addition to the phenomenological studies mentioned above, there have been scores of studies which have investigated correlations between alpha and all manner of psychological and behavioral variables (Shaw 1992). As expressed by (Mulholland 1972), in reported studies of alpha EEG, '...as an index of mental processes and behavior, it was overrated; as an orderly, predictable phenomenon, it was underrated'. Accordingly, for the investigation to be described in this thesis, it is the phenomenon of the reliable and predictable increase in alpha EEG after eye closure that is of primary interest. Specifically, this thesis will investigate issues relating to the use of the increase in alpha EEG activity following eye closure to enable persons to control their environment (Craig et al. 2000, Craig et al. 1999). This area of research has been given much emphasis recently due to the promise of environmental controls that could assist, for example, persons with severe physical disabilities. The use of systems which utilise EEG for external control are generally known as brain-computer interfaces.

1.2 Brain-computer interfaces

The use of the electroencephalogram (EEG) has been an essential tool in clinical medicine since the first human recording was done by Berger. Since this discovery it has been a goal of many to use the electrical signals of the brain for the purpose of direct control of the environment. Although this vision of a 'thought-controlled future' is often considered a preoccupation of science fiction devotees, the development of technology which can be controlled via the EEG has many less frivolous applications. A significant group which would benefit from EEG controlled devices are those people who, through nerve trauma or neural deterioration, are unable to perform tasks

which require limb control. Such a condition may be caused by high break tetraplegia, amyotrophic lateral scherosis, or other high-level impairments. For such people, physical manipulation or simple communication may be impossible and alternatives are required. 'When some level of dexterity remains, devices such as chin-press switches (Ha\vleyet al. 1992), electromyographic sensors (Horn 1972), mouthsticks, 'suck-puff' switches, eye blink detectors (Thornett 1990) and voice control units can offer assistance. However, for levels of disability which are more severe, devices which take commands from higher cognitive functions are needed. A device which can translate EEG activity into useful actions (a Brain-Computer Interface, or BCI) could possibly improve the quality of life of such individuals. There has been much research devoted to the development of BCl's, and this body of work has increased significantly in recent years. BCl's may be summarised into three broad categories,

- **Techniques which depend on mental associations or are linked to physical processes.** Such BCl's include those which operate by detecting EEG changes during imagined movement of hands, feet, etc. (Babiloni et al. 2000, Penny et al. 2000, Pregenzer & Pfurtscheller 1999, Schloegl et al. 1997), or during actual physical movement (Birch & Mason 2000, Funase et al. 1999, Barreto et al. 1996, pfurtscheller et al. 1994). The use of imagined limb movement has also been shown to be successful for amputees (Pfurtscheller et al. 2000). A specific EEG component which is often used for studies related to limb movement is the mu-rhythm - this rhythm shows attenuation over the central region of the scalp, associated with self-generated movement or imagined movement (Pineda et al. 2000).

  A BCI may operate on detection of EEG changes brought about by

mental tasks performed by the subject, such as solving a mathematical problem (Skidmore & Hill. 1990, Penny et al. 2000, Anderson et al. *1995b),* composing a letter, manipulating geometric shapes (Keirn & Aunon 1990, Anderson et al. *1995a,* Anderson & Sijercic 1996) or thinking or 'no' (Ryu et al. 1999).

- **Techniques which rely on external stimuli.** These types of BCI incorporate external stimulus. One such method utilises the P300 (or P3) evoked potential, which is a response to a rare (but anticipated) task relevant stimulus (Donchin et al. 2000, Bayliss & Ballard 2000). For example, if each letter of the alphabet is flashed on a PC screen, a P300 response will be observed when the letter on which a subject is concentrating on appears.

  Another stimulus may take the form of many constantly changing stimuli, which vary at different rates. This enables an algorithm to determine at which stimulus the subject is looking, by monitoring the steady-state visual evoked response (SSVER) (Sutter 1992, Cilliers & der Kouwe 1996, Calhoun & McMillan 1996, Calhoun & McMillan 1998, Ming & Shangkai 1999). For example, if a PC monitor is split into many sections, and each section flashes (or changes colour) at a different frequency, the SSVER will oscillate at the frequency associated with the section of the screen at which the subject is gazing.

- **Self-learned techniques.** These BCI methods are not linked to any specific mental processes or stimuli, but rely on feedback from the BCI system, and as thus the operation of such a BCI must be 'learned' by the subject (Birbaumer et aI. 2000). Such systems include the control of a cursor by processing the EEG in bulk (Kostov & Polak 2000), or

monitoring specific components, such as the mu-rhythm (not associated with limb movement) (Wolpaw & Mcfarland 1994, Mcfarland et al. 1993).

These categorisations are an approximate guide, and many BCI methods may apply to more than one category, or none at all. All the BCI techniques described above have respective advantages and disadvantages. The use of alpha EEG for BCI offers advantages over other methods in some areas.

1.2.1 Alpha EEG for environmental control

The use of alpha as a control mechanism has been demonstrated in basic forms by previous researchers. Dewan (1967) demonstrated a morse code system which was operated by a subject who increased alpha activity by rolling the eyes upwards. Using the system, a single letter could be typed approximately every 35 s. Bozinovski (1990) enabled the control of a mobile robot using eye closure; the robot could be instructed to start and stop (Bozinovski et al. 1988). More recent studies have demonstrated that reliable control based on alpha EEG can be achieved using eye closure (Kirkup et al. *1997a,* Kirkup et al. *1997b,* Kirkup et al. 1998). The attractive features of using the alpha EEG in conjunction with eye closure for environmental control have shown to be:

- The phenomenon of alpha increase after eye closure is reliable and consistent. Craig et al. (1999) have shown that an increase in alpha EEG amplitude following eye closure was observed in at least 90% of disabled and non-disabled subjects.

- Subjects require no training. This contrasts with some BCl methods which use feedback mechanisms to train suhjects to modulate con-

sciously aspects of the EEG. For example, Mcfarland et al. (1993) used a feedback system with the mu-rhythm to enable subjects to control a cursor on a screen. After several weeks, 3 out of the 4 subjects were able to control successfully the cursor position in one dimension (later, 2-dimensional control was added (\Volpaw & Mcfarland 1994)).

- No external stimuli are required. This allows great freedom in the design of the 'front end' to the BCl system, as opposed to SSVER or feedback systems which require specific interface designs to enable proper operation.

- No specific mental process is required.

- A minimum number of electrodes are required which may be placed discreetly on the scalp. This is important as, in the case of application to the disabled, unintrusive technology may significantly lessen the chance of reduced self-esteem that arises when equipment is necessary which makes the user 'look more disabled'.

Basic forms of alpha EEG manipulation using eye closure have been demonstrated previously. However, for efficient control using alpha EEG the method which detects a change in the alpha signal must act quickly and in a robust manner. This entails the time interval between eye closure and detection of an increase in alpha to be small, and the ability to filter, attenuate, or ignore artifact signals which may cause false detection of alpha EEG increase. Additionally, the physical aspects of the BCl should be convenient for the user. The functional design of a BCl is not part of the research for this thesis, rather, the emphasis is on aspects which will enable an alpha-based BCl to operate more effectively, and with greater reliability for the user. This emphasis can be segmented into two investigative objectives which are required

for a successful BCl using alpha EEG:

1. Convenient and reliable pickup of EEG signals from the scalp using electrodes. Conventional electrodes, which use conductive gels, are designed primarily for clinical use and are not suitable for application by the user or carer. Some expertise is required when attaching electrodes to avoid impairing electrode effectiveness through gel smearing. Also, the performance of conventional electrodes degrades after periods of time, which is unsuitable for devices such as BCl's which are required for sustained usage. Long-term use of conductive gels can also lead to skin irritation.

2. Effective processing of the alpha EEG signals associated with eye closure. This involves detection of expected alpha changes, and rejection of artifact signals from a wide range of sources.

Sources of artifact common in EEG recording are briefly described in the following section.

1.3 Artifact sources in EEG

There are several sources of artifact which may be present in EEG recordings. This discussion does not include the influence of powerline noise and other electric fields, which can be attenuated by effective circuit design and electrode construction (as shall be investigated in Chapters 6 and 7). Major sources of artifact are:

Muscle artifacts The movement of muscles in the neck, jaw, and face routinely contaminate EEG recordings. The occurrence of eye blinks[1] and

[1]blink artifacts are not strictly caused by muscle activity, but by changes in ocular conductance produced by contact of the eyelid with the cornea (Jung et al. 2000).

eye movement (saccadic activity) will also cause the appearance of unwanted signals in the EEG.

Electrode movement The movement of electrodes with respect to the skin may disrupt electrochemical or electrical balances, causing the appearance of an artifact signal. The type and severity of artifact depends on the electrode construction, as will be investigated in Chapters 5 and 7.

Skin potential There is an electric potential present across the top layers of the stratum corneum. This potential changes when the skin sweats, stretches or is under mechanical pressure (Webster 1984, Burbank & Webster 1978). Thus movement of the skin (or an electrode on the skin) will cause an artifact signal.

In principle, all of these artifacts could be minimised by ensuring that the EEG subject remains completely still. This may be feasible for short, clinical trials where a subject can be asked to remain still, and eye blinks manually removed after recording, but for a system intended for long-term unsupervised use the presence of some artifacts must be accepted and accounted for. Even for the target group, those people with high level impairments, some muscle movement may still remain, or indeed there may be involuntary muscle tremor (Srikureja et al. 2000). Thus a BCI system needs to be sufficiently robust to cope with artifact signals. A further constraint is that any system designed to exploit changes in EEG activity must be able to operate in real time, as offline analysis is of no practical use for control applications.

1.4 Objectives for this thesis

A substantial amount of research has been devoted to the characteristics of alpha EEG activity. for its use in a BCl, investigations are required in order to develop signal processing algorithms which perform quickly and robustly in unconstrained environments, i.e. environments in which the subject is allowed freedom of movement. Additionally, the electrode technology to be used with such a BCl requires research, as traditional gel-based electrodes are not ideal for long-term, unsupervised use. Therefore, broad objectives for the studies in the thesis are:

- develop new methods for the detection of alpha EEG increases associated with eye closure. The new techniques should be capable of rapid detection of the increase in alpha activity following eye closure, and should operate reliahJy in the presence of artifact signals.

- To derive a means of directly and evenly comparing the performance of alpha detection methods.

- To compare the performance of conventional, and newly developed alpha EEG detection algorithms through studies on volunteers. The performances should be established and compared when sources of artifact are and when they are absent.

- To investigate the use of electrodes for application to EEG, with particular emphasis on long-term, unsupervised EEG monitoring.

- To quantitatively compare the performance of bioelectric electrodes. This includes the impedance characteristics of such electrodes, and performance in the presence of electrode-related artifacts.

1.5 Structure of thesis

This thesis is structured as follows:

Chapter 2 introduces conventional methods for alpha EEG detection and monitoring. These methods will be compared with each other, and with enhanced algorithms developed by the author which offer potential advantages in detection time and errors encountered. Techniques in this chapter use signals from a differential pair of EEG electrodes. The chapter introduces a new method for comparing the performance of methods designed to detect the increase in alpha signals. Comparisons are made using EEG data gathered from human subjects. This new quantitative comparison technique is also utilised in Chapters 3 - 4.

Chapter 3 describes preprocessing techniques which can be applied to EEG signals before the alpha EEG detection techniques described in Chapter 2 are applied. The algorithms described take advantage of EEG signals recorded from many electrode sites.

Chapter 4 describes research into the development of alpha EEG detection methods which are based on monitoring the apparent location of alpha activity in the brain.

Chapter 5 introduces electrode construction techniques which are able to be used for EEG recording, and presents respective advantages and disadvantages. The impedance characteristics of such electrodes is also explored.

Chapter 6 investigates the impedance of the skin/electrode interface, and its effect on bioelectric signal fidelity. Impedance measurement techniques are investigated and the design of a new measurement system is described. This system is evaluated using data gathered on volunteers.

Chapter 7 compares the performance of three types of bioelectric recording electrodes in a direct and quantitative manner. The performance with

regard to impedance and susceptibility to artifacts is investigated.

Chapter 8 describes conclusions of the study and suggestions for further work.

At the beginning of each chapter, a survey of the literature pertaining to specific studies in that chapter is presented. Some of the work reported in this thesis has been published in the literature or presented at conferences, as detailed in Appendix A.

Chapter 2

Methods for detection of alpha activity in the EEG

2.1 Introduction

Much of the literature concerning the detection of alpha wave activity derives from biofeedback studies which aim to use alpha signals as the basis of an indicator that facilitates enhancement of the alpha signals, or as a measure of physiological state. Alpha EEG feedback treatment has been applied to hyperactivity in children, anxiety disorders (Hare et al. 1982), epilepsy, obsessional neuroses and pain suppression. Alpha feedback techniques have also attracted attention among competitive sportsmen as a tool for psychological preparation for competition (Druckman & Bjork 1992). The wide range of applications for alpha wave feedback (and a period of 'alpha obsession' (Gatchel & Price 1979, Shaw 1992) in the 1960's and 70's) has meant substantial research and commercial venture has been dedicated to the area. Unfortunately, the popularisation of alpha wave technology did not necessarily

produce a significant improvement in the standard of equipment available[1].

There are few instances in the literature where the main goal is to effect control via alpha waves (rather than simple feedback), and fewer still where the control is effected by eye closure. As outlined in Section 1.2.1, such control via eye closure is attractive because of its reliability, simplicity and the lack of training requirements. For control use, either a binary output *(on/*off) or a graded output (to enable, for example, cursor control) is required. In this study we concentrate on a binary output, but it is a straightforward task to convert any graded measure to a binary one by using a thresholding operation.

An overview of past alpha quantification methods and the use of alpha EEG in control situations follows.

2.1.1 Conventional methodologies for alpha wave detection

The alpha wave detection techniques utilised by researchers in published studies all differ from each other to some extent. A large proportion of these studies use alpha quantification methods that can be categorised as either *percent time* or *integration* techniques.

2.1.1.1 The Percent Time and Integration alpha measurement methods

The percent time method (also called criterion alpha, alpha abundance or alpha index) monitors the amount of time in which the maxima of the alpha EEG signal (suitably bandpass filtered) are above a selected threshold. This

[1]One manufacturer recommended the use of its equipment in large, open fields, away from power lines (Gatchel & Price 1979, p. 188)

threshold can be defined as a voltage (a voltage threshold has limitations due to possible dependence on the equipment used (Lansky et al. *1979b)* and electrode locations) or a relative measure using various statistics of the EEG maxima. Although the process used to produce the output signal differs between researchers (Knox 1980, Valle & Levine 1975, Mulholland 1971, Mulholland & Evans 1965), the results are similar: a visual or audible representation of the fraction of time that alpha characteristics are present in the EEG signal. Bohdanecky et al. (1978*a)* favour the median (or quantile) values of the EEG maxima when determining threshold level, as this is less affected by artifact presence during the threshold determination period (Lansky et al. *1979b,* Maras et al. 1979). These methods can be adapted to indicate the presence or absence of alpha waves as a binary output. For example, an 'alpha period' may be denoted when three peaks occur above a threshold in 140 ms (Bohdanecky et al. 1984., Bohdanecky et al. *1978b)*

The integration method gives an output proportional to the time integral of the full wave rectification of the bandpass filtered EEG signal (Basmajian 1983, Kemp & Blom 1981, Boudrot 1972). Although not usually stated, the integrator needs to be imperfect (or lossy) to avoid the output saturating at a value close to the supply rails (or reaching a maximum value in a software implementation), as the input is consistently positive.

Hardt & Kamiya (1976) expressed preference for the integration method over the percent time technique for alpha EEG detection due to its continuous, analogue output, and the absence of a threshold (in feedback studies). These works also assert that the percent time method does not take EEG amplitude into consideration: the signal is simply above or below the threshold regardless of how far above the threshold a signal may be. Further claims are that alpha-enhancement studies using biofeedback have succeeded when us-

ing the integration method, and failed when using the percent time method. This view is supported by Knox (1980). Lansky et al. *(1979a)* present a contrary viewpoint that the percent time measure can also be represented as a continuous, analogue form. Further, they contend that the values of the percent time measure are meaningful and a known range (0-100%) compared to the possible infinite values obtainable from the integration method, and that the damping effect of the integration introduces a delay into the feedback process. There have also been experiments using hybrid alpha wave detection techniques (Hare et al. 1982), for example, Cram et al. (1977) uses integration methods to find a threshold, which is then applied to percent time calculations.

2.1.1.2 Other methods

Various techniques that do not fit into the broad percent time or integrator categories have been applied to alpha wave detection. As with methods mentioned above, the applications were primarily feedback studies. Zhang & Chen (1988) use spectral analysis preference to integration and percent time methods for feedback studies for reasons of accuracy and reliability. Spectral methods are also used by Ray & Cole (1985) to return a power estimate in the 8-15 Hz band. An extension of the percent time technique is employed by Bozinovski (1990), using a training session to obtain a distribution of raw EEG amplitudes and waveform periods for eyes open and closed periods. This distribution is then used as a basis for comparison during real-time operation.

Classifiers have also been applied to the task of alpha wave detection; Shimada et al. (2000) trained neural networks and Keirn & Aunon (1990) used a Baysian classifier trained on frequency spectra. These researchers returned

data containing other EEG information, in addition to alpha information.

In contrast to the experiments which utilise the changing amplitude of the alpha waves, there have also been investigations into the temporal characteristics of alpha EEG. For instance, de Rooij & Smeyers (1974) monitored variance in the periods between zero crossings of bandpass filtered EEG, from which promising results were reported for discrimination between eyes open and eyes closed cases. Although the periods showed little difference between eyes open and eyes closed segments, the variance in periods did exhibit change.

The experiments by Morrow & Casey (1986) used thresholded EEG to create a series of digital pulses when the signal exceeded a set limit. A microcomputer continuously monitored the pulse stream, determining whether the data was 'in or out' of the alpha band by using an algorithm in which the number of pulses in given time period were llsed as a guide to the presence of alpha activity. Similar experiments were done in which a digital pulse was returned proportional to the time between zero crossings of EEG; alpha was reported only when the height of these pulses fell between an upper and lower limit (Basmajian 1983).

Few biofeedback studies directly use the Root Mean Squared[2] (RMS) value of the alpha EEG as a feedback indicator, possibly because its 'waxing and waning' (Kemp & Blom 1981) characteristics are too variable for feedback that is understandable. Boudrot et al. (1978) used the RMS voltages as feedback by directly using a moving iron meter. In a different way, Pasquali (1969) demonstrated a polyphase envelope detector that does not suffer from the distortion or exponential lag inherent in a rectify-then-lowpass-filter circuit. Another method to detect the alpha EEG envelope is complex de-

[2] $V_{RMS} = V_{PEAK}/\sqrt{2}$

modulation (HardIe et al. 1984, Dick & Vaughn 1970). Finally, Ghiyasvand et al. (1994) noted differences in EEG covariance between eyes open and eyes closed, but little data was presented in the literature.

Kirkup et al. (1998) report a study in which three methods of alpha detection were compared; The integration method, a power spectrum method (using a 1 s sliding window to monitor frequencies in the alpha range) and a peak counting technique which used a differentiated EEG signal as the input. These workers found that the spectral method was marginally more effective than the integration technique, and significantly better than the peak counting method. Although the time to detect alpha onset was consistently less than the other methods, the spectral method also gave more false positive results compared to the integration method over the range of threshold settings used.

2.1.2 Alpha as a control mechanism

Any of the techniques mentioned in Section 2.1.1 could be modified to give a binary output denoting the presence or absence of alpha activity in an EEG signal (by adding a threshold to the output, or by some other simple means). Some experiments are now considered whose principle aim was to use alpha as a control mechanism, rather than in a feedback study. The alpha-driven morse code experiment (using eye closure) by Dewan (1967) used a bandpass filter (10 Hz) on EEG from left and right occipital locations. The filtered signal was digitised by a Schmitt trigger (with a controlling threshold) and fed to a computer. A computer program determined if the resulting pulse train was a dot or dash, depending on length, or whether the pulse train was artifact (too short to be either a dot or dash).

Ghiyasvand et al. (1995) monitored the shift of the dominant alpha wave frequency during eye closure to investigate the possibility of using the shift in frequency for control of prosthetic devices. Favorable results were reported, though it is not known whether the use with prosthetics was a success. In order to control a small mobile robot, Bozinovski et al. (1988) used a distribution of EEG peak values to decide whether the subjects eyes were closed or open (for example, if three successive peaks were inside the distribution space, the eyes were determined to be closed (Bozinovski 1990)). This is similar to the method used by Kirkup et al. (1998).

To test cursor control for use with disabled persons Patmore et al. (1994) used the alpha EEG envelope (rectifier and band-pass filter) and an EMG sensor on the cheek (presumably over the masseter muscle). An increase in alpha activity due to eye closure changed the direction of cursor movement from lateral to longitudinal, or vice versa. Using typing program, typing speeds of 3.0 - 6.3 keys per minute were reported.

Other methods of control using the EEG introduced in Chapter 1 will not be covered again in detail here. However, it should be noted that although the mu-rhythm (or wicket rhythm) occupies approximately the same frequency space as the alpha rhythm (8-12 Hz), the signal is located centrally rather than occipitally, and is associated with motor activity rather than visual (Shaw 1992). Some experiments using the mu-rhythm, however, do employ similar detection techniques to those described above; for example Mcfarland et al. (1993) used the average spectral power in the 8-12 Hz range to control a cursor.

2.1.3 Alpha EEG detection and artifacts

For reliable, unsupervised control of devices using alpha EEG the detection process needs to be sufficiently robust to cope with many sources of artifacts (as introduced in Section 1.3). Reliability is an especially important requirement if the alpha EEG detection system is to be used with disabled subjects. The effect of artifact on alpha EEG detection is an aspect not addressed in previous studies discussed in this chapter (apart from Patmore et al. (1994), who mention that the muscle artifact over the occipital area for one subject led to his exclusion from the study). One reason for this is that artifact is not as significant a problem in biofeedback studies, which form a large proportion of alpha wave detection work.

Apart from exploring new possibilities for alpha EEG onset determination, the aim of of the following study involved investigations into the effect of different artifact types, and strategies to minimise their interference. In order for the data collected for this study to reflect the environments in which we may envisage such a system being used, minimal constraints must be placed on the subjects involved. Many studies put a number of restrictions on subjects, for example, Ghiyasvand et al. (1995) required subjects to avoid body movement, eye blinks and eye movement. This is acceptable for the study in question but such requirements do not suit the study undertaken and reported in this thesis. It is unlikely that a person using an alpha EEG control system would be able to minimise such activity for long periods of time, especially eye movement. The only instructions for subjects in the study reported here were to remain comfortably still and curtail excessive head movements.

2.1.4 Scope of alpha wave detection study

The following study provides a comparison of many of the alpha detection methods discussed in this overview. Each performance was rated its on ability to

- detect an alpha EEG increase due to eye closure
- time to detect an alpha EEG increase due to eye closure
- the number of false positive errors
- resistance to artifact signals

The methods of data collection for the study are outlined, followed by descriptions and results for the alpha detection techniques. All detection methods are applied to the same data sets to facilitate a fair comparison of performance.

2.2 Data Collection

The EEG data was collected using a custom made elastic headband employing 19 evenly spaced electrodes. This number was chosen because of the minimum inter-electrode spacing (to avoid electrolyte smearing between electrodes) and channels available on the recording equipment. EEG signals were acquired using the Neurosearch-24 (Lexicor Medical Technology, Boulder, Colorado), which has 19 channels available for EEG, and auxiliary channels for EMG and EeG. Electrodes were 10 mm cup type, gold plated. The non-standard electrode positions were chosen to be consistent with the most probable electrode geometry for use with an alpha signal detection system. The locations of the electrodes are shown in Figure 2.1 and are

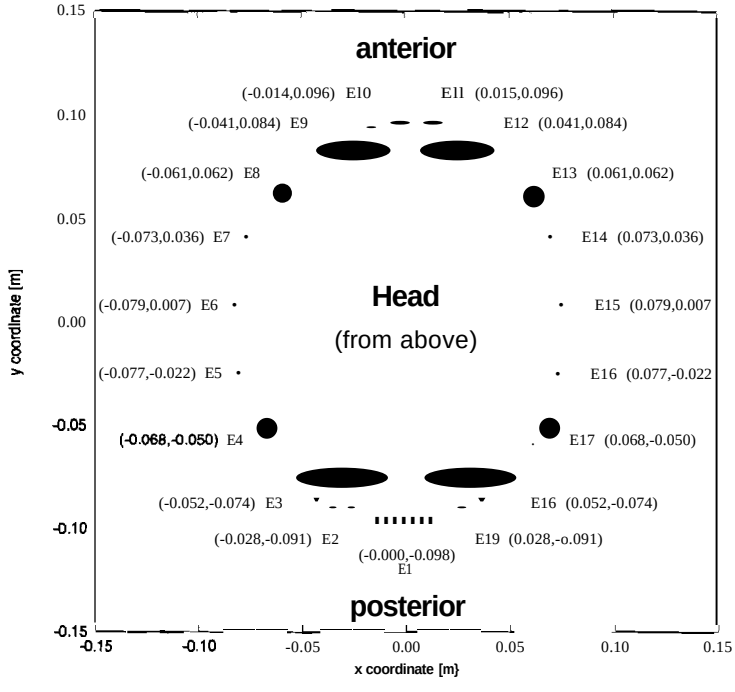

Figure 2.1: Positions of the 19 electrodes on the head band. Coordinates are mm.

labeled E1-E19. These labels are used as the electrodes positions are 'non-standard' and do not correspond to the standard 10-20 placement system (see Appendix B). The procedure for determining the electrode positions is described in Appendix C.

2.2.1 EEG recording procedure

Eleven subjects agreed to take part in the study (mean age 29.8 yr, standard deviation 8.3 yr). One subject was found to have no change in the alpha signal amplitude upon eye closure. Data from this subject was not used in these studies. The headband containing the electrodes was fitted to each subject, and conductive gel applied through holes in the cup electrodes by

means of a syringe with a blunt needle. Reference electrodes were applied to both earlobes using clips, and a ground electrode (a self-adhesive Red Dot™ EeG electrode) was attached to the forehead. Three self-adhesive electrodes were applied over the masseter muscle on one side of the face (the subject's right side) to record EMG signals from the jaw region. All data were recorded with sampling rate of 512 Hz, and a gain of 90 dB. Subjects were asked to perform four tasks, each of 90 s duration. These tasks were as follows:

Eye closure Subjects to remain still with eyes open for initial 30 s, then close eyes for 30 s, and have eyes open for the final 30 s.

Clenching of jaw muscle Subjects remain still with eyes open for an initial 34 s, then clench their jaw muscles in periods 34-37 41-44 s, 48-51 sand 55-58 s. The subject then remained still for the rest of the trial (32 s).

Movement of Head Subjects remained still with eyes open for initial 34 s, then turn their heads left and right alternately at times 34, 37, 41, 44, 48, 51, 55 and 58 s. The subject remained still for the rest of the trial (32 s). The subject was given objects to look at (at fixed positions), and asked to turn their heads and look at these objects by turning their heads only (rather than changing their gaze).

Reading out aloud Subjects remained still with eyes open for initial 30 s, then to read aloud from a book for 30 s, then remain still and silent for the final 30 s.

All tasks were repeated four times for each subject. The subjects' blinking and saccadic eye movement were not restricted. An audible short duration tone was used to alert subjects to perform tasks at the required times in a

consistent manner. The last three tasks were designed to simulate situations where a previously reported analogue alpha signal detection system (Kirkup et al. 1998, Kirkup et al. 1997*b)* failed to perform satisfactorily. That is, false positive readings often occurred when a person clenched his/her teeth, moved around (causing movement of the electrodes relative to the head) or engaged in conversation.

Figure 2.2 shows EEG spectra averaged over the 10 subjects for eyes open and eyes closed periods[3]. The change in the 8-13 Hz region is distinct. Fig-

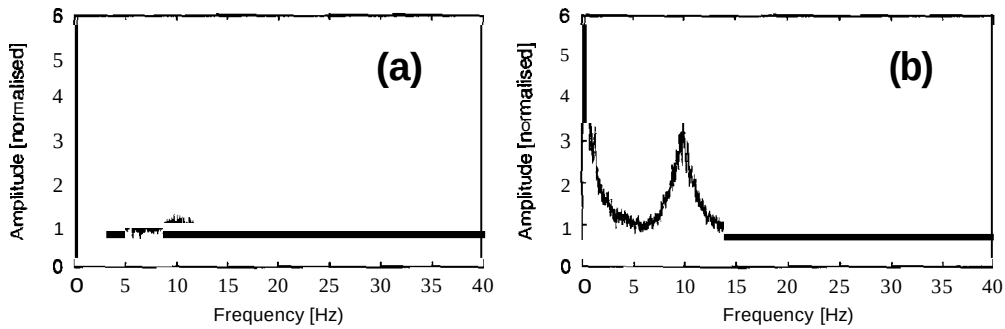

Figure 2.2: Spectra for (a) eyes open and (b) eyes closed, averaged over 10 subjects. The spectra are normalised to the mean value in the 8-13 Hz range during eyes open.

me 2.3 shows separate spectra for all tasks performed by the subjects; for clarity the spectra have been smoothed using cubic splines. The wideband artifact signals introduced by clenching the jaw (O'Donnell et al. 1974), moving the head and talking are apparent, and the overlap of such signals into the 8-13 Hz region ultimately means that such artifacts cannot be separated from the alpha rhythm by simple frequency domain filtering techniques.

3Before averaging, each spectra was normalised to the mean value in the 8-13 Hz band during eyes open.

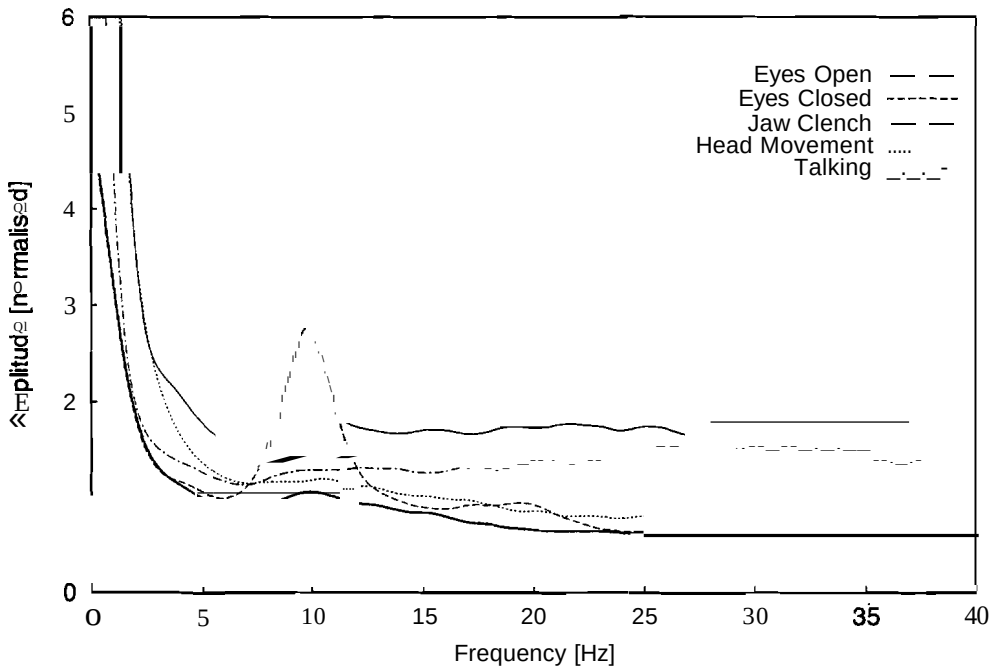

Figure 2.3: EEG spectra averaged over 10 subjects showing eyes open, eye closure, jaw clenching, head movement and talking. For clarity spectra have been smoothed using cubic splines. The spectra are normalised to the mean value in the 8-13 Hz range during eyes open.

2.3 The Integration method

The integration method is examined first as it has been used in previous experiments implemented in an analogue hardware form (Kirkup et al. 1998, Kirkup et al. *1997b).* The hardware implementation produced an output proportional to the integrated RMS value of the bandpass filtered EEG signal input. The circuit is summarised in Figure 2.4. Previous experiments with this system utilise three electrodes; one placed at O1[4], one at T5 and a driven reference placed on the forehead. The EEG signals are passed through DC-

[4] using the 10-20 electrode position classification system: see Appendix B

coupled (gain 26 dB) and AC-coupled (gain 50 dB) amplifiers. A biquadratic bandpass filter (centered at 10 Hz, bandwidth of 2 Hz) selects the alpha portion of the EEG spectrum. An RI'vIS-to-DC converter followed by a lossy integrator (with a time constant of 2.3 s) provides a slowly varying DC representation of the alpha component present in the EEG signals. Finally, a comparator (with hysteresis) was used to give a binary output at a selected threshold. Hysteresis is used to prevent the production of 'bounce' signals as the input to the comparator moves past the threshold level.

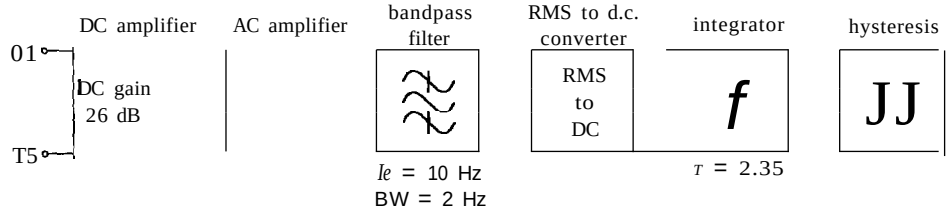

Figure 2.4: Schematic diagram of the analogue alpha detection system. The system consists of amplification, a bandpass filter, RMS-to-DC converter, lossy integrator and a comparator (with hysteresis).

2.3.1 Implementation

The analogue signal conditioning shown in Figure 2.4 was emulated digitally using C code. The input used was data from the Neurosearch-24 data files for electrodes E2 and E4 (see Figure 2.1). The differential signal was obtained by taking the difference between these two data arrays, followed by filtering. Filtering was done by a 512 tap Finite Impulse Response (FIR) bandpass filter with 3 dB points at 8 Hz and 13 Hz, using a triangular window (the response for this filter is shown in Figure 2.5). The lossy integration was achieved by convoluting the data (after filtering and RMS-to-DC conversion) with an exponential decay function $(y(t) = e^{-t/\tau})$ truncated to 512

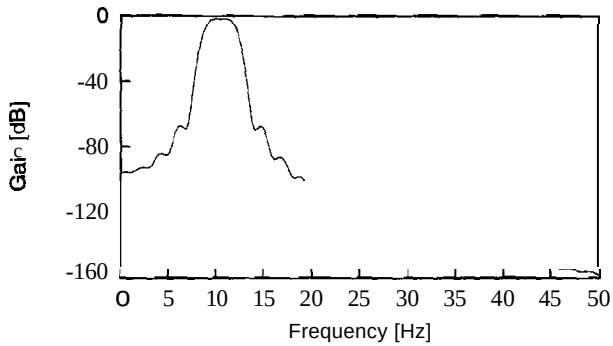

Figure 2.5: Frequency response for the 512 tap FIR bandpass filter.

samples. The time constant used was τ = 2.3 s, consistent with the hardware implementation (Kirkup et al. *1997b).*

2.3.2 A note on algorithm implementation

All signal processing programs and data manipulation routines for this thesis were written in entirety by the author, with the exception of an eigendecomposition function[5]. All programming was done in standard C code, and run on a Linux 2.0.32 operating system. At the beginning of these studies, routines were performed using Mathematica™, but processing times involved with the large EEG data files were prohibitively long. The C implementations in Linux showed completion times up to two orders of magnitude lower than using Mathematica™. This does not imply that Mathematica™ is a product of limited value, but rather that it is more appropriate for symbolic mathematics than it is for number crunching.

5The eigendecomposition function was linked from a Mathematica™ library

2.3.3 Threshold determination

When using the analogue system in normal laboratory circumstances th threshold voltage is empirically chosen. It is determined by examining th subjects' integrated alpha signal with the aid of a voltmeter. For a rigorou study, a pre-defined strategy for determining the threshold level is required This continues the use of a statistical method of threshold setting as introduced by Kirkup et al. (1998). The method determines a baselin level by sampling the output of the algorithm described in Section 2.3.1 an determining a mean, $\bar{x}$, and standard deviation, sx, of the data while th subject is sitting still with eyes open (this is the 'baseline'). Threshold level can then be defined using these statistics. For this study the nth threshol is defined as

$$nth \text{ threshold level} = \bar{x} + n\ Sx \qquad (2.1$$

Figure 2.6 shows a sample of the output for the integration method with th 10^{th} threshold level indicated.

2.3.4 Interpretation of results

The data presented here is for the integration method. To allow for efficien comparisons,- the procedure used to format results is followed for all th techniques of EEG signal processing to be used in this thesis. The dat for the 10 subjects were processed by the integration algorithm at threshol levels ranging from 1 to 20 standard deviations. The data were also processe by the algorithm with the integration step omitted (this will be called 'RMS only') for comparison.

The results from processing the EEG data via these algorithms is char acterised by:

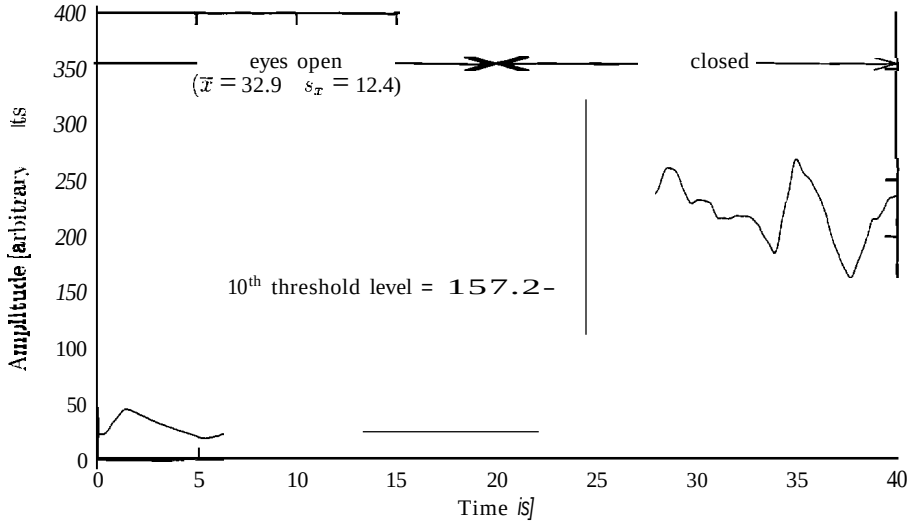

Figure 2.6: An example of the output from the integration method. The subject holds both eyes open for the first 20 seconds. At t=20 s the subject closes both eyes. An example of threshold selection is also shown; the first 20 seconds are used to determine the mean and standard deviation of the baseline (eyes open) signal. The 10^{th} threshold is shown for illustration at 32.9 + (10 x 12.4) = 157.2.

Detection Time During eye closure trials, the time after eye closure for the processed signal to rise above the threshold level. The time is measured from the moment when the audible signal is given, and thus the time includes individual's reaction time to the audible signal.

Eye Closure Errors Errors encountered during the 90 second eye closure trials. Three kinds of errors defined are

- Baseline errors (1) : The signal exceeds the threshold level when the eyes are open (before the eyes closed period), thus giving a false positive.
- Baseline errors (2) : The signal exceeds the threshold level when

the eyes are open (after the eyes closed period), also giving a false positive.

- Threshold errors: The eyes are closed but the signal fails to exceed the set threshold.

Artifact Errors Errors encountered during the 90 second trials involving jaw clenching, head movement and talking. There are three kinds of errors defined:

- Baseline Errors (1) : The signal exceeds the threshold level before the activity period, giving a false positive.
- Baseline errors (2) : The signal exceeds the threshold level after the activity period is complete, giving a false positive.
- Artifact errors: The specified artifact activity causes the signal to rise above the threshold, which is incorrectly assigned as eye closure.

The results for the detection times after eye closure for the integration, and RMS-only algorithms are shown in Figure 2.7. The detection times increase with the threshold level, as would be expected. The detection times for the RMS-only algorithm are less than that for lower threshold levels by around 1 second. This reduced detection time is offset by the large number of errors generated when using the RMS-only algorithm, as compared to the integration algorithm. These error results (for eye closure only, not due to induced artifact) are shown in Figure 2.8. The numbers of errors caused by both algorithms decrease as the threshold is increased, though the integration algorithm shows little change above a threshold setting OHOUL Removing the lossy integrator improves eye closure detection time slightly, but the increase

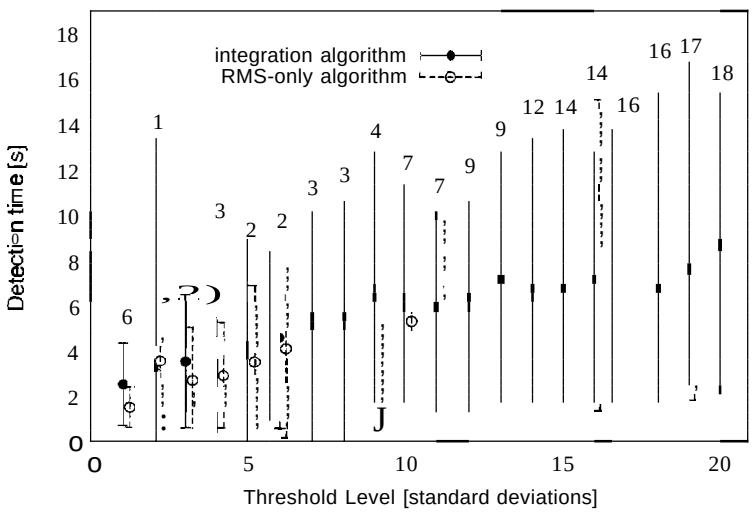

Figure 2.7: Detection times after eye closure for 10 subjects using the integration algorithm, and RMS-only algorithm. Mean and standard deviations are shown, along with numerals indicating the number of eye closure trials (out of 40) for which RMS-only detection was unsuccessful at each threshold setting.

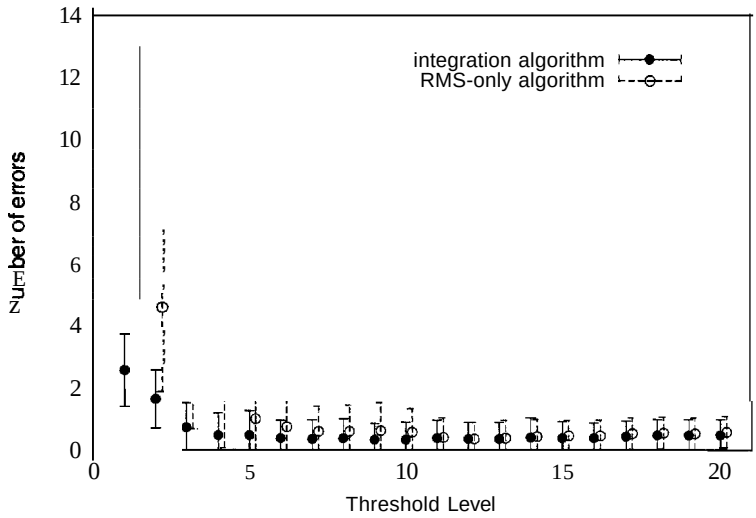

Figure 2.8: Errors experienced during eye closure trials for 10 subjects using the integration algorithm, and RMS-only algorithm. Mean and standard deviations are shown.

in errors is more than 100% for threshold settings less than four. From Figure 2.8 it could be assumed that the optimal threshold for use of the integration algorithm would be a value of $n = 4$. At this point the number of errors is at a minimum. Although the number of errors does not increase with larger thresholds, the detection time will increase (refer Figure 2.7). The opposing results from the error and detection time plots make a decision regarding the optimum threshold setting problematic; a lower threshold gives a reduced detection time but more errors. The threshold setting decision process also needs to include information about errors caused by artifact; this data is not included in Figure 2.8. Figure 2.7 may also be misleading as it does not denote how many subjects were able to reach a given threshold during eye closure. A low detection time result for a given threshold may mean that, on average, the method detected the alpha EEG increase for all subjects quickly, or perhaps that only one or two subjects managed to reach

the threshold (and did so quickly) whilst the other subjects did not reach the threshold at all, and as such their detection times were not included in results. Therefore the low detection time results do not reflect the possibility that the method may have been unsuccessful at a particular threshold setting.

2.3.5 An alternative method of comparing results

To enable a fair determination of the best threshold setting which can be used for many different alpha detection methods, the detection time data will be plotted against total errors (which includes the errors encountered during the eye closure trials and during the artifact trials). To ensure that data are representative of the majority of EEG trials, results are shown only when at least 75% of eye closure trials are successful in reaching the threshold. That is, the data point for a threshold setting is only shown when at least 75% of all eye closure data (including all subjects) show success in reaching the threshold level. This prevents data from a subject who has a very large and fast change in alpha amplitude after eye closure from causing a poor detection method to look very effective. Thus, data points linked to different thresholds displayed in plots for the figure of merit represent results from all data sets (i.e. from all subjects). Figure 2.9 shows a plot of this type for data from integration and RMS-only methods. Using this plot the best threshold setting can be denoted as the point closest to the origin (thus having the smallest combination of detection time and total errors). A figure of merit will be used in this study to denote the distance from the origin to a data point, denoted as $\overline{\chi}$ (since the value is an average of many data sets). In Figure 2.9 the best threshold setting (giving a value of *X=4.13)* is for the integration method, at a threshold of 3 standard deviations. Importantly this scheme weights errors and detection times in such a manner that a

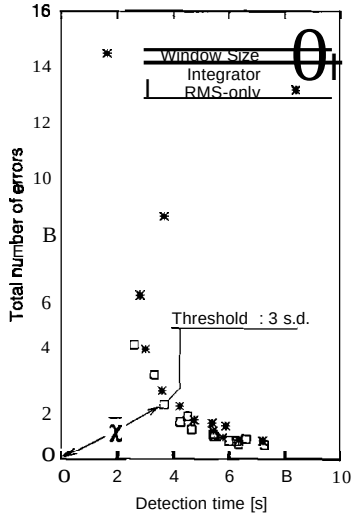

Figure 2.9: Data for detection times and total errors (eyes closed errors and artifact errors) for the integration and RMS-only methods. A range of threshold settings are shown (for which at least 75% of the data sets showed successful detection during eye closure) and the best threshold is identified.

reduction in detection time of one second is regarded of equal importance to a decrease in total errors by one. If different weightings of importance in favour of detection time or total errors were required, the data could be scaled so that the best threshold setting was still closest to the origin. For investigations with specific applications or subjects in mind, these scalings could be set a variety of reasons; this is not the case for the general study in the thesis, and the scales will be left as a ratio of 1:1.

2.3.6 Combinations of electrode pairs

The integration method applied in Section 2.3.1 used the electrode positions E2 and E4 (refer to Appendix C, Figure C.1), as these are closest to the 01 and T5 locations that have been used in previous experiments (Kirkup et al.

1998, Kirkup et al. *1997b).* Other combinations of electrodes on the headband can be used, perhaps with better results. The integration method was applied

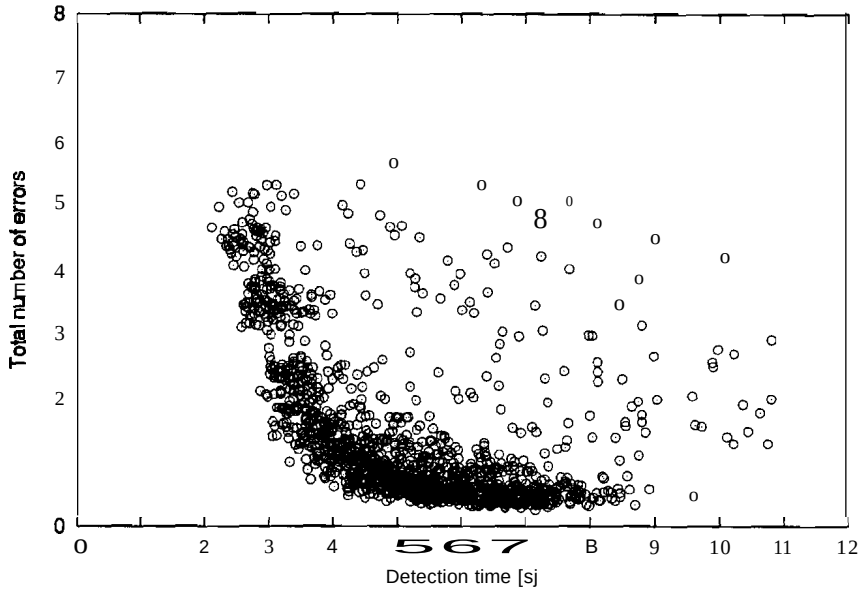

Figure 2.10: Results for all possible combinations of the 19 electrodes for all subjects using the integration alpha detection technique.

to all data sets using each possible combination of the 19 electrodes shown in Figure C.l. There are a total of $\binom{19}{2}$ = 171 combinations. Figure 2.10 shows results for the 171 combinations averaged over all data sets for the 10 subjects. The lowest $\overline{\chi}$ value came from the electrode pair E4 - E18 (at a threshold level of 4 standard deviations), although the difference between the pairs which show low $\overline{\chi}$ values is not great. The ten electrode pairs which showed the lowest $\overline{\chi}$ results are illustrated in Figure 2.1l(a). The pair used originally (E2-E4) do not appear in the top ten 'scores'. The $\overline{\chi}$ value for the E2-E4 electrode pair was 22% higher than the best electrode pair E4-EI8. For comparison, the difference between the best and tenth electrode pair (rated on $\overline{\chi}$ values) was 9%.

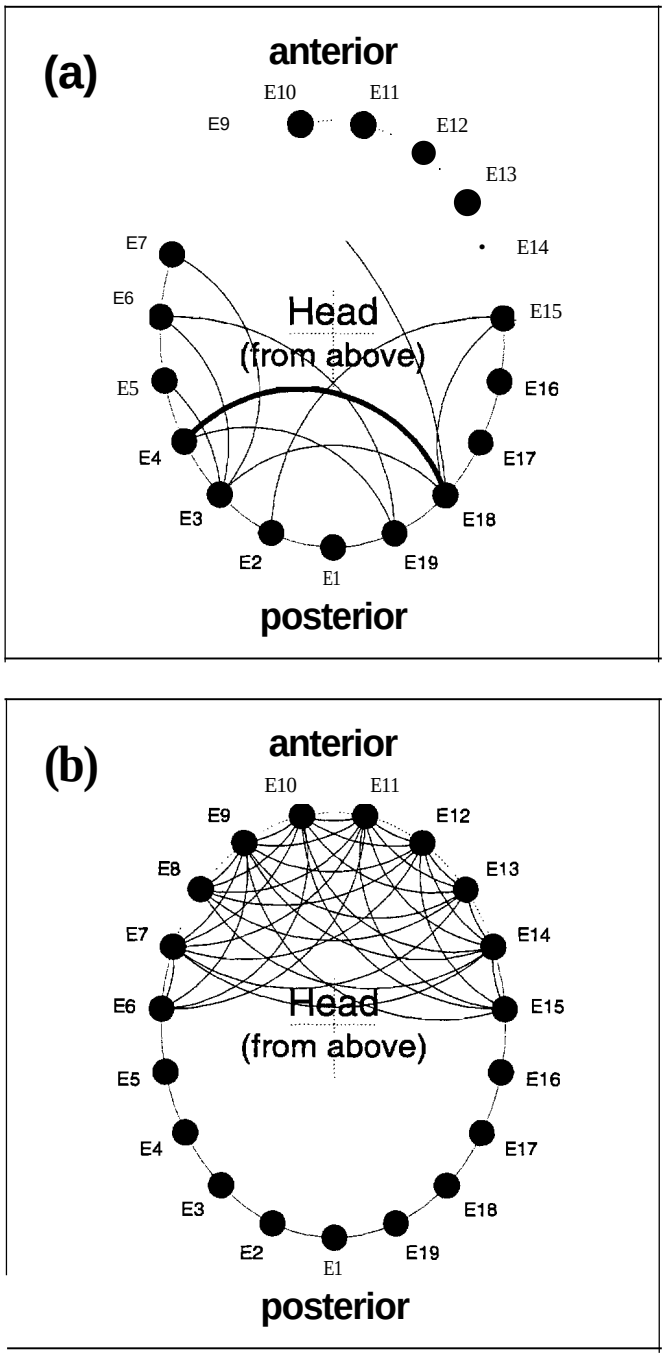

Figure 2.11: Results from applying the integration technique to all possible combinations of electrode pairs. The 10 electrode pairs with the smallest $\overline{\chi}$ values are shown in (a); in bold is the E4-E18 pair which showed the lowest $\overline{\chi}$ value. Plot (b) indicates those electrode pairs which did not perform satisfactorily for any threshold setting.

Figure 2.11 (b) shows the electrode pairs which showed poor performance. These were 36 pairs of electrodes which failed to detect an alpha rise (for at least 75% of eye closure trials) using any threshold setting. As might be anticipated, these pairs are concentrated at the front of the head, whilst the best electrode pairs occur at the rear of the head, near the occipital region where, in general, alpha activity is recognised to be greatest (Shaw 1992). Some of the best performing electrode pairs do make use of electrodes in the anterior region, which agrees with results found by Craig et al. (1999) who report that high activity resulting from eye closure is found in central and anterior regions, not just the occipital region.

The results for the integration method will be compared with many other alpha detection techniques in this thesis. For those methods which use a differential EEG signal, a common pair of electrodes need to be chosen so that all methods can be compared evenly, and the E2-E4 pair will be used for this purpose. Although this pair did not show the best performance in the integration trials, the E2-E4 pair will be used because of many studies in the past (e.g. Cram et al. 1977, Mulholland 1971) that have used differential readings from this cranial area (thus being useful for comparison) and because it cannot be assumed that the electrode pair that was best for the integration method will be equally good for other techniques. Although it would be ideal to compare all possible electrode combinations for all techniques to be used, the computing time required does not make this realistically possible. The processing for the integration technique required around 8 days of computing time to process all electrode combinations, and other methodologies to be introduced require even more computational resources, making the gathering of such results infeasible.

2.3.7 An extension to reduce the influence of false positive results

As shown in Figure 2.3, the frequency spectra from artifacts, such as EMG and head movement, overlap the alpha EEG frequency spectrum. The consequence of this is that signals from artifact sources may cause false positive results (i.e. the threshold may be exceeded despite the absence of an increase in alpha activity). Filtering in the frequency domain will not separate the true alpha EEG and artifact sources as the spectra overlap. However, since the alpha EEG is narrowband and the artifact signals show comparatively wideband spectral characteristics it is possible to detect the presence of artifact signals regardless of the current level of alpha EEG activity by monitoring the spectral power at frequencies outside the alpha band (8-13 Hz). **In** this way the output of the alpha EEG detection method can be disabled while the 'artifact activity' is high, on the assumption that high spectral power outside from the alpha band implies high spectral power inside the alpha band due to artifact. To implement this concept the following scheme was used:

1. Monitor the alpha EEG activity using the integration detection method (as described in Section 2.3.1).

2. Simultaneously monitor spectral power in the 'artifact band' (chosen to be 28-33 Hz). This was accomplished using the same algorithm as for the alpha integration detection method, but in this case the bandpass filter was set from 28 to 33 Hz (rather than 8-13 Hz). The thresholds were set in the same way as for alpha EEG (see Section 2.3.3). The threshold level used to denote the presence of 'artifact activity' was fixed at $n = 10$ standard deviations.

3. If the threshold for the 'artifact activity' was exceeded then the lossy integrator used for alpha activity was set to zero. Thus, while artifact activity is present the alpha activity output is disabled.

The operation of the 'artifact rejection' algorithm is demonstrated in Figure 2.12. Graphs (a) and (b) show the level of alpha EEG activity, as determined using the algorithm, during eye closure and jaw clenching respectively. Graphs (c) and (d) show the corresponding level of 'artifact activity' in the 28-33 Hz band. During eye closure, the level of alpha activity increases (Figure 2.12(a)) while the artifact activity is unchanged (Figure 2.12(c)). During the jaw clench trial, the artifact activity shown in Figure 2.12(d) is apparent, and while the artifact activity exceeds the threshold the 'alpha activity' output is disabled (Figure 2.12(b)). Plot (b) also shows what the alpha activity output would indicate without the use of the artifact rejection: the peak around 40-50 s would have caused a false positive result. This is prevented by the monitoring of the 28-33 Hz band by the artifact rejection algorithm.

Results obtained when the artifact rejection extension to the integration alpha EEG detection method was applied to all data sets are shown in Figure 2.13. The results are compared to values obtained when the original integration alpha detection method was used. As Figure 2.13 shows, the detection times for the two methods are the same for the range of thresholds shown, but the errors encountered when using the artifact rejection algorithm are consistently lower. Though the artifact rejection algorithm is incorporated in the integration alpha EEG detection method here, any of the other alpha detection techniques to be described in this chapter could be similarly modified.

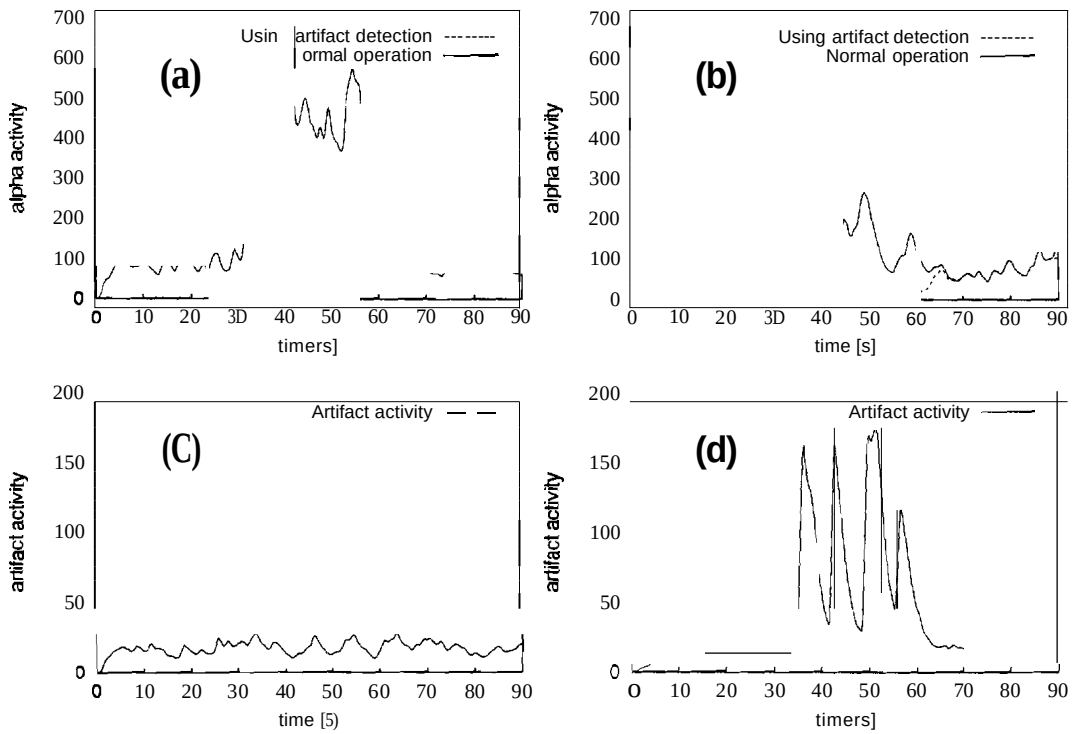

Figure 2.12: Operation of the artifact rejection algorithm. Plots (a) and (b) show the output of the integration alpha detection method with and without the artifact rejection algorithm. Plot (a) shows eye closure data (eyes closed from 30-60 s), while plot (b) shows data from a jaw clenching trial (also in the period 30-60 s). Plots (c) and (d) show the 'artifact activity' corresponding to the eye closure and jaw clenching trial. Note that no artifact is detected during the eye closure trial (plot (a)), thus the two curves in this plot overlap exactly.

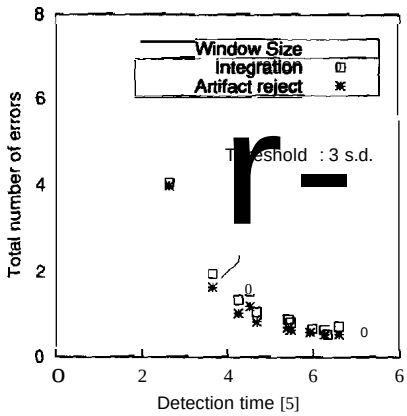

Figure 2.13: Results obtained when using the artifact rejection algorithm, applied to all EEG data sets for a range of threshold settings. The integration alpha EEG detection method (without artifact rejection) is shown for comparison.

2.4 The Percent Time method

This alpha detection method relies on the statistics of the alpha EEG signal to indicate when an alpha increase associated with eye closure occurs. Specifically, the distributions of peak amplitudes of the bandpass filtered, rectified EEG signals are calculated. The change in the statistics from eyes open to eyes closed periods can be used to detect an increase in alpha activity following eye closure.

2.4.1 Distributions of peak EEG amplitudes

Dick & Vaughn (1970) have found that the alpha EEG can be described effectively as narrow-band gaussian random noise. The probability density function for peaks of narrow-band gaussian random noise is given by the

Rayleigh probability density function (Nikookar & Hashemi 1993).

$$p(x) = \begin{cases} \frac{x}{\sigma_x^2} \exp(\frac{-x^2}{2\sigma_x^2}) & x \geq 0 \\ 0 & x < o \end{cases} \tag{2.2}$$

where σ_x^2 is the variance of the narrow-band gaussian random noise. An advantage of the Rayleigh probability density function is that it is described using a single parameter, 0". In Figure 2.14 the averaged distributions of peak alpha amplitudes for the 10 subjects are shown for periods of eyes open and eye closure. The best fitting Rayleigh distributions are also shown for the

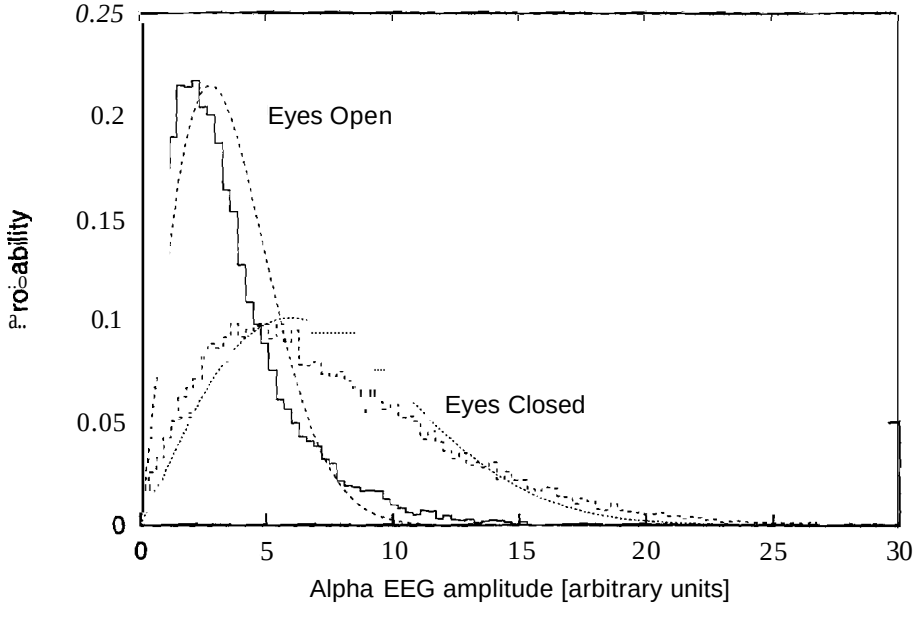

Figure 2.14: Probability distribution functions of rectified alpha EEG maxima for eyes open and eyes closed periods. The data is averaged over 40 data sets (10 subjects). Rayleigh distribution curves are shown for comparison.

eyes open and eyes closed cases.

Some studies (de Rooij & Smeyers 1974, Bozinovski 1990, Ghiyasvand et aI. 1995, Basmajian 1983) have, in addition to amplitude distributions,

used distributions of the time interval between EEG peaks to assist in determination of alpha activity. Data collected in this study did not show any appreciable difference eyes open and eyes closed periods for the time intervals between successive maxima, and thus this information is not included in any algorithms used here. This was shown using a single factor ANOVA test: there was no significant difference between the distributions of time interval values in each eyes closed or eyes open period. An illustrative time series example showing the periods between maxima for rectified EEG is shown in Figure 2.15.

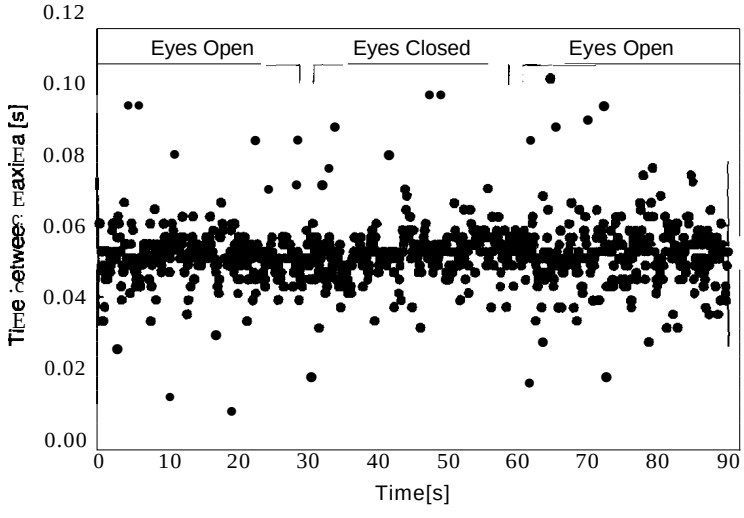

Figure 2.15: Pe!iods between rectified EEG maxima. There is no appreciable change from eyes open to eyes closed sections.

An attractive method for detecting changes m alpha EEG during eye closure would be to track the EEG maxima distribution, finding the best fit to a Rayleigh distribution and use the σ parameter as an indicator as to alpha EEG activity. Unfortunately the amount of data required to produce a reasonable distribution is too great, and thus the detection process would be very slow (assuming that rectified alpha EEG is used, approximately 20 data

points per second would be produced). The statistics of the distributions shown in Figure 2.14 are still valuable, and their use shall be demonstrated in alpha detection techniques in Sections 2.4.2 and 2.5.

2.4.2 Percent Time implementation

For the percent time alpha detection method the EEG signal is bandpass filtered, rectified and the distribution of amplitudes obtained with the eyes open. The percentage of time that the signal remains over the median peak amplitude is measured. To give a continuous measure of the percent time spent over the median a sliding window of predetermined width is required. **In** this implementation the algorithm counts the number of peaks above the median in the window; this gives a measure proportional to a percentage. This process is outlined in Figure 2.16. The mean and standard deviation of the resulting percent-time curve are obtained for eyes open (as in Section 2.3.3). The errors and detection times for each standard deviation level are determined. This process is repeated using window sizes of 512, 1024, 2048 and 4096 samples (corresponding to 1, 2, 4 and 8 seconds).

2.4.3 Results

Results from aPlJlying the percent time algorithm to all subject EEG data are shown in Figure 2.17(a). The best results comes from using a sliding window size of 2048 samples (4 s) at a threshold of 2 standard deviations. The EEG data were also processed by a modified version of the percent time algorithm in which a cutoff level of 90% quantile of the eyes open distribution was used instead of the median. Figure 2.17(b) shows the results when using a 90% quantile cutoff. The plots reveal that the higher cutoff level produces

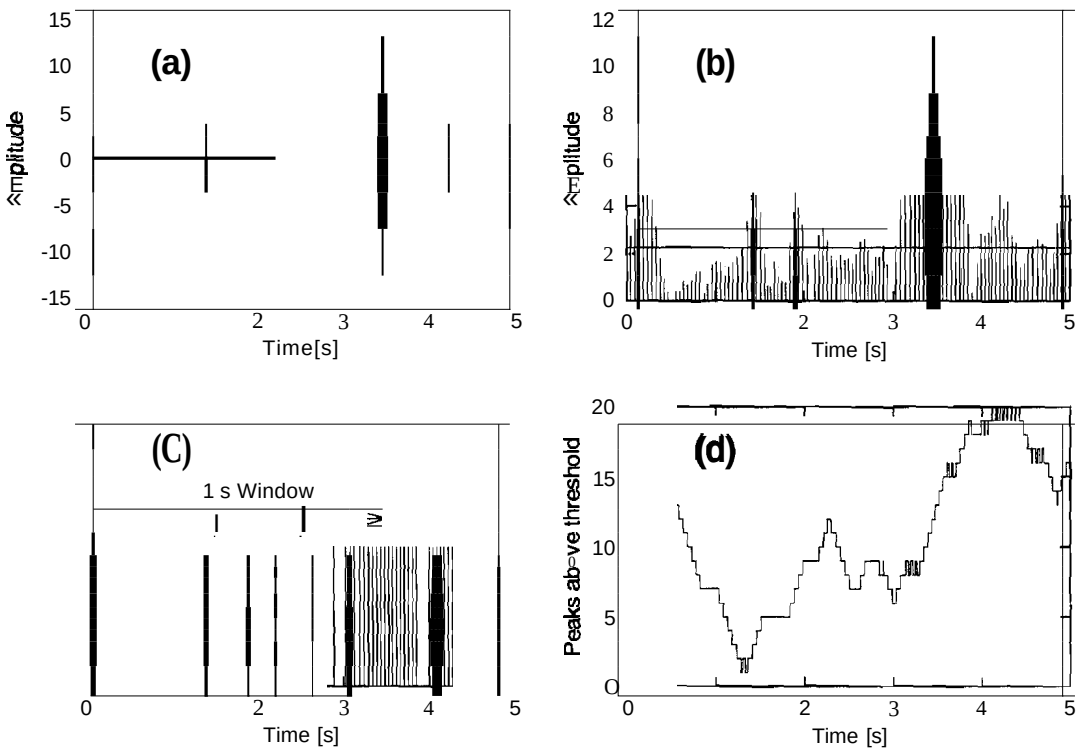

Figure 2.16: The process for the percent time alpha detection method. The EEG signal is (a) bandpass filtered, rectified and (b) peaks are identified. The distribution of peaks during eyes open is found and the median determined: the median value is shown as a horizontal line in (b). A sliding window moves along the set of peaks which are above the median (c), and the number of peaks in the window are counted giving a result such as (d). For this example the window size was 512 samples (1 s).

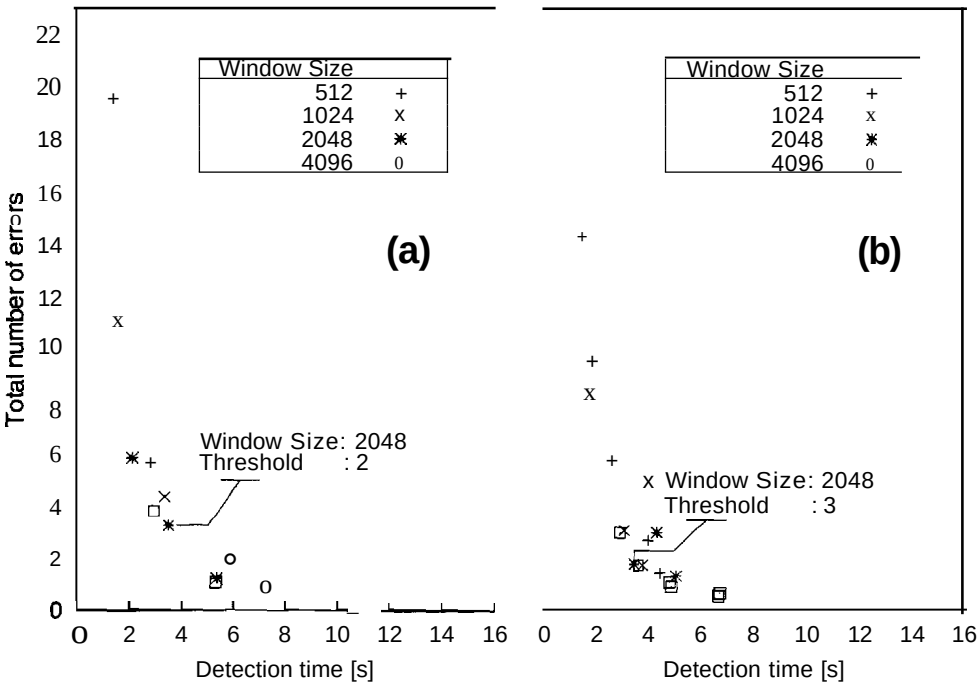

Figure 2.17: Results for Time calculation method using a median cutoff (a), and using a 90% quantile cutoff (b). Parameters for best results are shown.

a better result. Noticeably, the number of errors experienced is less and the detection time is slightly faster.

2.5 The Peak Counting method

This alpha detection method is a modification of the percent time technique. As in the percent time technique (Section 2.4.2) the EEG signal is bandpass filtered, rectified, maxima located and a distribution of the peak amplitudes during eyes open found. The number of peaks with amplitudes above the median value are monitored. If the number of consecutive peaks with amplitudes above the median exceeds a preset count limit then the algorithm

sets an alpha indicating that EEG alpha activity has been detected. Similarly, once alpha EEG has been detected (the flag has been set) the same number of peaks consecutively below the threshold must be counted for the alpha flag to be reset (indicating that alpha EEG activity is not present). The threshold for this implementation will be quantile levels of the eyes open peak amplitude distribution (an example of which shown in Figure 2.14). The threshold is varied from the 5% quantile to the 100% quantile in 20 steps. As before, the errors and detection times are calculated for all subjects for a range of threshold settings.

2.5.1 Results

Results for the peak counting method using a range of count settings are shown in Figure 2.18. The plot shows that the lowest $\overline{\chi}$ value is achieved

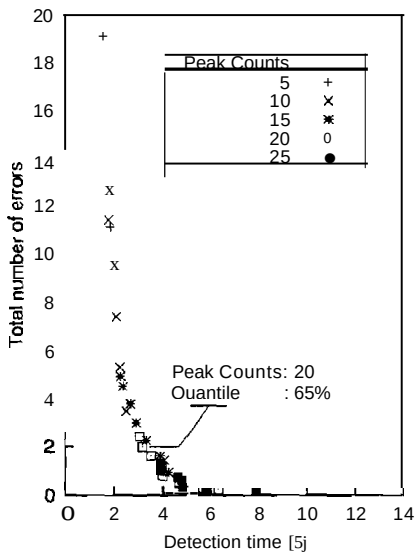

Figure 2.18: Results for the Peak Counting method using the peak amplitude distribution during eyes open

using the 65% quantile of the eyes open distribution as a threshold, and

requiring 20 counts to denote the presence of alpha EEG.

All statistical information used by the alpha EEG detection methods described thus far to set threshold levels has been from the amplitude distribution of signals during the eyes open periods. The peak counting method was also modified slightly to use the distribution of amplitudes found during eye closure. As many artifact signals are larger than the EEG signal present, it may be possible to limit the false information received from artifact signals by applying an upper threshold as well as a lower threshold. Thus a peak will only be counted if its amplitude exceeds a lower threshold (as before), but is also less than an upper threshold (thus preventing peaks of large amplitude, which may be due to artifact, from causing a false positive alpha EEG reading). This was done by obtaining the eyes closed peak amplitude distribution and only counting peaks which are between a lower threshold and upper threshold. As for the in Figure 2.18, the lower threshold is varied as a quantile of the distribution (this time between 4.5% and 90%) while the upper threshold is fixed at the 95% quantile level. This procedure requires prior knowledge of the eyes closed peak amplitude distribution for each subject. This information was obtained by taking the average of the distribution for eye closure during each of the four eye closure trials that each subject undertook (see p. 25). The results for the peak counting method using two thresholds and eye closure distribution are shown in Figure 2.19. The lowest $\overline{\chi}$ value shown in this plot requires 15 counts in the window to denote alpha activity, with a threshold setting at the 22.5% quantile of the eyes closed peak amplitude distribution (and the upper threshold at the 95% quantile level). This implementation of the peak counting method using the eyes closed distribution and an upper and lower threshold performs slightly worse than when using the eyes open distribution with a single (lower) threshold (shown

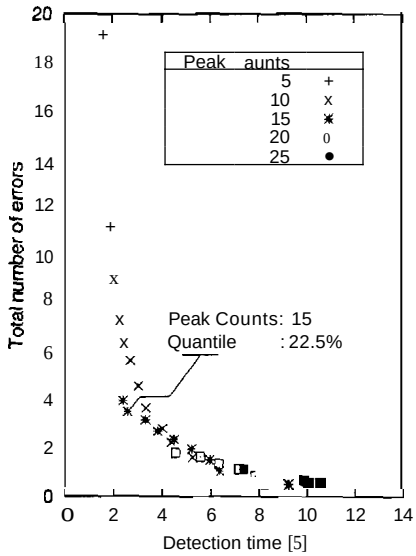

Figure 2.19: Results for the Peak Counting method using the peak amplitude distribution for eye closure with an upper and lower threshold.

in Figure 2.18). Results for the eyes closed distribution (Figure 2.19) are noticeably stretched along the horizontal axis, indicating increased detection times. It is surmised that the upper threshold is causing higher detection times by ignoring peaks that are not artifact, but are actually true alpha EEG. This has to occur to some extent since the distribution is taken from the eye closure trials for each subject, and the upper threshold is set to the 95% quantile of the distribution. Unfortunately, the increase in detection times due to the the upper threshold are not offset by lower total errors as hoped. To confirm that the upper threshold is affecting detection time, Figure 2.20 shows the results using the eyes closed distribution, but without the upper threshold. The results show a large improvement over those when using the upper threshold in Figure 2.19, and the best settings (using a 25% quantile threshold and a required peak count of 20) show better performance than those using the eyes open distribution (Figure 2.18).

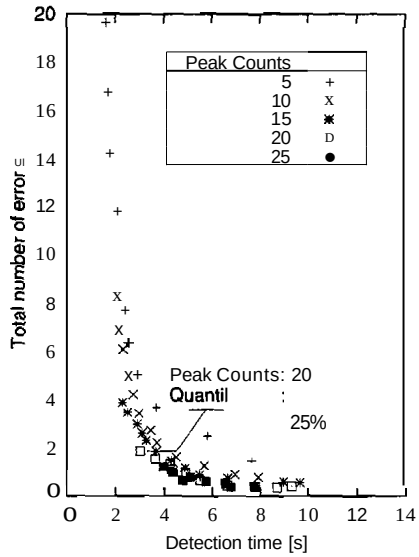

Figure 2.20: Results for the Peak Counting method using the peak amplitude distribution for eye closure without upper threshold

2.6 A comparison of results and discussion

Variability between subjects makes the direct comparison of results from different alpha EEG detection methods difficult. The large standard errors in data due to inter-subject variability means that comparing the mean $\overline{\chi}$ values may give misleading results. Instead a paired t-test is used to rank the different methodologies. To facilitate this all methods developed in this chapter will be compared to the integration alpha EEG detection technique, as this method has been investigated in past studies (Kirkup et al. 1998, Kirkup et al. *1997b).* A value for $\overline{\chi}$ is calculated using EEG from each of the 10 subjects applied to each alpha EEG detection method, and taken. The threshold used for each technique is the setting which was found previously to give the lowest $\overline{\chi}$ value for that technique. A p value from a paired t-test is found for each alpha detection technique compared against the

integration method using the ten $\underline{\ln(x)}$ values (one for each subject). Using the p value for each test the methods can be ranked in comparison to each other; the mean value for each method is used to determine whether the p value indicates a difference which is higher or lower than the integration alpha detection method. The rankings are shown in Table 2.1. Table 2.1 reveals that the use of the integration method with artifact rejection gives the best ranking. Also ranked highly were the peak counting method using the eyes open distribution (see Figure 2.18) and peak counting method using the eyes closed distribution (using one threshold). The peak counting method using the eyes closed distribution with two thresholds shows a relatively poor rank due to slower detection times caused by the more rigid algorithm (unfortunately the extra threshold did not reduce errors as anticipated).

The rankings for the percent time algorithms show that the performance depends very much on the the results which used a cutoff at the 90% quantile level of the eyes open distribution are ranked much better than those at the median (50% quantile) setting. The difference between the two quantile level settings for the percent time alpha EEG detection method is also evidenced by the small number of usable parameters for the 50% quantile results (few data points in Figure 2.17(a)) compared to the 90% quantile setting in Figure 2.17(b). The integration method fared better, as expected, than the RMS-only technique (which was affected by increased numbers of errors). However, in this study marginal improvements in detection time and error rates are of little importance even if they are found to be statistically significant. It is possible that, due to the smaller sample size, some detection methods may be considered as not a significant improvement over the Integration method, whereas a large sample size may give a different result; this is known as a type-2 error. In this study guarding against type-2 errors

Alpha Detection Method	mean $\ln(\bar{\chi})$ value and std error	p value	rank
Integration with artifact rejection	1.347 ± 0.102	0.139	1
Peak Counting: eyes open distribution	1.275 ± 0.092	0.281	2
Peak Counting: eyes closed distribution (one threshold)	1.277 ± 0.090	0.326	3
Percent Time (90% quantile)	1.343 ± 0.082	0.541	4
Integration	1.392 ± 0.093	-	5
Peak Counting: eyes closed distribution (two thresholds)	1.462 ± 0.080	0.601	6
RMS-only	1.472 ± 0.107	0.503	7
Percent Time (50% quantile)	1.732 ± 0.157	0.110	8

Table 2.1: Ranking of results fwm alpha detection techniques introduced in Chapter 2. Techniques are ranked using the p value from a paired two-tailed t-test, compared against the integration alpha EEG detection method.

is less important than finding an approach to detect the onset of alpha with low error rates that is shown to be superior than the other techniques, even with a small sample size. If the differences between results from methodologies are so slight that a type-2 error is likely to occur, then the advantage that the new method gives will be very slight, and thus not of interest anyway.

Four methods of alpha EEG detection have been introduced in this chapter. Two of these techniques are commonly used in alpha EEG feedback studies; the integration method and the percent time method. The results from this study show that the percent time method has a better performance ranking than the integration method, though the difference is marginal and the percent time algorithm is highly dependent on the percent quantile setting used (using a 90% quantile setting showed a significantly better $\overline{\chi}$ value than when a 50% quantile setting used). However, the use of artifact rejection improves the results obtained with the integration method, and it is anticipated that this improvement would be found if the artifact rejection algorithm were used with other alpha EEG detection methods. The comparative success of the integration and percent time alpha detection methods found in this study will not necessarily transfer to the application to feedback studies, where there is less emphasis on artifact rejection or detection time.

The method with the highest ranking in Table 2.1 was the integration method (when used with artifact rejection). artifact rejection is not employed, the highest ranking detection technique was the peak counting technique (using the eyes open amplitude distribution for a reference). The same method using the eye closed distribution (with one threshold) was also highly ranked (this reflects results found in an exploratory study using a

smaller data set by Kirkup et al. (1998)). Peak counting alpha detection methods are additionally attractive as their algorithms are simple, and could be easily run on a small microcontroller (or other simple dedicated electronics). One drawback is that the EEG peak amplitude distribution for each subject needs to be known prior to the algorithms use, thus a short training period for the algorithm is necessary. Further study is required to determine the optimal amount of data required to construct a satisfactory amplitude distribution for use with peak counting alpha EEG detection methods, and to decide whether an a-priori average distribution from a wide population can be successfully used. The results obtained when an upper and lower threshold were used in an effort to reduce the influence of artifact errors (rather than a single lower threshold) with the peak counting algorithm proved to be unsuccessful. The $\overline{\chi}$ values obtained from the use of two thresholds were larger than those obtained when a single threshold was used.

Chapter 3 will investigate the improvements offered by preprocessing EEG signals before the application of alpha EEG detection methods. The preprocessing techniques will involve the use of many electrode sites, rather than a differential pair as used for methods described in this chapter. By employing many electrodes, spatial information may be used in addition to amplitude information to prevent false positive detection of alpha activity in the presence of artifact signals.

Chapter 3

Multi-electrode methods for alpha EEG detection

3.1 Introduction

The alpha EEG detection methods described in Chapter 2 employed differential signals obtained from two EEG channels. Such methods perform satisfactorily, but in the presence of artifact false positive results may occur. In an effort to produce a faster and more reliable alpha detection system, more complicated techniques are introduced in this chapter which use the information from many electrodes, rather than from a single pair. Although the techniques to be described add complexity to the alpha detection process, it is anticipated that the new methods in this chapter will offer benefits such as:

- Using many electrodes to extract information specific to alpha EEG will decrease the detection times for alpha.
- By reducing the presence of non-alpha signals, lower threshold settings

can be used in the detection algorithms, thus enabling lower alpha EEG detection times.

- The number of artifact errors encountered will decrease

The procedures explored in this chapter have not been applied to the detection of alpha activity in EEG previously and thus the production of successful techniques is not a certainty. It will be shown that some of the alpha detection techniques developed in this chapter offer performance improvements over those described in Chapter 2.

The techniques described in this chapter can all be considered as filtering operations; these filters act on the array of EEG channels and create a single output signal. The resulting output signal may then be applied to an alpha detection method. Thus the topics introduced in this chapter can be considered as preprocessing operations to the alpha detection methods covered in Chapter 2. To enable a comparison between all methods to be described in this chapter, the same alpha detection method will be used after the preprocessing is done. The integration alpha EEG detection method (see Section 2.3.1) will be used, though any of the detection methods in Chapter 2 would be equally suitable for the task of comparing the preprocessing techniques. Before the first filtering technique is described, the basic concepts which will be used for many of the preprocessing techniques in the chapter are introduced.

3.2 Array sensor processing

Many of the concepts in this chapter originate from communications and radar theory, as these fields often utilise many antennae (i.e. a sensor array) to obtain desired effects than cannot be achieved using a single antenna. As

an example, arrays of antennae are routinely used to select the direction from which to receive a signal, while signals propagating from other directions are rejected. Conversely the antenna array can be used to determine from what direction a selected signal has arrived. These principles can be applied to the context of EEG in this chapter in that signals originating in one region of the head can be amplified, while signals from elsewhere can be attenuated. The task of investigating neural sources in the brain responsible for activity has long been a central focus of neurophysiological research because anatomical correlates are useful for many tasks (e.g. in studies of epilepsy or evoked potential work). The signals from a neural source at a required physical position may be extracted directly using depth electrodes, but this process cannot monitor every possible point in the brain, and is an highly invasive procedure. Thus the use of external processing methods to enable the probing of different locations in the brain very useful. Since it is widely accepted (refer to Section 1.1.1) that alpha waves are prominent in the posterior region of the head, a filter could be constructed which uses all of the EEG electrodes to focus on signals from the posterior area, while signals which originate from the front of the head (which may contain artifact, e.g. eye blinks or forehead EMG) can be attenuated. An introduction to the theory behind sensor arrays is contained in Section 3.2.1 and the mathematical notation that will be used in this chapter is summarised in Table 3.1.

3.2.1 Representation of signals impinging on sensor arrays

To introduce the concept of the sensor array, assume there exists a sinusoidal signal source *s(i)* and a number of sensors capable of detecting signals from that source (Cadzow 1990). Figure 3.1 shows a source and an arrangement

velocity	c	Frequency, wavelength	f, λ
Angular Frequency	w	Wave number	$k = \frac{2\pi f}{c} = \frac{\omega}{c} = \frac{2\pi}{\lambda}$
Vector, Matrix	a, A	Values of a are complex	$\mathbf{a} \in \mathbb{C}$
Complex Conjugate	A*	Hermitian Transpose	$AT = (A^*)T = (A^T)^*$
Unit matrix	I	Covariance of A	Cov[A]

Table 3.1: Mathematical notation for sensor array processing

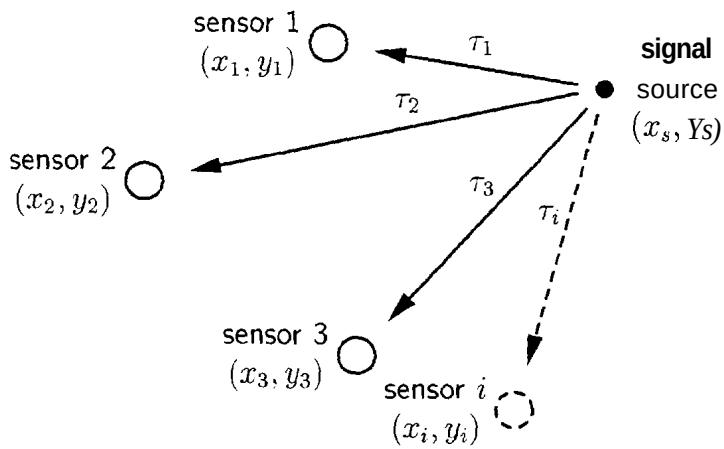

Figure 3.1: A signal source and four sensors, with propagation time τ to each sensor

of sensors. The time τ_i for a wavefront i to travel from the source at (X_S, Ys) to the i^{th} sensor at *(Xi, Yi)* is given by

$$\tau_i = \frac{1}{c}\sqrt{(x_i - x_s)^2 + (y_i - y_s)^2} \tag{3.1}$$

The input at sensor i will be *Xi(t),*

$$\begin{aligned} Xi(t) \quad - \quad & s(t - \tau_i) + n(t) \\ & s(t)e^{-jwT_i} + n(t) \end{aligned} \tag{3.2}$$

where $n(t)$ is a noise term. Thus the signals x received by an array of L sensors can be conveniently expressed in vector form as

$$x(t) = a(x, y)s(t) + n(t) \tag{3.3}$$

$$\text{where} \quad a(x, y) = \begin{vmatrix} & \\ & \\ & \end{vmatrix} \tag{3.4}$$

Vector a is known as the *steering vector* or *propagation vector* for the source with coordinates (x, y). If this model is extended to so that it includes M sources rather than one, we have

$$x(t) = [a(xl, y_1) \ldots a(xM' YM)] \begin{vmatrix} {}_{81}(t) \\ \\ 8M(t) \end{vmatrix} + nJ(t) \tag{3.5}$$

$$\text{or} \quad \underset{LxI}{x(t)} \quad \underset{LxM}{A(e)} \quad \underset{Mxl}{s(t)} + \underset{Lxl}{net)} \tag{3.6}$$

Where all elements are complex valued: x, A, s, $\in \mathbb{C}$.

3.2.1.1 Propagation speed of alpha waves

To use the equations in Section 3.2.1 either the wave speed or wavelength for the alpha EEG rhythm is required. The wave speed is not equal to the transmission speed- between neurons & Liley 1996), as this speed varies from 1 m·s-^{1} (thin unmyelinated neurons) to 10 m·s-^{1} (thick unmyelinated) to 100 m·s-^{1} (myelinated).

Work done on the propagation of electrical signals in the brain has revealed phase velocities of7 m's-^{1} to 11 m·s-^{1} (Burkitt et al. 2000). This range confirms theoretical predictions (Nunez 1995, Thatcher et al. 1986) which are calculated using mode frequencies and Maxwell's equations. For calculations in this study the alpha EEG wave velocity c is taken to be 10 m·s-^{1}.

3.2.2 The Uniform Linear Array (ULA)

If the situation in Figure 3.1 is simplified so that the signal is in the far field (i.e. the signal source is far enough away that wave fronts incident on the sensors can be assumed as parallel) and the sensors are linearly aligned with equal spacing *d,* the situation is as shown in Figure 3.2. This is called a

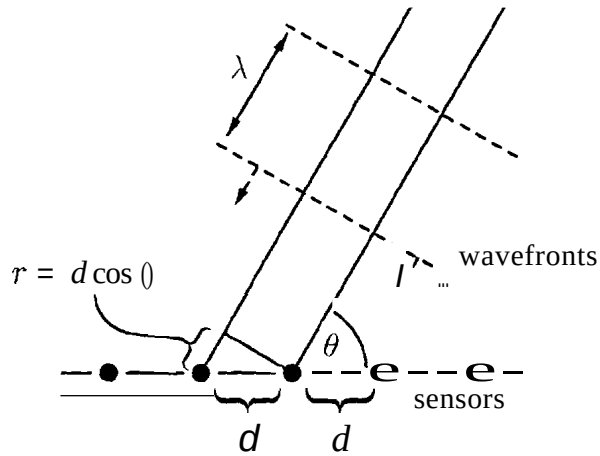

Figure 3.2: The Uniform Linear Array.

Uniform Linear Array (ULA). The delay in signal reception experienced by one sensor relative to an adjacent sensor is given by

$$\tau = \frac{r}{c} = \frac{d\cos()}{c} \tag{3.7}$$

The steering vector in Equation 3.4 becomes

$$a(()) = \begin{vmatrix} 1 \\ e\text{-}jkdcos(\} \\ \\ e\text{-}jk(L\text{-}l)dcos(\} \end{vmatrix} \tag{3.8}$$

Vectors with this type of structure are also known as *Vandermonde* vectors (Stoica & Nehorai 1989). Equation 3.3 becomes (neglecting the noise term)

$$x(t) = a(())s(t) \tag{3.9}$$

The response of a sensor array to a signal can be found by summing its inputs,

$$y(t) = \sum_{i=1}^{L} x_i(t)$$

$$S(t) \sum_{i=1}^{L} e\text{-}jk(i\text{-}1)d\cos O \tag{3.10}$$

The signal magnitude $G(\theta)$ for a signal arriving from direction () at aULA can be shown to be (Clarkson 1993),

$$|G(B)| = \frac{1}{L} \left| \frac{1 - e\text{-}jkdL\cos\theta}{1 - e\text{-}jkdcosO} \right| \tag{3.11}$$

The effects of varying the number of array sensors on the gain can be seen in the polar plots of Figure 3.3. These plots show the gain for signals ap-

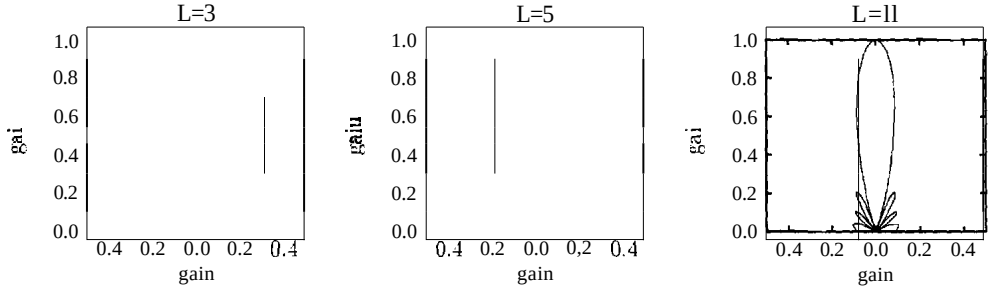

Figure 3.3: Effect of array size on the sensor array response for aULA.

proaching the sensor array in the range $0^0 < \theta < 180^0$. The highest gain is found at () = 90^0. As the number of sensors L increases the selectivity of the array increases (i.e. the beamwidth decreases), but more sidelobes appear.

Just as the sensor arrays in Figure 3.3 are selective towards signals coming from $\theta = 90^0$, the array can be made to be selective to other directions of arrival by including coefficients w as in Equation 3.12.

$$y(t) \qquad \sum^{L} 'W;Xi(t) \tag{3.12}$$

or y $\mathbf{x}, \mathbf{w} \in \mathbb{C}$ (3.13)

An example (using $L = 11$) is shown in Figure 3.4, where the array is configured to focus on signals coming from a direction of $\theta = 70°$. This process

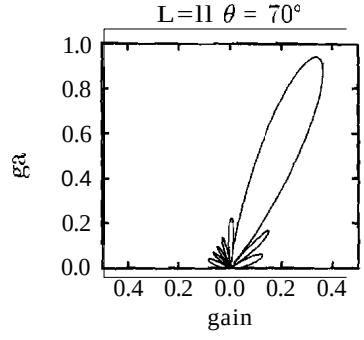

Figure 3.4: Using a coefficient array to steer the array gain to $\theta = 70°$.

of constructing a suitable w to achieve a desired magnitude response (or 'beamshape') is called beamforming.

3.3 Beamforming

As shown in Figure 3.4, a simple ULA beamformer can be used to select a desired direction for maximum gain. Returning to the generalised signal model (Figure 3.1) where the signal is not assumed to be in the far field, nor are the sensors assumed to be in a given geometry, beamformers can be used to focus on signals located at a desired point in space. In this way the beamformer is acting as a *spatial filter.* The beamforming equation is given by

$$y = \mathbf{w}^{\dagger}\mathbf{x} \tag{3.14}$$

The operation of a beamformer (a spatial filter) is directly analogous to Finite Impulse Response (FIR) filtering in the frequency domain. Thus windowing

operations on the coefficients will reduce the sidelobes seen in Figure 3.4 in an analogous way that ripple is reduced in a frequency domain filter.

The gain response of any beamformer to a signal at location (x, y) can be found from

$$r(x,y) = Iw^t a(x,y)1^2 \tag{3.15}$$

where a is given by Equation 3.4. The performance of a beamformer is dependent of the characteristics of the signal, the geometry of the sensors, and the choice of coefficients w. When EEG signals are recorded there is often little choice regarding sensor position or signal parameters, and therefore the determination of w has a significant effect on the beamformer. Considerable effort has been put into methods which determine the filter coefficients for different applications such as ultrasonic imaging (Sammur & Hutchens 1987) and hearing aid design (Greenberg & Zurek 1992). Two design techniques are outlined in the following sections.

3.3.1 The Bartlett, or Conventional, beamformer

The Bartlett beamformer is the simplest type and has a data independent design process. The aim of this beamformer is to maximise the signal power arriving from a point (x, y). The non-trivial solution can be shown (Krim & Viberg 1996) to be

$$w_{bart} = a(x, y) \tag{3.16}$$

where a is given by Equation 3.4. If the coefficients are constrained to $|w| = 1$, then

$$\frac{a(x,y)}{Jat(x, y)a(x, y)} \tag{3.17}$$

This is an intuitive solution, since the coefficients of a equalise the delays from the chosen location *(x, y),* so that the summation is maximised at the sensor array. Figure 3.5 shows an example of a Bartlett beamformer in two

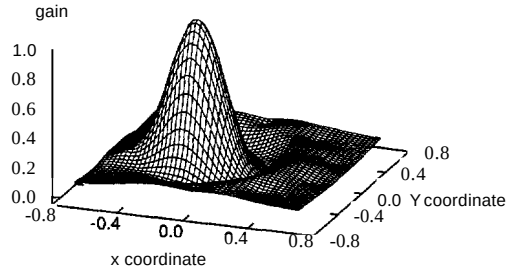

Figure 3.5: The response of an example Bartlett beamformer with $L = 10$, $w = a(-0.2,0.0)$.

dimensions. The sensors *(L* = 10) are arranged in a circle of radius 0.6 around (0,0), with the beamformer focused at (-0.2,0.0), i.e. w = a(-0.2,0.0). The waveform parameters were $f = 10$ Hz and c = 10 m·s-1. Figure 3.5 shows how a beamforrner can be used to focus the gain at a chosen point in space (in this case, in a 2-D plane). This approach can be extended to EEG data, in which L = 19 electrodes, and with the coordinate system shown in Figure C.l.

3.3.2 Results from the application of a Bartlett beamformer

A number of Bartlett bearnforrners were applied to EEG data sets for all subjects (N = 10, as detailed in Section 2.2.1). The calculations required to determine electrode coordinates are described in Appendix C. The procedure was

1. Choose coordinates (x, y) for the focus of the Bartlett beamformer and calculate filter coefficients w.

2. Filter EEG data using Equation 3.14, which gives a resulting signal y.

3. Use signal y as the input to the the integration alpha detection algorithm (refer Section 2.3.1).

4. Calculate detection times and errors for each data set (as in Section 2.3.5).

EEG data were filtered using five beamformers. As the alpha activity during eye closure is generally higher in the occipital region of the head, it is expected that filters with foci at the posterior of the head will give the best results. Such a filter would concentrate on occipital areas, while rejecting frontal areas which are more likely to be prone to eye and jaw artifact. For comparison, filters were tested which focus on the front of the head. The results are shown in Figure 3.6(a) for five different focus locations. The locations of focus points tested are shown in Figure 3.6(b). Only the coordinate for the y-axis (front/back) are shown; the x-axis coordinate was always set to zero (centered). Experiments using filters with x values set to values other than zero have shown that there is no improvement (i.e. symmetrical results are obtained, with the best being at $x = 0$). Also shown in Figure 3.6 for comparison is the result for a unity filter, i.e. all w coefficients are set to one (this gives the same results as using a focus at coordinate 0.00). Applying a unity filter is equivalent to finding the sum of all 19 EEG signals. The $\overline{\chi}$ parameter (as introduced in Section 2.3.5) will be used to compare the performance of techniques in this chapter. The results in Figure 3.6 show that the spatial filters which focus at the rear of the head (using coordinates of -0.09 and -0.20) give the lowest $\overline{\chi}$ values, as expected. The unity filter

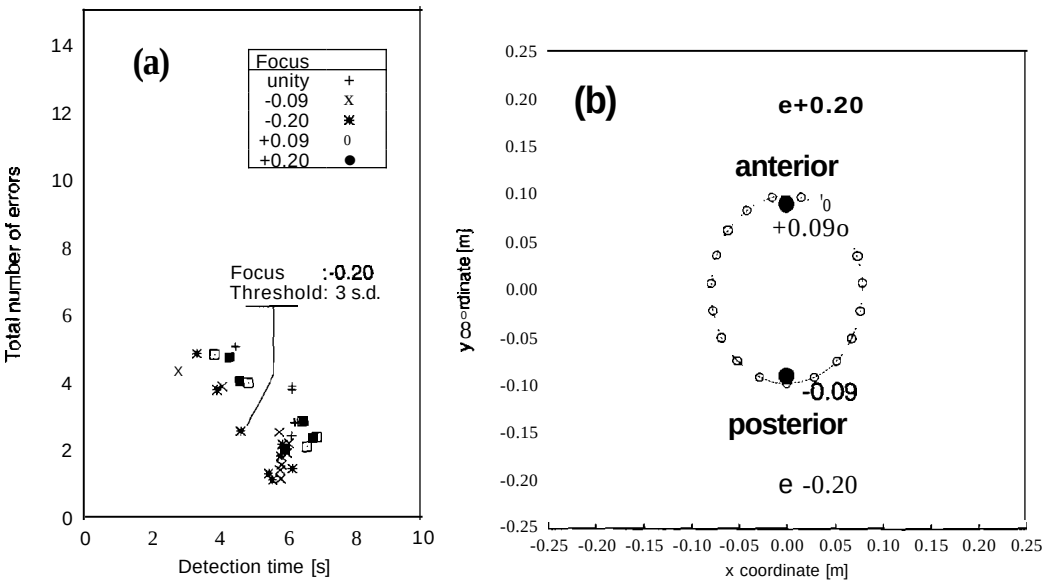

Figure 3.6: (a) Results obtained by applying a Bartlett beamformer to the 19 channels of EEG. Results for 5 different filters are shown: each filter is focused at a different y-axis coordinate, shown in **(b).** The result for unity filter is also shown.

and Bartlett filters which focus at the front of the head (using coordinates of +0.09 and +0.20) give higher $\overline{\chi}$ results. It is interesting that the filter with the lowest $\overline{\chi}$ value is designed with a focal point which is outside the confines of the head. There are no boundary conditions in the design procedure which prevent this, and the result reveals a drawback when using spatial filtering of this type with alpha EEG: the performance is limited by the spatial resolution.

3.3.2.1 Spatial resolution of beamformers

The frequency (10 Hz) and wavespeed (10 $m \cdot s^{-1}$) used for the calculations result in a wavelength of 1 m. This is much larger than the dimensions of the head and leads to reduced resolution in the spatial filters used. This is

illustrated by Figure 3.7. Plots 3.7(a) and (b) show the gain of spatial filters

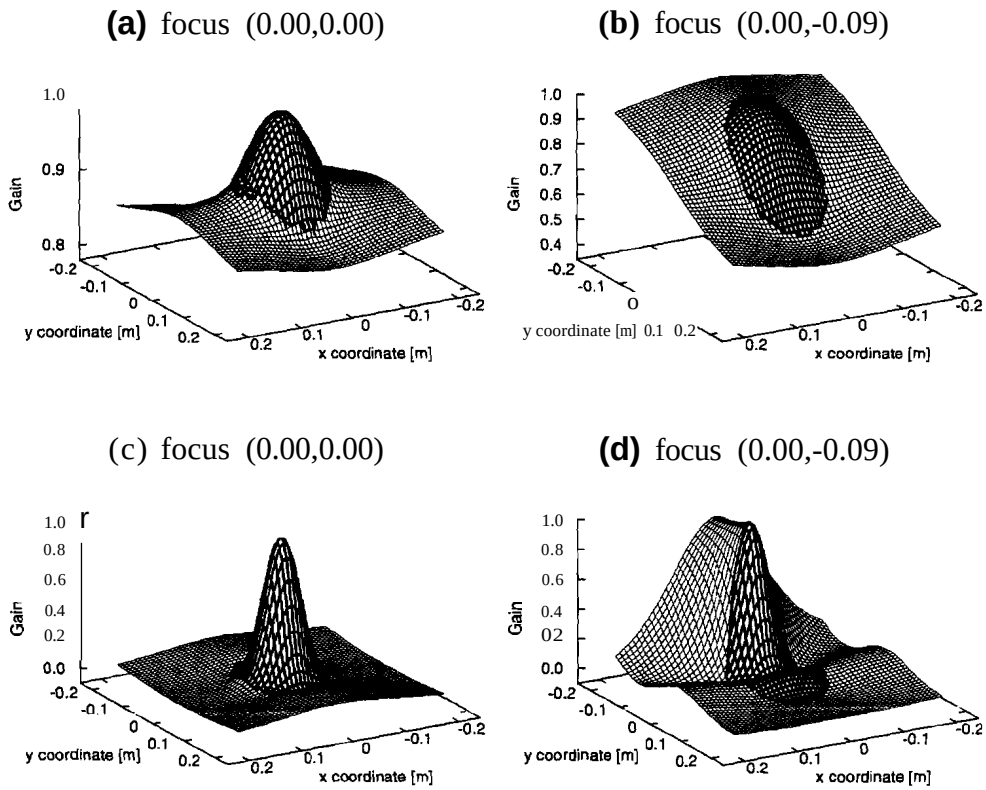

Figure 3.7: Gain of four different Bartlett beamformers. Dark regions **indicate** the confines of the head. Plots **(a)** and **(b)** use f= 10 Hz, c = 10 m·s-1, with the foci at two different locations. For comparison plots (c) and (d) use f = 50 Hz and c = 10 m·s-1. Note that scales for the z-axis differ.

(designed as Bartlett beamformers) using f = 10 Hz and c = 10 m·s-1. Two different focus locations are shown: (a) uses (0.00,0.00), and (b) uses (0.00,-0.09). The area of the head is shown as a darkened region. The filter which is focused at (0.00,0.00) shows localisation at the required point (although the gain does not drop to below 0.8). When the focus is shifted to (0.00,-0.09) the filter shows poorer characteristics; the rolloff around the focus point is low. This is due to the low spatial resolution, a direct result of the 1 m

wavelength of the signals in question. To show how this resolution affects filter design, the same filter characteristics are displayed in Figure 3.7(c) and (d) using a frequency of 50 Hz rather than 10 Hz (thus wavelength is 0.2 m). The rolloff for both focal points is much higher, and the gains away from the focal points are much closer to zero when compared with (a) and (b).

Since the curvature of the filter characteristics is low, designing a filter with a focal point outside the physical head area may give a better filter than one with a focal point within the head, as with the result using focal points of (0.00,-0.02) shown in Figure 3.6.

3.3.3 Capon's beamformer

Capon's beamformer is also known as the *mmzmum-variance beamJormer, Capon's estimator* or *adaptive beamJormer.* Unlike the Bartlett method, it is dependent on the data used. This beamformer works by minimising the total power output by the filter while constraining the gain of the filter at the focal coordinates to be a constant. The effect of this is to steer nulls in the directions of the interfering signals so that such signals do not contribute to the array output power. The weight vector $w(x, y)$ is given by

$$w_{capon}(x, y) = \frac{\mathbf{R}_x^{-1} a(x, y)}{a^t(x,y) R_x^{-1} a(x,y)} \tag{3.18}$$

where $a(x, y)$ is the steering vector. R_x is the array-covariance matrix, estimated using

$$\begin{aligned} & E[x(t) x^t(t)] \\ & \frac{1}{N} \sum_{t=1}^{N} x(t) x^t(t) \\ & xx^t \end{aligned} \tag{3.19}$$

where the sample size of x is *N*. The result in Equation 3.18 comes from solving the following relations

$$w(x, y) = \arg \min_{w} \mathrm{E}\{|w^{t}x(t)|^{2}\} \tag{3.20}$$

(i.e. minimise the power output of the beamformer) subject to

$$\mathbf{w}^{\dagger}\mathbf{a}(x, y) = 1 \tag{3.21}$$

This beamformer is actually of a class of more general beamformers *(linminimum variance* (Veen et al. 1997)) where Equations 3.20 and 3.21 are changed to

$$w(x, y) = \min_{w} \mathrm{E}\{|\mathbf{w}^{\dagger}\mathbf{x}(t)|^{2}\} \tag{3.22}$$

subject to

$$\mathbf{w}^{\dagger}\mathbf{C} = \mathbf{f}^{\dagger} \tag{3.23}$$

The solution to this general form is

$$\mathbf{w} = \mathbf{R_x}^{-1}\mathbf{C}[\mathbf{C}^{\dagger}\mathbf{R_x}^{-1}\mathbf{C}]^{-1}\mathbf{f} \tag{3.24}$$

Linearly constrained minimum variance filtering will be used further in Section 3.4.

The adaptivity of the Capon beamformer comes from the inclusion of x, the input signal, in the design equations so that the coefficient vector changes with the characteristics of the waveforms. Thus, a moving source of interference would still be nulled by a Capon beamformer. This leads to two possible techniques for the design of a Capon filter. The first way is to update the filter adaptively according to the data encountered. The second method is to design a Capon filter using simulated data, so that null point(s)

can be chosen before the filter is used on real data. This means that there is less overhead during the filtering process (the w coefficients are not updated continuously using Equation 3.18), but the process is no longer adaptive.

The use of simulated data can lead to problems when using the design Equation 3.18. To find a suitable w the inverse of the covariance matrix R_x must be computed. The inverse matrix is often not computable due to deficient rank (see Appendix D.1). In situations where R_x is rank deficient there are several possible solutions

- Veen & Buckley (1988) use a pseudo inverse $A+ = (AAt)-lA$. However, this still requires that AAt is invertible.
- a more general pseudoinverse is computable (see Appendix D.3) but this has to be used with caution, as it can easily become unstable and the results become meaningless.
- It is also possible to use Cholesky decomposition (Appendix D.4) to obtain $v = \mathbf{R_x}\text{-}1a$ by solving $Rxv = a$, as a numerically efficient method. However, this requires real valued covariance matrices, and thus introduces errors when (as in this study) imaginary components are required.
- Add G-aussian noise to the signal, thus ensuing a full ranked $\mathbf{R_x}$.

The preferred method is the addition of Gaussian noise as it is reliable and stable, and guarantees an invertible R_x. The use of Gaussian noise with simulated data to design a Capon beamformer is demonstrated in Section 3.3.3.1.

3.3.3.1 Design of an example Capon beamformer using simulated data

In this example the same sensor geometry is used as for the Bartlett beamformer example (Figure 3.5). The focus for the filter is again (-0.2,0.0), but it is assumed that there is an interfering signal at the location (0.0,0.0). A matrix x is constructed that simulates a sinusoidal signal at each sensor from a signal at (0.0,0.0). Using Singular Value Decomposition (SVD) (see Appendix D.2) it can be shown that the rank of $R_x = xx^t$ is equal to 1. This is to be expected as there is only one signal source, and further indicates that the array R_x will be singular. When Gaussian noise is added to the signal matrix x, we find that R_x now has full rank (equal to $L = 10$ in this case), and thus it is now nonsingular. Equation 3.18 can now be used to find suitable filter coefficients. The resulting beamformer response (found using

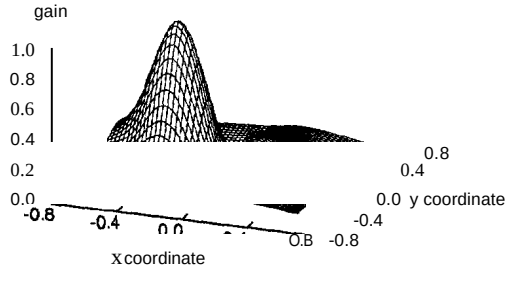

Figure 3.8: The response of an example Capon beamformer with $L = 10$, $w = a(-0.2,0.0)$.

Equation 3.15) is shown in Figure 3.8. A maximum is found as required at (-0.2,0.0), and there is now a null (compare to Figure 3.5) at (0.0, 0.0).

3.3.4 Results using Capon beamformers

As for the Bartlett beamformer, a number of Capon beamformers were compared. The procedure for this was

1. Choose coordinates (x, y) for the focus of the Capon beamformer.
2. (a) If the filter is to be updated adaptively according to the EEG data, Equation 3.14 is used to create a new vector of filter coefficients w once for every second of input EEG data.

   (b) If the filter is to be created artificially (using simulated data), choose a null point and calculate filter coefficients w as in Section 3.3.3.1.
3. Filter EEG data using Equation 3.14, which gives the resulting signal y
4. Use the signal y as the input to the the integration alpha detection algorithm (refer Section 2.3.1)
5. Calculate detection times and errors for each data set (as in Section 2.3.5)

The focus point used with the adaptive w updating was (0.00,-0.09). For Capon beamfouners with predetermined focus and null coordinates, four sets of focus/null coordinates were used. The results of all Capon filters used are shown in Figure 3.9; focus and null coordinate positions are as shown in Figure 3.6(b). The most conspicuous result is the poor performance of the adaptive Capon beamformer. On examination of the spatia] gains produced during the course of the algorithm it was discovered that the filters produced were not useful, and almost random in their gain characteristics. This is another side effect of the poor spatial resolution with alpha waves in the

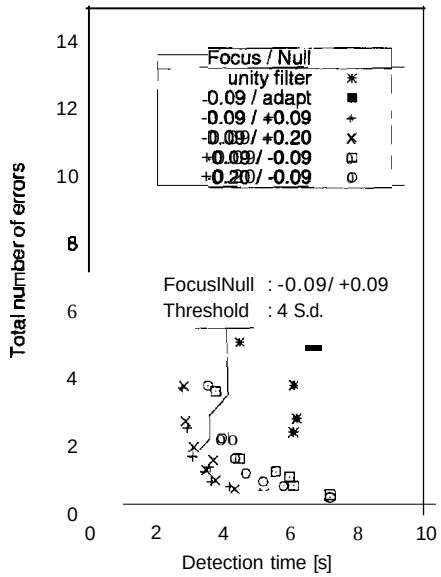

Figure 3.9: Results obtained by applying a Capon beamformer to the 19 channels of EEG. Results for six different filters are shown: One adaptive Capon beamformer, and five beamformers made with simulated data, with focus and null at different y-axis coordinates. The result for a unity filter is also shown for comparison.

EEG (refer Section 3.3.2.1). In an effort to steer a null toward interference the algorithm effectively destroys the characteristics of the filter. This shows how the filter design strategy for the Capon beamformer (to minimise output power) can cause cancellation of the desired signal, as it also contributes to the output power (Veen & Buckley 1988). The Capon filters designed ing simulated data worked more effectively as shown in Figure 3.9, with the lowest $\overline{\chi}$ score produced by a filter with a focus/null at (-0.09)/(+0.09), and a threshold set at 4 standard deviations. The unity filter showed poor performance when compared to the Capon beamformers designed with simulated data.

3.4 LCMV Filtering using the forward solution to EEG

Previously applied methods such as the beamforming techniques in Section 3.3 have assumed that signals from the brain propagate through an infinite, homogeneous medium. This is a satisfactory approximation for an initial and simple investigation. However, intuition suggests that this may not be a satisfactory representation of the human head, which consists of many differing tissue types with varying characteristics. To account for the smearing effect that the combination of different tissues has on EEG signals, a model of the head is used in this section which allows the formulation of a forward solution. This forward solution maps activity in the brain to potentials seen on the scalp. Such a forward solution can then be used to create appropriate spatial filters that account for the influence of the head on EEG signals. The forward solutions may also be used to localise regions of activity in the brain. The filter design method to be used will be Linearly Constrained Minimum Variance (LCMV), of which the Capon beamformer (Section 3.3.3) was a special case.

3.4.1 Electrically modeling the head

To produce a forward solution explaining the behaviour of signals in the head appropriate representations of the cranium and the neural signals are required. The cranial model used needs to incorporate anatomical dimensions and electrical properties of tissue types found in the head. A popular model is to represent the head by one or more concentric spheres, and to approximate the brain activity as dipolar sources. A single dipolar source in a homogeneous medium will result in lines of electric potential as shown in

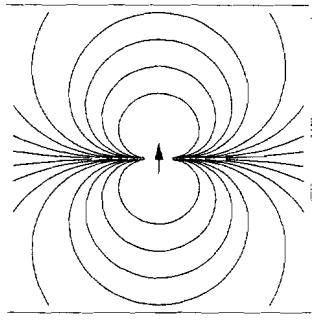

Figure 3.10: Lines of electric potential resulting from a dipolar source in a homogeneous medium.

Figure 3.10.

Earliest modeling attempts (used for cardiac applications) involving dipoles used a single homogeneous sphere (Wilson & Bayley 1950). A more accurate representation for the head is given by a 3-sphere model (Salu et al. 1990) where the three shells describe the brain, skull and scalp. A further development was given by the formulation of the 4-sphere model, which includes the cerebrospinal fluid (CSF) layer (Mosher et al. 1993, Cuffin & Cohen 1979). The 4-sphere model will be used in this study.

As the electrodes used in these experiments are in a headband (and thus are located in a plane), the model has been adapted to inc!ude only 2 dimensions. The head is modelled as in Figure 3.11. The diagram shows the head (with outer radius R) and the four spheres representing the brain, CSF, skull and scalp. The radii of the spheres are shown (as fractions of R) along with their respective conductivities (γ_{1-4}). These conductivities are as used by Mosher et al. (1993) and Cuffin & Cohen (1979). Many other researchers (8 out of the 13 surveyed in the literature) use a unity conductivity value for the scalp and brain, and an equivalent skull conductivity of 80. Though

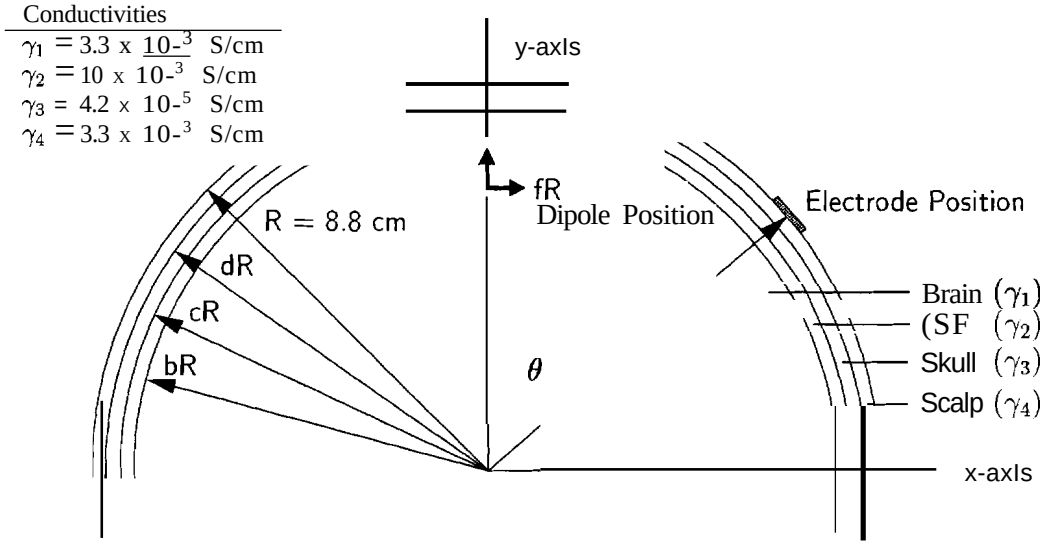

Figure 3.11: Four-sphere model for the head which enables the calculation of the potential at the electrode due to a dipole on the y-axis. This diagram represents a horizontal cross-section of the head (looking from above).

these values are not realistic, the ratio between conductivities are approximately the same and thus localisation results are not changed. The model in Figure 3.11 allows the computation of the potential (referenced to infinity (Mosher et al. 1993)) at an electrode due to a dipole on the y-axis. The electrode is positioned on the scalp (radius R) at an angle θ from the y-axis. The dipole, which has an x and y component, sits on the y-axis at a radius fR. The dipole may also have a z-component, but in this 2-D model it does not contribute to surface potentials. The potentials (in the x and y directions) are given by Equations 3.25 and 3.26 (modified from Mosher et al. (1993)).

$$V_x \quad \sum_{n=1}^{\infty} w(n) a_x P_n^1 \cos\theta \tag{3.25}$$

$$V_y \quad \sum_{n=1}^{\infty} w(n) a_y n P_n \cos\theta \tag{3.26}$$

$$w(n) \qquad \frac{1}{4\pi\gamma_4 R^2} \qquad \frac{fn\text{-}l(2n \pm 1)4(cd)2n+l}{nf(n)} \tag{3.27}$$

$$\begin{aligned}\Gamma[n] = {} & d^{2n+1}(b^{2n+1}n(k_1 - 1)(k_2 - 1)(n+1) \\ & + c^{2n+1}(k_1 n + n + 1)(k_2 n + n + 1)) \\ & . ((k_3 n + n + 1) + (n+1)(k_3 \_1)d^{2n+1}) \\ & + (n+1)C^{2n+1}(b^{2n+1}(k_1 - 1)(k_2 n + k_2 + n) \\ & + c^{2n+1}(k_1 n + n + 1)(k_2 - 1)) \\ & . (n(k_3 - 1) + (k_3 n + k_3 + n)d^{2n+1})\end{aligned} \tag{3.28}$$

$$k_1 = \frac{\gamma_1}{\gamma_2} \qquad k_2 = \frac{\gamma_2}{\gamma_3} \qquad k_3 = \frac{\gamma_3}{\gamma_4} \tag{3.29}$$

where $a_{x,y}$ are dipole moments. The Legendre Polynomials (P_l) and Associated Legendre Polynomials (P_l^m) are calculated numerically as outlined in Appendix D.5. For Equations 3.25 and 3.26 it was found that computation up to a value of $n = 60$ was sufficient for consistent results. To compute the scalp voltage seen by an electrode due to a dipole at a given point, the coordinates are transformed so that the dipole sits on the y-axis.

A survey of previously applied values for the thicknesses of the scalp, skull and CSF is shown in Table 3.2, along with values of head radii. The values of skull, scalp and CSF thickness used in this study were the approximate mean value of previously used dimensions. This gave radius coefficients (referring to Figure 3.11) of b = 0.852, c = 0.875 and d = 0.932. The value of the outer radii R used in this study was an average of the head width and head length found using 14 subjects (see Appendix C), which resulted in R = 88 mm.

The effect of applying Equations 3.25 and 3.26 is shown in Figure 3.12. This figure shows the potential experienced at an electrode (located at point 'A') due to a dipole in the x-y plane at varying positions within the confines

Reference	Head Radius [mm]	Thickness [mm]		
		Scalp	Skull	CSF
\Vard et al. (1998)	92	7	5	
Veen et al. (1997)	82.5	7	3	
Yvert et al. (1995)	90	7.2	4.5	
Fletcher et al. (1995)	100	8	5	
Mosher et al. (1993)	88	3	4	2
Roth et al. (1993)	92	7	5	
Veen et al. (1992)	80	5	7	
Cuffin (1990)	95	5	6	
Salu et al. (1990)	104.5	8.36	5.225	
Cuffin & Cohen (1979)	88	3	4	2
mean	91.2	6.05	4.87	2.0
this study	88	G.0	5.0	2.0

Table 3.2: Dimensions used in previous studies involving the 3- or 4-sphere model, and values used in this study.

of the head. The effect of dipoles orientated in both the x and y directions are shown. In contrast to the expected performance of a single homogeneous sphere, the potential for this 4-sphere increases nonlinearly as the dipole moves closer to the electrode position. The notch visible in the response to the x-orientated dipole is caused by the null point in the line of potential for a single dipole (refer Figure 3.10).

3.4.1.1 The suitability of the sphere-type head models

The 4-sphere model is an important step toward a satisfactory electrical representation of the head, but it should be emphasised that other models

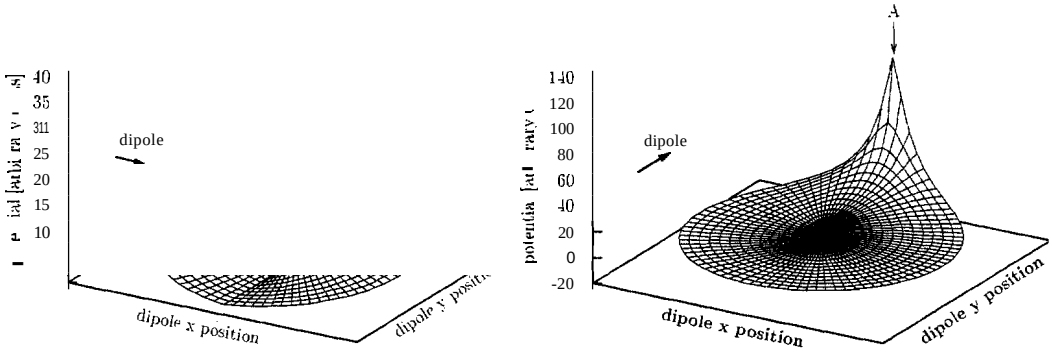

Figure 3.12: Potential at an electrode (point 'A') on the scalp due to dipoles (in the x and y directions) at various positions in the head. Potential values in this example are arbitrary.

of the head exist. The two major issues with the spherical model concern the shape of the head, and its tissue properties; a sphere is not the most accurate representation of the heads geometry, and the conductivities used assume that the tissue is locally homogeneous and isotropic, which is a gross simplification. Below is a brief discussion of more advanced models, and how they compare with sphere-type models.

As mentioned, the modeling of tissue layers in a homogeneous manner is a simplification: et al. (1999) and Arthur & Geselowitz (1970) investigated the effect of inhomogeneous tissues on models for the head and heart respectively. Similarly, Awada et al. (1998) found that uncertainties in conductivity values used were contributing factors to poor model performance, and that of these conductivities, the skull and scalp were most sensitive. The report also found that the conductivity values used by researchers varied by more than an order of magnitude.

Variations on spheres, such as the eccentric model, have been shown (Cuffin 1990) to improve on dipole localisation tests, but by less than 1 em.

Head models with realistic shapes can be constructed using finite element analysis with Magnetic Resonance (MR) images as templates (Chen et al. 1998, Yvert et al. 1995). These have improved localisation of dipoles by a few centimeters (Roth et al. 1993, Cuffin 1996), although for best results every subject would need to undergo the lengthy and expensive MR imaging procedure. Optimisation of such finite element problems (Awada et al. 1997, Fletcher et al. 1995) have improved efficiency of realistic head models, but such processes remain a computationally demanding exercise.

Though it is desirable to achieve the best resolution possible, computational tradeoffs mean that for the study described in this thesis the 4-sphere model is the appropriate choice. More advanced models are better suited to clinical environments involving evoked responses, where exact localisation is paramount, and processing time is a secondary issue. If real-time monitoring is required, as is the goal here, simpler model is needed. Localisation of alpha sources will not return a discrete location, but instead the centre of a distributed region of activity (Lopes Da Silva 1991), thus a high resolution method is less crucial. This contrasts with evoked potential studies (e.g. in Cuffin (1996)) which may aim to pinpoint or target very small regions of activity in the brain.

3.4.1.2 Incorporating the head model in a LCMV filter

The filters to be designed in this section differ from those used in Section 3.2 in that it is assumed for this study that the propagation delay is negligible (Spencer et al. 1992), whereas the previous beamformer design method used the delay between signal arrivals as its discriminating factor. For this localisation technique the LCMV design procedure uses the differences in amplitude between sensors rather than concentrating on temporal disparity

and assuming equal signal amplitudes.

In order to spatially discriminate between signals using the 4-sphere head model two filters are required, one for each dipole orientation (x and y). The two filters w can be combined as W, so that the spatial filter operation will be

$$\mathbf{y} = \mathbf{W}^{T}\mathbf{x} \tag{3.30}$$

This will give a 2x1 y vector for each time interval, representing the response to the two dipole orientations. For convenience, the magnitude of this dipole moment vector is used as the filter output.

Let H(q) be an N x 2 matrix representing the potential at N electrodes due to a dipole source at location q with unit dipole moments in the x and y directions. So, referring to Equations 3.25 and 3.26,

$$\mathbf{H}(\mathbf{q}) = \begin{vmatrix} V_{x(1,\mathbf{q})} & V_{y(1,\mathbf{q})} \\ V_{x(2,\mathbf{q})} & V_{y(2,\mathbf{q})} \\ & \\ V_{x(L,\mathbf{q})} & V_{y(L,\mathbf{q})} \end{vmatrix} \tag{3.31}$$

where $V_{x(n,\mathbf{q})}$ represents the voltage at electrode n due to an x-orientated dipole at location q

The ideal filter will satisfy the condition

$$\mathbf{W}^{T}(\mathbf{q}_o)\mathbf{H}(\mathbf{q}) \begin{cases} \mathbf{I} & \mathbf{q} = \mathbf{q}_o \\ \mathbf{0} & \mathbf{q} \neq \mathbf{q}_o \end{cases} \tag{3.32}$$

This means that the gain is unity at the location q_o and zero elsewhere. It is mathematically possible to design a filter to suit the constraints in Equation 3.32, but the number of degrees of freedom that are used in doing so may result in poor filter performance (Veen et al. 1997). The Linearly Constrained Minimum Variance (LCIVIV) filter design methodology instead satisfies the first (passband) requirement in Equation 3.32 while minimising the variance

in the filter output. This creates an optimal filter with minimised signal response in the stop band (i.e. the region $q \neq qo$). The filter coefficients are calculated using (Veen et al. 1997),

$$W(qo) = [H^T(qo)C\text{-}1(x)H(qo)\Gamma^1 H^T(qo)C\text{-}1(x) \quad (3.33)$$

where C(x) is the data covariance matrix given by (Veen et al. 1992),

$$C(x) \quad xx^T \text{ assuming } \bar{x}_i = 0 \quad (3.34)$$

3.4.2 Results using the LCMV filter

Filters designed using the four sphere head model and LCMV algorithm were applied to EEG data sets for $N = 10$ (as described in Section 2.2.1) subjects, using a range of focal coordinates. The x-coordinate was always set to zero, and the y-coordinates were set to -0.09, -0.07, -0.04, +0.04; +0.07 and +0.09. As with the filters designed using beamforming procedures in Section 3.3, it is expected that the coordinates that focus in the occipital area will give the best performing filters. Because the head model used in this section incorporates boundary conditions, coordinates outside the physical dimensions of the head are not meaningful (unlike the beamforming design process, where it was possible to use any desired coordinate value). After filtering, the resulting signal is processed by the integration alpha EEG detection method, and detection times and errors recorded, as previously described in Section 2.3.4.

Data resulting from the application of filters to EEG data is shown in Figure 3.13. Two groups of data can be seen in Figure 3.13(a), the plot shows a distinction between results recorded from filters focused at the anterior (positive focal coordinates) and posterior (negative coordinates), with the results for filters focused at the posterior of the head giving better results

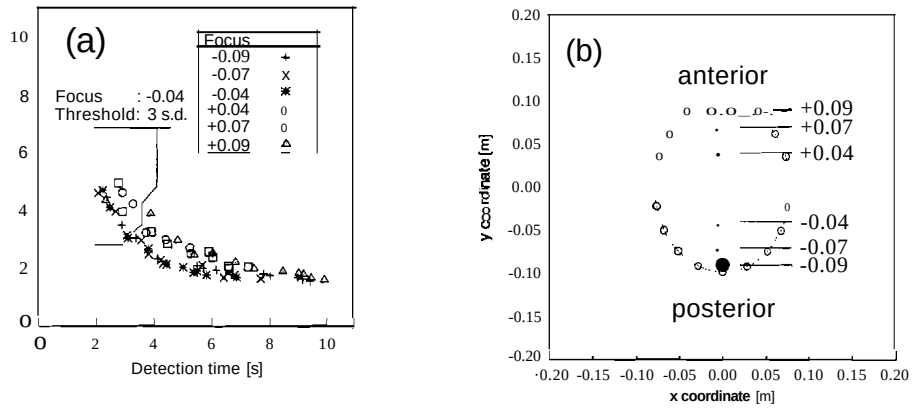

Figure 3.13: Results (a) obtained by applying filters designed using the four sphere head model and LCMV algorithm to EEG data. Six different focal coordinates in the y-axis were used as, shown in (b).

(The mean of the confidence intervals that show the posterior filters give better results than the anterior filters is 72%). There are no major differences between the filters focused at the rear of the head; the lowest $\overline{\chi}$ value is given when the filter is focused at (0.00,-0.04), using a threshold of n = 3 standard deviations.

All filters showed a poor performance with regard to error rates; notice that there is an almost asymptotic effect at total 1.8, where most detection methods discussed thus far approach very low error counts. On closer inspection of data collected the higher error count is primarily due to artifact errors encountered during jaw clenching trials. This reveals a limitation of the filter design process: the use of signal amplitude information rather than temporal characteristics has led the filter to assume that the EMG signals from the jaw are in fact EEG signals produced in the occipital region. Thus the use of the four sphere head model and LCMV filter design method as described here are more suitable for spatial filtering of clean signals

(such as in evoked potential tests) but do not perform well in an unregulated environment where artifact with high amplitudes are present, such as the data used in this study.

3.5 Adaptive filtering using all artifact reference

The first three sections in this chapter have dealt with preprocessing filtering methods that use the location of desired and unwanted signals for filter design strategies. The filtering method described in this section instead uses the characteristics of unwanted signals as a basis to produce clean EEG alpha data, a process generally referred to as 'adaptive filtering'.

An adaptive filter uses two source signals: the input signal which has been affected by some artifact, and a reference signal which ideally contains only the artifact source. To achieve this there must be a source of the artifact signal available for use with the filter. In this study the adaptive filter is used to iteratively adjust itself so that it can remove a version of the reference (artifact) signal from the input signal, leaving an output signal free from artifact.

3.5.1 Introduction

The adaptive filter consists of coefficient vector w(n) of size N which is continuously adjusted according to the characteristics of the input signal $d(n)$ and a reference signal $x(n)$. The filter attempts to model the relationship between $x(n)$ and $d(n)$. The relationship can be used in many ways, in this implementation the filter will be used to separate unwanted artifact signals

from EEG data, using a reference signal which contains a 'clean' verSIOn of the artifact in question. A representation of a general adaptive filter is shown in Figure 3.14. An algorithm is used to continuously update the filter

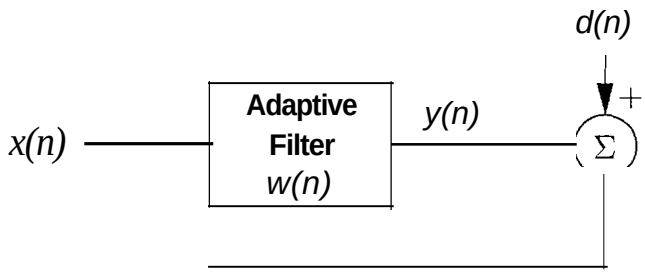

Figure 3.14: Functional diagram for an adaptive filter

coefficients *w(n).* An example of the operation of an adaptive filter is shown in Figure 3.15. This data shows a simulated EEG alpha (10 Hz) signal as *d(n)* which becomes contaminated with EMG (30 Hz) signal at t=1 s. The reference signal *r(n)* contains only the EMG signal which is assumed to have been collected at a different location to the EEG signal. The signals *y(n)* and *e(n)* correspond to Figure 3.14; *y(n)* is the output from the filter and *e(n)* is the error signal and also the desired output. The filter quickly adapts to the change in the reference signal and separates the unwanted noise (visible as *y(n))* which is subtracted from the original EEG leaving a signal clean from EMG as *e(n).* The difference in using an adaptive filter as opposed to simply subtracting the noise signal from the EEG is that the adaptive filter continuously adjusts the amplitude of the noise signal to be subtracted. A simple non-adaptive subtraction may (depending on the relative signal levels) actually introduce more artifact into the resulting signal than was originally present. The amplitude disparity of the EMG signals present in the reference data (which may be typically millivolts) and EEG data (which may be typically tens of microvolts) causes no problem to the algorithm.

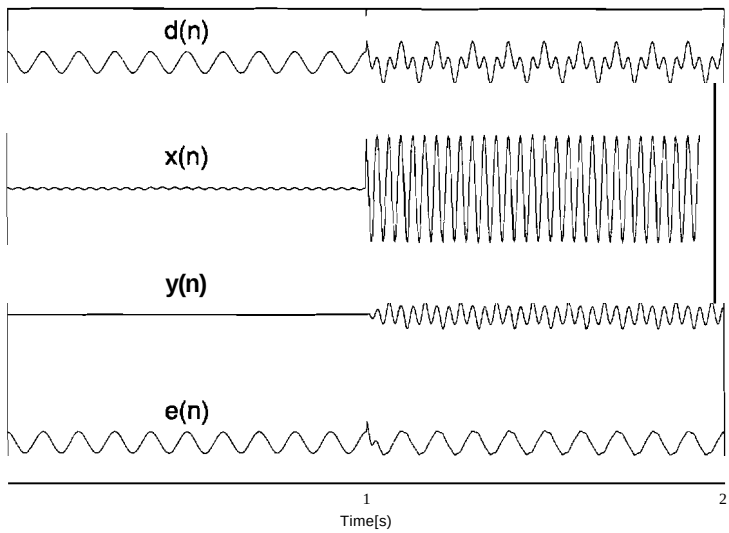

Figure 3.15: A demonstration of adaptive filter operation. An EEG signal *d(n)* has been contaminated at t=1 s by EMG artifact. A clean source of this artifact is available as the reference signal *x(n).* The filter quickly adapts to the change and separates the noise signal into *y(n)* which is then subtracted, leaving a clean EEG signal *e(n).*

3.5.2 The adaptive filter algorithm

The filter uses a coefficient vector w of size *N*

$$\mathbf{w}(n) = [w_0(n)\ w_1(n) \ldots w_N(n)]^T \tag{3.35}$$

The signals shown in Figure 3.14 are related by

$$y(n) \quad w(n)^T x(n) \tag{3.36}$$

$$e(n) \quad d(n) - y(n) \tag{3.37}$$

where *x(n)* is a vector of the last *N* values of *x(n).* The algorithm used to update the filter coefficients *w(n)* in this study is the Least-mean-square (LMS) algorithm. The algorithm has the form

$$w(n+1) = w(n) + \quad)x(n) \tag{3.38}$$

where μ is a step size parameter. The choice of Nand μ have a significant effect on the performance of the filter; a smaller N and larger μ will give faster convergence but poorer adaption than a filter with larger N and smaller μ. The stability of the filter depends largely on the value of the step size μ (Douglas 1998). For stationary signals the filter can be shown to be stable (i.e. the filter coefficients converge) when (Diniz 1997, p. 26)

$$O< \mu < \frac{1}{\lambda_{max}} \tag{3.39}$$

where λ_{max} is the largest eigenvalue in the correlation matrix of x. Equation 3.39 cannot be used for the data used in these studies due to the nonstationary nature of the signals (especially during trials such as jaw clenching). Although the μ value could be updated continuously using Equation 3.39 the calculation of correlation matrices and eigenvalues would add a significant computation burden to the process. Instead a more approximate but easily computable method is used here, where the step size is determined by (Douglas & Rupp 1998)

$$0 < \mu < \frac{0.1}{N\sigma_x^2} \tag{3.40}$$

where σ_x^2 is the input signal power.

Although many filter structures and algorithms are available, the LMS algorithm is applied here due to its computational simplicity, stable behaviour and proven convergence (at least in stationary environments). Figure 3.16 shows performance examples for the LMS adaptive filter algorithm using real data. Figure 3.16(a) shows EEG data *(d(n))* from electrode E4 (refer Figure *C.1)* contaminated with EMG signals, caused by clenching the jaw. The reference signal *x(n)* is taken from electrodes placed over the masseter muscle. As the filter output *(y(n))* shows, a large amount of EMG signal is separated from the EEG input. Although the signal has been cleaned to some

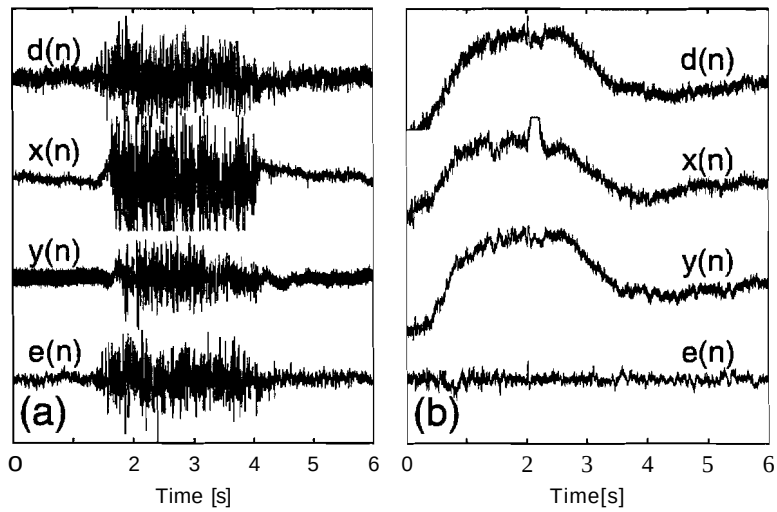

Figure 3.16: Examples of signals (taken from electrode E4) applied to adaptive filters showing input signal *d(n)*, reference signal *x(n)*, extracted component *y(n)* and 'cleaned' signal *e(n)*. Plot (a) shows the EEG contaminated with EMG due to jaw clenching, with the reference signal from over the masseter muscle. Plot (b) shows an artifact in EEG created by head movement, the reference signal is taken from an EEG electrode at the front of the head.

extent, the output e(*n*) reveals that there is still evidence of the EMG signal contaminating the EEG data. Figure 3.16(b) uses EEG data from electrode E4 which has been affected by movement artifact (during movement of the head). The reference signal *x(n)* is taken from electrode E10. As the output signal e(*n*) shows, the artifact has been removed effectively by the adaptive filter.

3.5.3 Results from the application of the adaptive filter algorithm

The LM8 adaptive algorithm was applied to EEG data for all 10 subjects using a range of filter lengths and reference electrodes. The input signals for the filter *(d(n))* were taken from electrodes in the occipital regions, E2 and E4. Both signals were adaptively filtered separately, then the difference of the output signals computed. This differential signal was then processed by the integration alpha detection method (see Section 2.3.1) and detection times and error counts determined as previously described. Filter sizes used were N = 10,20,50,100 and 200. The reference signal *(x(n))* was taken from electrodes E5, E7 or E10, as well as from the EMG electrode located over the masseter muscle. It is expected that the choice of reference signal will have a large influence on the results obtained: the EMG reference contains no EEG signal, but is far from the occipital region, thus the EMG present in the EEG signal may not be sufficiently correlated to the reference EMG to allow sufficient matching by the adaptive filter. Conversely, using EEG electrodes (such as E5) as the reference may show highly correlated EMG (or other) artifact, but desired signals such as the alpha EEG component may also be removed by the adaptive filter, as the alpha signal may be present in both reference and EEG electrode data.

Figure 3.17(a) shows results obtained when the adaptive filter algorithm is applied to EEG data for all subjects using the EMG signal (on the jaw) as the reference, and using a variety of filter lengths. The overlap of the data points reveals that the filter length has little effect on the performance of the algorithm in this situation. Tests for other choices of reference electrode showed similar findings; a change in filter length did not produce an appreciable change in alpha detection performance. Figure 3.17(b) shows the

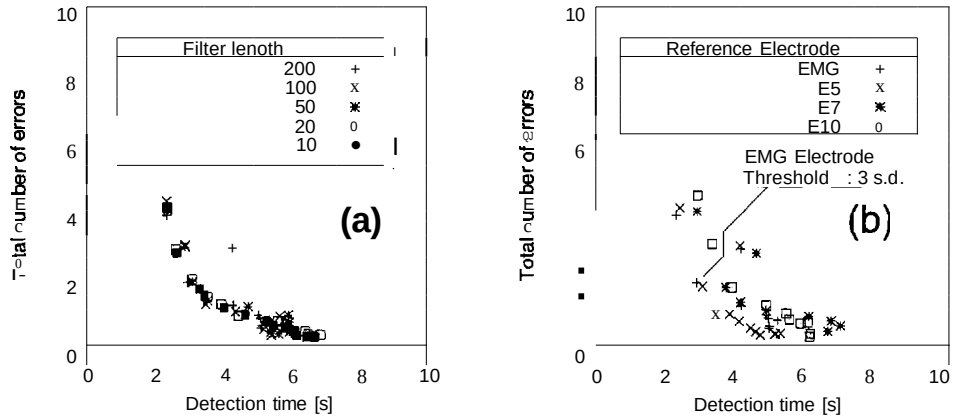

Figure 3.17: Results obtained by applying EEG data from all 10 subjects to the LM3 adaptive filter. Plot (a) shows results when the EMG electrode is used for the reference with varying filter lengths. Results in (b) use a filter length of $l'l = 200$ with different reference electrodes.

performance of the adaptive algorithm using a filter length of $l'l = 200$, and using different electrodes as the source for the reference signal. The lowest $\overline{\chi}$ value is obtained when using the EMG electrode as a reference and a threshold of $n = 3$ standard deviations. In general, however, the use of electrode E5 as the reference produces consistently low $\overline{\chi}$ values compared to the other electrode choices.

These results argue against the assertion that using a reference electrode close to the sites used for alpha detection will cause the alpha component of the EEG to be adaptively removed. In fact, the use of electrode E5 as the reference electrode to filter artifact from E2 and E4 electrodes shows promising results compared to the use of EEG electrodes which are further away on the head (E7 and E10).

To confirm whether the inclusion of the adaptive filter provides any benefit to the alpha EEG detection problem, results using the adaptive filter

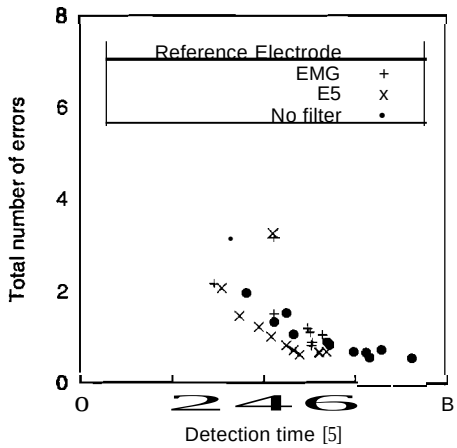

Figure 3.18: Comparison of alpha detection results when EEG data is applied to an adaptive filter (using reference electrodes E5 and EMG) and when the data is processed by the integration method without adaptive filtering.

(N = 200) with reference electrodes from the jaw (EMG) and E5 are compared to results obtained without using the adaptive filter (i.e. using the integration alpha detection method only, no preprocessing). These three sets of results are shown in Figure 3.18. Again the results using E5 electrode as the reference show consistently good results compared to the unfiltered method over many threshold settings. The results for the EMG electrode are less convincing, though the lowest $\overline{\chi}$ value is given by this electrode at threshold $n = 3$.

3.6 Blind Source Separation using Independent Component Analysis

The preprocessing methods introduced so far in this chapter have relied on some form of external information to enable the successful filtering of the

EEG electrode array data. For example, the beamforming method used location information to focus on the occipital area, and the adaptive filter used information from a reference electrode which is assumed to contain artifact signal. The filtering method to be described in this section uses no outside information, but instead performs its operations 'blindly'.

3.6.1 Introduction

Blind source separation (BSS) methods aim to decompose a set of data into many separate components without prior knowledge ('blindly'). Previously applied methods in this study, such as in the beamformers (Section 3.3) or the spatial filters using the forward head model (Section 3.4), have used location information in order to separate EEG and EMG signals. Blind methods use only information contained in the signals themselves to attempt separation of mixed signals.

One method that has shown recent promise for the blind separation of EEG signals is Independent Component Analysis (ICA) (Hyviirinen & Erkki 1999). The technique has also shown encouraging results for many other applications, such as separation of audio signals and finding structure in stock returns (Back & Weigend 1997). In this section the ICA algorithms will be used to separate alpha EEG signals from the other waveforms in the data sets (other EEG, EOG, artifact, etc.). Once separated, the alpha EEG signal will then be used as the input to the previously discussed integration alpha detection method. In principle this will offer better performance as only the alpha EEG will be present, and interfering signals or extraneous EEG will be discarded.

The ICA model is that of a linear mixture of independent signals

$$x = As \tag{3.41}$$

where s are latent sources that cannot be observed directly, A is a linear mixing matrix, and x are the observed values. For EEG, x are the signals as recorded by the Neurosearch-24, the mixing matrix A is an unknown function dependent on the the conductivities of the brain, scalp, skull and cerebrospinal fluids, as well as the type and locations of the electrodes used. The s signals are the many neural sources **in** the brain, ocular artifacts, electromagnetic interference and so on; these are the so-called 'independent components'. The aim of BBB is to find the mixing matrix A (which is effectively a set of spatial filters), so that the original source signals s may be computed, as shown below;

$$\mathrm{s} \qquad \mathbf{A}^{-1}\mathbf{x} \tag{3.42}$$

$$\mathbf{W}\mathbf{x} \tag{3.43}$$

The matrix W is assumed to be time invariant.

Additionally, a set of EEG signals may be 'cleaned' of an artifact which has been separated into a component and visually identified. The corrected EEG signals x' can be gained using

$$x' = W\text{-}1s' \tag{3.44}$$

where s' is the matrix of independent components with artifact components set to zero. For the purposes of this thesis we investigate whether ICA can be used to isolate the alpha 'source' component, which can then be further processed to detect the increase **in** alpha EEG associated with eye closure.

3.6.2 Theory

In general, the ICA algorithm makes the assumptions that (a) the source signals s_i are statistically independent, and (b) that they have nongaussian distributions. The algorithm works most effectively when (Makeig et al. 1995)

the medium is linear

11 propagation delays are negligible

iii the time courses of the source signals are independent

iv the number of sources is equal to the number of sensors *(N)*

Volume conduction in the head is thought to satisfy (i) and (ii) (though in Section 3.3 for filtering purposes it was assumed that propagation delays were finite). Point (iii) is acceptable since ECG, EMG, ocular artifacts etc are not locked to the mechanisms of EEG. Though (iv) is uncertain, it has been numerically shown that the algorithm performs well even with a large number oflow-level independent sources (Jung et al. 2000). The first issue is to determine how one measures the independence of one signal compared to others. Different approaches to lCA use various measures of independence in order to separate the components. Some of the more successful methodologies include,

- minimising higher order (or moments) (Back & Weigend 1997, Vigario et al. 1997, Hyvarinen & Oja 1997). This approach stems from use of the Central Limit Theorem, which predicts that (under certain conditions) the distribution of the sum of random variables tends toward the gaussian distribution - i.e. the sum of two random independent random variables has a distribution that is more gaussian than either of the original variables. The fourth-order cumulant (or kurtosis) can be used as a measure of how close a signal is to being gaussian in nature (or its 'gaussianity') (Hyvarinen & Erkki 1999), and thus as a measure of independence.

- minimisation of mutual information, or maximisation of the entropy, of the outputs (Bell & Sejnowski 1995, Hyvarinen 1999, Lee et al. 1999, Jung et al. 2000)

The structure of many of the algorithms used for ICA often leads them to be labeled as neural network algorithms. Although not the first treatment of the subject, much work on ICA stems from the development of algorithms by Bell & Sejnowski (1995), who used information maximisation (infomax) to facilitate component separation.

Advantages of lCA

- many classes of artifact may be dealt with using one method
- does not distort (in principle) signals, compared to spectral filtering which may remove parts of required signals
- does not require one 'clean' artifact reference (as in adaptive filtering, Section 3.3).

Limitations of lCA

- cannot determine ordering of IC's (thus running the algorithm repeatedly may produce the same IC's but in an unpredictable order)
- can only resolve at most N signals (where N is the number of sensors, only a problem when N is small)
- requires sufficient data for training
- needs visual inspections of results
- EEG signals may not satisfy nonstationarity conditions

3.6.3 Selection of leA algorithm

Many variations of the ICA algorithms have been developed. Two algorithms have been chosen to test on EEG data here, the Fixed Point algorithm (Hyvarinen 1999, Hyvarinen & Oja 1997) and the Extended ICA algorithm (Lee et al. 1999). The preprocessing required for the application of these methods to EEG are described below, along with the two algorithms and reasons for their suitability.

3.6.3.1 Are the signals of interest in this study gaussian or non-gaussian?

Since the overall success of lCA depends on how gaussian the signals are, we consider the statistics of some of the the signals we are interested in. Firstly 50 Hz line interference was separated from the differential E2-E4

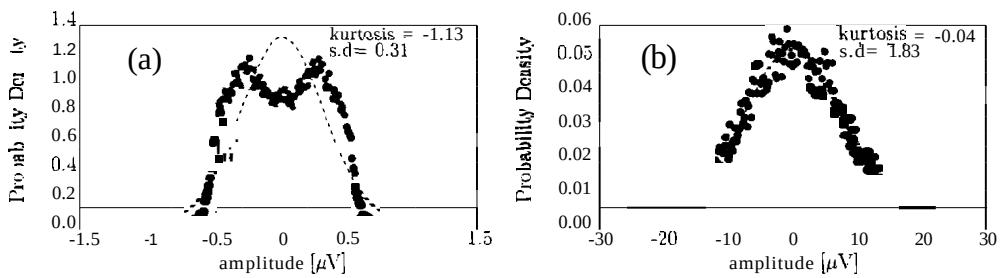

Figure 3,19:· Probability density functions of signal amplitude for (a) 50 Hz line noise and (b) alpha component of the EEG.

signal using an FIR bandpass filter (f_{3dB} = Hz). The probability density function (pdf) for this signal is shown in Figure 3.19(a), along with a reference gaussian distribution with the same standard deviation as the data, and zero mean. To confirm how 'gaussian' the signal is the value of the kurtosis is examined (Smith 1994). The kurtosis gives a measure of the flatness or

peaked-ness of a distribution.

$$\text{kurtosis} \qquad \left[\frac{1}{N}\sum_{j=1}^{N}\left[\frac{x_j-\bar{x}}{\sigma}\right]^4\right]-3 \tag{3.45}$$

If a signal is gaussian, the kurtosis will be zero. If the kurtosis is less than zero the signal is described as sub-gaussian (or platykurtic), and if the kurtosis is greater than zero, the signal is described as super-gaussian (or leptop-kurtic). Thus, the powerline interference signal shown in Figure 3.19(a) is sub-gaussian.

To establish the characteristics of the alpha EEG component, the filtered output from the differential E2-E4 signal of 4 different EEG trials (all from the same subject) was extracted. Only artifact-free signals during eye closure were used to create pdf's. The average of the 4 pdf's is shown in Figure 3.19(b). This suggests that the alpha component of the EEG during eye closure is approximately gaussian, which agrees with the statistical hypothesis by Dick & Vaughn (1970) and the Rayleigh distributions shown in Section 2.4. Since nongaussianity of the source signals is an assumption of the rCA algorithms (see section 3.6.2) this may mean that the alpha signal will not be able to be successfully separated from the other components. It is worth noting that the central limit theorem indicates that a mixture of non-gaussian components will appear gaussian, especially if there are a large number of sources (as may be present in the brain). Thus the apparent gaussian nature of EEG signals does not necessarily preclude them from use with the rCA algorithms (Makeig 1998) as the underlying nature of neural activity may still be non-gaussian.

3.6.3.2 Preprocessing

Before the algorithms are applied the data is centered (the mean is subtracted) and whitened (Hyvarinen & Erkki 1999). vVhitening (or sphering) linearly transforms the data variable x so that the components are uncorrelated and their variance equals unity, i.e. the transformed matrix is 'white', and $E\{xx^T\} = I$. This transformation is llseful since the mixing matrix to be found (A) is now orthogonal, and thus the number of parameters to be estimated is reduced. can be achieved a number of ways, though a simple method is to modify x by the whitening matrix V,

$$\tilde{\mathbf{x}} = \mathbf{V}\mathbf{x} \tag{3.46}$$
$$\mathbf{V} = \left(\sqrt{\Lambda}\right)^{-1}\mathbf{E}^{\mathsf{T}}$$

where A is a matrix with eigenvalues of covarince of x on the diagonal

E is a matrix with eigenvectors of covariance of x as columns

Covariance is found by $C = \frac{xx^T}{p}$ (p is sample size)

3.6.3.3 The Extended ICA Algorithm

This is an adaptation and extension of the Bell & Sejnowski (1995) algorithm (which is deficient in separation of sub-gaussian components: sources which have a negative kurtosis). The Extended lCA algorithm (Jung et a1. 2000, Lee et a1. 1999) is derived using the maximum likelihood formulation and is shown to be able to separate super-gaussian (eg. some sound sources) and sub-gaussian (50 Hz noise in EEG signals) into individual components. By contrast, the algorithm of Bell & Sejnowski (1995) spreads the 50 Hz noise over many components.

|The Extended lCA Algorithm|

Parameters required:

L Learning rate

LF Learning rate adjustment coefficient $(LF < 1)$

B Data block size $(B < p)$

α Momentum term (affects rate of convergence)

J Number of iterations to perform

Procedure:

1. Randomly permute x values to ensure stationarity of the input signals (Makeig et al. 1995)
2. Perform whitening on x
3. Set initial W as a unitary matrix
4. For each x_i in x (where x_i is a data block of size N x Band N is number of input channels):
   (a) u = $\mathbf{x}_i^T\mathbf{W}$
   (b) $\Delta W = L(I - K \tanh(u)u^T - \mathbf{uu}^T)W$
   where K is a matrix with diagonals k_i
   $k_i = \text{sign}\left(E\left(\text{sech}^2(u_i)\right)E(u_i^2) - E(Ui \tanh(ui))\right)$
   (c) $W = W + \left(\Delta\mathbf{W}(n) + \alpha\Delta\mathbf{W}(n-1)\right)$
   (d) If W coefficients blow up, lower L rate
5. $L = L \times LF$
6. Repeat from (4) until maximum iteration count j is reached

3.6.3.4 The Fixed Point Algorithm

This algorithm concentrates on a compact design with fast convergence. It avoids the need to find matrix inverses, and has cubic convergence (Hyvarinen 1999, Hyvarinen & Oja 1997, Vigario et al. 1997).

The Fixed Point ICA Algorithm

Parameter required:

ϵ Convergence limit for change in W

Procedure:

1. Perform whitening on x
2. Initial W is a random matrix
3. Normalise W
4. Decorrelate inputs:
   a $W = W / \sqrt{\|WW^T\|}$
   b $W = \frac{3}{2}W = \frac{1}{2}WW^TW$
   Repeat (4b) until convergence
5. $U = xTW$
6. $\frac{1}{p}W(U^3)$ - 3W (p is sample size of x)
7. Calculate change in W:
   change = 1 - [min(abs(diag($W; W_{i-1}$)))]
8. Repeat from (3) until change< ϵ

3.6.3.5 Comparison of the two algorithms

The characteristics of these techniques are shown in Table 3.3. For an example, both algorithms were trained on a sample of EEG from one subject. The segment of EEG data used is shown in Figure 3.20. At t = 30 s the subject was instructed to close both eyes and hold them closed. An eye blink can be seen at t = 28.5 s (especially prominent in electrodes near the front of the head), and a larger (clipped) artifact at t = 30 s when the subject closes both eyes. Alpha rhythm is evident in occipital electrodes (El-5 and E16-19) after t = 30 s.

Fixed point algorithm
Advantages: Requires only one user-defined parameter Fast convergence Disadvantages: Sub- and super-gaussian components cannot be separated well without further processing
Extended IeA algorithm
Advantages: Improved ability to resolve sub- and super-gaussian components. Disadvantages: Algorithm requires many parameters which can have a large effect on quality of resulting IC's. Slow convergence (speed also highly dependent on supplied parameters)

Table 3.3: Comparison of two ICA algorithms

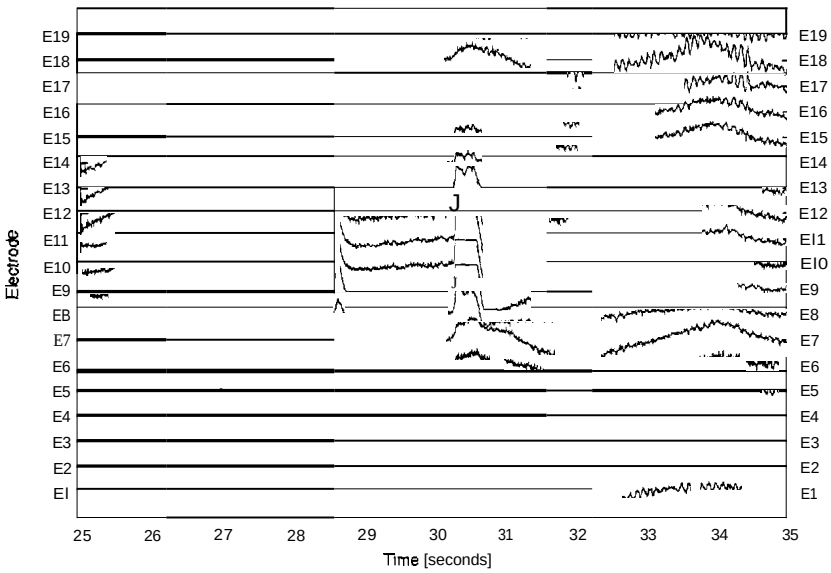

Figure 3.20: A segment of the EEG data collected usmg the 19 channel headband. At t = 30 s the subject closed both eyes and held them closed, Electrode numbering refers to Figure C,1

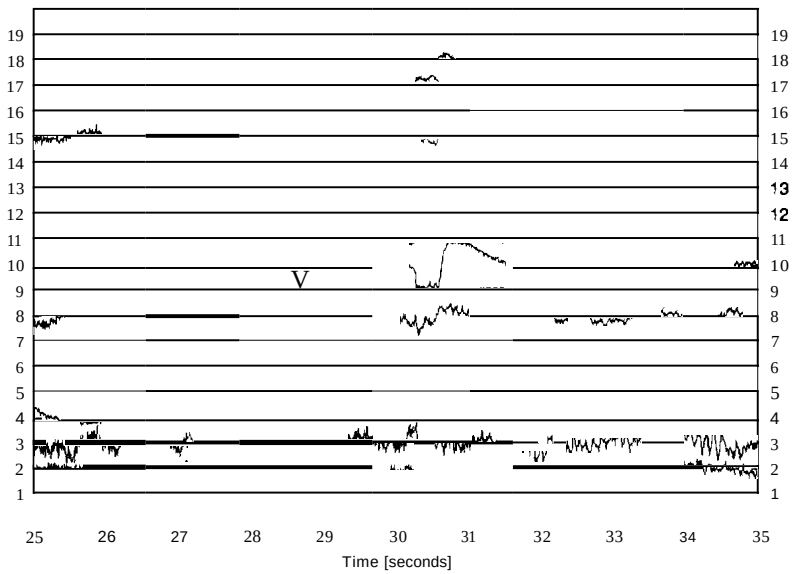

Figure 3.21: Independent Components separated using the fixed point ICA algorithm applied to EEG data shown in Figure 3.20.

The results of applying the two *ICA* algorithms to the 90 seconds of EEG data be seen in Figure 3.21 (Fixed Point) and Figure 3.22 (Extended). The IC's found by both algorithms have readily identifiable signals, especially that of the major eye blink (IC 10 in Figure 3.21, and IC 2 in Figure 3.22). The alpha increase due to eye closure is evident (as the signals become dominated by lower frequency contributions) chiefly in components IC 2 and IC 3 for fixed ICA, and in components IC 8 and IC 15 for extended ICA. On inspection the components containing alpha separated by the extended ICA algorithm are cleaner than those found using the fixed point algorithm, suggesting that other signal components are being separated along with the alpha rhythm by the fixed point algorithm. Thus it appears that the extended algorithm performs well on alpha signals, despite their gaussianity.

Another distinction between the results from the two ICA algorithms in Figures 3.21 and 3.22 is the difference in scale between components for each

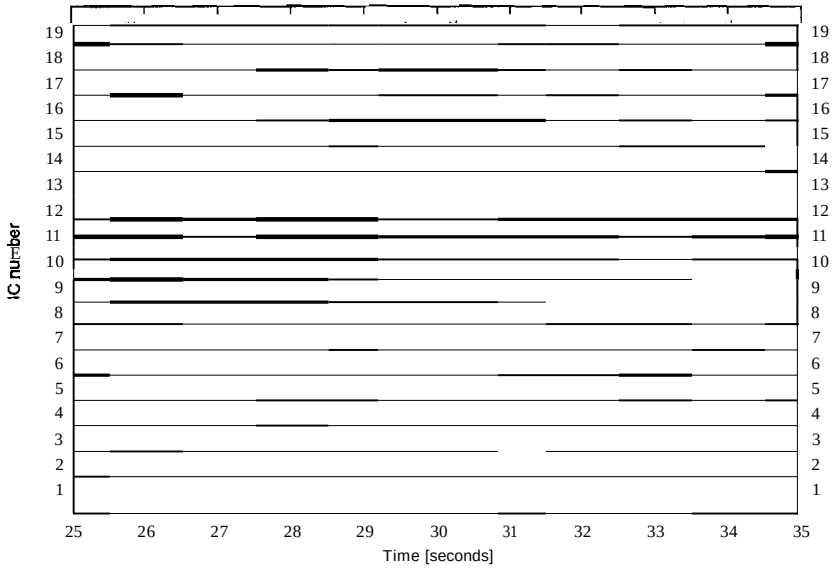

Figure 3.22: Independent Components separated using the extended ICA algorithm applied to EEG data shown in Figure 3.20.

algorithm. The scaling of each component cannot be predicted beforehand, nor can it be determined after the algorithm has been run. In order to be able to compare different components in a single data set, or between components in many data sets, the scales must be fixed. In order to do this each component is projected back onto the electrode sites; i.e. the contribution from a component at each electrode site is determined (Jung et al. 1998). This is done by applying W^{-1} to the selected component from Equation 3.42. An example of this projection is shown in Figure 3.23, where independent component 2 (which contains EOG artifact) from Figure 3.22 is projected onto electrode sites. The contribution from these components at each site is evident (compare to Figure 3.20) especially at frontal electrode sites. Now that it is possible to compare components on equal scales, the ability of each of the two ICA algorithms to separate alpha signals can be tested. To do this the Fourier transform was used to find the average spectral power in the

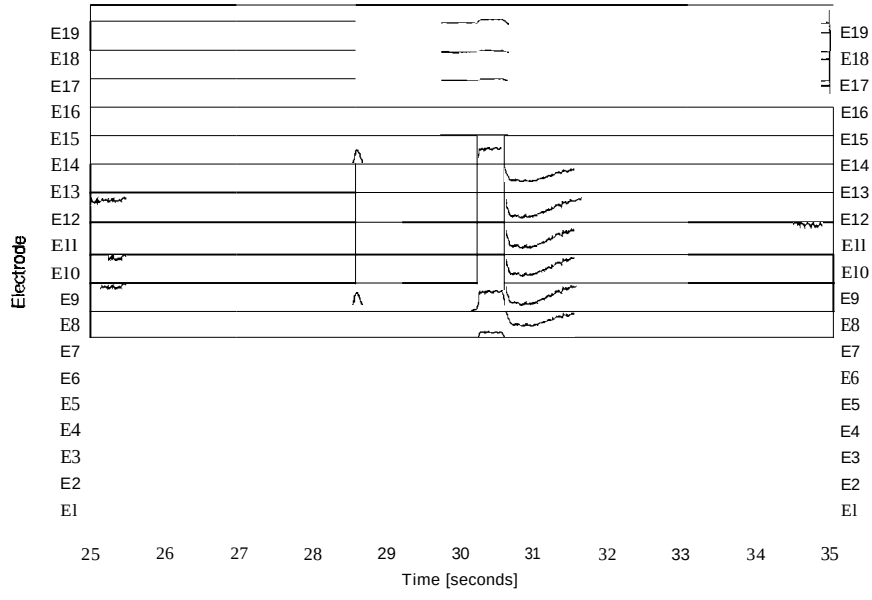

Figure 3.23: Independent Components projected onto electrode sites. These curves show the contribution to all electrodes resulting from component number 2 in Figure 3.22.

8-13 Hz band for each component (projected onto electrode sites) found by the two algorithms, averaged over all 10 subjects. The eye closure trials were used, as described on p. 25 in Chapter 2. The W coefficients were found for each of the four eye closure trials done by each subject. Each component was projected onto the electrode sites (so that scaling was correct) and the alpha spectral power in the seven posterior electrodes was averaged for the eyes open and eyes closed periods. The components were sorted by average alpha spectral power as the ICA algorithms will not necessarily deliver the IC's in the same order over successive trials. Finally, the average over all subjects was taken. The results are shown in Figure 3.24. The figures show that both algorithms concentrate the majority of alpha power during eye closure into a handful of components. The Extended ICA algorithm performs slightly

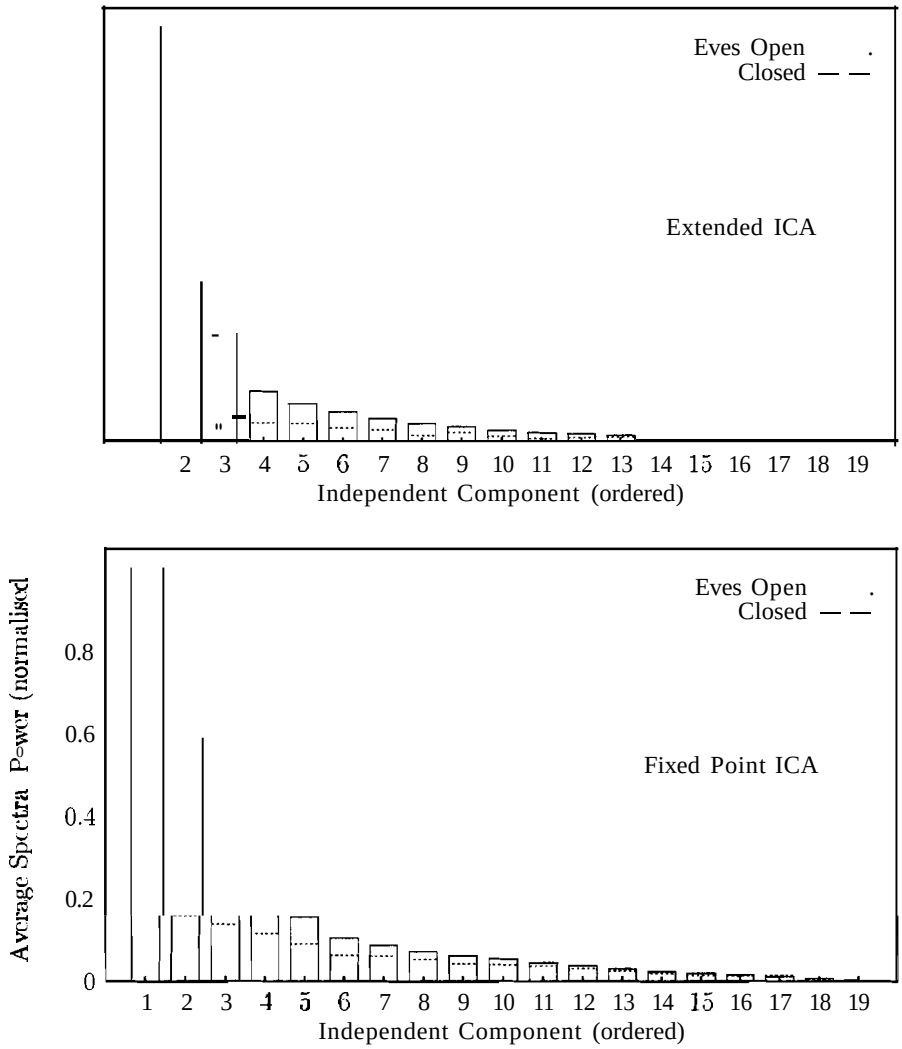

Figure 3.24: Average alpha spectral power for each of the 19 components found using Extended rCA and Fixed Point rCA algorithms during eye closure. Values for eyes open and eyes closed are shown.

better than the fixed point algorithm, with the power in the former's IC's dropping rapidly compared to the main alpha component. The Extended ICA algorithm concentrates 75% of the normalised alpha spectral power into the first three components, as opposed to 67% for the Fixed Point algorithm. This indicates that alpha EEG is being successfully separated from other EEG signals by the algorithms.

\Vhile these results are encouraging in that alpha signals are separated during eye closure, it needs to be established that the 8-13 Hz component of artifact signals is not separated into the same components as alpha EEG during eye closure. i.e. are the algorithms separating alpha from all other biological signals present, or do artifact signals appear in the component which was previously thought to contain only alpha EEG? Data presented in Figure 3.25 confirms that the components that have been separated with high alpha spectral power are due to eye closure, and not other artifact signals. Figure 3.25 shows the performance of the two ICA algorithms using W coefficients trained on four different eye closure trials (all from the same subject). The sets of W coefficients are applied to 16 EEG data sets. The 16 EEG data sets incorporate eye closure, clenching of the jaw, head movement and reading out loud. Each of the four W's are used to separate IC's from the 16 sets of data The average alpha spectral power for the each of the 19 IC's (projected onto the electrode sites) is computed. The most prominent feature of these graphs is the large increase in alpha power for some components in the jaw clenching trials. The ideal component choice is one which shows high alpha power during eye closure and low alpha power for all other test types. This would indicate that that the component contains alpha EEG but not other artifact signals. Components which show this quality have been marked in bold on the plots in Figure 3.25. Each of the four W matrices obtained

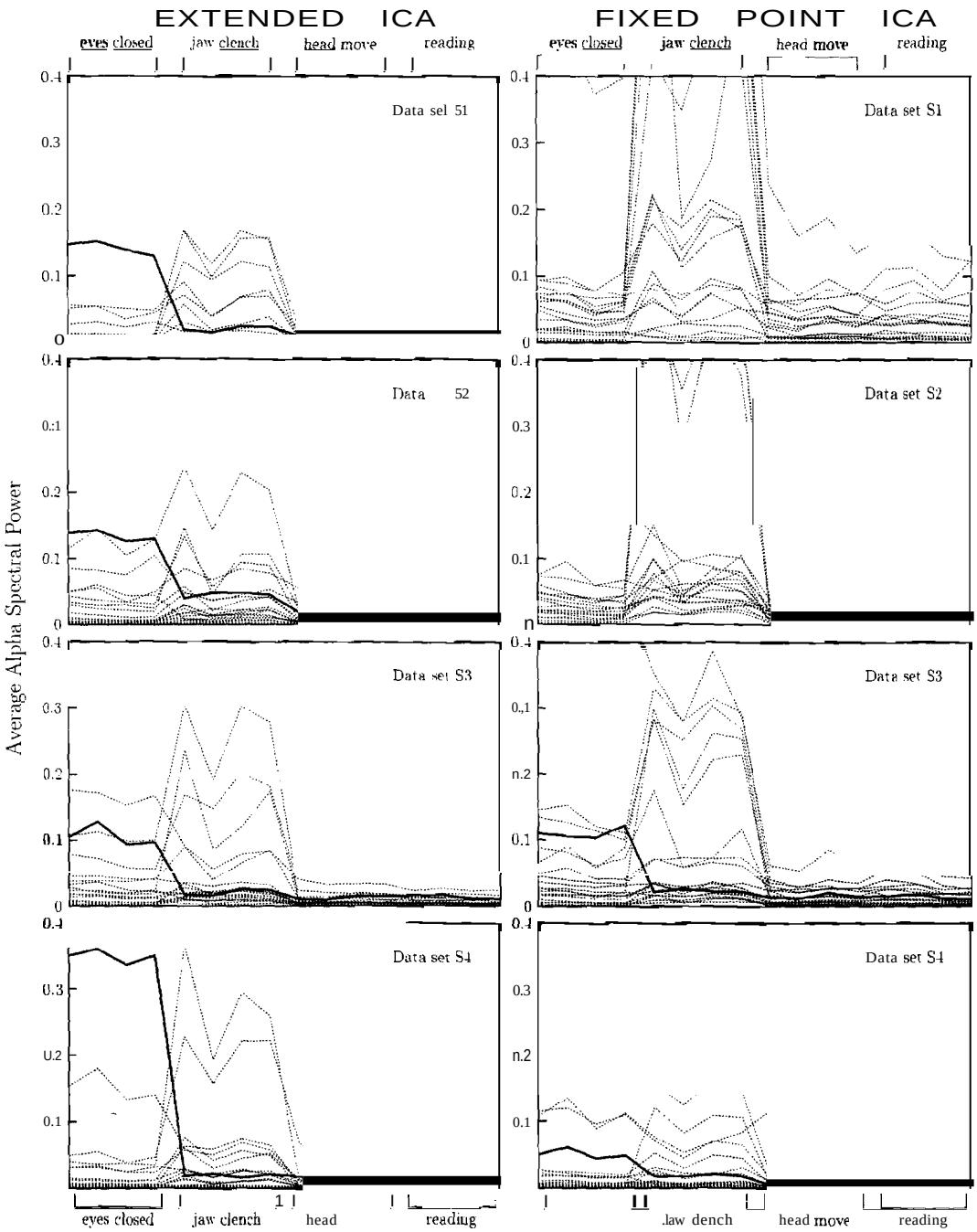

Figure 3.25: Comparison of performance of the Extended and Fixed Point rCA algorithms with regard to alpha EEG spectral power. The algorithms were applied to four sets of EEG data (81-4) involving eye closure. The ICA coefficients from these trials were then used to separate 19 Ie's for 16 different EEG data sets involving eye closure, clenching of the jaw, moving the head and reading out loud (as labeled on the x-axes). The IC's visually determined to be satisfactory for alpha separation are shown as a bold line.

by using the Extended ICA algorithm show at least one component which has the desired characteristics. The Fixed Point algorithm did not perform well in this regard, with only two satisfactory components found; all other components which showed high alpha power during eye closure also contained high alpha power during artifact trials (especially during jaw clenching). The graphs in Figure 3.25 support two important findings:

- The Extended ICA algorithm is superior to the Fixed Point algorithm for the purpose of alpha signal separation, despite initial concerns that no ICA algorithm would satisfactorily separate alpha rhythms due to the gaussian nature of alpha EEG signals, and EEG signals in general.
- Coefficients which are gained by training on one set of data are suitable for use on other data sets from the same subject, recorded during the same session.

Accordingly, the Extended ICA algorithm will be used for the remainder of ICA experiments in this thesis.

3.6.4 Results obtained for leA analysis

The Extended ICA algorithm was applied to eye closure EEG data sets for all subjects and the resulting W coefficients recorded. To determine the most appropriate IC to use for each data set the components must be visually examined. To enable a decision to be made as to which component contained the most alpha EEG signal (while avoiding artifact signals) plots similar to those in Figure 3.25 were constructed for each eye closure data set. i.e. the W coefficients found for each eye closure data set are applied to all EEG data for that subject, and the alpha power in each of the 19 components is plotted. In this way the best W coefficients and Ie are found for each subject. It

was found that for, 5 out of the 10 subjects, determination of an appropriate component to use was immediately obvious, and a straightforward choice was made. The choice of component for the remaining 5 subjects was more difficult; it was noted that for these same 5 subjects convergence using the fixed point ICA algorithm was slower when compared to the remaining subject data sets.

The chosen IC for each subject is separated in all sets of EEG data for that subject. This component is then used as the input to the integration alpha EEG detection method, and detection times and errors are calculated as previously shown. Note that the components do not need to be projected onto electrode sites for this procedure as the integration alpha EEG detection method is scale independent (since the threshold is set by the mean and standard deviation of the baselines, see p. 30). The detection time and errors obtained when the ICA components are used as an input to the integration alpha detection algorithm are shown in Figure 3.26. Despite problems in

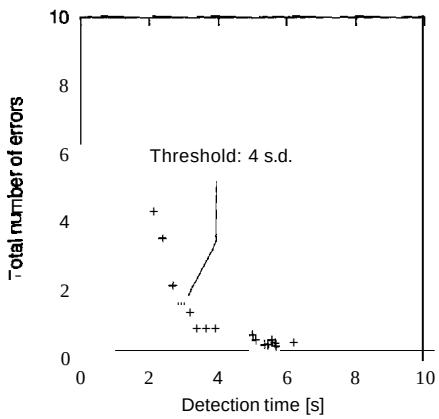

Figure 3.26: Results obtained when using ICA components as an input to the integration alpha detection method.

separating appropriate components for use with alpha detection algorithms

in some subjects, the results are good, showing low detection times and error counts. The best $\overline{\chi}$ result is obtained when using a threshold setting of 4 standard deviations.

3.7 A Comparison of results and discussion

A comparison of results for preprocessing methods used in this chapter is shown in Figure 3.4. The rankings are determined as described previously in Section 2.6 (p. 52). The rankings show the significantly poorer performance of the simple filtering methods; the unity and Bartlett filter which suffered from poor spatial resolution. Also evident is the very disappointing results for the adaptive Capon filter, whose algorithm was not able to cope with the poor spatial resolution of the alpha EEG, and damaged the characteristics of the filters designed. rather than enhancing them. The results using simulated data to design Capon filters are much better, showing that appropriate algorithm choice can overcome some of the the problems caused by the low spatial resolution inherent with the alpha EEG signals.

Adaptive filtering using reference electrodes showed some improvement over the integration algorithm used with no preprocessing, but the improvement is marginal. Similarly the use of the four sphere head model and LCMV filter design algorithm did not give the low $\overline{\chi}$ values that were expected. This was primarily due to the poor performance of the filter with respect to artifact signals; the filter design which uses signal magnitude rather than temporal disparity was not able to discriminate sufficiently between EEG signals and the overpowering presence of artifact, especially EMG from the jaw.

The most highly ranked preprocessing method was the Independent Component Analysis technique, using the Extended ICA algorithm. This algo-

Alpha Detection Method	mean $\ln(\overline{\chi})$ value and std error	p value	rank
Independent Component Analysis	1.220 ± 0.071	0.107	1
Capon's Filter (simulated data focus: -0.09 null: +0.09)	1.238 ± 0.101	0.185	2
LM8 Adaptive Filter (reference electrode: EMC)	1.292 ± 0.053	0.333	3
LM8 Adaptive Filter (reference electrode: E5)	1.307 ± 0.063	0.343	4
Integration	1.392 ± 0.093	-	5
LCMV filter using four sphere head model (focus: -0.04)	1.471 ± 0.065	0.546	6
Unity filter	1.780 ± 0.141	0.037	7
Bartlett Filter (focus: -0.20)	1.653 ± 0.118	0.030	8
Capon's filter (adaptive w update)	2.087 ± 0.143	<0.001	9

Table 3.4: Ranking of results from alpha detection techniques introduced in Chapter 3. Techniques are ranked using the p value from a paired two-tailed t-test, compared against the integration alpha EEG detection method.

rithm proved successful despite concerns that the algorithm would not cope with the apparent gaussian nature of EEG (and alpha EEG in particular), and despite findings that the separation of components for some subjects was much more efficient than for others. Since the time that ICA experiments for inclusion in this thesis were completed, a report by other researchers has been published with demonstrates the ability of the ICA algorithm to enhance EEG signals in preparation for brain-computer interfacing. The experiments by Makeig et al. (2000), which concentrate on the show that preprocessing by the ICA algorithm improved the performance of the methods used, as it does for alpha EEG detection in this thesis and demonstrated in Section 3.6. Unfortunately, the ICA algorithm is also the most computationally demanding of all the methods covered in this chapter (as an example, the time to separate components for a single EEG data file was an order of magnitude longer than the time it took to process a EEG data file using the integration alpha detection method). Although the algorithm only needs to be trained once to obtain a W matrix for each subject, data needs to be inspected visually to choose an appropriate component to use, and W coefficients may not necessarily be suitable for use over successive trials (i.e. a subject on two different days may give very different W matrices due to electrode placement differences.

The preprocessing techniques covered in this chapter have all been used as an input to the integration alpha EEG detection method introduced in Section 2.3.1. The preprocessing filters described could similarly be applied to any of the other alpha detection methods that have been mentioned. Chapter 4 will introduce alpha detection methods which again use many electrodes in an attempt to produce a fast and reliable alpha detection technique. In contrast to all methods discussed so far in this study, which use amplitude

information to enable the detection of alpha onset following eye closure, the methods described in Chapter 4 will use the apparent location of alpha EEG activity in the brain as a discriminator between alpha and non-alpha periods.

Chapter 4

Location-based methods for alpha EEG detection

4.1 Introduction

The concept of the sensor array was discussed in the introductory section of Chapter 3. As well as the spatial filtering operations which were used in Chapter 3 to select regions of the head from which to receive signals, sensor arrays may be used to determine the regions of highest EEG activity in the head. This leads to a possible method of alpha EEG detection: rather than assuming the location of alpha EEG in the head, constructing a spatial filter to focus on that region and processing the resulting signal, it may instead be possible to track the location of highest alpha EEG activity in the head, and use this as an indicator of an increase in the alpha EEG activity caused by eye closure (Searle & Kirkup (2001)). Although this does not imply that the source of alpha activity moves, it may be feasible to monitor the location of highest alpha EEG activity. Between periods of eyes closed and eyes open the region of dominant alpha activity may shift

in the brain; this chapter will investigate whether this shift can be utilised for eye closure detection. Techniques introduced in this chapter will use the estimated location of highest EEG activity to indicate alpha EEG changes.

4.2 Source localisation using a Bartlett beamformer

One method of signal source localisation can be implemented using beamformers. This is achieved by scanning the area of interest with a beamformer and testing the signal power at each location. A physical area to be monitored is selected and a series of beamformers are designed with focus points directed at evenly spaced locations covering the chosen region. The power of the signal from each beamformer is calculated and the point of maximum power is designated as the signal source location. The signal power from a Bartlett beamformer focused at (x, y) can be found by (Krim & Viberg 1996)

$$P(x, y) = \mathrm{at}(x, y)\mathrm{Rxa}(x, y) \tag{4.1}$$

where R_x is the covariance matrix (Equation 3.19) and a is the steering vector (Equation 3.4). An example of source localisation using Equation 4.1 is shown in Figure 4.1. This plot shows the result of localisation using artificial EEG data, simulating a single 10 Hz point source at coordinates (-0.04,-0.04). A maxima is present at the source location, though the limited spatial resolution means that it is not well defined.

To see how localisation using the Bartlett beamformer performs on real EEG data (which is assumed to have sources which are distributed in nature, rather than single point sources) illustrative EEG data from four eye closure trials were processed, and the results shown in Figure 4.2. The area was

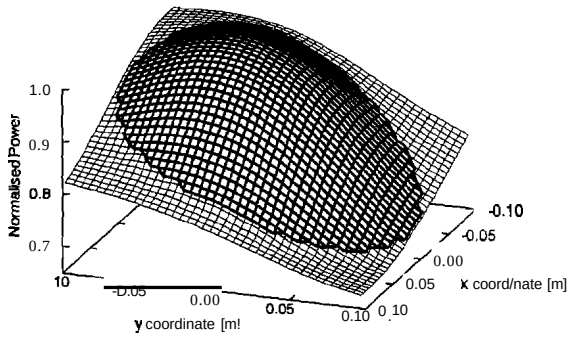

Figure 4.1: Example of source localisation using a Bartlett beamformer. Data used was simulated EEG of a point source at coordinates (-0.04,-0.04). The darkened area represents the area covered by the head.

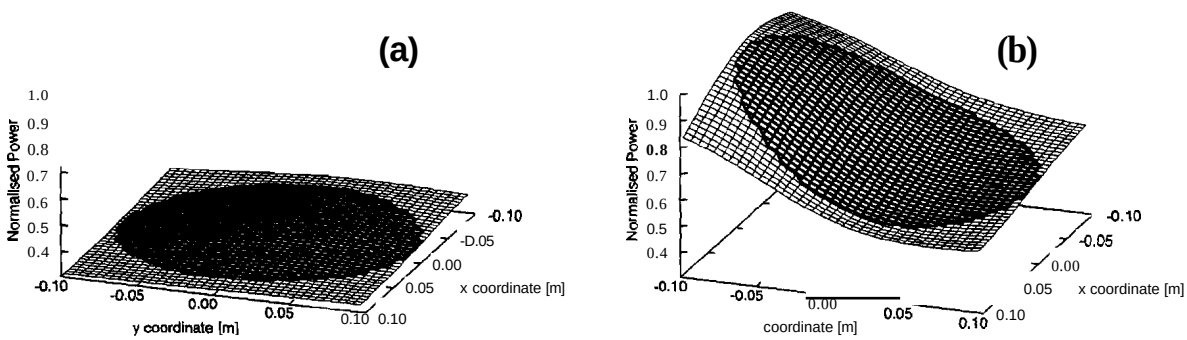

Figure 4.2: Localisation using a Bartlett beamformer applied to illustrative EEG data from eye closure trials. The plots show results averaged over four eye closure trials for periods of (a) eyes open and **(b)** eyes closed. The darkened area represents the area covered by the head.

divided into a 40 x 40 grid, and Equation 4.1 was used to calculate the signal power from each point on the grid during eyes open and eyes closed periods (30 s each). The results for eyes open and eyes closed periods from the four EEG data sets (all from the same subject) were averaged. Coordinates used in in Figure 4.2 correspond to those used previously (see Figure *C.1).* There are no maxima discernible in Figure 4.2 which indicate specific locations of alpha activity, however the results from the eyes open and eyes closed cases are sufficiently different to warrant the investigation into the use of Bartlett beamformer localisation for alpha EEG detection. That is, it may still be possible to use the kind of non-specific results in Figure 4.2 to differentiate between eyes open and eyes closed states.

4.2.1 Using the Bartlett beamformer for alpha EEG detection

To use the localisation process for alpha EEG detection the EEG data was processed in blocks *b* samples long. Smaller blocks mean better temporal resolution, (i.e. the use of a data block 2 seconds long means a result can only be obtained once every 2 seconds), larger blocks will give better spatial resolution. An alpha EEG detection algorithm needs a parameter to operate on, ideally for localisation methods this parameter would be an estimate of the source location. The absence of maxima in the results obtained from applying a Bartlett beamformer to EEG data (e.g. Figure 4.2) means that a search of the result surface for a maxima will not give a meaningful parameter. As an alternative, the gradient of the surface for coordinates at the rear of the head will be calculated and used as the defining parameter in the detection algorithm. It is expected that lack of neural activity (when a subject has eyes open and resting) will give a small gradient (as in Figure 4.2(a)), while

high occipital alpha activity associated with eye closure will produce a surface with a large positive gradient (as in Figure 4.2(b)). Artifact will produce high signal activity at the front of the head (or evenly distributed over the head) thus giving a negative or near-zero gradient. Thus alpha EEG detection can be achieved by monitoring the presence of positive gradients. The algorithm for alpha detection using localisation is:

- Divide the EEG data into blocks b samples in length
- For each data block
  - Perform localisation by applying Equation 4.1, using coordinates covering the head area in a 20 x 20 grid
  - Construct a surface of the signal power from the beamformers at each point
  - Calculate the gradient of the surface parallel to the y-axis at the rear of the head

Additionally, this algorithm may be modified to significantly lower computational expense, as it implies that only a few points are required to calculate the gradient at the rear of the head. Examples obtained by applying this algorithm to EEG data are shown in Figure 4.3. The EEG data sets used in the example were an eye closure trial and a jaw clench trial (see p. 25 for details) using a data block size of $b = 256$ samples (of duration 0.5 s). Results for one eye closure trial in Figure 4.3(0,) shows that the period of eye closure is distinct from the eyes open periods by the positive gradient values. As predicted, artifact is visible as negative or low-valued gradients as shown by the jaw clench trials shown in Figure 4.3(b).

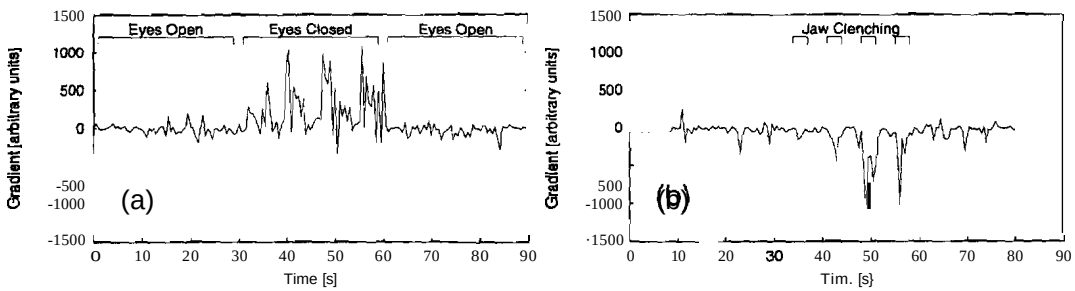

Figure 4.3: Results from the alpha EEG detection using Bartlett beamformer localisation. Two EEG data sets are shown, (a) an eye closure trial and (b) a jaw clench trial. Periods of eyes open, eyes closed and jaw clench are indicated.

4.2.2 Application of a sliding window averager

Even though the major features in the plots of Figure 4.3 are discernible there is still significant variability in the gradient values, thus smoothing of the gradient points needs to be performed before the final step of calculating alpha detection times and error rates. The smoothing is done by a moving window averager which has a length dependent on the data block size b. The alpha EEG detection algorithm using Bartlett beamformer localisation will be tested using five different b sizes. The corresponding averager window length i for each block size is shown in Table 4.1. The window lengths were chosen so that $bl \geqslant 1280$ samples ($\equiv$ 2.5 s). This time product of 2.5 s was discovered empirically to give best results for a range of data block sizes, but also closely corresponds to the 2.3 s time constant successfully used with the integration alpha EEG detection technique (see p. 29).

Once the gradient values have been averaged by the sliding window, thresholds for detection are set using the baseline and standard deviation of the eyes open period, as previously described in Section 2.3.3.

data block size		averaging
samples *(b)*	seconds	window length *(l)*
128	0.25	10
256	0.50	5
512	1.00	3
1024	2.00	2
2048	4.00	1

Table 4.1: Averaging window sizes to use with different data block lengths

4.2.3 Results using Bartlett beamformer localisation

The alpha EEG detection method using Bartlett beamformer localisation was applied to EEG data for all subjects, and detection times and errors were calculated as previously described in Section 2.3.5. The results are shown in Figure 4.4. The plots show good performance the poor

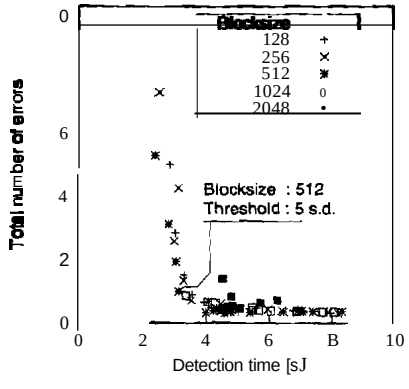

Figure 4.4: Results obtained for alpha EEG detection using Bartlett beamformer localisation.

spatial resolution of the Bartlett beamformer with EEG signals. The smaller blocksizes show lower $\overline{\chi}$ values compared to larger (*b* = 1024 and 2048) blocksizes, which suffer from high detection times. The lowest $\overline{\chi}$ value is

found when using a blocksize of $b = 512$ and a threshold of $n = 5$ standard deviations.

4.3 Minimum variance beamformer for source localisation

The minimum variance approach used to create a spatial (Capon) filter as described in Section 3.3.3 can also be used for signal source localisation. The array output power of a Capon beamformer at coordinates (x, y) is given by (Gonen & Mendel 1998)

$$P(x, y) = \frac{1}{\mathbf{a}^{\dagger}(x, y)\mathbf{R}_x^{-1}\mathbf{a}(x, y)} \tag{4,2}$$

(compare to the Capon beamformer design criteria, Equation 3,18).

Utilising the same artificial EEG test data used for Figure 4.1, the results of performing localisation using Capon's beamformer are shown in Figure 4.5. Localisation using Capon's beamformer with artificial EEG data gives a sharp peak at the source coordinates. As indicated in Section 3.3 the superior characteristics of Capon's beamformer over the Bartlett beamformer using simulated EEG data did not translate to good performance on real EEG data. This is also found to be the case here, as indicated by the illustrative data shown in Figure 4.6. These plots show localisation curves using Capon's beamformer applied to four sets of eye closure EEG data (all from the same subject, as used for Figure 4.2). Figure 4.6 reveals that there is little difference between the localisation results for eyes open and eyes closed cases. This difference is too small to enable an algorithm to successfully detect the onset of alpha EEG due to eye closure. Upon inspection of results obtained using the Capon beamformer localisation on EEG data

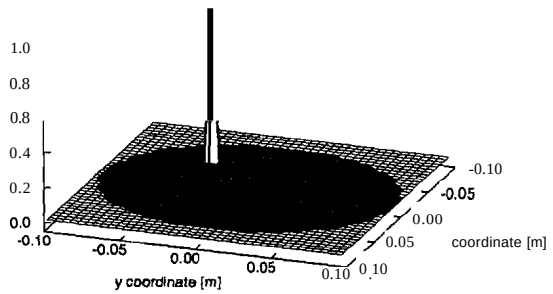

Figure 4.5: Example of source localisation using Capon's beamformer. Data is simulated EEG of a point source at coordinates (-0.04,-0.04). The darkened area represents the area covered by the head.

for all subjects *(N=10),* the lack of consistent and usable difference between eyes open and eyes closed results was found in all cases. The poor performance of Capon's beamformer on EEG data (as discussed in Section 3.3.4) can be attributed to the inability of the algorithm to steer nulls effectively due to the poor spatial resolution inherent with alpha EEG. In addition to disabling the filter characteristics, the attempt at nulling also sacrifices noise suppression capability (Krim & Viberg 1996).

4.4 MUSIC
(MUltiple SIgnal Characterisation)

The beamforming methods for source localisation (apart from having low spatial resolution) are limited physically by the signal to noise ratio (SNR) of data provided. This section introduces a source localisation method which has no theoretical SNR limit (Le. the results the method returns are inde-

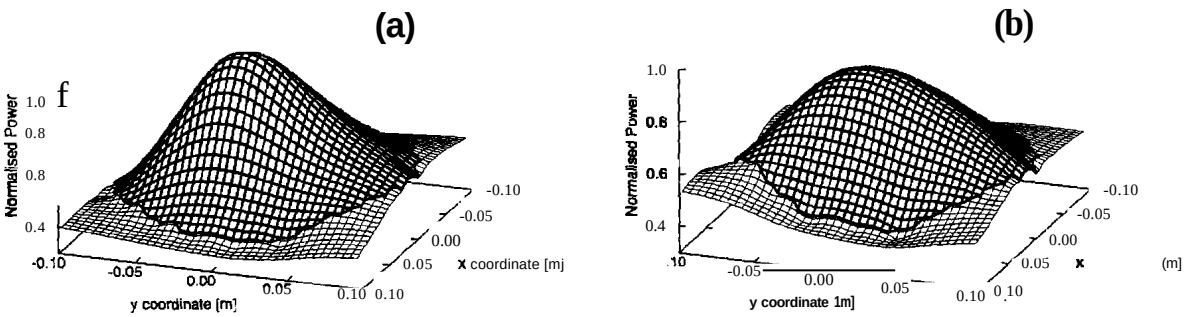

Figure 4.6: Localisation using Capon's beamformer applied to illustrative EEG data from eye closure trials. The plots show results averaged over four eye closure trials for periods of **(a)** eyes open and **(b)** eyes closed. The darkened area represents the area covered by the head.

pendent of SNR in an ideal situation.) This is achieved by using properties of second order statistics in signals, namely the covariance matrix R. The basis of the technique, called MUltiple SIgnal Characterisation (MUSIC), is based on separating signal characteristics into signal and noise subspaces.

4.4.1 Signal and noise subspaces

The sensor array model was introduced in Section 3.2.1 as

$$x = As + n \tag{4.3}$$

The spatial covariance matrix of x is $\mathbf{R}_x$ (estimated by Equation 3.19) which can be represented as

$$\mathbf{R}_x \quad \text{Cov}[x]$$
$$- \quad \text{Cov}[As] + \text{Cov}[n]$$

and using the 'Law of separation of this gives

$$= \mathbf{A}\mathbf{R}_s\mathbf{A}^\dagger + \mathbf{R}_n \tag{4.4}$$

Where R_s and R_n are the signal and noise covariance matrices. If it is assumed that all signals are uncorrelated, and that the noise is spatially white (i.e. the noise is uncorrelated among all sensors and has a common variance σ^2 at all sensors) then Equation 4.4 becomes

$$\mathbf{R}_x = \mathbf{A}\mathbf{R}_s\mathbf{A}^\dagger + \sigma^2\mathbf{I} \tag{4.5}$$

This assumption that signals are not correlated has significant impact on the performance of the algorithm, as will be demonstrated. A *k* x *k* matrix can be expressed in terms of its k eigenvalue/eigenvector pairs (Johnson 1998),

$$B = \sum_{i=1}^{k} \lambda_i \mathbf{e}_i \mathbf{e}_i^\dagger \tag{4.6}$$

where λ_i and ei are eigenvalues and eigenvectors of B respectively. This is called *eigendecomposition.* Furthermore (Swindlehurst & Kailath 1992),

$$\underset{kxk}{B} \quad \underset{kXk}{P} \quad \underset{kxk}{A} \quad \underset{kxk}{pt} \tag{4.7}$$

where

$$\mathbf{P} = [\mathbf{e}_1 \ldots \mathbf{e}_k]$$

$$A \quad \begin{bmatrix} \lambda_1 & 0 & \ldots & 0 \\ 0 & \lambda_2 & & \mathbf{O} \\ & & & \\ \mathbf{O} & 0 & & \lambda_k \end{bmatrix}$$

lThe Law of Separation of Errors states (Johnson 1998, Monzingo & Miller 1980),

if Y Ax

COylY] = ACov[x]At

So, continuing from Equation 4.5

$$\mathbf{R_x} = \mathbf{A}\mathbf{R_s}\mathbf{A}^\dagger + \sigma^2\mathbf{I}$$
$$\mathbf{P}\Lambda\mathbf{P}^\dagger \tag{4.8}$$

If we have a L sensors, and M independent (or partially correlated) signal sources, it can be shown (Gonen & Mendel 1998) that ARsAt has rank M. Thus ARsAt has M non-zero eigenvalues and $M' = L - M$ zero eigenvalues. Consequently (Krim & Viberg 1996) R_x has M' eigenvalues equal to σ^2, and M eigenvalues that are larger than σ^2. We can partition the eigenvalue/eigenvector parts into noise eigenvectors (corresponding to eigenvalues $\lambda_{M+1} = \ldots = \lambda_L = \sigma^2$) and signal eigenvectors (corresponding to eigenvalues $\lambda_1 \geq \ldots \geq \lambda_M > \sigma^2$). Thus Equation 4.8 can be separated into

$$\underset{LxL}{\mathbf{P}} \quad \underset{LxM}{\mathbf{P_s}} \quad \underset{MxM}{\Lambda_s} \quad \underset{MxL}{\mathbf{P_s}^\dagger} + \underset{LxM'}{\mathbf{P_n}} \quad \underset{M'xM'}{\Lambda_n} \quad \underset{M'xL}{\mathbf{P_n}^\dagger} \tag{4.9}$$

The matrices P sand P n are called the signal and noise subspaces.

4.4.2 The MUSIC algorithm

Utilising either the noise or signal subspace, the MUSIC 'spatial spectrum' is given by

$$D(x, y) = \frac{\text{at}(x, y)a(x, y)}{\underline{\text{at}}(x, y)\ \underline{\Pi}\ \underline{a}(x, y)} \tag{4.10}$$

$$\Pi = \text{pnpnt}$$

$$\text{I-PsPst} \tag{4.11}$$

The denominator of Equation 4.10 is small at source locations (x, y), and thus maxima are produced for source positions. In practice the noise variance is not known, so to separate the noise and signal subspaces the number

of signal sources M must be predetermined. The performance of the MUSIC algorithm is compared to beamforming (Bartlett and Capon) in Figure 4.7. The example curves in the figure are created using $M = 3$ simulated far-field signal sources. Due to the source being in the far-field, direction of arrival (angle) is shown, rather than a source location. The plots show the ability of the algorithm to resolve closely spaced sources (graphs (a) and (b)); the Bartlett beamformer fails to resolve the sources when they are close together. Under low SNR (graph (c)) the MUSIC algorithm shows superior performance to both beamformers: if the covariance matrix were able to be computed exactly, the SNR would have no effect on the MUSIC spectrum, only computational rounding lowers the SNR performance. One complication with the MUSIC algorithm (and Capon beamformer) is shown in Figure 4.7(b); when signals are correlated the sources are unable to be resolved. In contrast, the Bartlett beamformer suffers little degradation in performance when the signals are correlated. Figure 4.7 highlights similarities between the Capon beamformer and MUSIC algorithm: the MUSIC algorithm is equivalent (Ganen & Mendel 1998) to the Capon beamformer when the covariance matrix is exact, and the SNR infinite.

4.4.3 EEG data and the MUSIC algorithm

It has been established that source localisation using the Capon beamformer (Section 4.3) is not suitable for use as a basis for alpha EEG detection. Tests in this section will determine whether the superior SNR performance of the MUSIC algorithm will enable source localisation with alpha EEG.

As shown in Section 4.4.2 the number of signal sources must be known before the algorithm can be applied (to allow the separation of R_x into signal and noise subspaces). Experiments with alpha EEG data have

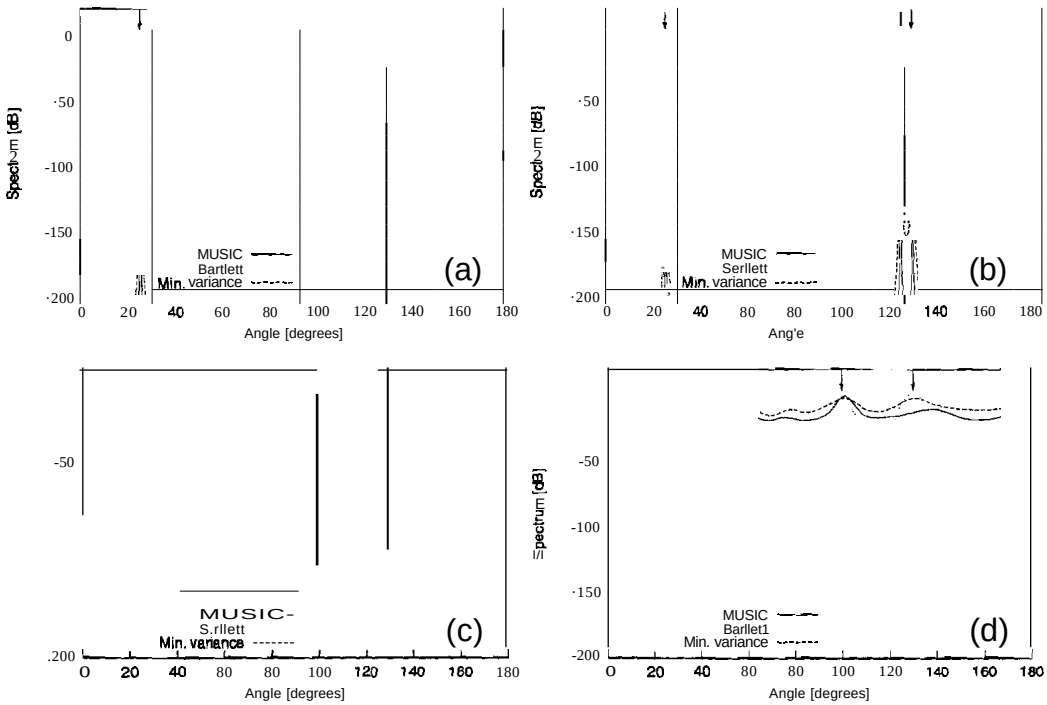

Figure 4.7: Comparison of the Bartlett beamformer, minimum variance (Capon) beamformer and MUSIC source localisation algorithms. Plots show the signal strengths arriving from different angles (specified on the x-axis). Plot (a) shows. results using three far-field sources with frequencies of 9, 10 and 11 Hz (all of equal amplitude). Arrows show source directions, and the SNR of the test signals is 50 dB. (b) shows the same signals with two sources moved closer together. (c) shows the signals with a SNR of 10 dB. (d) shows the results when all three signals have the same frequency of 10 Hz.

shown that setting the number of signal sources to $M = 1$ returns the best results, though higher settings do not change the results considerably. Techniques are available to estimate the number of signals, for an overview see Krim & Viberg (1996).

For the MUSIC algorithm to perform successfully, the input data needs to have a real and imaginary component (Le. an analytic signal). To make the EEG data analytic, the Hilbert transform is applied (see Appendix D.6 for details) before the MUSIC algorithm is used. Figure 4.8 shows the results from applying the MUSIC algorithm (Equation 4.10) to EEG data from eye closure trials. There is a visible difference between the eyes open and

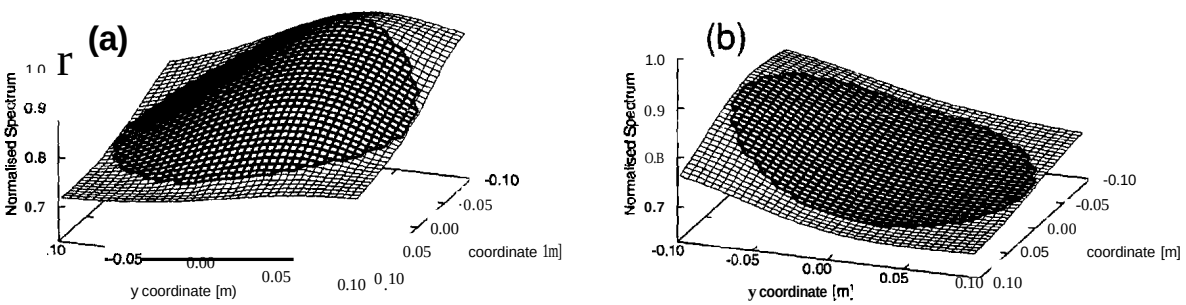

Figure 4.8: Localisation using a music beamformer applied EEG data from to eye closure The plots show results averaged over four eye closure trials for periods of **(a)** eyes open and **(b)** eyes closed. The darkened area represents the area covered by the head.

eyes closed states. As with Bartlett beamformer source localisation it is not possible to use maxima from the surfaces, thus the gradient technique is applied again. Example plots of gradient values found using the MUSIC algorithm with an eye closure and jaw clench EEG data set are shown in

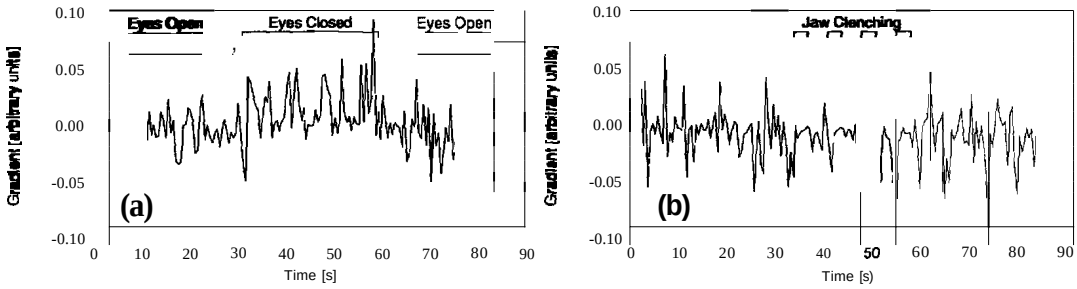

Figure 4.9: Gradient values obtained after applying the MUSIC algorithm to (a) eye closure and **(b)** jaw clenching EEG data sets. A blocksize of $b = 256$ samples was used.

Figure 4.9. The blocksize used in the example was $b = 256$ samples (of duration 0.5 s). There is a change in the data trend during eye closure there though it is not as distinct as the example shown for the Bartlett beamformer (Figure 4.3). As Figure 4.9(b) shows, artifact presence causes negative gradient values. As in the method using Bartlett beamformer source localisation, an averaging sliding window will be used to smooth the gradient values before detection times and error rates are computed.

4.4.4 Results

The results when the MUSIC algorithm is applied to all sets of EEG data (from subjects as described in Section 2.2.1) are shown in Figure 4.10. There are noticeably few results obtained (as mentioned in Section 2.3.5, only threshold settings which successfully detect the alpha activity increase due to eye closure in at least 75% of subjects are displayed) and the two settings shown have relatively high $\overline{\chi}$ values. The lower of the two uses a blocksize of $b = 128$ samples (=0.25 s), and a threshold setting of $n = 3$ standard deviations. Since the spatial resolution and SNR performance of the MUSIC

Figure 4.10: Results obtained when the MUSIC algorithm is applied to all sets of EEG data. Five different blocksize settings were used (though only two provide satisfactory results).

algorithm arc superior to the Bartlett beamformer this leads to the conclusion that it is the poor resolving power of the MUSIC algorithm when dealing with coherent signals that leads to the disappointing results shown in Figure 4.10. This problem with coherent signal sources also reflects on the poor performance of minimum variance (Capon) beamformer localisation, smce there is a strong link between it and the MUSIC algorithm.

4.5 Use of the LCMV forward solution for source localisation

The construction of spatial filters using the four sphere head model and LCMV design algorithm was introduced in Section 3.4. The same head model can also be used for the localisation of signals. This section will test the localisation algorithm using the four sphere head model to see whether the change in location of alpha EEG can be tracked and used to determine eye

closure successfully.

As with the Bartlett (and Capon) beamformer, localisation is performed by testing neural activity at many locations over a grid. Since the four sphere head model is used here, localisation is focused on dipole activity. Dipole localisation is measured in this case by the variance of activity at location *qo,* estimated by

$$\widehat{\mathrm{var}}(\mathbf{q}_o) = \mathrm{tr}\left(\left[\mathbf{H}^{\mathsf{T}}(\mathbf{q}_o)\mathbf{C}^{-1}(\mathbf{x})\mathbf{H}(\mathbf{q}_o)\right]^{-1}\right) \tag{4.12}$$

where Hand C are given by Equations 3.31 and 3.34 respectively, and tr(·) represents the trace of a matrix. To perform localisation, Equation 4.12 is evaluated at many *qo* locations resulting in a result matrix that is easily displayed as a surface. This method assumes that regions of large variance are regions of substantial neural activity. This method does not presume that of from single dipoles but rather a weighted combination of dipoles (de Munch et al. 1992), thus source geometries may be distributed in nature. Another advantage with this localisation method (especially when compared to the MUSIC algorithm, Section 4.4) is that no assumptions are made about the number of neural sources.

One possible problem with the LCMV localisation approach is that noise signals (in this case interference or background EEG) may be nonuniformly spatially distributed. This means that the variance of the noise signal will be larger in some regions of the head, and thus when the localisation algorithm is applied maxima will appear at these locations and may lead to mislocalisatio of alpha EEG signals. This may be corrected by normalising the previous result of Equation 4.12,

$$\widehat{\mathrm{var}}(\mathbf{q}_o) \qquad \frac{\mathrm{tr}\left([\mathrm{H}^{\mathrm{T}}(qo)C\text{-}1(x)H(qo)]^{-1}\right)}{\mathrm{tr}\left([\mathrm{HT}(qo)\mathrm{Q}\text{-}1\mathrm{H}(qo)\mathrm{r}^{1}\right)} \tag{4.13}$$

Here Q is the noise covariance matrix. As the noise covariance matrix is unlikely to be known, an estimate may be calculated using a signal that is free of the source to be investigated. The assumption is that the noise signals will be stationary, thus the results from Equation 4.13 will only show changes in remaining, nonstationary signals.

4.5.1 Example of source localisation

Examples of source localisation are shown in Figure 4.11 using the unnormalised (Equation 4.12) and normalised (Equation 4.13) localisation algorithms. The data used in these figures was collected from the eye closure trials (see p. 25). Localisation was performed on segments of EEG data with a blocksize of $b = 1024$ samples (2 s), and the resulting surfaces averaged over the eyes open and eyes closed periods. For normalisation, the Q covariance matrix was estimated using the first 30 seconds of the trial (during eyes open). Both pairs of plots show a discernible difference between the eyes open and eyes closed scenarios. Note that the normalised graph for eyes open (Figure 4.11 (c)) shows little activity because normal 'baseline' alpha behaviour has been recognised as 'noise' due the the calculation of the Q matrix using the initial 30 seconds of the trial. Also apparent in Figure 4.11 is the effect of the boundary conditions for the head model: activity is zero outside the dimensions of the head. This was not true for localisation when using the Bartlett beamformer or MUSIC algorithm. The results using the four sphere head model algorithm do not suffer from the poor spatial resolution which affects the beamforming and MUSIC algorithms (which gives the localisation surfaces from these methods the (curved' appearance). This is because the four sphere head model uses amplitude information rather than temporal characteristics to achieve localisation.

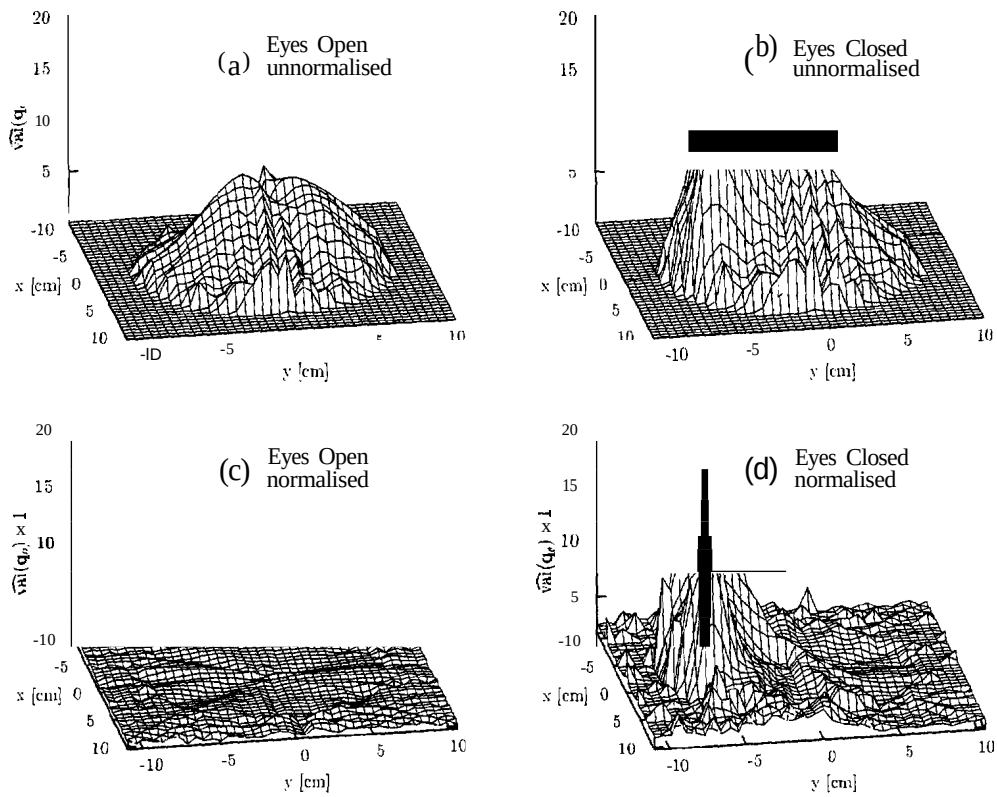

Figure 4.11: Results from source localisation using unnormalised, and normalised algorithms. Graphs show the average of four data sets from the same subject. EEG data was processed using a blocksize of $b = 1024$ samples (2 s). Coordinates are as used in Figure C.l, where negative y-values denote the rear of the head.

In addition to suggesting that the bulk of alpha EEG activity occurs i the posterior region, the results in Figure 4.11 are useful in distinguishin between eyes-open and eyes-closed states by tracking the focus of neura activity. A basic procedure for monitoring the surface maxima location woul not be appropriate, since there are many local 'spiky' minima which ma mislead an algorithm. Rather the 'centre of gravity' (COG) of the generate surface data will be used to give an indication of shifting neurological activit locations. It was empirically found that the surface of localisation is (o average) symmetrical across the x-axis, and thus the COG is always in th center (at $x = 0$). Since little information is gained from the data in th x-axis (the left-right axis of the head) the COG will be computed only fo the y-direction (front to back). The procedure to find the COG is shown i Figure 4.12. The surface plot is 'compacted' into two dimensions by summin

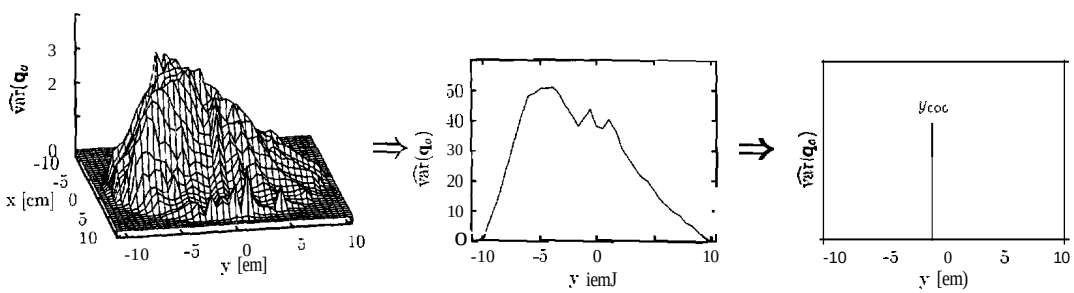

Figure 4.12: Procedure to find the centre-of-gravity (COG) for a source lo calisation surface. The surface of localisation results in summed over th x-coordinates, then Equation 4.14 is applied to find y_{COG}.

all data across the x-dimension, then the COG of this data is found usin Equation 4.14.

$$y_{COG} \quad \frac{\sum \widehat{var}(\mathbf{q}_o) \; x \; y}{\sum \widehat{var}(\mathbf{q}_o)} \qquad (4.14$$

4.5.2 The influence of the data block size

In order to use COG as a localisation method the EEG data must be processed in finite blocks. As with the Bartlett beamformer and MUSIC localisation algorithms, an important consideration in the estimation of the neural activity location is the size of the data blocksize b to use with Equation 4.12 or Equation 4.13. To use the technique for eyes open/eyes closed determination, a short data block size is desirable (to give more COG location estimates per second and thus a faster detection time), but conversely a small data block size may give poor positional discrimination compared to large block sizes. The influence of the data block size on COG values during eye closure is shown in Figure 4.13. EEG data from eye closure trials for all subjects was processed, and histograms of the predicted COG locations were derived separately for eyes open and eyes closed periods. The processing for the example in Figure 4.13 was performed with Equation 4.12 (without the noise normalisation) using five different data block sizes. The ideal result for eyes open and eyes closed data on these plots would be a large separation between the means for the two COG distributions, with each distribution having a small standard deviation. Figure 4.13 shows that as the block size increases, the separation in means of the eyes open and eyes closed distributions increases, and standard deviations decrease. This is emphasised in Figure 4.13(f) which plots the change in separation of means, and the standard deviations for each distribution as the data block size changes. Thus the most ideal distributions are given when using a blocksize of 2048 samples. However, as will be seen in Section 4.5.4, a blocksize of such length may lead to longer detection times for alpha EEG increases, despite the better discrimination between eyes open and eyes closure cases.

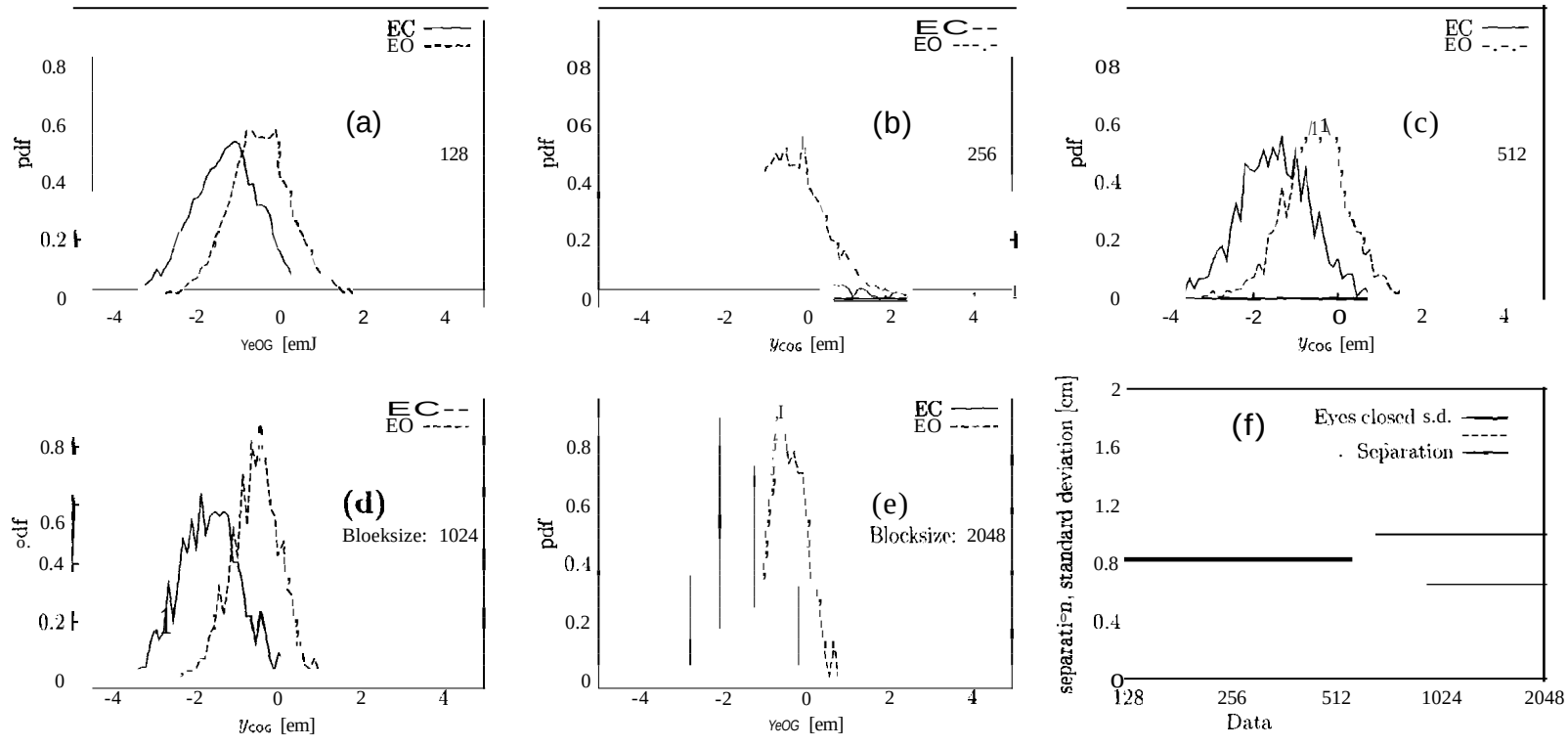

Figure 4.13: Histograms (plots (a)-(e)) showing the probability density fUllctions (pdf) for estimated COG values *(YCOG)* for eyes open and eyes closed periods data using the non-normalised method for five different data block sizes. Data from all eye closure data sets from all subjects were used to create the histograms. Plot (f) shows the separation of means, and standard deviations of the eyes open and eyes closed distributions from the COG histograms in Plots (a)-(e).

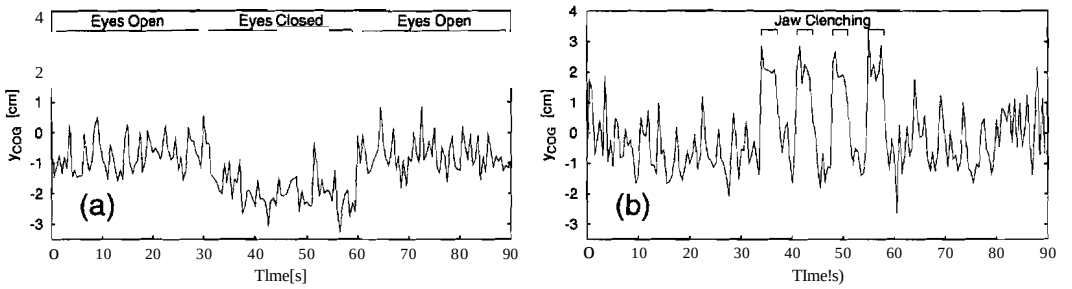

Figure 4.14: Example of localisation using the four sphere head model and y_{COG} during (a) an eye closure and (b) jaw clenching trial. Blocksize $b = 256$.

4.5.3 Examples of localisation

The use of source localisation using the four sphere head model is demonstrated in Figure 4.14, which shows the change in y_{COG} during eye closure and jaw clench trials. The blocksize used is $n = 256$ samples (of duration 0.5 s). The eye closure is visible by the decrease in y_{COG} values, caused by increase occipital alpha EEG activity. The positive y_{COG} values during artifact (Figure 4.14(b)) are also apparent. Due to the variability of the y_{COG} values, a sliding window averager is required (as used with the Bartlett beamformer and MUSIC algorithm). The size of the window is determined by the blocksize, and window lengths are as described in Section 4.2.2.

After smoothing by the sliding window the thresholds for detection can be computed, and detection times and errors calculated. One minor difference in the procedure in this section (compared to Bartlett beamformer or MUSIC) is that eye closure leads to a decrease in the parameter used in alpha detection; as is evident in Figure 4.14, y_{COG} decreases upon eye closure. This means that the smoothed data needs to be inverted about $y_{COG} = 0$ so that the previously described threshold determination (Section 2.3.3) and detection time calculation (Section 2.3.4) procedures (which assume the parameter

increases with alpha activity) can be followed.

4.5.4 Results for alpha EEG detection using localisation with the four sphere head model

The alpha detection method using the four sphere head model was applied to all sets of EEG data, and detection times and errors computed as previously described. The results for the algorithm with and without noise-normalisation, and for five different blocksize settings are shown in Figure 4.15. The plots reveal that the use of normalisation gave lower $\overline{\chi}$ scores

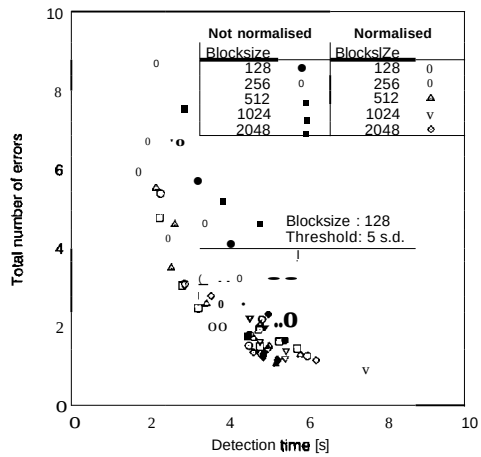

Figure 4.15: Results obtained for alpha EEG detection using the four sphere head model source localisation.

for the range of blocksizes tested. The lowest $\overline{\chi}$ score was given using normalisation with a blocksize of n = 128 (=0.25 s) and a threshold setting of 5 standard deviations.

4.6 Localisation using the power source location coefficient

This technique uses source localisation as a basis but does not return an estimate of the source location that is physically meaningful. This lack of a physical relation is irrelevant for the purpose of this study as the result is nonetheless useful for the detection of the increase in alpha EEG activity. Appropriately, the result is termed a location coefficient (rather than a location estimate) so as not to be misleading. This determination of the power source location coefficient uses a direct approach which is computationally simple, and thus can be implemented easily. This contrasts with the other localisation techniques discussed so far in this chapter which require many calculations, especially the MUSIC algorithm and four sphere head model. The power source location coefficient method uses signal amplitude information (as does the four sphere head model) rather than temporal information (as the MUSIC and beamformer localisation methods use). The algorithm uses the alpha (8-13 Hz) power present in the EEG signal at each of the 19 electrodes to indicate the location of highest alpha EEG activity in the head. If the position of electrode i is denoted by a vector $\vec{e_i}$, and the alpha EEG power present at that electrode is P_{α_i}, the process can be represented by

$$\vec{d} = \sum_{i=1}^{L} P_{\alpha_i} \vec{e_i} \tag{4.15}$$

where $\vec{d}$ is a vector which gives an indication of source location, and the number of electrodes is $L = 19$. The vector $\vec{d}$ does not give a physically meaningful result as its units are not of displacement. An example of the resulting vectors $P_{\alpha_i} \vec{e_i}$ during eye closure are illustrated in Figure 4.16. The figure shows that vectors relating to electrodes at the posterior of the head are

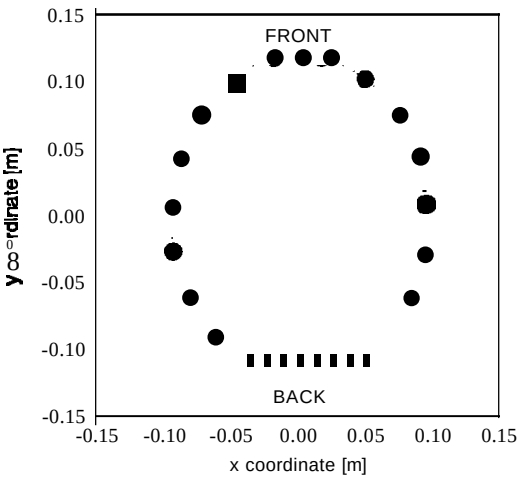

Figure 4.16: Graphical example of the power source localisation technique. This figure shows vectors $P_{\alpha_i}\vec{e_i}$ for the 19 electrodes during eye closure.

noticeably larger compared to those for other regions. Though this method is not useful for clinical source localisation, it is sufficient for the requirements here, where the actual location is unimportant, so long as there exists an appreciable difference between the alpha and non-alpha states.

The y-component only of the location coefficient $\vec{d}$ will be used for alpha EEG detection, as it was found that the x component does not offer any contribution to the determination between alpha and non-alpha periods. The results when Equation 4.15 is applied to EEG data (in segments of length b=blocksize, as previously used) is shown in Figure 4.17. The periods of high alpha activity are evident in Figure 4.17(a) by the negative d_y values. Other baseline activity or artifact signal (Figure 4.17(b)) primarily results in positive d_y values. Two notable EOG artifacts are visible in Figure 4.17(a) as two positive spikes at the beginning and end of the eye closure period (t=30 sand 1,=60 s) when the subject closes, then opens both eyes.

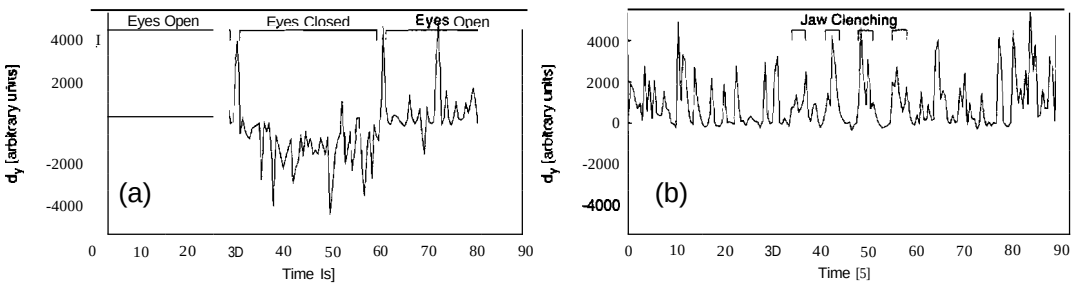

Figure 4.17: The y component of the location coefficient (d_y) obtained when Equation 4.15 is applied to example EEG data sets containing (a) eye closure and (b) jaw clenching trials. For this example data was processed with a blocksize of $b = 256$ samples.

The data from eye closure trials shows that no information regarding alpha increase is present in the positive d_y values, and thus they may effectively be discarded. The algorithm for the power source localisation technique is

- Apply Equation 4.15 to EEG data in segments of blocksize b
- Use only the y component of the location coefficient (d_y)
- Set all values $d_y = \begin{cases} d_Y & d_y \geq 0 \\ 0 & d_y < 0 \end{cases}$
- Negate d_y values such that alpha EEG activity now gives positive values.
- Determine threshold setting as in Section 2.3.3
- Compute detection times and error rates as previously described m Section 2.3.4

The removal of positive d_y values gives a lower standard deviation of the baseline when threshold settings are calculated: this leads to lower thresholds

and thus lower detection times (and conversely the possibility of more errors).

4.6.1 Results using the power source location method

The alpha EEG detection algorithm using power source localisation was applied to all sets of EEG data and detection times and errors rates computed. Five different blocksizes were used for comparison. The results are shown in Figure 4.18. The results show noticeably low detection times for smaller

Figure 4.18: Results after applying the power source localisation alpha EEG detection method to all sets of EEG data. Five blocksize settings b were tested (no results were obtained for $b = 1024$ or $b = 2048$).

blocksizes; larger blocksizes ($b = 1024$ and $b = 2048$) did not return results for any threshold settings. The lowest $\overline{\chi}$ value was found using a blocksize of $b = 512$ samples (=1 s) and a threshold setting of $n = 9$ standard deviations.

4.6.2 A simplification of the power source localisation method

In essence the power source localisation method monitors whether the majority of alpha EEG activity is apparently occurring at the front or rear of

the head. This may be achievable using only two electrode positions (one at the front, and one at the rear of the head) rather than using all 19 electrodes. To test the effectiveness of this modification, the power source localisation algorithm was applied to all EEG data again, but using only electrode positions E2 and E10 (refer to Figure *C.1).* The results using the simplified algorithm are shown in Figure 4.19 The plots show that good results are

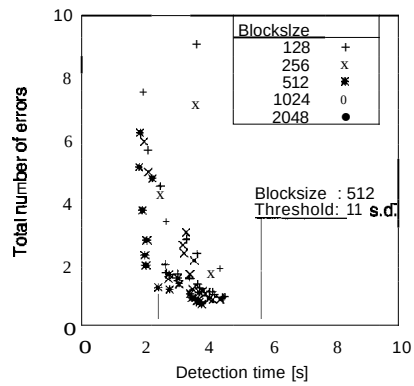

Figure 4.19: Results after applying the simplified power source localisation alpha EEG detection method to all sets of EEG data. Five blocksize settings b were tested (no results were obtained for $b = 1024$ or $b = 2048$).

still achieved with the simplified method, though localisation using all 19 electrodes (Figure 4.18) gives lower $\overline{\chi}$ values in general. The lowest $\overline{\chi}$ value using the simplified method was found using a blocksize of $b = 512$ samples ($=1$ s) and a threshold setting of $n = 11$.

4.7 A comparison of results and discussion

The performance of the location-based alpha EEG detection techniques discussed in this chapter were compared against the integration technique following the ranking method outlined in Section 2.6. The rankings are shown

Alpha Detection Method	mean $\ln(\bar{\chi})$ value and std error	p value	rank
Source power localisation	0.930 ± 0.080	<0.001	1
Source power localisation (simple)	0.945 ± 0.176	0.006	2
Bartlett beamformer localisation	1.187 ± 0.141	0.165	3
Four sphere head model localisation normalised)	1.360 ± 0.146	0.787	4
Integration	1.392 ± 0.093	-	5
Four sphere head model localisation (not noise normalised)	1.540 ± 0.162	0.256	6
MUSIC algorithm localisation	1.985 ± 0.162	*0.001*	7

Table 4.2: Ranking of results from alpha detection techniques introduced in Chapter 4. Techniques are ranked using the p value from a paired two-tailed t-test, compared with the integration alpha EEG detection method.

in Table 4.2. The highest ranking alpha EEG detection technique was the source power localisation method (Searle & Kirkup (2001)), which showed statistically significantly lower $\overline{\chi}$ values compared to the integration method. The simplified source power localisation method (using only two electrodes) also showed significantly lower $\overline{\chi}$ values, though its performance was not as good as when all 19 electrodes are used for localisation. The Bartlett beamformer localisation technique also ranked well despite concerns about its low spatial resolution. The more complicated localisation techniques fared poorly in the rankings shown in Table 4.2. Localisation using the four sphere head model did not show a significant improvement over the integration method (though the use of noise-normalisation ranked more highly than when the algorithm is used without noise-normalisation). The lowest ranking method shown in Table 4.2 is the MUSIC algorithm. Despite the advantages of improved spatial resolution and better performance in situations of low SNR, the MUSIC algorithm's inability to deal with coherent signals caused significantly higher $\overline{\chi}$ values compared to the integration method. This problem with coherent signals also explains why the Capon beamformer showed poor localisation ability when compared to the simpler Bartlett beamformer. Work on localisation techniques for alpha EEG detection developed in this chapter have been reported in the literature (Searle & Kirkup (2001)).

4.8 Discussion of alpha EEG detection techniques

This chapter concludes the extent of investigation into methods for the detection of alpha activity increase in EEG associated with eye closure. Three approaches to alpha EEG detection have been investigated,

1. The techniques in Chapter 2 used EEG information from a pair of electrodes, and determine an increase in alpha activity using amplitude-based techniques. The methods which gave the lowest $\overline{\chi}$ values were the integration technique (when used with artifact rejection) and the peak counting technique (used with the distribution of amplitudes during eyes open).

2. The methods described in Chapter 3 were used as preprocessing algorithms for the alpha detection techniques in Chapter 2. These preprocessing techniques used information from 19 electrodes in order to enhance the alpha EEG signals. The enhanced alpha EEG signal could then be used with the detection techniques from Chapter 2. The techniques which resulted in the lowest $\overline{\chi}$ values were the Independent Component Analysis (ICA) algorithm, and the Capon spatial filter (designed using simulated BEG data).

3. Chapter 4 used the location of highest alpha EEG activity in the head to detect the onset of alpha increase associated with eye closure. This contrasts with the methods used in Chapters 2 and 3, which used amplitude of EEG signals to detect the alpha activity increase. The most successful location-based methods were the source power localisation technique, and the Bartlett localisation technique.

The detection times and error counts for the most successful methods investigated are shown in Figure 4.20, the result for the integration method is shown for comparison. Only the result corresponding to the threshold with the lowest $\overline{\chi}$ value for each technique is presented. Additionally, the ranking of these techniques compared to the integration method is shown in Table 4.3. As described in Section 2.6, the rankings are based on the p value from a paired

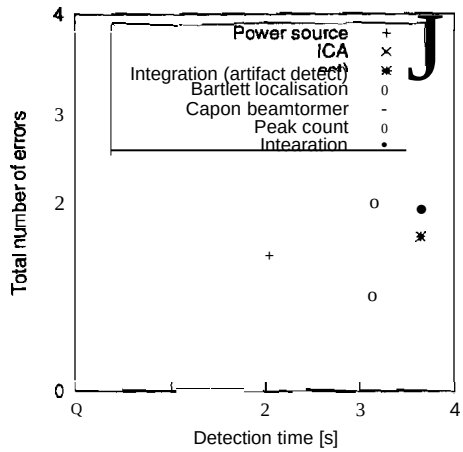

Figure 4.20: Results for the best alpha EEG detection techniques discussed in Chapters 2 - 4. Only the data corresponding to the threshold which gave the lowest $\overline{\chi}$ value for each technique is displayed. The result for the integration method is shown for comparison.

t-test, compared to the integration method. The data in Figure 4.20 and Table 4.3 clearly shows that the power source localisation method gives the best performance. This technique is also computationally very simple (and still operates successfully with reduced numbers of electrodes, as demonstrated in Section 4.6.2). The technique which ranks second in Table 4.3 is the lCA algorithm which, in contrast with the mathematical simplicity of the power source localisation method, is computationally intensive. An indication of the relative computational expense of the best performing alpha detection techniques is shown in Table 4.4. The normalised times shown are an approximate guide, as there are numerous factors and optimisations that could be applied to the processes. Preprocessing times are shown for two methods: the Capon spatial filter (time taken to calculate the filter coefficients) and lCA (time to separate components in EEG data). The time required to visually inspect lCA components (as described in Section 3.6.4) is not

Alpha Detection Method	p value	rank
Source power localisation	<0.001	1
Independent Component Analysis	0.107	2
Integration with artifact rejection	0.139	3
Bartlett beamformer localisation	0.165	4
Capon's Filter (simulated data focus: -0.09 null: +0.09)	0.185	5
Peak Counting: eyes open distribution	0.281	6
Integration		7

Table 4.3: Ranking of the best results, chosen from all alpha detection techniques discussed in this thesis. Techniques are ranked using the p value from a paired two-tailed t-test, compared with the integration alpha EEG detection method.

Alpha Detection Method	Normalised Time	
	Processing	Preprocessing
Source power localisation	1.0	
Peak Counting: eyes open distribution	1.5	
Integration	2.5	
Capon's Filter (simulated data)	2.5	0.1
Integration with artifact rejection	2.9	
Bartlett beamformer localisation	6.5	
Independent Component Analysis	2.7	19

Table 4.4: Processing time for the alpha EEG detection methods listed in Table 4.3. Times are normalised to the source power localisation method.

included, but is substantial. The coefficients for the Capon filter need only be calculated once, but the components from ICA need to be recomputed for every subject, and each time a subject has electrodes re-applied. The good performance of the ICA alpha EEG detection method is negated by the high computational expense, and the need for human intervention in the process.

The inclusion of artifact rejection to the integration method showed a consistent improvement, as indicated in Table 4.3. Data in Figure 4.20 reveals that the improvement, though consistent, is not substantial. Note that the artifact rejection extension (Section 2.3.7) to the integration alpha detection technique could also be used with any of the other detection techniques used in Chapter 2. This also applies to the preprocessing methods introduced in Chapter 3 (including ICA and the Capon beamformer, shown in Figure 4.20), they could be performed as a front end to any of the Chapter 2 alpha EEG detection techniques. The use of alpha detection techniques, other than the integration method, after the preprocessing algorithms may result in further improvements with regard to reducing detection time and error counts. It is unlikely that any improvements will match the consistently low $\overline{\chi}$ values obtained when using the power source alpha EEG detection method. The very high statistical significance of the improvement in performance shown for this method compared to the benchmark integration technique (even though the subject sample size is not large) means that the use of extra electrodes for the algorithm is justified.

If any of the alpha detection methods are to be used in an environmental control system, it is a requirement that the processing can be feasibly done in real time (either digitally, or with an analogue system). Of the methods shown in Figure 4.20 and Table 4.3, those which could easily be implemented *in* real time systems are the integration method (already used in analogue

form (Kirkup et al. 1998, Kirkup et al. 1997*b)),* the source power method, peak counting method and integration with artifact rejection (also demonstrated **in** analogue form (Kirkup et al. 1997*a)).* More complicated, but still feasible, are Capon spatial filtering and lCA (once the preprocessing task of separating components has been completed). The use of Bartlett beamformer localisation for real time alpha EEG detection would require the most optimisation.

The remainder of this thesis considers the use of electrodes in an unsupervised alpha EEG detection system designed for long-term use. This involves an introduction to electrode types and background theory, as well as common causes of electrode- based artifacts and their dependence on skin/electrode impedance. The performance of 'traditional' electrode types will be compared to less widely used construction techniques.

Chapter 5

Electrodes for biosignal sensing applications

5.1 Introduction

Chapters 2 - 4 described and investigated new methods for the detection of the increase in alpha EEG activity following eye closure. The EEG data for use in these studies were recorded using gold-plated electrodes and saline gel. The use of such (and similar) electrode arrangements is widespread for the monitoring of EEG and many other bioelectric signals. It is recognised that one of the most challenging aspects of acquiring, analysing and interfacing electrical activity of the brain is the performance of the electrodes used to sense the biosignals. It is important to evaluate in a qualitative manner the performance of electrodes used to sense biosignals so that their potential for application to EEG-based control systems can be considered. The processing of any signals is much simplified if the signals as tranduced electrodes are of low noise, reliable and have long-term stability. 'While wet (*Agj*Agel) electrodes have a dominant position in biosignal sensing, the assessment of

other electrodes should be considered for specialist applications such as the long-term monitoring of alpha activity. For an alpha detection system intended for long-term, unsupervised usage, the necessity for an electrolyte gel will become a hindrance. The unaided application of electrodes which require gels (especially to the head) is difficult, messy and time consuming, and long-term performance degrades as the electrolyte dries. As a consequence, research into alternative electrode methods is warranted.

This chapter introduces the major types of electrodes, as well as their respective advantages and disadvantages. The source of electrode-based artifacts associated with the different construction techniques will be discussed. Chapter 6 will investigate the combination of the skin/electrode impedance, and its influence on signal quality. Chapter 7 will detail a study on the comparison of three types of electrode and the relative effects of artifact on each. Some of this work on contact impedance and electrode performance has been reported in the literature (Searle & Kirkup 1999, Searle & Kirkup 2000).

5.1.1 Historical background

The use of electrodes for detecting electrical signals from the body are now commonplace, both **in** research and clinical environments. Some of the earliest electrophysiological transducers were immersion electrodes. As an example, buckets of saline solution into which the subject would place their extremities[1] were not uncommon. The use of plate electrodes (metal plate and cotton soaked in saline) and suction electrodes (metals cups which used suction to adhere to the body and make better contact) soon followed. A. D. Waller

[1] This method is still used occasionally, as by Yamamoto & Yamamoto (1977) where a conventional electrode was used on the arm, while the ankle was placed in a saline filled container.

advanced the science of biopotential recording by measuring the electrical activity of the heart in 1872. This was achieved by attaching electrodes (constructed from zinc covered in chamois leather and moistened with brine) to the front and back of the chest. Willem Einthoven furthered developed

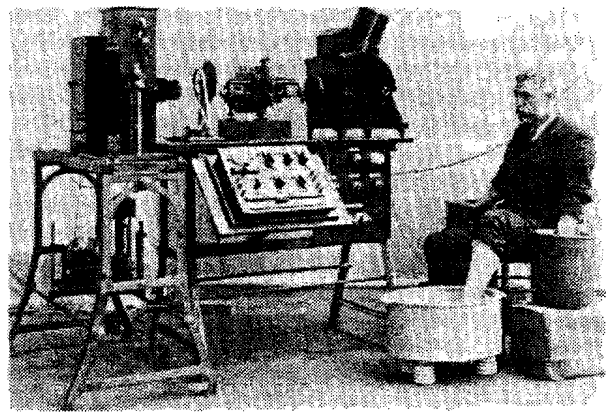

Figure 5.1: Einthoven's electrocardiograph with immersion electrodes (taken from Aston (1990)).

the instrumentation with his string galvanometer variation (see Figure 5.1), and after much work in the area he received the Nobel Prize for Medicine in 1924. Electrodes for use in recording bioelectric events can be classed into the following broad categories:

Wet A gel or other liquid electrolyte is used in conjunction with a metal electrode to enable ionic conduction. The most commonly used electrolyte is dilute saline gel.

Dry An electrode technique, almost always using bare metal, which does not require an artificial electrolyte, but depends on perspiration or other body secretions for ionic pathways.

Insulating These electrodes do not have a direct current path, but use

capacitive coupling to detect bioelectric activity.

There are also electrodes which do not directly fit into any of these categories but have advantages of their own, these are outlined in Section 5.5. The most commonly used bioelectric electrode is the wet type. Most work in the area of alternative electrode types (i.e. those which are not of the wet type) has involved EMG or ECG, few reports are found which utilise alternative electrodes for EEG use (with the exception of Taheri et al. (1994), Taheri et al. (1995) and Gevins et al. (1990)).

In biomedical literature it is commonplace to describe both dry and insulating electrodes as "dry". Engineering literature makes the distinction between the two more clearly, and this distinction will be adopted in this thesis. The following sections cover the characteristics for each of the three electrode types, as well as the electrochemistry involved.

5.2 Wet electrodes

A factor to be considered when measuring biopotentials (be it ECG, EMG, EEG or other) is that current in the body (which for the moment can be considered simply as a bulk electrolytic solution) is carried by ions, whilst in the electronic equipment current is carried by electrons. The sensing electrode needs to provide a mechanism where the ionic conduction can be transduced into useful electron currents. This occurs at the electrode/electrolyte interface.

5.2.1 The electrode/electrolyte interface

\Vhen a metal and an electrolyte are brought together, a charge distribution is created as metal ions go into solution, and ions in the electrolyte combine

at the metal surface. Since no free electrons exist in the electrolyte, nor free cations in the metal, the reaction depicted in Figure 5.2(a) takes place, where C^{n+} are the cations and A^{m-} represent anions. In the region near

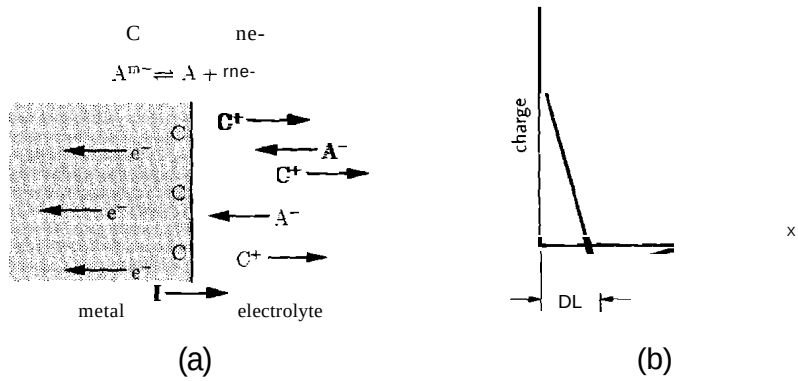

Figure 5.2: (a) Reactions at an electrode/electrolyte interface and (b) Stern's model for charge distribution at the interface, where DL is the 'Double Layer Region'

the electrode, charge neutrality is not maintained, thus the bulk of the electrolyte is at a different potential to the solution near the metal. A number of models exist for the charge distribution at this interface, for example, that of Helmholtz, Gouy, Stern and others (Geddes & Baker 1989); Stern's model is shown in Figure 5.2(b). The region of activity close to the electrode is called the 'Electrolyte Double Layer Region'. According to standard electrochemistry, the potential developed across this region is the 'half cell potential' (measured relative to a Pt(Hz)H+ electrode). Some typical figures for half cell potentials are shown in Table 5.1. The standard half cell potentials only apply when there is no current flowing through the cell; in practice however this is rarely the case and when current does flow the observed potential is different. This observed and theoretical difference is referred to as the *over-potential.*

Metal and Reaction	Potential at 25°C [V]
$Al = Al^{3+} + 3e^-$	-1.662
$Pt(Hz)H^+$	0.000
$Ag + CI^- = AgCI + e^-$	+0.2225
$Cu = Cu^+ + e^-$	+0.521
$Ag = Ag^+ + e^-$	+7.991

Table 5.1: Electrode half cell potentials

5.2.1.1 Overpotentials and electrode polarisation

The overpotential has three main components:

Ohmic Overpotential This is due to the potential difference created by the current flow through the resistance of the electrolyte. Depending on the ionic concentration this does not necessarily follow Ohm's law.

Concentration Overpotential Because the half cell potential results from the charge distribution at the electrode/electrolyte interface when the reactions shown in Figure 5.2(a) are in equilibrium, any current flow will disturb this equilibrium and affect the potential developed.

Activation Overpotential The oxidation/reduction reactions involved are not entirely reversible. For metal ions to go into solution, the atoms need to overcome an activation energy, and vice versa for the reduction of cations in the electrolyte. The oxidation and reduction activation energies are not necessarily the same. Thus, depending on the direction of current flow, oxidation or reduction will dominate and the difference in energy will appear as the Activation Overpotential.

When overpotentials are present the electrode is popularly said to be *polarised.* Because polarisation has a dependence on current density, the prob-

lem can be reduced by increasing the electrode area. The effective surface area of an electrode may also be increased by sandblasting, possibly followed by platinizing (were the metal surface is plated with colloidal platinum black, which is characteristically grainy). This procedure can increase the effective surface area by up to 10^4 (Ferris 1974). Electrode polarisation is not a problem when monitoring signals with frequencies which are higher than 1 kHz, but can present difficulties at frequencies less than 20 Hz, which is a region where many bioelectric signals are found. In biomedical fields, electrodes are often classed into the following theoretical performance categories

Perfectly Polarisable No charge passes across the electrode/electrolyte interface when current is applied. The flow is only by displacement current, thus the electrode behaves capacitively.

Perfectly Nonpolarisable In this opposing case, current is able to flow freely and no energy is required to make the transition. (Thus there are no overpotentials).

Although neither of these electrodes can be made in practice, some materials come reasonably close. Inert metals display close to perfect polarisable properties, since they are difficult to oxidise and dissolve. By far the most commonly used bioelectric electrode is the silver/silver chloride *(Agj* AgCl) type, which displays many qualities of perfectly nonpolarisable electrodes. The properties of Ag/AgCl electrodes will be discussed in the following section.

5.2.2 Silver/silver chloride

SilverjSilver Chloride electrodes are constructed from silver (or a coating of such) plated electrochemically with silver chloride. The availability of silver

loaded graphic inks has also made possible the production of screen printed sensors (Zhou et al. 1994). Two reactions occur in the electrode system:

$$Ag \rightleftarrows Ag^+ + e^- \tag{5.1}$$

$$Ag^+ + Cl^- \rightleftarrows AgCl \tag{5.2}$$

The reaction shown in Equation 5.2 occurs soon after the formation of the Ag^+ ions in Equation 5.1. The solubility of AgCl in water is low, so most of the compound precipitates onto the electrode, contributing to the silver chloride deposit. The concentration of Cl^- in biological fluid is high, but even so an intermediate electrolyte is used containing the anion, usually saline gel (NaCl), or sometimes KCl solution. The use of Ag/AgCl electrodes externally has been reported to have no toxic effects (Jackson & Duling 1983) but skin reactions may result from chronic use and skin preparation rituals (Godin et al. 1990, David & Portnoy 1972, Bergey et al. 1971).

5.2.3 Wet electrode impedance

Because the electrode/electrolyte region contains two layers of opposing charge, this theoretically indicates some capacitive behaviour. Due to the molecular dimensions between the layers, the capacitance can be reasonably large per unit area. All electrodes also display resistive effects since no electrode is perfectly polarisable. At first inspection the electrode/electrolyte interface can therefore be modelled as a resistor and capacitor in series (Warburg (1899) was one of the first to propose this). The components in this series equivalent model are frequency dependent such that the resistance and reactance vary

in the following way;

$$R = R_s f^{-\alpha_1} \qquad (5.3)$$
$$C = C_s f^{-\alpha_2}$$

where f is frequency

R_s is a resistive coefficient

C_s is a capacitive coefficient

α_1 and α_2 are constants, and many researchers have found that $\alpha_1 \simeq \alpha_2 \simeq 0.5$ and $R \simeq X$, where

$$X = \frac{1}{2\pi C f} = \frac{1}{2\pi C_s f^{1-\alpha_2}} \qquad (5.4)$$

although effective surface areas will alter these coefficients (Geddes *1973b).* These resistive and reactive elements are often lumped into a "Warburg impedance" (McAdams et al. 1995) denoted as *Zw,*

$$Z_w = (1-j)\sigma f^{-\alpha} \qquad (j = \sqrt{-1}) \qquad (5.5)$$

This expression uses a 'diffusion coefficient', $\sigma = R = X$. This model can be converted in a way that it lends itself to physical analogies of the electrode/electrolyte interface, and which allows the experimentally observed passage of DG current. This involves conversion of the Warburg series model to its parallel equivalent and coupled with an additional resistance, as shown in Figure 5.3. The voltage E_{hc} source represents the half cell potential, C_a and R_a are due to interface effects and polarisation mechanisms, and R_b is caused by interface effects and electrolyte impedance. Component values C_a and R_a are still frequency dependent. It was reported that many materials did not always conform to this rather restrictive model, especially at low frequencies. The reference to capacitors and resistors which are frequency

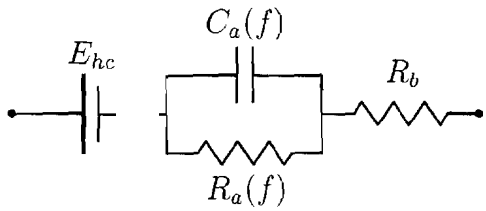

Figure 5.3: Model for electrode/electrolyte interface using frequency dependent components

dependent is also confusing, so a more flexible and abstract model is preferred.

To allow for variations in the phase angle ϕ so that its value is not necessarily 45°, a circuit element called a *Constant Phase Angle Impedance,* or *ZCPA,* is used. At a given frequency, the relation between the complex impedance and the phase angle is

$$\frac{X}{R} - \tan\phi \tag{5.6}$$

$$\phi \quad \beta\frac{\pi}{2} \tag{5.7}$$

Equation 5.7 is also known as Fricke's Law (Geddes & Baker 1989). Using the constant phase angle impedance element, two models of electrode impedance are needed (McAdams & Jossinet *1994a),* one for high frequencies and another variation for low frequencies. At these frequencies the impedance is modelled as (McAdams & Jossinet 1995, McAdams & Jossinet *1994a,* de Boer & Oosterom 1978):

$$\text{high frequencies} \quad Z \quad K(j\omega)^{-\beta} = ZCPA \tag{5.8}$$

$$\text{low frequencies} \quad Z \quad \frac{R_c}{1 + \frac{R_c}{K}(j\omega)^{-\beta}} \tag{5.9}$$

Equation 5.8 is the constant phase angle impedance and, although it implies infinite impedance at DC, it is more commonly used than Equation 5.9. *ZCPA* may also be referred to as a *constant phase element* or *polarisation*

impedance. The term *impedance* is used occasionally but this may create confusion with the commonly used Warburg model where R = X and ϕ = 45°. 'When β = 1 the *ZCPA* element is purely capacitive, when $\beta = -1$ the element is purely inductive, and ,8 = 0 gives a resistive effect (Kontturi et al. 1993). In biological systems the value of β is usually around 0.8 (McAdams et al. 1995). The low frequency representation (Equation 5.9) is equivalent to a *ZCPA* element in parallel with a resistor, R_c, whose value is not frequency dependent. The behaviour of these equations is depicted in Figure 5.4. The distinction between "high" and "low" frequencies is not

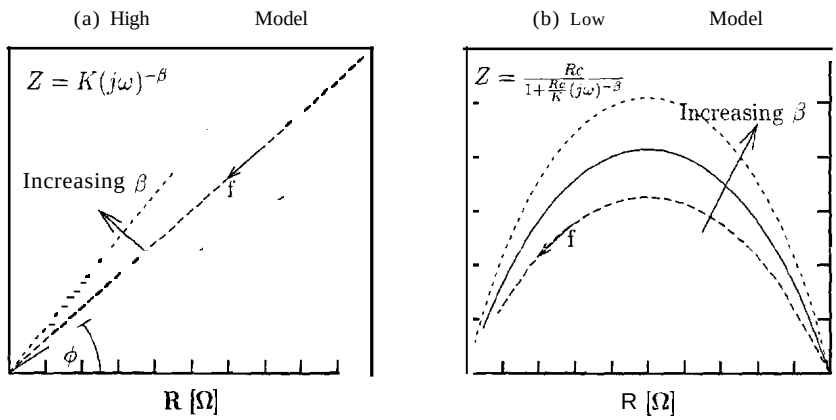

Figure 5.4: Plots for the Electrode/Electrolyte Interface Impedance using the Constant Phase Angle Models. At high frequencies (a) the change of phase angle ϕ on the impedance locus is shown, varying as in Equation 5.7. At low frequencies (b) the impedance locus of Equation 5.9 traces a semicircular path with a depressed centre, approaching Z = 0 as $f \rightarrow$ oo.

rigid, but for a general guideline, figures from Nowotny & Nowotny (1980) and McAdams et al. (1995) indicate 1 Hz as the lower limit. Below 1 Hz the high frequency model no longer applies.

As well as being highly dependent on frequency, the impedance of the

electrode/electrolyte interface is affected by the current density used. At higher current densities (for a given frequency) the resistance decreases and capacitance increases. At low frequencies this effect is more pronounced. The term 'limit current of linearity' was introduced by Schwan (1968). Studies show (Schwan 1968, Onaral & Schwan 1982) that this limit of linearity approaches zero as frequency decreases. This suggests that caution should be exercised when using electrodes of small surface area: as the electrodes area gets smaller and smaller, the system will be permanently in the nonlinear region, regardless of current density. In the high frequency range the 'limit current of linearity', i_L, can be represented (McAdams & Jossinet 1998, Simpson et al. 1980, Onaral & Schwan 1982) as

$$i_L \propto f^{\beta} \tag{5.10}$$

where β is the same coefficient used in Equations 5.6 and 5.7.

Some researchers have instead defined a *voltage* limit of linearity. de Boer & Oosterom (1978) represent this voltage limit in the constant phase angle model (Equation 5.8) as a pair of opposing zener diodes in parallel with the interface impedance. Sadasivan & Dutt (1994) present a treatment where they show that the voltage limit gradually increases with frequency between two limits, whereas it was previously thought to be independent of frequency.

The motivation for the extensive volume of work that has been done in formulating analogous models for all kinds of electrode behaviour is the convenience of attaching parameters to experimental data. The ability to fit data points to a modelled curve and find these parameters allows researchers to easily compare results with other data, and with that of other published works (if a similar model has been utilised). Thus it is most convenient to have the least possible number of elements/parameters in the model used. Taking this idea of minimal characterisation coefficients even further, some

research has been reported on fractal models for electrodes. One of the fractal concepts is that the roughness of a surface can be characterised by a single parameter, and since the effective surface area has such an enormous impact on the electrode's performance this parameter may be able to singularly describe this activity. So far this type of model is not widely used or accepted (McAdams et al. 1995).

5.2.4 Limitations of wet and Ag/Agel electrodes

The ubiquitous application of wet (especially *Agj*AgCl) electrodes suggests they are reliable and provide good performance. However, wet electrodes have some limitations. Movements of wet electrodes relative to the skin cause voltage artifacts due to the disruption of the charge gradient at the double layer region (termed the electrokinetic effect by Khan & Greatbatch (1974)). This artifact can be minimised by using recessed electrodes (Toole 1977), so that the electrodejelectrolyte interface is protected by a bulk of electrolyte solution and less likely to be affected by extraneous movement.

It could be assumed that two like electrodes in an electrolyte would show no net potential, however in practical situations fluctuations in voltages between electrodes occur. For *Agj*AgCI electrodes this has been found to be between 0.2-5 mV, which is quite large when it is considered that biopotential readings are in the low mV or μV range. This artifact is often at a frequency lower than the standard recording bandwidths (Tassinary et al. 1990). If left to settle to equilibrium over hours these fluctuations decrease, but minute impurities or scratching of the AgCI coating will upset the steady state of the system and produce this artifact once more. It is for this reason that many researchers keep reusable *Agj*AgCI electrodes in saline solution with all leads short circuited when not in use, amongst a host of other complicated storage

arrangements (Tassinary et al. 1990).

Silver/Silver Chloride electrodes are photosensitive (Geddes *1973a),* such that changes in light will produce a potential, and chronic exposure will damage reusable electrodes. An experiment conducted for this thesis using commercially available Ag/AgCI electrodes[2], illustrated in Figure 5.5, shows this phenomenon. To perform this experiment, two Ag/AgCI electrodes were

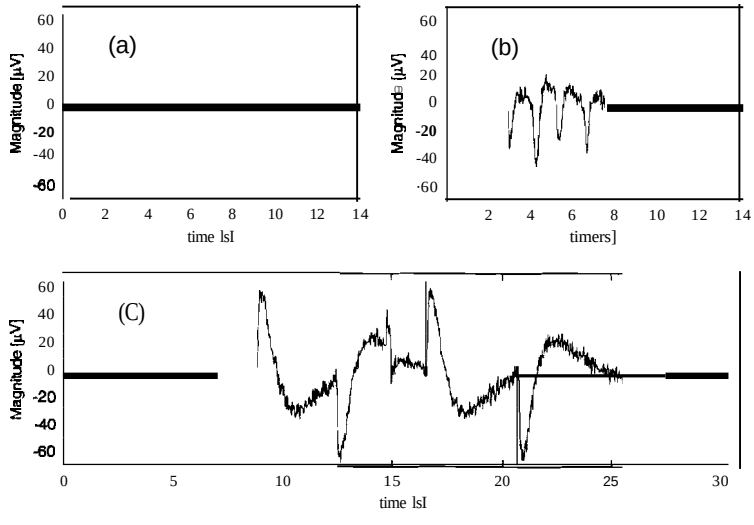

Figure 5.5: Photosensitivity of Silver/Silver Chloride electrodes. (a) Baseline voltage. (b) Waving hand between electrodes and light source. (c) Switching light source on and off.

connected to a biopotential amplifier. Electrodes were positioned facing a light source with a bridge of saline solution between them. It can be seen that changing the illumination by moving a hand over the electrodes, or turning a light source on and off causes a substantial deviation in the electrode voltages. This is especially applicable to EEG studies where the artifact seen in these tests is the same order of magnitude as signals that scalp recordings will

2Red Dot™ 2258 EeG electrodes

produce. although in practical situations the face of an electrode will not face outward, caution is advisable in experiments using highly changeable lighting conditions (e.g. evoked potential studies).

Skin irritation and growth over long recording periods (days), and drying of the electrolyte degrades electrode performance. (Ko & Hynecek 1974, Richardson et a1. 1968, Richardson 1967). Furthermore, if many electrodes are close together, gel can smear and cause conductive bridges between electrodes. Such conductive bridges would effectively 'short-circuit' the bioelectric signals. This is especially a problem in EEG when hair movement can quickly disperse gel and render electrode sites useless: short of washing and drying the hair completely other sites must be used. If hair is damp or wet, or if excessive perspiration is on the skin, this will also degrade the signal quality significantly. This problem is illustrated by difficulties faced by Masuda & Sadoyama (1988). These researchers constructed an
consisting of a grid of 30 x 24 gold plated electrodes 2.54 mm apart to investigate the spatial activity of muscle motor units. Gel was used to lower contact resistance, but to avoid short circuiting contacts a small amount of gel was spread evenly over the recording area. Because of the tiny amount of gel involved it dried almost immediately, and the site had to be washed and the gel reapplied every few minutes.

Some of these disadvantages are addressed by using hydrogel electrodes (Perrault 1998, McAdams et a1. 1994) which are 'solid' gels and have hydrophilic properties. These characteristics mean that contact areas are more exact, there is no shorting due to gel spread and some designs allow repositioning of electrodes.

5.3 Dry electrodes

5.3.1 Usage

Dry electrodes offer an advantage to wet electrodes when the drying of electrolytic gels over long periods or skin irritation is a concern, or if electrolyte use is not practical. Dry electrodes work in same manner as wet electrodes, in that an electrode/electrolyte interface is created. The difference is that the skin supplies the electrolyte in the form of perspiration, rather than relying on an artificial electrolyte. This accumulation of moisture has been verified by a number of sources (McLaughlin et al. 1994, Geddes et al. 1973, Geddes & Valentinuzzi 1973, Bergey et al. 1971). Furthermore, Lewes (1965)3 collected and analysed this perspiration to determine the NaCl content (which was found to be 6 mg under an electrode area of 15 cm^2). The impedance of dry electrodes can be much higher than that for wet electrodes, so a buffer must be used to convert high impedance to low impedance. The necessity of low contact impedance and techniques associated with this problem are discussed in Chapter 6. The most common material for dry electrodes has been stainless steel (Nishimura et al. 1992, Padmadinata et al. 1990, Luca et al. 1979, & Mahler 1964, Geddes & Valentinuzzi 1973). Other materials include silver (Geddes et al. 1973), dry Ag/AgCl (Griss et al. 2000, McLaughlin et al. 1994) and a tin/lead alloy (Gevins et al. 1990). Weinman & Mahler (1964) compared the performance of stainless steel, platinum and tungsten, finding that the impedance of the tungsten electrodes varied depending on the signal amplitude present at the electrodes. This is more of a problem for stimulation or impedance mea-

3Interestingly, this author also compared the performance of traditional EeG jelly to such items as toothpaste, mayonnaise, French mustard and tomato paste.

surement electrodes but the lack of an explanation for this behaviour makes other, more consistent, metals more attractive. Bergey et al. (1971) investigated aluminium, among other metals mentioned, and found that that signals received were too noisy for any useful bioelectric information to be obtained. A comparison of metals for dry electrode use will be presented in Chapter 7.

5.3.2 Dry electrode impedance

As the mechanism of signal conduction is the same as for the wet electrode type, the theory introduced in Section 5.2.3 holds for dry electrodes. However, since the accumulation of perspiration is not instantaneous, the interface impedance decreases steadily from an initially high value. Geddes et al. (1973) found that, when using silver discs for electrooculography, the resistance decreased exponentially with time. Lewes (1965) conducted temporal measurements using dry electrodes and displayed how, in addition to the impedance, the interference in ECG readings decreased steadily over 6 minutes to a level comparable to measurements taken with artificial electrolyte added. Geddes & Valentinuzzi (1973) compared the performance of stainless steel and silver electrodes, concluding that the impedance achieved with silver was nearly half that for steel. In order to reduce the skin/electrode impedance for their dry Ag/AgCI electrodes, Griss et al. (2000) formed the face of electrodes with spikes ($\sim$100 μm long) to pierce the high impedance upper layers of skin.

5.3.3 Limitations of dry electrodes

Dry electrodes suffer from many of the problems that affect wet types (see Section 5.2.4) since the recording mechanism is still dependent upon ionic conduction at the electrode/electrolyte interface. Namely, fluctuations due

to changes in the chemical composition of the electrolyte (principally perspiration) and disruption of the charge gradient in the double layer interface (which cannot be protected by recessed electrodes as in wet types). Dry electrodes do offer the advantage that no gel is needed (thus reducing problems with skin irritation and conductive bridging from gel) but time is needed for satisfactory impedance between skin and electrode to be achieved (Geddes et al. 1973, Lewes 1965). Dry electrodes require extra impedance conversion circuitry because of their naturally higher impedance levels compared to wet types. This topic is discussed in Chapter 6.

5.4 Insulated electrodes

Insulating electrode types depend on capacitive coupling between the metal electrode and the body for signal transmission. The body and electrode substrate are separated by an insulating, or dielectric layer. AC coupling eliminates DC drift that is a problem (due to overpotentials and differing ion activity) **in** wet and dry electrode types.

5.4.1 Usage

Some of the insulating materials used in the past are shown **in** Table 5.2. Authors often state many possible uses for these electrodes, but only the actual application demonstrated in the literature is shown **in** Table 5.2. Until the work of David & Portnoy (1972) all films had been grown by electrochemical or thermal oxidation. To obtain a wider range of dielectrics with less dependence on substrate material, David & Portnoy employed sputtering deposition methods to create their electrodes.

Year	Insulating Material	Author	Use
1967	Anodic Al_2O_3	Richardson	ECG
1968	Anodic Al_2O_3	Richardson et al.	ECG
1969	Anodic Al_2O_3	Lopez & Richardson	ECG
1969	Silica (SiO_2)	Wolfson & Neuman	ECG
1970	Pyre Varnish	Potter & Menke	EMG
1971	Tantalum Oxide (Ta_2O_5)	Lagow et al.	ECG
1972	$BaTiO_3$,TiO_2,Ta_2O_5,SiO_2	David & Portnoy	ECG
1973	Barium Titanate ($BaTiO_3$)	Matsuo et al.	EEG
1974	Silica (SiO_2)	Ko & Hynecek	ECG
1994	Silicon Nitride (Si_3N_4)	Taheri et al.	EEG
1995	Silicon Nitride (Si_3N_4)	Taheri et al.	EEG

Table 5.2: Insulating materials used in bioelectric measurements

Matsuo et al. (1973) found that signal noise when using their barium titanate electrodes was less than that for Ag|AgCl type. Furthermore the noise was shown to be constant over the recording period regardless of electrolyte presence, whereas wet and dry electrode types need some time to settle and for contact impedance to drop. However, these workers found that mechanical stress on the barium titanate electrodes would give large values of noise (order of 10mV) which was later attributed to the piezoelectric properties of the $BaTiO_3$.

Because the capacitive electrode type has no direct current path, some interesting grounding precautions have been required. Lagow et al. (1971) used grounded electromagnetic shields surrounding their electrodes, a pair of which were used for ECG sensing. They found that if both ground shields made suitable ohmic contact with the skin (by the same mechanism as for

dry electrodes) then the bioelectric signal was effectively short circuited. If neither ground shield made contact only powerline interference noise was present in the signals. If the patient is grounded (or if one ground shield made good contact whilst the other was insulated from the patient) then a suitable signal was obtained.

In contrast to most authors, Bergey et al. (1971) asserted that capacitive electrodes have characteristics which make them less suitable than dry types. They compared alumina coated electrodes with dry electrodes, in situations involving dry and perspiring skin. They observed that the alumina electrodes had a fall in skin/electrode impedance at lower frequencies (more than the dry electrodes displayed). A reason for this was not suggested, and whether this is due to corrosive problems caused by chloride ions is not clear.

5.4.2 Insulated electrode impedance

Experiments have shown (David & Portnoy 1972, Taheri et al. 1994, Bergey et al. 1971) that, as would be expected for a capacitive element, the electrode impedance for an insulating electrode decreases as frequency increases. Taheri et al. (1994) proposed that, for the use of insulating electrodes, it is important to maintain electrode contact impedance dominant over the skin impedance, as the skin impedance is not constant (unlike the electrode contact impedance). As the electrode impedance becomes lower at high frequencies, variations in the bioelectric signal sensed will result if the variable skin impedance, rather than that of the electrode contact impedance, becomes dominant, as the two impedances are in series. No studies have been performed which investigate the relationship between capacitive electrode impedance and signal variability.

5.4.3 Limitations of insulated electrodes

In his early work, Richardson (1967) reported that motion induced artifacts were a problem with insulating electrodes. This may be partly explained by the dependence of capacitance value on the distance between the skin and metal. If the electrode is considered as one side of a plate capacitor, and the skin is the other plate, the capacitance, C, of the combination will vary with the distance, d, between the skin and electrode, as governed by:

$$C \quad \frac{\epsilon A}{d} \tag{5.11}$$

where C capacitance [F]

A area of capacitor [m^2]

ϵ permittivity [Fm^{-1}]

d distance between layers [m]

Any movement will change the d value and thus substantially change the capacitance. The problem of variation in coupling distance was reiterated in further work by Richardson et al. (1968), and later by Griffith et al. (1979). Lagowet al. (1971) noted that, despite promising initial results, further testing of their anodic alumina electrodes (Richardson 1967, Richardson et al. 1968) revealed that they became noisy and unreliable over time. This was caused by the structure and chemical characteristics of Al_2O_3. Alumina (especially when electrochemically deposited) is porous and will absorb perspiration from the skin. The chloride ions in the solution attack the dielectric causing it to break down and reduce electrical resistivity. The group opted to use tantalum oxide (Taz05) which they reported to form a denser film. This film is easier to manufacture and is resistant to chloride activity. This problem with alumina films was also described by Potter & Menke (1970) and Ferris (1974), and may explain unsatisfactory results by Bergey et al.

(1971) when using dry aluminium electrodes, as mentioned on p. 173.

5.5 Miscellaneous electrode structures

5.5.1 NASICON ceramIC

NASICON (Na Super Ionic Conductor) is the name of a proprietary ceramic material which is a good conductor of Na+ ions at room temp (conductivity = 0.1 Sm^{-1}) (Gondran et al. 1992). This material (chemical formula Na3Zr2Si2P012) is described as mechanically resistant, machinable, and able to be deposited in thin films. In a bioelectric environment the NASICON conducts Na+ ions from the skin. However, as with all electrodes involving ionic conduction (wet and dry types) there must be a transduction from ionic to electron currents. As shown in Figure 5.6 this is done using saline gel and

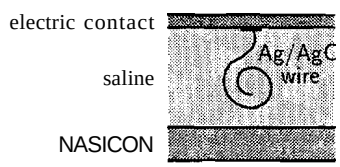

Figure 5.6: NASICON electrode construction

Ag/AgCI in the same way as for wet electrodes, described in Section 5.2.2. The advantage with NASICON electrodes is that the saline solution is not in contact with the skin so it does not need to be applied, cleaned or replaced. The sodium ions in the skin are conducted through the ceramic and saline solution to react with the silver/silver chloride wire. This construction is encapsulated in a non-reactive housing with only the electrical contact and the NASICON accessible externally. This electrode offers the advantages of the (nearly) non-polarisable Ag/Agel wet electrode without the need for gels,

but the increased complexity in construction (and therefore size) may disadvantage it in comparison to dry and insulated electrodes, which are mechanically simple. The NASICON electrode is reported (Gondran et al. 1995) to be temporally stable, with no significant electrode impedance increase over a month. Excess noise was found in the low frequency region «100 Hz) which could not be attributed to thermal noise or polarisation overpotentials, but is thought to be of chemical origin (Yacoub et al. 1995, Gondran et al. 1996). This noise can add signals of 5-60 $\mu V_{pp,}$ which may limit use in EEG applications.

5.5.2 Balsa

Richardson et al. (1968) used balsa wood impregnated with Lithium Chloride (LiCl) as an alternative to previously discussed types. The electrodes were specially designed for long-term ECG recording in space-flight simulations. The lithium chloride was impregnated using a vacuum method which left the balsa feeling "soapy" but not wet. Although the wearer took off the special belt holding the three electrodes when bathing during chronic recording trials, the actual electrodes were not modified physically or chemically during the 32 day trial. No skin reaction effects were reported at the end of this trial, nor during_a subsequent 21 day trial. This electrode type suffered from the problem of motion induced artifact, similar to those indicative of insulated and some dry electrode types.

5.6 Conclusion

In this chapter the basic types of bioelectric recording electrodes have been introduced, along with the mechanisms by which they operate. Depending

on their nature, electrodes may be classed as polarisable or nonpolarisable. In practice, electrodes do not exclusively exhibit the characteristics of a single class. Three types of electrode construction were wet, dry and insulating. An overview of characteristics for the three electrode types is

	Advantages	Disadvantages
Wet Type (Assume AgjAgCl)	Close to non-polarisable Reduced motion artifact Common, available 'off the shelf'	Electrolyte required Gel smearing Requires time for impedance to drop
Dry Type	No electrolyte required Easy construction Easy application	Highly polarisable Requires long time for impedance to drop Movement artifacts
Insulating Type	No electrolyte required Easy application No impedance settling time No skin preparation Reusable	High input impedance Static interference Movement artifacts Requires local power supply for buffers

Table 5.3: Comparison of Electrode Types

contained in Table 5.3. For electrode experiments conducted for this thesis (to be described in Chapters 6 and 7), the AgjAgCI electrodes used were commercially available. By contrast, the dry and insulating electrodes were designed and constructed by the author specifically for this thesis.

The behaviour of electrodes is of interest to researchers involved in electrophysiology, and a common parameter to study is that of electrode impedance. The characteristics of this impedance were introduced in Sections 5.2.3, 5.3.2

and 5.4.2. Many models have been utilised in the past to explain such behaviour during changes in frequency, current density and electrode surface area. There is no 'universal' model which can be applied in all situations. Chapter 6 considers the impedance of skin (which can be modeled electrically in similar ways to the electrode impedance) and the influence that the combined skin/electrode impedance has on the sensing of bioelectric signals. Methods for monitoring the skin/electrode impedance are introduced, and a new measurement method described.

Chapter 6

Skin/electrode impedance: characteristics and a new measurement method

6.1 Introduction

Signals derived from electrodes used for bioelectric monitoring applications must be of acceptable quality, regardless of the respective ease of use of the electrodes. A primary influence on signal quality is the amount of external interference present in the signal, and in turn this is significantly affected by the skin/electrode skin impedance. This chapter considers the impedance contribution from the skin, and the effect that contact impedance (a combination of skin and electrode impedance) has on signal fidelity. Measurements are required to quantify the effect of contact impedance on bioelectric signals. Existing methods for impedance measurement are introduced, and a new method for skin/electrode impedance monitoring is described. This novel method of impedance spectroscopy is used to demonstrate the

influence of electrode contact impedance on bioelectric signal fidelity. Elements of work in this chapter have been described in the literature (Searle & Kirkup 1999, Searle & Kirkup 2000).

6.2 The electrical properties of skin

The impedance characteristics of electrodes were introduced in Chapter 5, involving wet electrode impedance (Section 5.2.3), dry electrode impedance (Section 5.3.2) and insulated electrode impedance (Section 5.4.2). Another important factor that requires consideration when using bioelectric recording electrodes is the impedance characteristics of the skin. Researchers have suggested electrical models to explain the properties of skin and its changes with time, temperature, test frequency and psychophysiological state. The basic structure of skin is shown in Figure 6.1(a). The stratum corneum is a

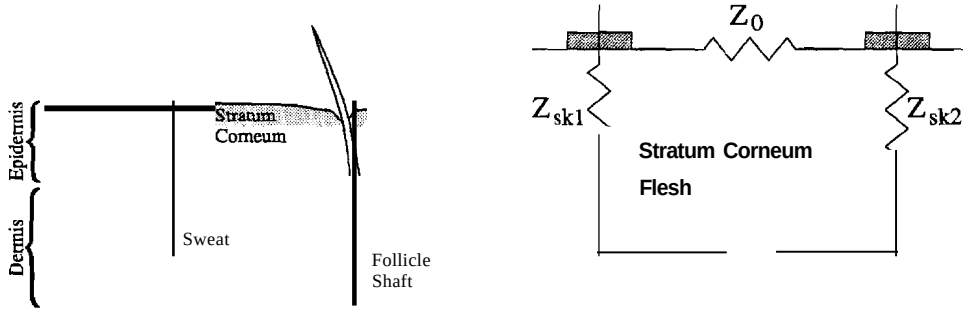

Figure 6.1: **(a)** Skin Structure and **(b)** Major impedance areas in skin measurements as seen by two surface electrodes.

collective term for the upper layers of skin, and these layers exist in varying stages of hydration. The outermost layer is mainly dead, dry skin and as

a result has very high impedance. Many practitioners scrape through this barrier with light sandpaper or a blunt needle to expose more hydrous layers below, and thus reduce skin/electrode impedance. describing the measurement of skin impedance, the basic framework shown in Figure 6.1(b) can be considered (Khalafalla et al. 1971). As long as the electrodes are not close together the surface impedance Z_o (which is very high due to dry upper layers of skin) can be neglected. This is also true for the impedance of the deep flesh, Z_j, because the impedance here is very low. The major components of impedance are contained in the stratum corneum, denoted by Z_{sk1} and $Z_{sk2'}$ The resulting skin impedance measured using two electrodes will be $Z_{sk1} + Z_{sk2}$, though this is rarely mentioned, and in most cases is it sufficient to lump the sum of these two impedances into one value.

If the real and imaginary components of skin impedance are measured and plotted on an argand plane with varying frequency, the result is similar to that shown in Figure 6.2. The plot is an arc with its centre below the axis, subtending an angle ϕ with the real axis. This plot is often referred to

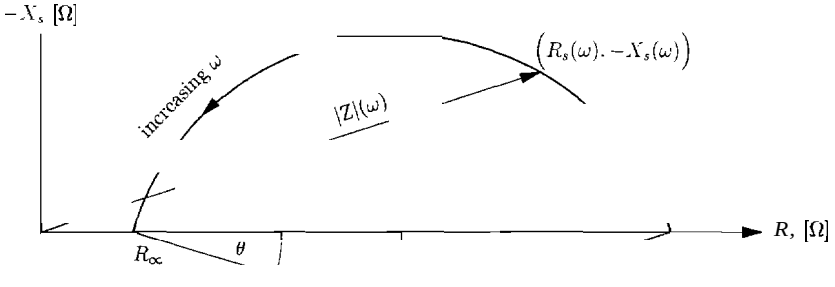

Figure 6.2: Impedance locus for skin

as a 'Cole-Cole plot'l, stemming from the much cited paper by Cole & Cole (1941), though the description is often attached to many other representations of data which are not strictly of this type (McAdams & Jossinet 1995).

lCole acknowledged that the idea came from the work of Carter (1925).

In this thesis, plots of this type will be referred to as an impedance locus. The negation of the imaginary axis is a common convention used to place the information in the first quadrant of the plot.

One of the earliest electrical analogue models proposed to explain the behaviour shown in Figure 6.2, and one which is still used extensively, is the 'three-component model' by Lapicque in 1907 (McAdams & Jossinet 1995), shown in Figure 6.3. Referring back to the argand diagram, it can be equated

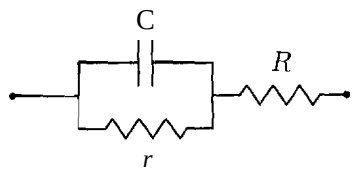

Figure 6.3: Simple 'three component' skin electrical model

that $r = R_0 - R_\infty$ and $R = R_\infty$. It is apparent that this model does not account for the depressed centre of the locus seen experimentally, and shown in Figure 6.2. From 1932 to 1940 K. S. Cole developed the idea of using frequency dependent components in the skin impedance models to better approximate physical impedance observations. He used a constant phase element (discussed on p. 163 in reference to electrode impedance) in parallel with a frequency independent resistor to achieve a locus plot which displayed the depressed arc centre. This model is shown in Figure 6.4(a). The impedance of the constant phase element is given by

$$Z_{CPA} \qquad K(j\omega)^{-\alpha} \tag{6.1}$$

$$\alpha \frac{\pi}{2} \tag{6.2}$$

where the angle ϕ is shown on the impedance locus for a constant phase element in Figure 6.4(b). In this chapter the exponent α is used in the Z_{CPA}, to distinguish it from the exponent β used in the electrode impedance models in Chapter 5 (e.g. Equation 5.8).

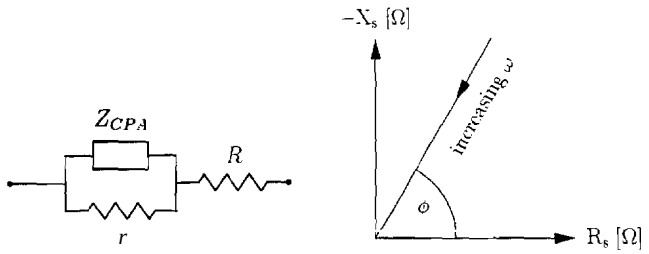

Figure 6.4: (a) Skin impedance model using constant phase element and (b) Impedance locus for a constant phase element only

A general form for an equation to describe the impedance locus for skin was first used by Cole in and later by Cole & Cole (1941) in this more complete form,

$$Z \quad R_\infty + \sum_i \frac{R_0 - R_\infty}{1 + (j\omega\tau_i)^\alpha} \tag{6.3}$$

$$\phi = \alpha\frac{\pi}{2} \qquad 0 \leq \alpha \leq 1$$

The angle ϕ subtends the arc in the argand diagram, and τ_i is termed the 'relaxation time'. Most often Equation 6.3 is used with $i = 1$. Confusion can arise when using Equation 6.3 as some reports use the exponent '$1 - a$' (e.g. Cole & Cole (1941)) and others use 'α' (as in McAdams et al. (1995) and is used here). The exponent used depends on the reference angle used, ϕ or θ, in Figure It can be shown (see Appendix D.7) that the model using resistance in parallel with a constant phase element, as in Figure 6.4(a), gives the same impedance locus as the empirical model in Equation 6.3.

Although it is not possible to achieve a depressed arc with conventional frequency independent components, Rajewsky attempted in 1938 (Khalafalla et al. 1971) to formulate an electrical analogue by constructing a model which

2For additional confusion, the exponent is also referred to in literature as α, m or /3. (m is usually associated with the angle e).

mirrored the physical construction of skin. The model included parameters for extra-cellular fluid, the skin membrane, and cell membranes. In a similar fashion Montagu & Coles (1966) based their model on the activation of sweat glands, mainly to account for the mechanism of Galvanic Skin Response (GSR), which can serve as a physiological indicator of arousal. The model is similar to the three component skin model, except that a number of extra resistive elements may be added in parallel to the capacitor to simulate the hydration of skin. However, despite its many parameters it could not describe the arc accurately with a finite number of frequency independent components.

In his paper of 1957, Schwan (Khalafalla et al. 1971) formulated a mathematical model which included an infinite number of $R \parallel C$ elements in series, with the relaxation times (T) for each element assigned according to a distribution. This treatment explained the behaviour observed **in** skin impedance (in fact, Equation 6.3 is a special case of this model). This 'distributed relaxation time' or 'transmission line' model is not favoured by many researchers (Khalafalla et al. 1971) as the distribution does not allow a direct correspondence between parameters in the model and physiological indicators, even though results correlating such parameters and physical processes (Yamamoto & Yamamoto 1978, Qiao & Morkrid 1995) are variable. Fortunately, for those researchers less interested in detailed mathematics, a simple $ZCPA$ is mathematically equivalent to using a distribution ofrelaxation times (Kontturi et al. 1993) since the constant phase element can be described as an infinitely long network of resistors and capacitors. This concept is also discussed by Kontturi & Murtomaki (1994), who consider the inclusion of an inductive element in the transmission line unit, as well as the usual resistor and capacitor.

Burton et al. (1974) used an analytical technique to obtain a skin imped-

ance model in contrast to much of the work already mentioned, made no assumptions about the biological system under investigation. The tissue was treated as a 'black box', and investigated using the technique of Bode Analysis, which is a popular and important tool in electrical circuit theory. The procedure allows the formulation of an equivalent circuit based only on the frequency response of the system under test[3]. The circuit obtained using this procedure was the same as the popular three component model (Figure 6.3). This requires an explanation, as the three component model cannot produce an arc with a depressed centre due to its frequency independent components. This is explained by an important restriction inherent in Bode analysis, in that the analysis is only valid for non-distributed elements. This omits transmission line and constant phase elements, and thus it is not possible for the Bode analysis to produce an electrical model of skin impedance which gives a locus with a depressed centre. Although this restriction prevents the Bode method giving the 'universal' model (Equation 6.3), it is interesting to those who prefer a more analytical approach rather than the more popular physiological simulation method.

Other forms of the frequency dependent model have been created since Cole's early work. For example, the circuit model in Figure 6.5(a) used by Yamamoto & Yamamoto (1978), refined from a more complex form in Yamamoto & Yamamoto (1977). The values for Co and R_o are

$$\text{Co} \qquad \frac{1}{R_2}\tau^{\beta}\sin\frac{\beta\pi}{2} \tag{6.4}$$

$$R_o = R_2 \Big/ \left(\tau^{\beta}\cos\frac{\beta\pi}{2}\right) \tag{6.5}$$

This model can be shown to be equivalent to the simpler model which uses *ZCPA* in parallel with a resistor (see Appendix 0.8). Simpler again, but

[3]In engineering literature this may also be referred to as the Device Under Test (DUT).

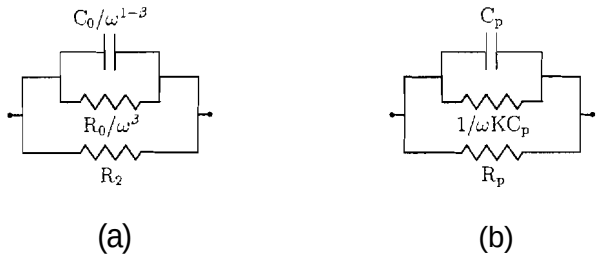

Figure 6.5: (a) Frequency dependent impedance model used by Yamamoto & Yamamoto (1978) (b) model Used by Khalafalla et al. (1971)

still equivalent to the empirical depressed-locus formula, is the model (Figure 6.5(b)) used by Khalafalla et al. (1971).

6.2.1 Nonlinearity

As with electrodes (see p. 165), the skin exhibits nonlinearity effects when current is applied. The volume of research into this effect is much less than that concerned with electrode nonlinearities. This is mostly due to much of the electrode research being undertaken by chemists as part of their studies into the impedance of chemical solutions, but who are not concerned with similar effects in biological tissue. As with electrode nonlinearity, the effect in skin is more pronounced at higher current densities and low frequencies (Yamamoto et al. 1996). Yamamoto & Yamamoto (1981) demonstrated that the skin impedance locus reduces toward the origin as current densities increase. The choice of current density to be used in an experiment remains a tradeoff between linearity considerations and the need to achieve sufficient voltage levels on the skin in order to avoid signal-to-noise ratio problems.

6.3 Impedance and signal fidelity

Standard practice in bioelectric recording dictates that electrode contact impedance (i.e. the combination of skin/electrode impedance) should be as low as possible (Iguchi et al. 1994). The major reason for this requirement is to minimise interference from powerline sources. There are many possible reasons for the appearance of powerline interference in bioelectric recordings, some of the significant mechanisms are:

(a) Time-varying magnetic fields induce voltages into conductive loops. This may be avoided by twisting cables together (thus minimising loop area).

(b) Electric fields from power lines capacitively couple onto the body, inducing displacement currents. This displacement current flowing through the impedance of the body causes a fluctuating common mode voltage. Additionally, two electrodes placed on the body experience a potential difference due to the displacement current flowing through the portion of body impedance which exists between the electrodes.

(c) Unequal skin/electrode impedances effectively convert common mode voltages on the body to differential voltages, by acting in series with amplifier input impedances. This is called the 'potential divider effect' (\Van & Nguyen 1994, Overton 1974).

(d) Currents induced due to capacitive coupling onto leads cause differential voltages at amplifier inputs if skin/electrode impedances are unequal.

For the purposes of the study described here, only the causes which are influenced by electrode and/or skin impedance are considered (points (c) and (d)). Although these effects can be reduced by guarding cables and using

a driven-right-leg circuit, contact impedance still has a large influence on interference voltages at amplifier outputs. For details regarding other sources of powerline interference, several review articles are available (Chimene & Pallas-Areny 2000, Marshall & Neilson 1984, Webster 1984, Overton 1974). After considering the causes of powerline interference, it can be seen that the major reason for the common requirement oflow electrode/skin contact impedance is that this minimises the impedance mismatch between electrodes. The mismatch between impedance at electrode sites is a major influence on the quality of signals obtained, rather than the magnitude of contact impedance. Thus the primary objective is to minimise electrode contact impedance mismatch, which occurs as a consequence of lowering the contact impedance of both electrodes: a reduction in magnitude of both contact impedances also has the effect of reducing the impedance difference between them. The effects of impedance mismatch can be illustrated by pairing two electrodes of different design and measuring the powerline interference suffered. For this thesis, an experiment was conducted to illustrate this effect using three electrode pairs (Searle & Kirkup 1999) on one subject (male, aged 27). Table 6.1 shows the 50 Hz interference component for the three pairs of electrodes 20 minutes after application to the forearm. One pair of electrodes was stainless steel,

Electrode pair	Interference $[,uV_{RMS})$
Two Ag/AgCl	3.2
Two Stainless Steel	74.2
One Ag/AgCl, One Stainless Steel	762.7

Table 6.1: Powerline interference evident in bioelectric recordings from three electrode pairs made up of 2xwet, 2xdry and a mixed pair

one pair was disposable Ag/AgCl ECG electrodes, and the third mismatched

pair used one of each electrode type. All six electrodes were positioned at the same time with 30 mm between their centres. The signals were not buffered at the electrode sites. nor were cables shielded. Results showed that, due to higher contact impedance, the impedance mismatch for stainless steel electrodes was higher than that for Ag/Agel, and as a result more powerline interference occurred. The increase in powerline interference suffered by the mismatched electrode pair (caused by the large difference in contact impedance of the dissimilar electrodes) is significantly larger than that for the other two electrode pairs.

Although this degree of contact impedance mismatch is unlikely in operational situations, the results emphasize the need for low, stahle contact impedances in electrodes. Other work has shown that manually matching the contact impedances using capacitors and a potentiometer significantly reduced powerline interference (Adli & Yamamoto 1998). The effect of the skin/electrode impedance, and skin/electrode impedance mismatch will be demonstrated in Section 6.6.

There are many ways to prepare the skin to further reduce the skin/electrode impedance, such as abrasion with fine sandpaper, scraping the stratum corneum with blunt needles and cleaning with alcohol and other fluids (Wan & Nguyen 1994, Geddes & Baker 1989). An effective reduction in impedance when using dry and insulating electrodes is achieved by using an amplifier of unity gain, or buffer, at the electrode site. Electrodes which use this active impedance conversion are often termed 'active electrodes',

6.3.1 Active impedance conversion

Bioelectric signals are often buffered electronically at a location spatially immediate to the electrode site. This has two main advantages:

- The bioelectric process 'looks into' a very high impedance, thus current load on the signal is very low and associated artifacts are minimised. Since the input impedance is very high compared to normal skin impedance, there is less emphasis on skin preparation and artificial electrolytes.

- The buffered signal is transmitted along wires to ancillary equipment with a low output impedance driver, thus reducing the effect of induced current noise in trailing leads.

The circuitry of impedance conversion also comes under the terms 'buffer', '[source] follower' and 'unity gain amplifier'. It is advantageous to have this buffer circuitry spatially immediate to the electrode, with power supplied either locally by batteries or through the trailing leads from a distant source. Caution should be given against using a spatially local instrumentation amplifier with high gain connected to a 'non-polarisable' electrode pair, even if a differential bioelectric signal is desired. The half cell potentials from the electrodes often cause the amplifier to saturate (even if the AC signal of interest is tiny) so it is advisable to use a medium gain in the initial instrumentation amplifier, then an AC-coupled second stage amplifier may be used for the remainder of the required gain (MettingVanRijn et al. 1996, MettingVanRijn et al. 1994). It is most common, however, to use unity gain buffers at the source of each electrode and process signals away from the subject.

The utilisation of impedance converters is usually restricted to dry and insulated electrode types due to their habitually high impedance compared to wet types. Impedance converters are, however, occasionally used in conjunction with 'low' impedance AgjAgCl electrodes to allow longer leads, less concern about skin preparation and impedance levels (Dunseath & Kelly 1995), and when concerns about AC power pickup in trailing leads are present

(Iguchi et al. 1994). It has been shown (Hagemann & Luczak 1985) that some motion artifacts are also reduced when these active electrodes are used. This is because of a reduction in lead flexing artifacts; the movement artifact due to disruption of the double layer interface will not be changed by the use of buffers. One drawback is that power must be supplied to the sensing area, though this is a minor problem since the power may be supplied through the same bundle of leads used to transmit signals, or by using batteries (Burke & Gleeson 2000, Taheri et al. 1994). Some commonly used buffering techniques are outlined in the following sections.

6.3.1.1 FET buffers

The very high impedance at the input of field effect transistors (FETs) makes them suitable choices for use in electrode buffer amplifiers. A brief introduction to FET devices can be found in Appendix E. A unity gain amplifier can be made incorporating a FET with a minimum of additional parts, for example, the circuit in Figure 6.6 modified from Wolfson & Neuman (1969), which uses only a single current limiting diode in addition to the MOSFET[4]. The current limiting diode is simply a prepackaged JFET with the gate con-

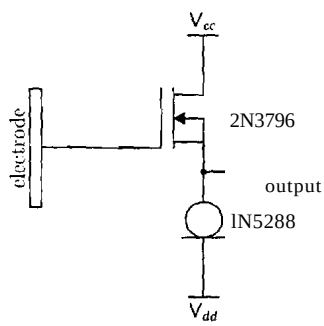

Figure 6.6: FET input active buffer with high input impedance, modified from Wolfson & Neuman (1969)

4Metal Oxide Semiconductor Field Effect Transistor.

nected to the source internally, acting like a constant source and improving the performance of the voltage follower (see section E.1.2). Constant-current source-followers are also used by Luca et al. (1979) and Palko et al. (1995), using BJT transistor arrangements for the active load, while Matsuo et al. (1973) uses a zener/JFET combination for the current source. The input resistance for this configuration is reported to be about $10^{ID}\ \Omega$. Ko & Hynecek (1974) investigated the performance of many FET-input buffers, which they integrated into single chip packages. The size and shape of 'metal can' FET casings (often made of steel) has been utilised by Norris (1983) and Luca et al. (1979), as the impedance conversion and signal pickup can be performed by one discrete component. In both cases the steel surface of the cans were polished to provide a suitable electrode surface.

6.3.1.2 Operational amplifier buffers

Integrated circuit technology and smaller package sizes (especially with Surface Mount Technology, SMT) means that it is convenient to use operational amplifier packages as buffers at the electrode site (Ko 1998). The buffer configuration is shown in Figure 6.7. Op-amps with inputs incorporating FET

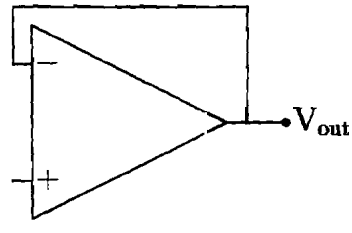

Figure 6.7: Operational amplifier buffer

technology have comparable input impedances to discrete FET devices used for buffering. This buffer type has been utilised by Iguchi et al. (1994) and Nishimura et al. (1992) using dual-in-line (DIL) packages, and by David &

Portnoy (1972) using a metal can type. Although it is not recommended due to dangers of saturation from polarisation voltages (with wet and dry electrode types), Dunseath & Kelly (1995) used an op-amp in a non-inverting configuration, with a gain of 10. A pair of opposing diodes in parallel across the inputs of the op-amp, in conjunction with a resistor prevented possible damage from static electricity, while not compromising input impedance. Padmadinata et al. (1990) fabricated an integrated BJT op-amp device of their own design, enabling them to have the circuitry on the same substrate as the electrode, thus minimising the physical size of the sensor.

6.3.1.3 Using buffers with insulating electrodes

A further consideration must be made when using insulating electrodes with buffers. Assuming that the electrode is purely capacitive, the electrode and the input impedance of the buffer form a high pass filter, as shown in Figure 6.8. Thus the lower 3 dB frequency5 of the filter depends very much on

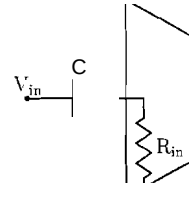

Figure 6.8: Combination of electrode capacitance and input impedance forming a high pass filter

the values of the electrode capacitance and input impedance of the buffer (Matsuo et al. 1973). For the simple R-C combination in Figure 6.8, the

5The 3 dB frequency is defined as the frequency at which the output signal from the filter has dropped to 71% of its original level.

3 dB frequency is given by

$$\frac{1}{2\pi\tau} \qquad \text{where} \quad \tau = RC \tag{6.6}$$

David & Portnoy (1972) found f_{3dB} frequencies for various dielectrics and dielectric thicknesses to be between 0.012-1.1 Hz. Further caution is required due to the fact that it is most common for the signals to be applied to a differential amplifier after buffering. The differing values of capacitance and input impedances will mean different effective gains for each buffer, and this may affect the Common Mode Rejection Ratio (CMRR) of the electrode system.

The product of R and C, or τ is also known as the *time constant* and is directly related to the time taken for a capacitor to discharge through a resistor to 37% of its starting voltage in the presence of a DC step. This becomes a problem when large capacitances and input impedances are used because large artifacts will take considerable time to dissipate (Ko & Hynecek 1974). Some work has been done (David & Portnoy 1972) where an earthing resistor is used at the input of the buffer to prevent charge buildup on the capacitive electrode which would ultimately saturate the amplifier (or even destroy a FET device). This naturally introduces a tradeoff between the input impedance (now reduced effectively to that of the earthing resistor) and a requirement to dissipate unwanted electrical charge. This charge effect was also noticed by Ko & Hynecek (1974) who showed that, even with grounded shielding around electrodes, the output was affected by electrostatic fields near the devices. This charge sensitivity of insulating electrodes has also been reported by Bergey et al. (1971) and Lagow et al. (1971).

In order to investigate the effect of skin/electrode impedance on signal

quality further, a method which is capable of measuring impedance for the skin/electrode system in real time is required. Established techniques for impedance measurement are introduced in Section 6.4, and the development of a new system impedance monitoring is described in Section 6.5, as has been reported in the literature (Searle & Kirkup 1999).

6.4 Techniques for the measurement of the skin!electrode impedance

Many methodologies have been used previously to measure the impedance of skin and/or electrodes. Some of these techniques are also common to impedance measurements in other scientific fields. Depending on the method used for measurement, the skin/electrode impedance may be measured as a single entity, or reduced into the skin impedance and electrode impedance separately. Electrode impedance has already been introduced in Chapter 5. There are a number of possible methods to measure the impedance of skin without the effect of electrodes. One is to measure the impedance of two electrodes with their recording surfaces touching (face-to-face), concurrent to the measurements taken of the skin/electrodes impedance (Khalafalla et al. 1971). The impedance can then be subtracted from the measured skin impedance (which in fact is the skin + electrode impedance). There are also methods, by using multiple electrodes, that can separate the impedance components, as will be outlined in Section 6.4.1. This section outlines the possibilities concerning the number of electrodes used in the measurement, and the measurement techniques themselves.

6.4.1 Electrode configurations

The placement and arrangement of the electrodes used in impedance measures needs to be understood before the interpretation of results, or before the design of equipment can be undertaken.

6.4.1.1 Two electrode configuration

This is the most basic and intuitive setup to measure impedance. One pair of electrodes is used to supply current and simultaneously to measure the voltage across the impedance sample. The simplest such setup is a power source in series with the subject and a resistor of low value to indicate the current magnitude (Lykken 1970). Unfortunately the impedance of the electrodes will affect the voltage read, and thus the impedance result will be the summation of the skin and electrode impedances. The effect will depend on the electrode type used and the frequency of the current supply. Figure 6.9(a) shows the setup. The use of small electrodes is specified in this di-

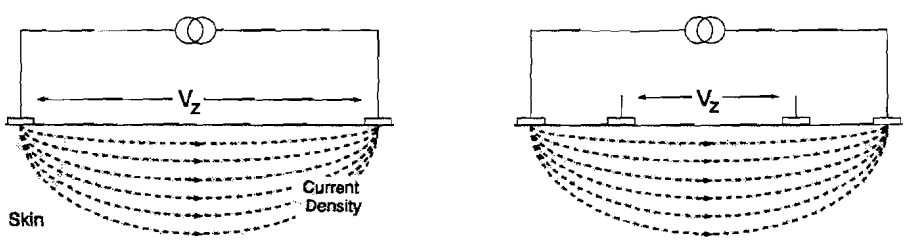

Figure 6.9: Two and four electrode configuration (using small electrodes)

agram: alternatives to small electrodes such as plate, concentric (Yamamoto et al. 1986) or band (Baker 1989) electrodes result in different current density distributions and thus gives different impedance values.

6.4.1.2 Four electrode configuration

This has also been termed the tetrapolar current method (Palko et al. 1995). In this configuration, shown in Figure 6.9(b), two outer electrodes are used to supply the excitation current, whilst two inner electrodes detect the differential voltage across a portion of skin. Since no current flows through the sensing electrodes (assuming the differential amplifier is of instrumentation quality) there is no electrode impedance effect present in the resulting waveform of V_Z. Although the use of this method requires slightly more complicated circuits and increased electrode counts, its proven accuracy make it a popular choice for many researchers (Ristic et al. 1995, Lozano et al. 1990, Ackmann 1993).

6.4.1.3 Three electrode configuration

The three electrode technique allows readings to be taken from a single electrode site, with the remaining two electrodes acting as current source/sink (Yamamoto & Yamamoto 1981). As in the four electrode configuration the electrode effect can be neglected if a high input amplifier is used, thus assuring that no current flows through the sensing electrode (Yamamoto et al. 1996, McAdams et al. 1994). Some researchers have not taken this precaution (Qiao & Morkrid 1995), instead using a current to voltage converter after the sensing electrode, providing a path for small currents which could possibly affect impedance values by the inclusion of the sensing electrode impedance.

6.4.1.4 Multiple electrodes

Devices which use impedance to image parts of the human body (known as Electrical Impedance Tomography, or EIT) frequently employ large num-

bers of electrodes for good spatial resolution. Most often these are arranged evenly, surrounding the area of interest. For example, Hutchison & Kulkarni (1995) used 16 electrodes, sequentially using two electrodes for current injection whilst the other fourteen electrodes monitored the resulting voltages (in a similar fashion to the four electrode technique). In contrast, Cook et al. (1994) used 32 electrodes and one ground reference, using all sites to supply current and detect voltage simultaneously, akin to the two electrode approach. Note that some EIT systems do not necessarily use large electrode arrays, but may employ as few as two electrodes (Lozano et al. 1990).

6.4.2 Impedance measurement techniques

The measurement of currents through biological specimens was restricted mainly to DC (resistance) instrumentation before the widespread use of the vacuum tube around 1910 (McAdams & 1995) made the generation of high frequency AC signals more convenient and reliable. At this stage impedance measurements, which require AC waveforms, became possible. Improvements in instrumentation have paralleled the advances made in the analysis and use of the electrical models. A brief survey of methods used since the early 1900's follows.

6.4.2.1 Impedance bridges

Early measurements of complex impedances were performed accurately with Wien impedance bridges. The unknown impedance was in one arm, and a variable capacitance and resistance (Hague & Foord 1971) on another, the theory being that the resistive, then the capacitive components are matched separately (Coombs 1995, Geddes *1973b),* using an AC source for excitation at various frequencies. This makes the assumption that the impedance *Zx*

is comprised of a capacitive and resistive part (C_x and R_x). The variable capacitance and resistance may be in series or parallel configuration, as shown in Figure 6.10. In both diagrams the unknown quantity is *Zx*. The null

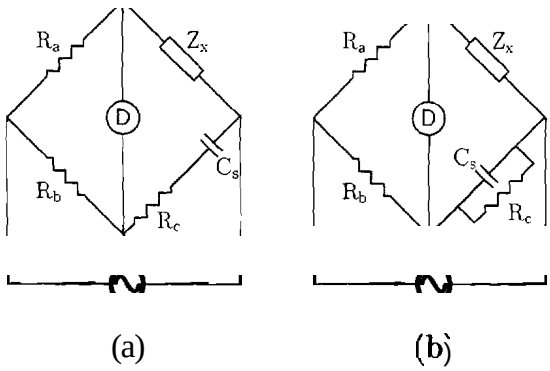

Figure 6.10: Impedance measurement circuits in the (a) series and (b) parallel configuration

detector (D) shows the out-of-balance error signal, and the values of R_c and C_s are adjusted until a zero reading is obtained (or in more practical terms, when the error signal is indistinguishable from the noise level.) For both series and parallel techniques the values for C_x and R_x, once the bridge has been balanced, are given by

$$C_s \frac{R_b}{R_a} \tag{6.7}$$

$$R_x = R_c \frac{R_a}{R_b} \tag{6.8}$$

R_a and R_b are ratio resistances, usually preset and of high precision. In the case of biological impedances, commonly $R_a = R_b$ and $R_a \gg |Zx|$ so that the sample under test *(Zx)* is assured of a constant current (Geddes *1973b).* Note that this impedance is only valid for the frequency which is employed in the exciting current. The null detection system must have a good signal-to-noise-ratio (SNR) so that the error signal (which in many biological sample cases is

only a few millivolts) can be determined with some accuracy. Problems arise when harmonics are generated by the sample, since near balance the second harmonic amplitude will be far greater than the base frequency, making visual minimisation difficult on a cathode display. Differing magnitudes of the impedance components can lead to reduced sensitivity in the determination of the minor component, since the SNR affects the observation of balance of one component more than it does the other. In response to both of these difficulties, a phase-sensitive detection system can be employed.

In phase sensitive detection (Armstrong et al. 1968) the error signal is phase-shifted by a variable amount and, along with the signal from the AC source, is fed into a phase detector. The phase detector gives a DC voltage proportional to the fraction of phase-shifted error signal that is in phase with the oscillator signal at the exact same frequency. The term phase sensitive detection is also used in a wider sense in quadrature techniques, to be described in Section 6.4.2.5. Using this method the effect of SNR is reduced (since a DC signal is used for display, and a coil or digital meter can be used as the null detector) and each component of Zx has comparable accuracy.

It is often assumed (Ackmann 1993) that bridge techniques restrict the observations to two electrode configurations (Sec 6.4.1.1), however the use of more advanced bridges' have been used with three and four electrode configurations (Barnett 1938), allowing the advantage of skin impedance readings free from electrode impedance contributions.

6.4.2.2 Phasemeters

Early researchers were mostly concerned with finding the phase angle (and not so much the magnitude (Barnett 1938)) of the body impedance. Phasemeters simplified the determination of phase angle by offering a way to find the

phase reading directly, with only one adjustment required. Simple phasemeters were made of three separate components; an oscillator, phase changer and an indicator (to act as the null phase instrument). The phase changer is adjusted until the body phase is accounted for, and a direct reading can be made from the null indicator by replacing the body by a purely resistive component. A single phase measurement could be made by this method in the order of two minutes (Barnett 1935).

6.4.2.3 Lissajous' figures

Lissajous' figures are formed by the composition of two perpendicular waveforms, most commonly this is done on an oscilloscope. From these curves the relative phase and frequency of the two waveforms can be established. The

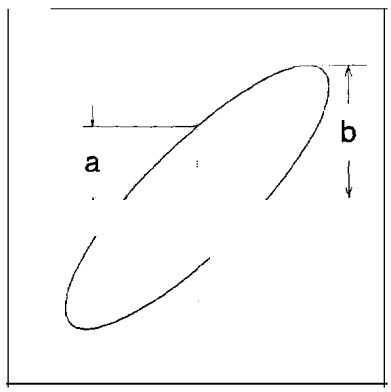

Figure 6.11: An example of a Lissajous' Diagram

phase is gained from the x-y plot on an oscilloscope, plotter etc. as follows. If it is assumed that there exist two signals of the same frequency, and with a phase difference ϕ, then the vertical and horizontal deflections are governed

by the equations (Malmstadt et al. 1963),

$$y = b\sin(\omega t + \phi) \tag{6.9}$$

$$x \quad \text{csin(wt)} \tag{6.10}$$

Consider the case where $y = a$ when $x = 0$ (see Figure 6.11), since this gives values of a and b which are easily gathered from the Lissajous image, the phase difference is given by

$$\phi = \arcsin(\frac{a}{b}) - 2n\pi \qquad n = 0,1,2 \ldots \tag{6.11}$$

The value of n is usually simply set to zero. Lissajous' figures have the advantage over sinusoidally driven universal bridge techniques in that it is immediately apparent when nonlinearity effects are present. The graphical nature of the approach lends itself to signals of low frequency, since the figure can be traced on an x-y plotter (paper, digital or otherwise). Where the technique is applied to biological impedance, the input current (usually from a constant current source) and the resulting output voltage are applied to the two axis of the recording device to produce the Lissajous' figure (Plutchik & Hirsch 1963, de Boer & Oosterom 1978). Yamamoto & Yamamoto (1981) used this technique to examine the nonlinear effects which occur at low frequencies and high currents.

6.4.2.4 Active-impedance conversion

The circuit shown **in** Figure 6.12 can be used to deliver a controlled current to an impedance sample, under the proviso that the sample does not require one grounded terminal, since the op-amp provides only a virtual ground (Greef 1978). To minimise the offsets due to bias currents **in** the op-amp, set $R_x \simeq R111Z$. The current through Z is

$$I_{R_1} = \tag{6.12}$$

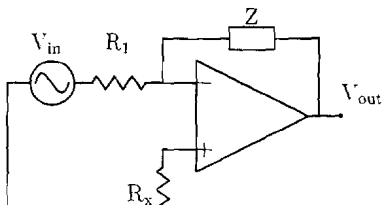

Figure 6.12: Active impedance converter

This is essentially an inverting amplifier circuit, thus the output and impedance value is

$$-\frac{V_{in}Z}{R_1} \tag{6.13}$$

$$z = \frac{V_{out}R_1}{V_{in}} \tag{6.14}$$

Using Equation 6.14 the magnitude of Z can be directly determined using V_{out}, or the signal can be split into rcal and imaginary components using quadrature techniques (Section 6.4.2.5) or Fourier transforms (Section 6.4.3.1).

6.4.2.5 Quadrature techniques

This is also commonly known as Phase Sensitive Demodulation or Phase Sensitive Detection, but not to be confused with the phase sensitive detection method used in AC bridge measurements (Section 6.4.2.1). Variations on this method use the waveform providing excitation to the impedance sample as a reference to extract in-phase and quadrature[6] results. A current proportional to a sinusoidal signal is driven through the impedance sample. The resulting voltage across the sample is then amplified and multiplied either by the driving waveform, or by a quadrature version of the driving waveform.

690° out of phase from the reference signal

The products are then low-pass filtered and the resulting voltages are proportional to the real and complex impedance (R_s and X_s) for the sample. There are many variations in the driving circuitry (Ristic et al. 1995) and the sampling stage, where digital techniques are an attractive alternative to analogue multiplication and filtering; integrators with sample-and-hold are utilised instead (Cook et al. 1994). Commercial phase sensitive detectors are available and are usually termed Lock-in Amplifiers. Often these instruments can be programmed to sweep through frequencies, thus making the gathering of readings much simpler. Most commercial lock-in amplifiers are not designed for biological signal testing, so external amplification and isolation circuits are usually required 1993).

6.4.2.6 Step input and square wave applications

The use of square waves to determine the transient response of circuit elements is standard in electrical engineering methodologies (Kuo 1991, p. 308). The application of a square wave can be considered equivalent to a series of step impulses, so long as the period of the waveform is significantly longer than the expected time constant of the system under test.

All methods thus far have utilised techniques to gather impedance information at set frequencies, and if the impedance locus is to be plotted this requires a large number of readings, or at least an automatic sweep of frequencies. It is known that the skin impedance can change rapidly (Geddes & Valentinuzzi 1973), and thus over the course of a number of readings the results can change dramatically. Some early researchers (Teorell 1947, Tregear 1974) realised that using square waves could allow them to obtain impedance values at many frequencies in one measurement, thus avoiding the need to repeat impedance measures over a range of frequencies.

6.4.3 Multifrequency measurement techniques

In this thesis the term 'multifrequency' relates to a multitude of frequency components combined into a single waveform, with results for each frequency available simultaneously. Many reports, particularly those involved with EIT use multifrequency when referring to "dual-frequency" systems, or to those where the frequency spectrum is swept (Gudivaka et al. 1996, Griffiths 1992, Palko et al. 1995).

6.4.3.1 Fourier analysis

According to Fourier Theory, all waveforms can be considered as comprising of a number (often an infinite series) of sinusoidal components. For example the Fourier expansions for a square wave and a sawtooth wave are shown in Equations 6.15 & 6.16, with their associated spectra shown in Figure 6.13 (where the amplitudes of the waveforms are $A = \frac{V\pi}{4}$ and $\frac{V\pi}{2}$ respectively, and V is the amplitude of the base frequency component).

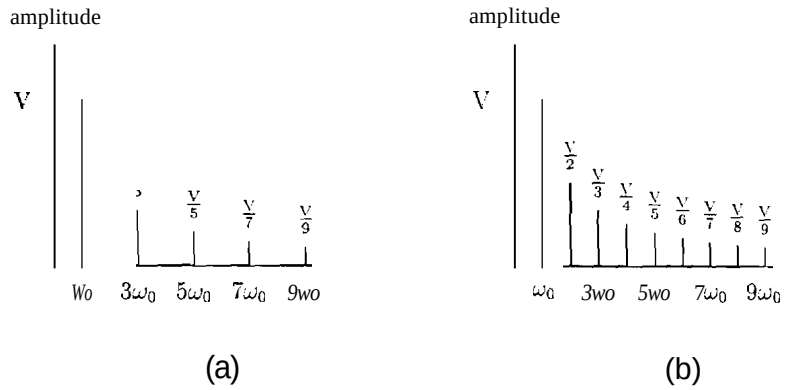

Figure 6.13: Spectra for square and sawtooth waveforms

$$f_{square}(t) \qquad A(\cos\omega_o t - \frac{1}{3}\cos 3\omega_o t + \frac{1}{5}\cos 5\omega_o t - \ldots) \qquad (6.15)$$

$$f_{sawtooth}(t) \qquad A(\sin\omega_o t - \frac{1}{2}\sin 2\omega_o t + \frac{1}{3}\sin 3\omega_o t - \ldots) \qquad (6.16)$$

The sawtooth waveform has all discrete harmonics, whereas the square spectra only contains odd harmonics. Despite this, the square wave is almost the only waveform used for impedance studies due to the simplicity of its generation. Tregear (1974) stated that the use of a square wave voltage would be 'theoretically elegant', but that in practice the use of a sinusoidal voltage at a series of different frequencies would be easier. However, 28 years earlier Teorell (1947) had used exactly this technique to examine the skin of frogs under the effect of NaCl and KCl. Using fourier equations the sinusoidal components of the square waves can be examined, thus allowing the determination of impedance at a large number of frequencies simultaneously. Using photographs of responses on an oscilloscope and manual fourier calculations, Teorell obtained an impedance locus diagram with a total of 6 data points (from 12 waveform coordinates). More recently Yamamoto et aJ. (1996) used computers (taking advantage of the Fast Fourier Transform, FFT) to acquire and process waveforms resulting from square wave current application to palmar skin.

A major disadvantage inherent in both of these techniques is that the amplitude of the sinusoidal components in the square wave drops off rapidly (following a $\frac{1}{n}$ series) at higher harmonics, thus making readings at higher frequencies less accurate (refer to Figure 6.13(a)). The sawtooth function shown in Figure 6.13(b) has more harmonics, but the amplitudes also follow an inverse law. The ideal spectra for instantaneous multifrequency measurements would be one which has all frequency components at an equal amplitude: in other words a flat, or "white", spectrum. If the fourier equations are applied to this approach we find

$$f(t) = \mathcal{F}^{-1}\left\{g[\omega]\right\} = \mathcal{F}^{-1}\{1\} = \frac{1}{2\pi}\int_{\infty}^{\infty} ejwtdw = \delta(t) \qquad (6.17)$$

The current waveshape that is needed, $\delta(t)$, is the delta impulse function; a

pulse approaching zero width and infinite height, with an area equal to one unit. Besides being impractical to implement, such a current spike would be damaging to the skin, and possibly ancillary electrical equipment. There are alternatives which can produce fiat spectra, at least over a selected range, without being impractical. Kinouchi et al. (1997) used an approximation to the impulse function, which was stored on a computer and generated via a DAC. Creason et al. (1973) undertook a thorough investigation into various waveforms which could be produced by computer for use in impedance measuring instruments. These included white noise (bandwidth limited, pseudo-random and phase varying), rectangular pulses, odd-harmonic arrays and near-periodic signals.

6.4.3.2 Commercial spectrum analysers

'iVith the addition of some current conversion and isolation circuitry, commercial equipment can be utilised to obtain the impedance locus, though most analysis equipment sweeps through a range of selected frequencies (McAdams & Jossinet *1994b,* Onaral & Schwan 1982, Patterson & Latterell 1995, Armstrong et al. 1977) thus allowing for errors due to temporal skin impedance changes. Some newer spectrum analysers operate with FFT algorithms (Nowotny & Nowotny 1980) and thus can take **full** advantage of characteristics described in section 6.4.3.1. However, a customised system offers many advantages over spectrum analysers, which are rarely devised with biological applications in mind. Specialised impedance analysers are also available, usually intended for testing of discrete components or systems. Many such analysers have the facility for four-terminal testing (equivalent to a four electrode configuration), but Ackmann (1993) warns that some instruments have these terminals connected internally and so are in effect two terminal devices.

6.5 A new method for impedance plots with arbitrary frequency components

As outlined in Section 6.4, many methods for measuring impedance are available. the impedance spectrum (i.e. the impedance of a sample at many different frequencies) is required, the options become more limited, especially when the impedance characteristics of the sample are nonstationary, as is the case with skin/electrode impedance. The impedance measurement system described in this chapter, and reported in the refereed literature (Searle & Kirkup 1999), offers the following advantages:

- It is capable of measuring impedance at many frequency values simultaneously.
- The system is flexible; the frequencies at which to measure are arbitrary in value and number.
- The impedance measurements have equal fidelity at all frequency values (unlike, for example, methods which use a square wave for excitation).
- The impedance spectrum may be determined at a fast rate, limited only by the lowest frequency value utilised.
- The system is inexpensive and may be constructed from readily available parts.

The term 'impedance spectrum' is used rather than 'multifrequency impedance analysis' as the latter term is usually applied to bioimpedance techniques which sample at a limited number of preset frequencies (Griffiths 1992), or else sweep across a range of frequencies to build a complete spectrum (Gudivaka et al. 1996, Palko et al. 1995). Examples of contact impedance

using the new impedance spectroscopy system are examined, and in Section 6.6 the system is used to demonstrate the effect of contact impedance on bioelectric signal fidelity.

6.5.1 Introduction

Since changes in the skin impedance (and the skin/electrode interface) characteristics occur over short time periods (of the order of seconds), a method that determines the impedance at a large number of frequencies simultaneously was required. If the impedance monitoring method restricts the user to a single impedance value per measure, many separate evaluations must be performed to construct a complete spectrum. In situations where temporal information is required, the delay in constructing the entire impedance spectra may distort the final result. For comparison, to sweep from 1 Hz-l kHz at discrete of 1 Hz, and assuming we need only one complete sinusoidal cycle at each frequency for a measurement, then a sweep would take (using divergent harmonic series)

$$t = \sum_{1=1}^{1000} \frac{1}{f} = 7.48 \ s \tag{6.18}$$

If the total time delay for processing, which includes a short break between frequency steps, is 10 ms per frequency, this results in a sweep time of nearly 20 s. The effect of long sweep times on the impedance locus (discussed in more detail by McAdams et al. (1993)) is shown in Figure 6.14 (Searle & Kirkup 1999). This figure shows impedance spectra of skin with applied Ag/Agel electrodes. Three loci are displayed, two of which were measured at time t=O sand t=90 s. These spectra were obtained in a single measurement (using the method to be described) every 3 s, with values at 30 separate frequencies over the range 1-950 Hz. The third, intermediate curve,

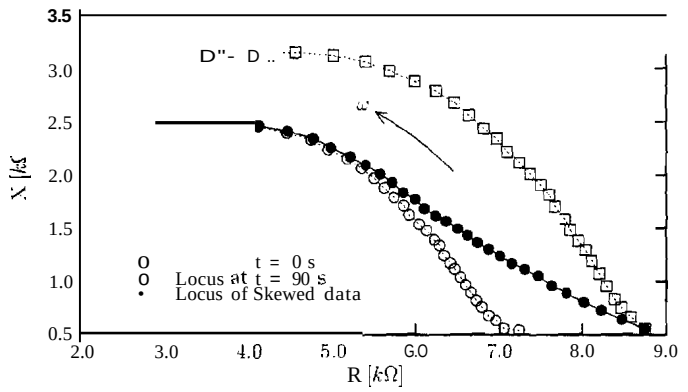

Figure 6.14: The effect of swept impedance readings, as opposed to impedance spectra obtained from a single measurement. Two impedance curves are shown whose loci were determined in single measurements at t=O sand t=90 s. The intermediate curve displays the effect if readings were instead taken at single frequencies over the same time period

simulates the result that would occur jf the frequency range was stepped through at three seconds per frequency, rather than three seconds per complete impedance locus. The form of this distorted data depends on whether the impedance increases or decreases during the readings, and on the direction of frequency sweep; in this simulation the impedance was decreasing and the sweep begins at low frequencies. It is clear that the resulting impedance locus is not representative of the true data, thus the swept frequency method is unsuitable for measuring the impedance spectra of samples which have temporally changing electrical characteristics, such as some biological tissues.

As introduced in Section 6.4.3, methods exist to measure the impedance at many frequencies simultaneously, but all have disadvantages with respect to use with biological samples which have nonstationary characteristics. The new technique developed in this study and described here uses a waveform

which is the summation of a finite number of sinusoids. It was designed to be useable on an IBM compatible computer with a DAQ (data acquisition) board, convenient to construct (minimum of external componentry and specialised equipment), yet to still be able to operate in real time with a reasonable impedance spectra refresh rate. To the author's knowledge there are no reports in the open literature or commercial literature of an instrument which offers these facilities and performance.

6.5.2 Description of system

The impedance measurement system, shown schematically in Figure 6.15, consists of a PC with data acquisition board, and an impedance conversion circuit. The DAQ board has analogue-to-digital (ADC) and digital-

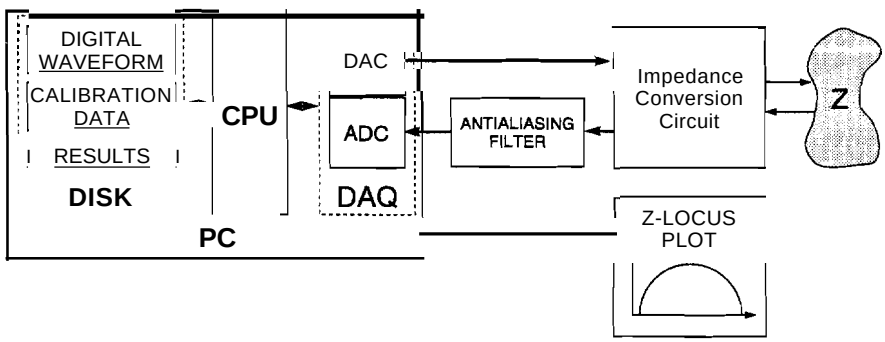

Figure 6.15: Physical layout of impedance spectroscopy system.

to-analogue (DAC) converters capable of simultaneous analogue input and output (National Instruments PCI-MIO-16E-4). The software was written in the graphical programming language Labview 4.0 (National Instruments, Austin, TX, USA). The impedance conversion circuit is in Figure 6.16. This circuit is used to deliver a current proportional to V_{in} to an electrically

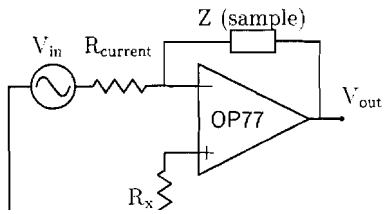

Figure 6.16: Impedance conversion circuit

floating sample.

The development of this technique enables the monitoring of impedance of the electrode-electrolyte-skin interfaces over time, utilising different metals for electrode construction, as well as the study of the impedance change of conventional wet electrodes. This allows a comparison between wet and dry electrodes. Thus it is of interest to observe the contributions due to the presence of recording electrodes, as well as impedance of the skin tissue itself and for this reason the two-terminal method is used. Other applications may benefit from the three terminal method (Section 6.4.1.3) which can measure the impedance from one electrode/skin interface and a portion of tissue (depending on the configuration) or the four terminal method (Section 6.4.1.2) which measures tissue impedance only. The current through the sample, Z, is controllable via $R_{current}$ as in Equation 6.19,

$$I_{R_{current}} = \frac{V_{in}}{R_{current}} \tag{6.19}$$

The value for $I_{R_{current}}$ should be chosen with consideration of the skin impedance, such that the voltage created across the skin does not exceed the maximum voltage for the amplifier and induce clipping of the waveform. **In** experiments carried out using this system, currents used were usually less

than 50 μA. The output voltage and impedance values are given by,

$$V_{out} \quad \frac{-V_{in}Z}{RCUTTent} \tag{6.20}$$

$$Z \quad \frac{\text{- VoutRcurrent}}{V_{in}} \tag{6.21}$$

Using Equation 6.21 the magnitude of Z measured with a sinusoidal signal can be directly determined using \lout. Alternatively, an applied waveform composed of many frequency components may be used, and the FFT applied to the input and output waveforms. If the discrete time series for the digitised versions of the applied and result waveforms are *fa[k]* and *fr[k]* respectively, the spectral components can be determined by the FFT:

$$F_a[j] = FFT\left\{f_a[k]\right\} \qquad F_r[j] = FFT\left\{f_r[k]\right\} \tag{6.22}$$

Thus an array of impedance magnitude values is obtained as in Equation 6.23.

$$\left|Z\right|_J = \frac{\text{IFr[j]!Rcurrent}}{\text{[PaU] I}} \tag{6.23}$$

FaU] and *Fr[j]* are the Fourier coefficients, as described in Equation 6.22. Alternatively the real and imaginary components of the impedance may be obtained by applying complex Fourier transform methods.

6.5.2.1 Frequency determination

As discussed in Section 6.2, the basic form for an impedance spectrum for skin (only) can be electrically modelled by the 'three component model', as shown in Figure 6.3, which has a semicircular locus on an argand diagram. If impedance values are obtained at frequencies which are evenly spaced, the resulting impedance locus will have few data points in the low frequency region, and many clustered points as the frequency approaches infinity. This is demonstrated in Figure 6.17, which simulates impedance values using the

three component model (refer Figure 6.3) with C = 22 nF, r = 47 kΩ and R = 0. Impedance values were calculated from 1-1000 Hz in steps of 50 Hz.

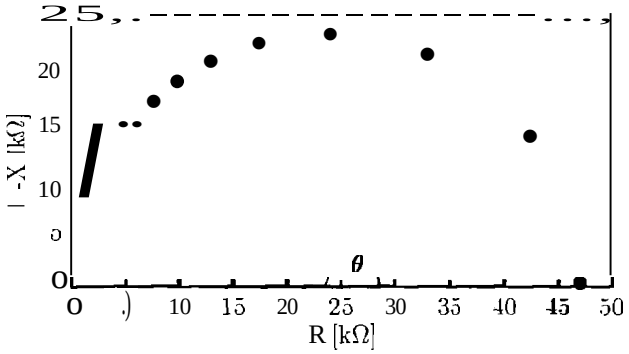

Figure 6.17: Theoretical impedance values calculated from the three component model at evenly spaced frequencies between 1 and 1000 Hz.

The alternative approach used in the technique described here is to generate a waveform which has specific frequencies such that the resulting data points will be evenly spaced around the theoretical impedance locus. This involves estimating the component values for the three component model that will match the anticipated skin impedance. Additionally, the desired frequency range and number of data points are also needed for the calculation. Although experimental data shows that the three component model generally does not fully explain the skin's electrical behaviour (in that the experimental locus has a depressed centre), this approximate model is sufficient for the purpose of frequency selection. Equations 6.24 and 6.25 are utilised' to calculate the frequencies required,

$$e(f) = \cos^{-1}\left[\frac{2}{2\pi r^2 C^2 f^2} + 1 - 1\right] \qquad (6.24)$$

$$f(e) = 1/2\pi \left[\frac{2/(\cos\theta + 1)}{r^2 C^2} - 1\right]^{1/2} \qquad (6.25)$$

[7] see Appendix D.9 for derivation details.

where θ corresponds to the angle in Figure 6.17, and C,r correspond to values in the three component model. The maximum and minimum values for θ can be determined by substituting values for C, r and the maximum/minimum frequency required,], into equation 6.24. The angular increment can be determined by dividing this range by the number of points required, and finally the frequencies required for the evenly spread points are found from Equation 6.25.

For example, if impedance values for 20 points in the frequencies range 1-1000 Hz are required: using Equation 6.24, the start and finish θ values would be ()(1 Hz)=0.74° and ()(lOOO Hz)=162.50°. The span of these angles can be divided into 20 values, and the respective frequency values found using Equation 6.25:](0.74°) = 1.0 Hz,](8.83°) = 11.8](16.9°) = 22.8 and so on.

The impedance monitoring system developed includes a program with a graphical interface so the user can select the values for r, C, frequency range and the number of points, and the algorithm will calculate the required frequency values. Alternatively the program may produce a set of frequencies evenly spread across the spectrum in steps, or the user may manually specify each individual frequency. Once required frequencies are calculated the values are rounded to integers, the waveform is constructed digitally of sinusoids with equal amplitudes, and finally stored on hard disk.

6.5.2.2 Calibration

A calibration is performed once settings have been finalised to account for distortion due to gain and phase transformations in the preamplifier and antialiasing filter, and to avoid the need to enter data regarding the settings for $R_{current}$ and preamplifier gain (as these can be determined from calibration

data). A resistive element of known value is used in the calibration. The phase and magnitude for each selected frequency in the applied signal and resulting waveform are recorded for ten repetitions. The average of the ten results is calculated for each frequency in order to improve estimates of the phase and magnitude corrections.

6.5.2.3 Acquisition

During acquisition the stored waveform was applied via the DAC and the result simultaneously recorded through the ADC. For experiments reported in this thesis, the lowest frequency used was 1 Hz, thus the composite waveform needs to be of 1 s duration to contain at least one complete cycle for each frequency component used. For use with lower frequency components, waveforms of longer duration would be required. To avoid transient effects at the initial application of the waveform, the signal twice over a 2 s time period, and the last second only was used as data. Because the waveform was constructed from sinusoids which all have an integer number of periods within the waveform data set, spectral leakage was avoided and windowing operations before the application of the FFT were therefore unnecessary (Benetazzo et al. 1992, Ramirez 1985). An FFT was performed on the applied and result waveforms. The phase and magnitude of the Fourier coefficients for the result waveform were adjusted by the values calculated in the calibration procedure, described in Section 6.5.2.2. The impedance values for each applied frequency were then determined using Equation 6.23. The impedance spectrum was plotted in real time, thus observations and equipment/subject adjustments may be made without the need to record and process data offline. When desired, the impedance spectra values were able to be transferred to disk without restarting the program.

6.5.3 Results

To test the fidelity of the system for a known locus, a parallel combination of a 47 kΩ resistor and a 22 nF capacitor were used to provide a semicircular plot. The result is shown in Figure 6.18. The experimental points are shown,

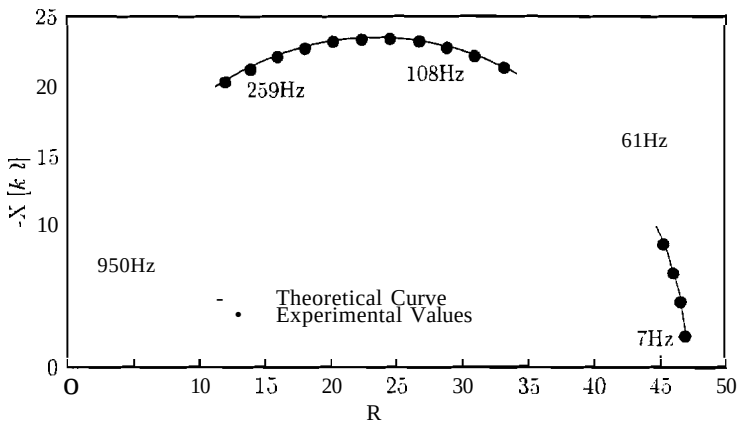

Figure 6.18: Impedance values when the system was tested on a parallel RC combination with R = 47 kΩ and C = 22 nF. The theoretical locus is also shown for comparison.

along with a curve of the theoretical values for the parallel R-C combination. The driving waveform was a composite of 30 frequency components covering 7-950 Hz, chosen such that the data points will be evenly spaced around the impedance locus (see Section 6.5.2.1), as is evident in Figure 6.18. The waveform was acquired at 5000 samples/s, with a peak current of 128 μA (in a biological sample, a current of this magnitude may introduce nonlinearities).

To further explore the benefits of the arbitrary waveform method for impedance spectroscopy, as compared to the use of a square wave, tests were done to examine the stability of locus results. Power spectra were recorded over 100 trials for waveforms applied to a resistive element. Two waveforms were used: the first was a simple square wave, and the second a composite

waveform comprised of 30 evenly spaced frequencies spread from 1 Hz to 950 Hz. The coefficient of variation (V_x) of impedance magnitude for the data sets was calculated as in Equation 6.26 across the frequency range being considered, and expressed as a percentage.

$$v_x = \frac{s_x}{\overline{x}} \text{ x } 100 \quad [\%] \tag{6.26}$$

Here s_x is the sample standard deviation for the sample, and $\overline{x}$ is the sample mean. Figure 6.19 shows the results. v_x for the composite waveform is

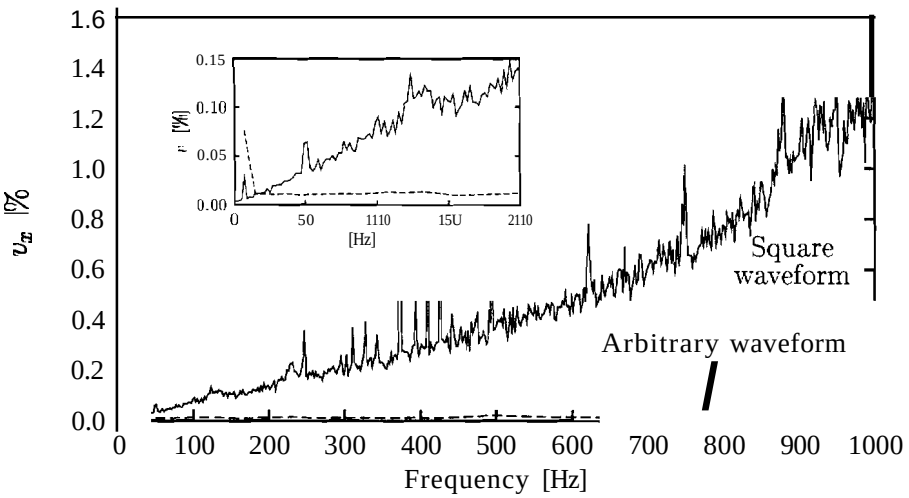

Figure 6.19: Comparison between coefficient of variation of power spectra for arbitrary and square waveform methods. Insert shows detail in frequency range DC-200 Hz.

constant at around 0.015%, whereas v_x for the square wave spectra grows steadily with increasing frequency, due to the decrease in the magnitude of the waveform's spectral components.

6.5.3.1 Application of system to skin/electrode impedance measnrements

Examples of the system applied to physiological samples are shown in Figures 6.20 and 6.21. Figure 6.20(a) shows the variation in the impedance

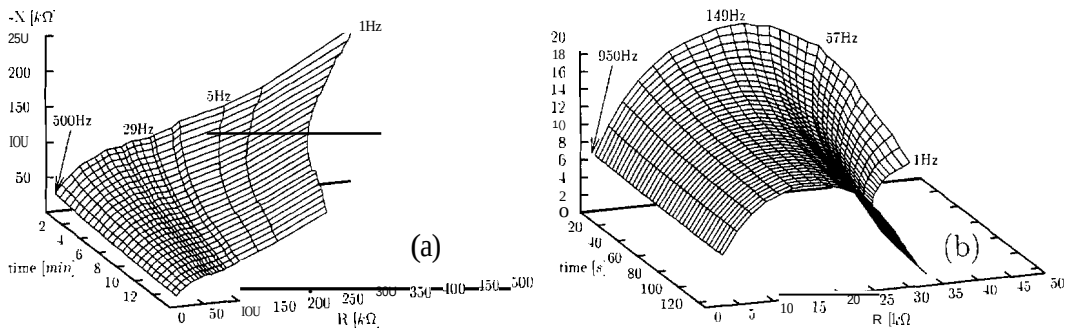

Figure 6.20: Variation over time of the impedance locus for stainless steel electrodes (a) and pre-gelled AgjAgCl (b) in contact with skin.

Figure 6.21: Variation over time of impedance values at each recorded frequency for stainless steel electrodes (a) and pre-gelled AgjAgCI electrodes (b) in contact with skin.

spectrum for stainless steel electrodes in contact with skin over 13 minutes. The skin was lightly stroked with sandpaper before the application of the electrodes, but no gel or other liquid was applied to the skin. Impedances

were monitored at frequencies in the range 1-500 Hz at a peak current of 42 μA. Figure 6.20(b) shows the change in impedance spectrum of pre-gelled Ag/AgCI electrodes in contact with skin over 120 s. Again, the skin was lightly stroked with sandpaper before application. Impedances were monitored at frequencies in the range 1-950 Hz at a peak current of 23 μA. Both sets of measurements were done on the forearm (antibrachium). Clearly, the Ag/AgCI electrodes stabilise more rapidly, and have lower impedance values, consistent with expectations (Geddes & Valentinuzzi 1973). Figures 6.21(a,b) show a different representation of the same data used in Figure 6.20, over the same time periods. Figure 6.21 plots the variation in the impedance at each frequency (in Figure 6.21(a) some curves have been omitted for clarity). Although it was not the purpose of this experiment to draw further conclusions from this illustrative data, the effect of a natural accumulation of perspiration under the dry electrodes used in Figures 6.20/6.21(a) contrasts with the use of an artificial electrolyte (the gel used in Figures 6.20/6.21(b)).

In another example, as illustrated in Figure 6.22, the superposition of contributions from the skin impedance and the electrode interface impedance can be seen. The plot shows the change in the electrode/skin interface impedance on the forearm using Ag/Agel electrodes. Before the application of the electrodes the skin was scraped with sandpaper (more so than for the previous examples), and thus the impedance values obtained are lower (compare to Figure 6.20(b)). As the skin impedance is low, the separate impedance contributions from the electrode interface and skin can be seen clearly. The skin impedance appears as the semicircular portion (dominant at higher frequencies), and the electrode impedance contributes the nearly linear portion at lower frequencies (this is described by the high frequency electrode impedance model, see Figure 5.4(a)). The data in Figure 6.22 were

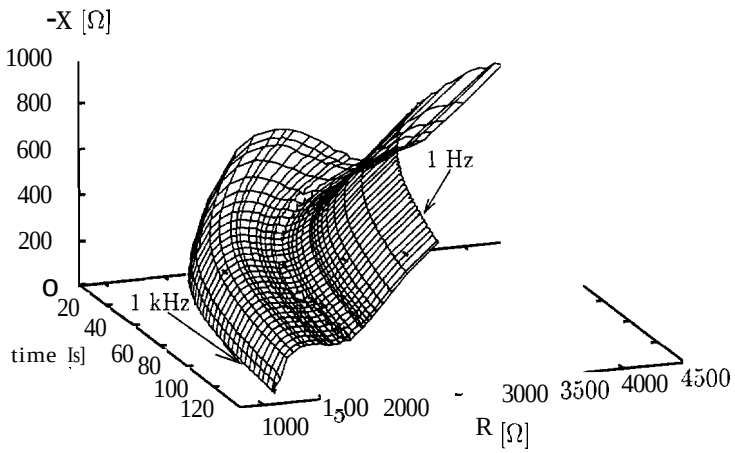

Figure 6.22: Variation over time of the impedance locus for two Ag/Agel electrodes applied to the forearm. The different contributions from the electrode impedance and skin impedance are visible.

obtained using impedance values measured at frequencies ranging from 1 Hz to 1 kHz, with measurements taken over two minutes.

6.6 The relationship between contact impedance and powerline interference, revisited

The influence of the skin/electrode impedance (and more importantly, the skin/electrode impedance mismatch) was explored in Section 6.3. The development of a fast and reliable impedance monitoring system enables the exploration of the dependence of signal fidelity on skin/electrode impedance, and the effect of active electrodes. These experiments have been reported in Searle & Kirkup (2000).

6.6 The relationship between contact impedance and powerline interference, revisited 222

To establish the relationship between impedance and powerline interference the following test was conducted on one subject (male, aged 27). Three identical pairs of stainless steel electrodes (diameter 11 mm) were placed on the forearm, all with the same distance between their centres (20 mm). One pair was used to monitor the contact impedance at 57 Hz using the method described in Section 6.5. The remaining two electrode pairs were used to simultaneously monitor the 50 Hz signal component. Of these, one pair was actively buffered at the electrode site (using OPA132 op-amps in unity gain configuration) while the other pair was not. A standard Ag/AgCl electrode was used as a reference on the wrist and no attempt was made to shield the cables. Recordings were performed for 20 minutes. Figure 6.23 shows how

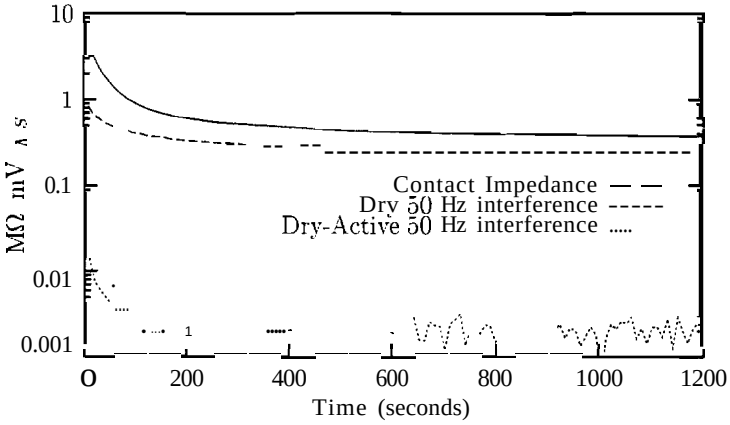

Figure 6.23: Interference performance of two pairs of stainless steel electrodes compared to contact impedance. One pair of electrodes is actively buffered.

the powerline interference reduces directly with contact impedance (which decreases as perspiration accumulates under electrodes) for both dry and dry-active electrode pairs. The dry-active pair results in interference approximately two orders of magnitude lower owing to its reduced output impedance (and thus reduced impedance mismatch). The skin/electrode impedance still

influences the interference of the dry-active electrodes, revealed by the initial decrease in the curve in Figure 6.23. This is due to capacitive coupling onto the electrodes and wires that occurs before the buffers, and the finite input/output impedance of the buffers. These results reflect data reported by Chimene & Pallas-Areny (2000), and by Nishimura et al. (1992), who found in experiments with EMG that the averaged power spectra at 50 Hz for the electrodes with impedance conversion was 1% of that for a passive type.

The change in skin/electrode impedance over time appears to follow an exponential decay; this can be seen in Figures 6.20, and more clearly for a single excitation frequency in Figure 6.23. Although the impedance $Z(t)$ at a given excitation frequency appears to decrease exponentially (as noted by Olson et al. (1979) and Geddes et al. (1973)), to obtain an acceptable fit a polyexponential function must be used, of the form

$$Z(t) = a_1\ e^{b_1 t} + a_2\ e^{b_2 t} + c \tag{6.27}$$

where aI, a_2, $b]$, b_2, and c are constants. An example is shown in Figure 6.24, which shows the impedance at 15 Hz for two Ag/AgCI electrodes applied to the forearm over 13 minutes. The plot shows that the double exponential function gives a good fit to the experimental data points. This function worked equally well for impedance data from 6 subjects tested, and for all excitation frequencies which were used. One possible reason for the structure of $Z(t)$ is that two slightly differing processes occur at each of the two electrodes. However, this is in conflict with the parameters obtained from fitting procedures, shown in Figure 6.24. Specifically, the analysis indicates that b_1 and b_2 consistently differ by an order of magnitude for all electrodes (the short and long time constants are approximately 27 seconds and 200 seconds respectively). Similar processes occurring at each of the two electrodes should lead to $Z(t)$ being adequately described by a polyexponential

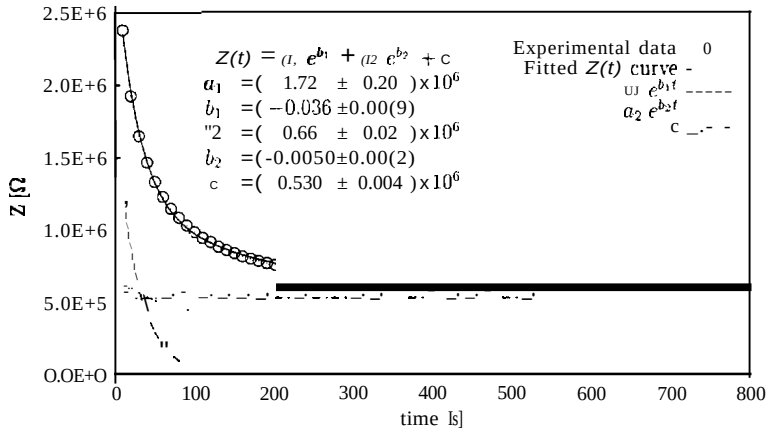

Figure 6.24: Impedance values for two Ag/Agel electrodes applied to the forearm. Impedance data at 15 Hz is shown, along with best fit, fitting parameters and standard error in fitting parameters.

equation in which b_1 is similar to b_2. More work is required in the future to resolve the mechanism responsible for the form of the curves appearing in Figure 6.24.

6.6.1 Conclusion

The new system introduced in this section obtains an impedance spectrum from the singular application and acquisition of a driving waveform (Searle & Kirkup 1999). This is preferable to traditional swept-frequency methods which may distort results if impedance characteristics of the sample (in this case the skin/electrode interface) change with time. The system employs a digitally constructed waveform with arbitrarily selected frequency components. The equality of all frequency component magnitudes offers improvements over previously used square wave methods, which experience reduced precision at high frequencies due to $1/n$ attenuation. The system will be useful for studies where there is an interest in the temporal change in imped-

ance values, including psychophysiological phenomena (such as rapid changes in skin impedance with mental state), characterisation of differing electrode and electrolyte designs, and other dermal properties. The impedance spectroscopy system will be further applied in Chapter 7 for comparison of the performance of differing electrode types.

Chapter 7

A Comparison of electrode types for biosignal sensing

7.1 Introduction

There is a substantial amount published literature regarding the respective advantages and disadvantages of alternative electrode types for sensing biosignals. This includes dry and insulating electrodes, as introduced in Chapter 5. Making a direct comparison of performance for these electrode types is difficult as most experimental data on these electrodes is qualitative, or have been gathered in isolation from other electrode types. A quantitative comparison of the performance of electrode types is important if informed decisions are to be made about the merits of a particular bioelectrode for any application. The work described in this chapter compares and contrasts the performance of wet, dry and insulating electrodes. To the author's knowledge such a direct comparison of the performance of bioelectrodes has not been attempted by other researchers. Some of the work described in this chapter has been reported in the literature (Searle & Kirkup 2000).

Some studies suggest that dry and insulating electrodes are unacceptable for biosignal use due for example, excessive movement artifact and charge sensitivity. By contrast, other workers in the area have reported favorable findings, or fail to mention any difficulties. The aim of this study was to compare the three electrode types in the same test environment. To achieve this all measurements were made on three electrode pairs simultaneously, and on tissue which had a contiguous area large enough to accommodate all electrodes. The study detailed in this chapter assessed the three electrode types over a number of parameters, including susceptibility to movement artifact and moving electric charges.

7.1.1 Background

Reasons given for past investigations into alternatives to gel-based electrodes for bioelectric applications include:

- The performance regarding powerline interference of wet types is limited by electrode/skin contact impedance (as described in Sections 6.3 and 6.6). The use of active electrodes (where buffering/amplification takes place at the electrode site) provides much less emphasis on the skin-electrode impedance (Fernandez & Pallas-Areny 1996, Taheri et al. 1994, Nishimura et al. 1992, Ko & Hynecek 1974).

- The use of an electrolyte is inconvenient. For long-term use, the reliance on an electrolyte leads to reduced signal quality as the gel dehydrates (Padmadinata et al. 1990, David & Portnoy 1972, Lagow et al. 1971, Richardson et al. 1968, Richardson 1967) and the reapplication of gel may not be feasible. The recording may be in a sensitive area (near the eyes, for example, (Geddes et al. 1973)), previous

skin treatment may disable standard electrodes (such as the use of petroleum based burns ointment (Oosterom & Strackee 1983)) or the spacing required between electrodes may be so small that smearing of the electrolyte (and thus short circuiting of the bioelectric signal) may occur (Taheri et al. 1994, Godin et al. 1990). Additionally, and perhaps most importantly, the application and removal of electrolyte gels is a somewhat unpleasant process for the subject, and time consuming for the clinician or carer (McLaughlin et al. 1994, Taheri et al. 1994, Padmadinata et al. 1990, Luca et al. 1979, Ko & Hynecek 1974, Lopez & Richardson 1969, Richardson 1967).

- There are toxicological concerns with electrolyte gels. Although, as expressed by Cochran & Rosen (1980), dermatitis from gels used in bioelectric recordings is "exceedingly rare", concerns regarding dermatological responses are common (Godin et al. 1990, Padmadinata et al. 1990, Oosterom & Strackee 1983, Ko & Hynecek 1974, David & Portnoy 1972). The few reports of dermatitis in the literature indicate a variety of possible gel ingredients as the culprit (Uter & Schwanitz 1996, Dwyer et al. 1994, Coskey 1977). Naturally, if an alternative to wet electrodes is sought, the new construction material/s must be toxicologically acceptable.

The results of many experiments involving dry and insulating electrodes are available. A cross section of these are outlined in Table 7.1, along with a brief description of the findings, if any were provided. Hybrid electrode construction, such as the NASICON ceramic types introduced in Section 5.5.1, are not considered here. The main concerns that are expressed in the articles listed in Table 7.1 regarding dry and insulating electrodes are:

Year	Reference	Dry	Ins.	Construction	Summarised findings
1995	Taheri et al.		•	Si_3N_4	High signal-to-noise ratio (SNR). Uses four redundant sites
1994	McLaughlin et al.	•		Screenprinted AgjAgel (no gel)	
1994	Taheri et al.		•	Si3N4 on steel	High SNR. Low frequency signal present due to electrode movement
1992	Nishimura et al.	•		Stainless Steel	
1990	Padmadinata et al.	•		Silver, Stainless Steel	
1989	Geddes & Baker	•	•		Effective dielectric thickness changes with dry skin layer and perspiration
1979	Griffith et al.		•	Tantalum Pentoxide	Films robust until heavily scratched
1979	Luca et al.	•		Stainless Steel	
1974	Ko & Hynecek		•	Si02 on Si	Electric field problems. Motion artifact a problem due to long settling time from RC constant
1973	Matsuo et al.		•	Barium Titanate	Material is Piezoelectric
1973	Geddes et al.	•		Silver	
1972	David & Portnoy		•	$BaTiO_3$, TiO_2, Ta205, SiO_2	Insulated electrode less affected by movement artifact. Some loss of low frequency information
1971	Bergey et al.	•	•	Ag, Au, brass, Stainless Steel, Anodised Al	Charge sensitive, Al_2O_3 erratic. Movement artifact least with stainless steel, most with Al_2O_3
1971	Lagow et al.		•	Anodised Ta and Al	Careful Shielding arrangement required
1970	Potter & Menke		•	Pyre Varnish	
1969	Wolfson & Neuman		•	Silicon Oxide	
1969	Lopez & Richardson		•	Anodised Aluminium	
1968	Richardson et al.		•	Anodised Aluminium	Movement artifacts
1967	Richardson		•	Anodised Aluminium	

Table 7.1: Summary of literature published since 1967 dealing with dry and insulating electrodes

- Movement artifact caused by absence of a thick electrolyte layer (as is present in gels, which provides a "shock absorber" function). An added concern with insulating types is that the large RC constant (existing at the input of the unity gain amplifiers) prolongs the effect of large artifacts (as described in Section 6.3.1.3). By contrast David & Portnoy (1972) cite improved movement artifact performance when insulating electrodes are used.

- The effect of charged bodies near electrodes. This problem is caused by the high input impedance of the amplifiers (as introduced **in** Section 6.3.1.3). Insulating electrodes especially have been described as acting "as an electrometer" (Bergey et al. 1971).

The above-mentioned concerns and related issues are considered and tested experimentally in this chapter. The capacitive electrodes developed for experiments **in** this chapter were made from silicon dioxide (on a silicon substrate). The manufacture and characterisation of these electrode films is described in Section 7.2. Section 7.3 describes experiments carried out to compare the performance of wet, dry and insulating electrodes. Finally, Section 7.4 demonstrates practical use of the electrodes. Portions of the work presented **in** this chapter has been published in the literature (Searle & Kirkup 2000).

7.2 Silicon as a substrate for insulating electrodes

The use of silicon as a substrate for thin films provides a clean, continuous surface, and offers a medium which lends itself to electrical uses. Silicon diox-

ide is is stable in water and at elevated temperatures, an excellent electrical insulator, and capable of forming a nearly perfect electrical interface with its substrate. Silicon and its oxide do not have major toxicological concerns, and are biocompatible (Hoogerwerf & Wise 1994, Williams 1981). Although silicon and its insulating oxide have these desirable qualities, making an electrical connection to the surface of a silicon substrate is not as straightforward as to a metallic substrate, where the application of conductive cement gives a satisfactory bond. The contact to a silicon substrate may result in rectification of signals if the bond is not created correctly. The issues concerning the electrical contact to silicon are described in Section 7.2.3.1. Firstly, the method of oxide production is outlined.

7.2.1 Thermal growth of silicon dioxide

Thermally grown silicon dioxide is used extensively in a large array of microelectronic devices. This has resulted in a large body of research into the growth mechanisms of the oxide. The oxidation process may be done in either dry oxygen or water vapor. Equations 7.1 and 7.2 show these reactions.

$$\text{dry} \qquad Si + O_2 \longrightarrow SiO_2 \tag{7.1}$$

$$\text{wet} \qquad Si + 2H_20 \longrightarrow SiO_2 + 2H_2 \tag{7.2}$$

One of the more widely accepted models for the Si/SiO_2 oxidation process was developed by Deal & Grove (1965). This model assumes that the oxidant is transported from the bulk gas through the oxide layer to the silicon/oxide interface, where it reacts to form new SiO_2. The model involves reactions occurring at both boundaries of the oxide layer, as well as the diffusion

process. The thickness varies with time as in Equation 7.3.

$$x(t) \qquad D\left(\frac{1}{k_s} - \frac{1}{h}\right)\left|\sqrt{1+\frac{8DC^*(t-T)}{\left(\frac{h}{ksh}-\frac{ks}{}\right)2N}}-1\right| \tag{7.3}$$

D Diffusion coefficient of oxidant through oxide

k_s Rate constant of oxidising reaction at interface

h gas transfer coefficient

C* Equilibrium concentration of oxidant in oxide

N Number of O_2 molecules in unit volume of the oxide

τ Offset to account for a pre-existing native oxide layer

Two simplifications of Equation 7.3 can be made. For short oxidation times the equation is the linear relationship

$$x(t) \cong \frac{C^* k_s h(t+\tau)}{N(h-k_s)} \tag{7.4}$$

For longer oxidation times the thickness is given by the parabolic relation

$$x(t) \simeq \sqrt{\frac{2DC^*t}{N}} \tag{7.5}$$

The transition between the linear and parabolic behaviour for the oxide occurs when the -thickness reaches approximately 100 nm (Grovenor 1989). Equations 7.3-7.5 are often collectively referred to as the Deal-Grove or linear-parabolic relationship. The Deal-Grove model is accepted to be accurate for wet oxidation generally, and for dry oxidation above 750°C and with film thicknesses greater than 500 A.

During the oxidation process a 1 μm thick layer of silicon dioxide is produced for every 0.44 μm of silicon consumed (Grovenor 1989, p. 293). The rate determining factor in these reactions is the indiffusion of O_2 (or H_2O)

from the oxide surface to react at the Si/SiO_2 interface. Since the volume increase is localised at this interface, large stresses can occur with very thick films, especially during cooling. Besides temperature and treatment time, the orientation of the silicon wafer can also effect the oxide growth rate (Grovenor 1989, p. 297).

For insulating electrodes used in this thesis, a silicon dioxide layer was produced by heating a silicon wafer for 1 hour at 1000°C; this produced a SiO_2 layer 150 nm thick. The thickness of this layer (and other films produced during testing) was determined using a technique developed for this study, incorporating optical spectroscopy.

7.2.2 Thin film thickness determination using optical spectroscopy

In order to thermally grow silicon dioxide films to a desired thickness, a method of determining the thickness is required. Direct measurement methods such as step profilometry cannot be used, as the SiO_2 film is grown rather than deposited (step profilometry is routinely used for films created using vacuum deposition methods). Due to the hostile environment of the furnace, in-situ monitoring of the thickness is not feasible. Ellipsometry measurements can -provide accurate thickness measurements of multi-layer films (Lu & Cheng 1984, Yamabe & Taniguchi 1985, Naito et al. 1986), but such an instrument was not available at the time of these experiments. X-ray reflectivity can indirectly provide thickness values by fitting curves from theoretical models to the experimental data. However, alignment of the x-ray equipment before use, and lengthy acquisition times makes the use of this technique infeasible to scan more than a handful of samples. As an ellipsometer was not available, an alternative optical method was devised for

measurement of films prepared as part of the experimental studies for this thesis, using a spectrophotometer.

The method to be described involves obtaining the optical reflectivity spectrum of the thermally grown oxide film using a spectrophotometer. The data obtained can be matched to a calculated spectrum, thus giving the thickness of the film. The spectrophotometer obtains the reflectance spectrum by stepping over a range of wavelengths, measuring the intensity at the detector for each wavelength value. The operation of the spectrophotometer is briefly described in Appendix F. The reflectance spectrum is denoted by $R_{sample}(\lambda)$. A theoretical model of the spectrum for the SiO_2 on Si film can be compared to the reflectance spectrum, $R_{sample}(\lambda)$, to determine the thickness of the sample film.

The calculation of the reflectance spectrum requires knowledge of the optical properties of the oxide and the substrate, the wavelengths used, and the thickness of the oxide. In this case the thickness is unknown, thus this parameter is used to obtain the closest fit of the model to the measured reflectance spectrum, $R_{sample}(\lambda)$. The substrate and film can be represented as in Figure 7.1. Note that the indexes nl and n_s are complex, and so are

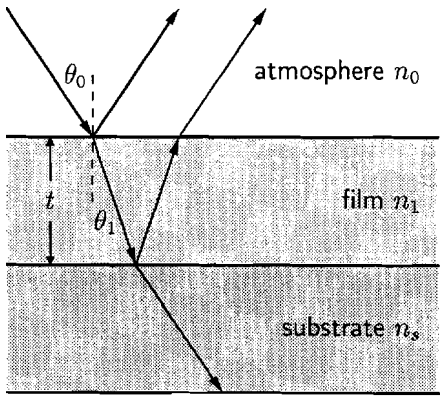

Figure 7.1: Reflectance for a single layer film on substrate

more correctly written

$$\tilde{n}_1 = n_1 + i\ k_1$$

$$\tilde{n}_s = n_s + i\ k_s$$

The index n_0 is air in this case, and so only carries a real unity value. Two reflected beams are shown in Figure 7.1, for two traversals of the thin film, the phase difference between these two reflected waves is

$$\delta = \frac{4\pi}{\lambda} \tilde{n}_1\, t\, \cos\theta_1 \tag{7.6}$$

For the normal case ($\theta_1 = 0^\circ$). The reflectance R is given by

$$R = |r|^2 \tag{7.7}$$

where (see Appendix G),

$$r = \frac{\tilde{n}_1(\tilde{n}_0 - \tilde{n}_s)\cos\delta + i\ (\tilde{n}_0\tilde{n}_s - \tilde{n}_1^2)\sin\delta}{\tilde{n}_1(\tilde{n}_0 + \tilde{n}_s)\cos\ + i\ (\tilde{n}_0\tilde{n}_s + \tilde{n}_1^2)\sin} \tag{7.8}$$

A consideration when forming the mathematical model is that the refractive and absorptive indexes (n,k) vary with wavelength for each material present in the sample. Discrete values of n and k are available from standard texts, such as Palik (1985). For example, Figure 7.2 shows the refractive index (n) for varying with wavelength. To enable fitting of experimental data at wavelengths for which (n,k) is not given, a piecewise continuous function was constructed by interpolating between available data points (the use of a high order polynomial approximation to n and k was investigated but was found to be unsatisfactory). Fitting was done using a recursive linear search on the thickness parameter; the modeling and fitting algorithms were implemented by the author in C code, as this approach offered greater processing speed. Similar methods using spectrophotometer to obtain silicon

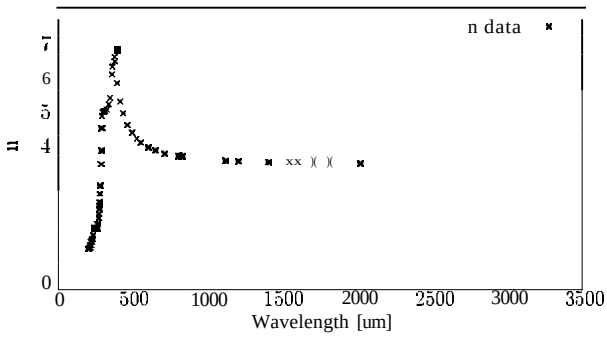

Figure 7.2: Data for *n* of silicon (raw data from Palik (1985)).

dioxide thickness have been applied by Reizman (1965) and Barrick (1971), who used minima/maxima pair(s) from the reflectance spectrum to estimate thickness, rather than fitting the entire spectrum as described here.

7.2.2.1 Results

To verify the accuracy of the oxide thickness determination method described in Section 7.2.2, three films consisting of SiO_2 on a Si substrate were prepared using E-beam vacuum deposition. This method is more time consuming and complex than using thermal oxidation, but it allows the use of step profilometry, and thus samples with films of a known thickness can be used to verify the usefulness of the optical measurement technique. The three films manufactured the E-beam were 550 Å, 2400 Å and 4400 Å in thickness, respectively. Reflectance spectra for the three SiO_2 films were obtained using the spectrophotometer. The thickness value, *t,* which gave the best fitting theoretical reflectance spectra (calculated using Equations 7.7 and 7.8) were found. The experimental and the best fit theoretical reflectance spectra are shown in Figure 7.3.

The results show that the use of reflectance spectra of silicon dioxide for

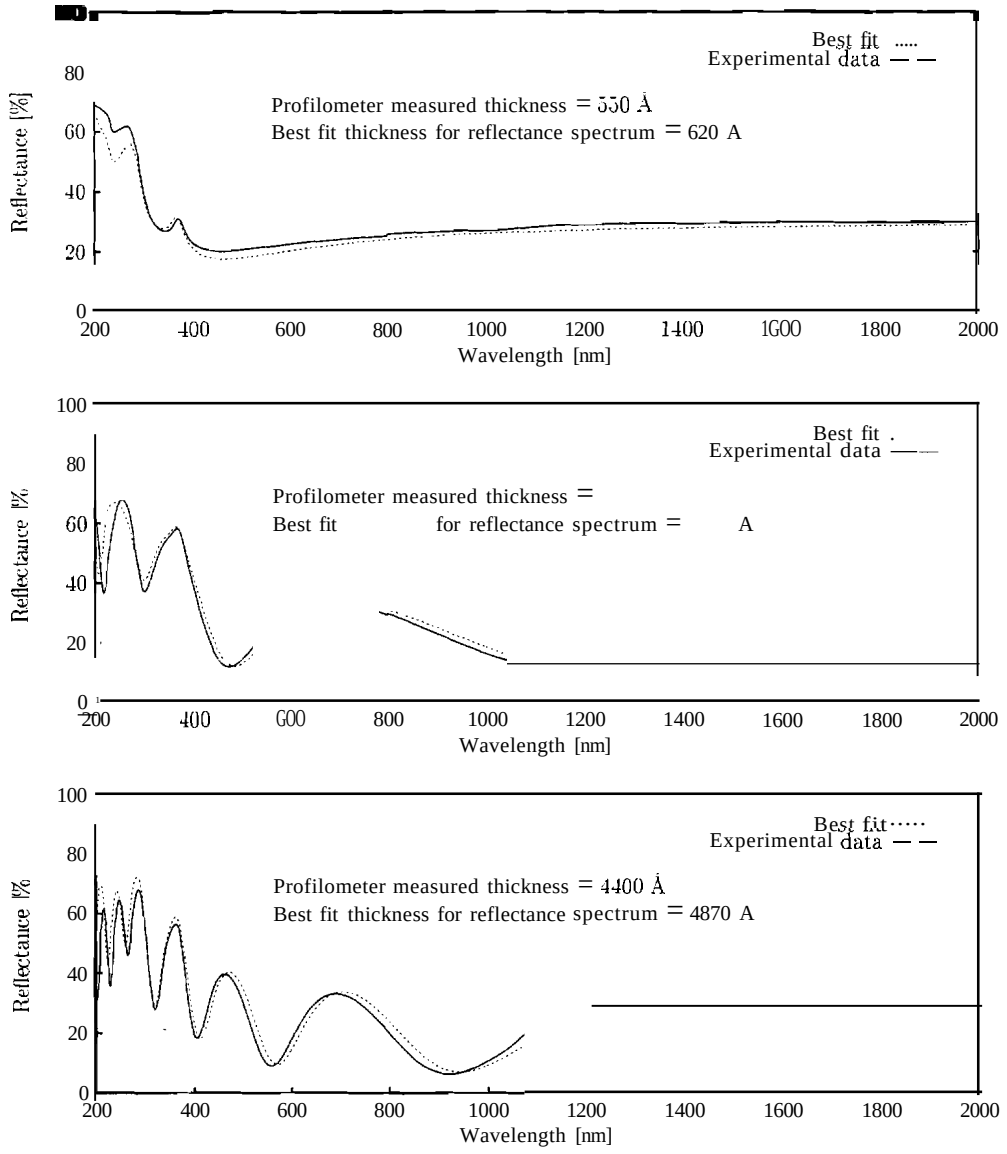

Figure 7.3: Experimental data and best fits for reflectance spectra of $Si0_2$ on Si substrate, showing three different thicknesses of $Si0_2$.

oxide thickness determination gives values which average to within 10% of those obtained using profilometry. These are regarded as satisfactory for the purposes of this studyl.

7.2.3 Metal-semiconductor heterojunctions

Making ohmic contact to a silicon substrate is more challenging than making a good electrical contact to a metal. The join between a metal and a semiconductor has characteristics which need to be understood before the join can be made, so that an ohmic contact can be created, rather than a rectifying one. First, conditions that lead to the formation of a rectifying contact will be covered.

7.2.3.1 Rectifying contacts

When a metal is brought into contact with an extrinsic (doped) semiconductor, the connection is not ohmic, but may form a rectifying contact known as a Schottky barrier diode. The transport mechanisms and electrical behaviour in such a metal-semiconductor (heterogeneous) diode are different to that in a p-n (homogeneous) semiconductor diode. As an example consider, an n-type semiconductor (with a work function of ϕ_s) and a metal (with a work function of ϕ_m). Figure 7.4(a) shows the metal and semiconductor before joining when $\phi_m > \phi_s$. The vacuum level is used as a reference point. Figure 7.4(b) shows the junction once the two materials are joined. To make the fermi levels[2] equal throughout the system, electrons flow from

[1]It should also be noted that the optical constants of E-beam deposited oxide may vary from that of thermally grown oxide

[2]The energy level at which half of the possible energy levels in a band are occupied by electrons.

ϕ_m metal work function

ϕ_s semiconductor work function

ϕ_{Bn} Schottky barrier

ψ electron affinity

E_f fermi level

E_c conduction band

E_v valence band

assume $\phi_m > \phi_s$

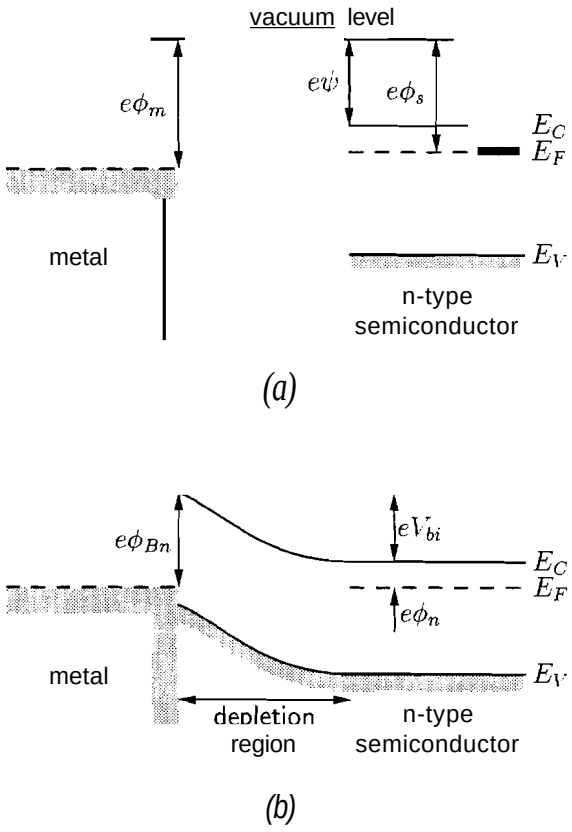

Figure 7.4: (a) The metal and semiconductor before being joined, and (b) the heterojunction after joining

the semiconductor into the metal. In the metal the electrons fill lower energy states while positively charged donor atoms remain in the semiconductor, creating a charge space region. The barrier height seen by electrons in the metal trying to move into the semiconductor is ϕ_{Bn}, given by $\phi_{Bn} = \phi_m - \psi$. This barrier is called the Schottky barrier. Similarly, on the semiconductor side, the potential barrier is V_{bi}. If a positive voltage V_A is applied to the semiconductor with respect to the metal the semiconductor barrier height V_{bi} is increased by V_A: this is the reverse bias case. The electrons in the reverse bias case need to overcome the Schottky barrier ϕ_{Bn} (which remains unchanged). Conversely, if a positive voltage is applied to the metal with respect to the semiconductor, the semiconductor-to-metal barrier decreases by V_A, allowing easier flow of electrons from the semiconductor to the metal. The value of ϕ_{Bn} is again unchanged. This is the forward bias condition.

1.2.4 Ohmic contacts

Ohmic contacts can be grouped into two categories: the ideal non-rectifying barrier, and the tunneling barrier. A heterojunction where $\phi_m > \phi_s$ (for an n-type semiconductor), will result in a rectifying contact. If a different metal and/or n-type semiconductor combination is used such that $\phi_m < \phi_s$, an ohmic, rather a rectifying contact will be produced[3]. When the metal and semiconductor are joined in this scenario, electrons flow from the metal into the semiconductor, making the surface of the semiconductor more n-type (Neamen 1997, p. 326) shown in Figure 7.5. If a positive voltage is applied to the metal with respect to the semiconductor, there is no barrier to stop the electrons flowing from the semiconductor to the metal. If a positive voltage

3If p-type semiconductor is used, the $\phi_m < \phi_s$ case will give a rectifying contact, while materials with $\phi_m > \phi_s$ will form an ohmic contact.

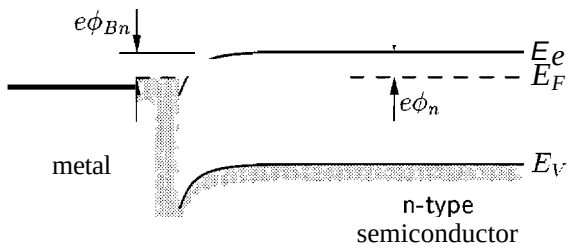

Figure 7.5: Ohmic heterojunction

is applied to the semiconductor with respect to the metal, the barrier height seen by electrons in the metal is ϕ_n, which will be small for a moderately doped semiconductor. This is an ideal non-rectifying, or ideal ohmic, contact.

In practice, surface states alter this ideal model, and consequently ohmic contacts of this definition with a perfect I-V characteristic are rare (one exception is the contact between indium and n-type cadmium sulphide). Since a metal does not generally exist with a low enough work function to yield a low ϕ_n barrier (Sze 1981, p. 306), a variety of techniques have been developed to force materials to approximate an ideal ohmic contact, most of which involve using a heavily doped surface layer. As the doping in the semiconductor surface increases the width of the depletion region decreases, and thus the probability of tunneling through the barrier rises until it becomes the dominant current mechanism. This is shown in Figure 7.6. One way to

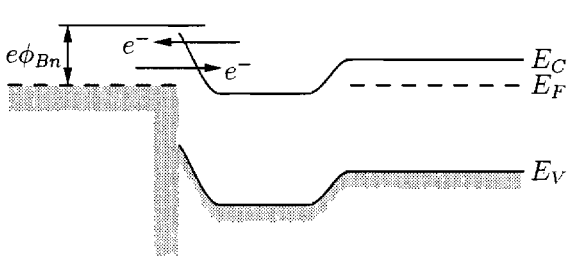

Figure 7.6: A pseudo-ohmic tunneling heterojunction

achieve this heavy surface doping is to in-diffuse aluminium into a p-type

silicon substrate by applying a heat treatment. The aluminium acts as the p-type dopant and the contact resistance that results from the tunneling mechanism is of the order of 10^{-6} Ωcm^{-2} (varies depending on fabrication method). Another initial advantage of this process is that the aluminium will decompose locally any silicon dioxide on the silicon surface, whether this is the native oxide layer or was produced by other means. Thus, for silicon-aluminium heterojunctions there are two practical possibilities: Al on n-type silicon (lightly doped) will give a Schottky diode with barrier 0.7 eV, while Al on p-type silicon (heat treated) will result in Pseudo-ohmic contact with barrier 0.4 eV. Thus for this study p-type silicon wafers were used.

Experiments conducted for this thesis have found that heating the silicon in contact with aluminium in an oven at a temperature of 620° for 20 minutes results in a good ohmic contact. The aluminium used is in the form of wire (99.9% AI) which has been flattened. At higher temperatures the in-diffusion of aluminium is excessive, and in extreme cases the molten metal eventually diffuses to the opposite side of the wafer. This heat treatment does not cause any appreciable silicon dioxide accumulation, as the growth rate at these temperatures is less than lA/hour (Lee et al. 1993).

The production of silicon dioxide films and the preparation of reliable ohmic contacts, as described here, allows for the development of capacitive electrodes and permits comparison of these electrodes with the conventional wet and dry types. The comparison of wet, dry and insulating electrode types is detailed in Section 7.3.

7.3 A comparison of wet, dry and insulating electrode types

Sections 7.3.1 to 7.3.3 consider experimental data relating to the major concerns for electrode use, as introduced in Section 7.1. Section 7.3.1 examines the temporal change in contact impedance for a number of electrodes. Section 7.3.2 describes the effect of non-stationary charged bodies near recording electrodes. Section 7.3.3 quantifies the effect of electrode movement artifact on the three electrode types. This work has been reported in Searle & Kirkup (2000).

During experiments where signals were recorded from the electrodes (in Sections 7.3.2 and 7.3.3), the dry and insulating electrodes incorporated active buffers, whereas the wet electrodes did not. This reflects the 'way each electrode design is normally used. *Agj*Agel electrodes are consistently used "as is" (with the exception of Fernandez & Pallas-Areny (1996), and Iguchi et al. (1994)), whereas dry and insulating electrodes are rarely used without buffering, for reasons outlined in Sections 6.3 and 6.6. No skin preparation was done before the trials, as cleaning the skin would introduce another experimental variable which cannot be easily controlled or quantified. Additionally, this reflects an environment where the electrodes are used by a person or carer, in a way which is consistent with requirements that such electrodes to be quick and easy to apply. For all waveform recording a data acquisition card (sampling rate 5 kHz) was used with the Labview programming language, along with pre-amplification and antialiasing low pass filters (10th order, f_{3dB} = 1 kHz). The input impedance of instrumentation amplifiers utilised was 10^{10} Ω.

7.3.1 Temporal dependence of contact impedance

The influence of electrode/skin contact impedance has been described in Section 6.3 and an additional illustrative example shown in Section 6.6. This section examines the influence of electrode construction on contact impedance by monitoring the contact impedance of four different electrodes simultaneously. The four electrode pairs were compared over time when applied to the forearm (posterior surface oflower arm). These measurements include the bulk tissue impedance that exists between the electrode pairs, but as this can be considered equivalent for all electrode pairs, a fair comparison can be made. Insulating electrodes were not included in this experiment as the mechanism of signal sensing does not rely on ohmic contact. Although the issue of skin/electrode impedance would seem to be irrelevant when active buffers are employed, the initial decrease shown in the RMS interference of the dry-active electrode pair, as indicated in Figure 6.23(p. 222), suggests that the electrode to skin interface still deserves attention.

7.3.1.1 Experiment

The four types of electrodes used were stainless steel, titanium, aluminium, and disposable Red Dot™ 2258 Ag/AgCI ECG electrodes. The metals were chosen for their _biocompatibility, and/or their use in previously published reports. The three pairs of metal electrodes (all 12 mm diameter) were mounted together on a plastic assembly with 14 mm between their centres. This assembly was held in place on the forearm with a Velcro strap, as shown in Figure 7.7. The Ag/AgCl electrodes were placed adjacent to the dry electrodes so that the same distance (14 mm) separated their centres. The contact area of the Ag/AgCl electrodes is the same (assuming that the saline gel does not smear) as for the metal electrodes. Using the technique

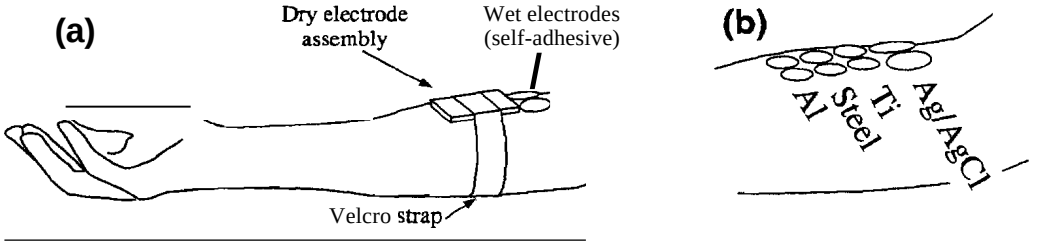

Figure 7.7: (a) Location on the forearm of wet electrodes, and of the assembly containing the three dry electrode pairs. (b) Cutaway showing relative positions of electrodes.

described in Section 6.5 (Searle & Kirkup 1999), the impedance between each pair of electrodes was recorded over 20 minutes. It is not possible to monitor the impedance of all four electrode pairs at exactly the same time due to the close proximity of the electrodes; the potential difference due to current injected to one electrode pair will be present at other electrodes sites, thus the impedance contributions from each site cannot be separated. As the impedance for all pairs could not be monitored at the same time, a multiplexing system was designed and constructed to apply the stimulating current (peak value 500 nA) to each electrode pair alternately. The multiplexing circuitry is shown in Figure 7.8. The switch positions (implemented using a MAX313 analogue switch) were controlled by digital outputs from the Labview program. The impedance of the analogue switches is accounted for during the calibration of the impedance spectroscopy system (as described in Section 6.5.2.2). Using the multiplexing circuits, the impedance for all electrodes (at 20 frequency values, over a range of 1-950 Hz) was recorded every 12.8 seconds. Only data for impedances at 57 Hz will be presented here for the five subjects used (ages $\bar{x}$=28.4 yr, s_x=9.0 yr). While impedance values recorded here are useful for comparing the relative performance of electrodes,

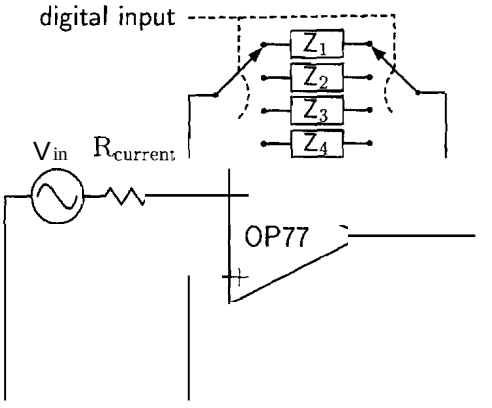

Figure 7.8: Operation of multiplexing device to monitor the contact impedances (Z_{1-4}) for four electrode pairs.

the individual values obtained will vary with electrode location, size, excitation frequency and excitation current (Onaral & Schwan 1982, Yamamoto & Yamamoto 1981).

7.3.1.2 Results

Figures 7.9(a-d) show the averaged impedance change with time for the four electrode pairs, along with the minimum and maximum values for the five subjects. Figure 7.10 presents the average curves on one plot; all data sets display a similar shape as the buildup of perspiration reduces the contact impedance. All the curves representing the reduction of contact impedance over time shown in Figure 7.9 and 7.10 can be shown to exhibit a polyexponential relationship between impedance and time, as described in Section 6.6.

As anticipated, the *Agj*Agel pair had a considerably lower contact impedance, though time is still required for the electrode impedances to settle to a constant value. All three pairs of dry electrodes converge to approximately the same value with time. None of the dry electrode pairs have impedance values which show a statistically significant difference to any other pair

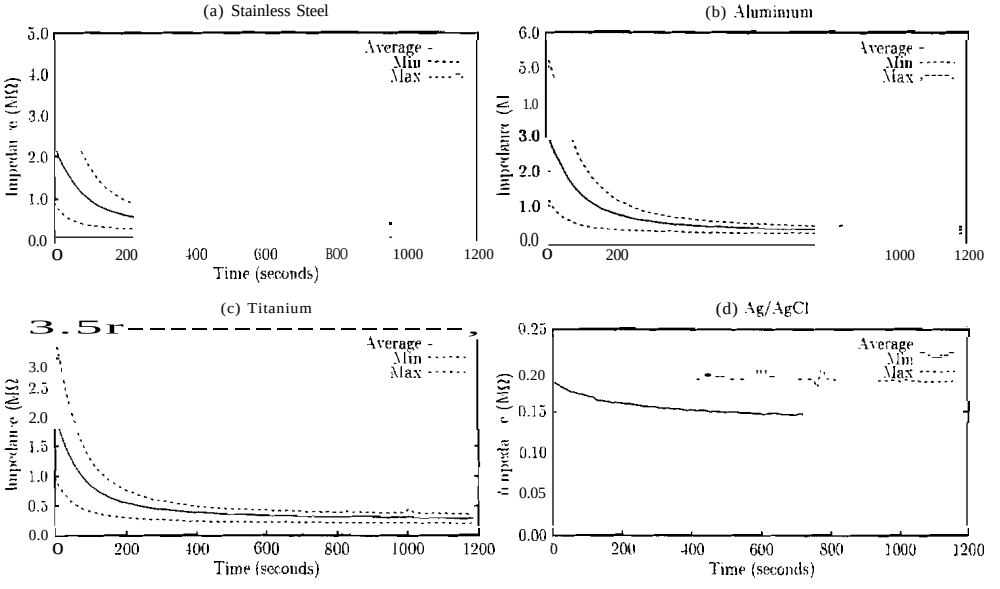

Figure 7.9: Contact impedance vs time for four electrode pairs, averaged over five subjects. These plots also show minimum and maximum data sets for each electrode type.

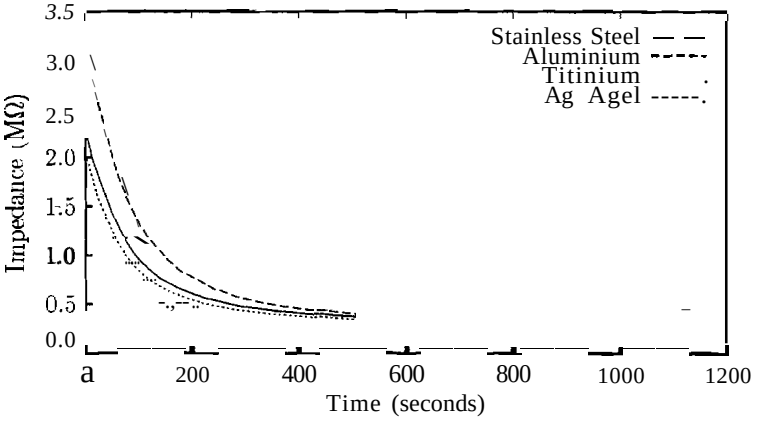

Figure 7.10: Contact impedance vs time for four electrode types, averaged over five subjects.

(using two tailed t tests at $p<0.05$). The electrode positions on the arm (Figure 7.7(b)) will have some effect on the impedance values measured, especially the relative values of the three dry electrode pairs. The important finding from the data in Figures 7.9 and 7.10 is that the differences between each of the dry electrode impedances is small (and not significant) when compared to the variation between subjects. The data recorded for a single subject (male, age 27) over five days shows a similar trend: the diurnal variation was much larger than the difference between the three metals in any one recording.

7.3.2 Charge sensitivity of electrodes

A major problem noted previously for dry and insulating electrodes is the charge sensitivity of the devices due to their very high input impedance, especially with insulating types, as described in Section 6.3.1.3. The experiments in this section were designed to investigate the effect of an electrically charged object moving near wet, dry and insulating electrodes, and the effectiveness of shielding used around these electrodes.

7.3.2.1 Experiment

To allow the continual and reproducible creation of a time-varying electric field, the following experiment was devised. Three pairs of electrodes were used;

1. one pair Red *Dot*™ AgjAgel electrodes.
2. one pair dry stainless steel (11 mm diameter) buffered using OPA132 op-amps.

3. one pair of insulating electrodes constructed from a high purity silicon wafer, with a 150 nm layer of silicon dioxide grown thermally (1000°C in air for 1 hour, as described in Section 7.2), buffered using OPA132 op-amps. Each insulating electrode was 9 mmx8 mm.

The insulating and dry electrodes were mounted flush on a plastic plate, and contained in the same housing (50 mm x 60 mm). The housing was built in such a way that the back casing was interchangeable between plastic and steel (grounded), so that the effects of shielding the electrodes could be observed. The electrodes were placed on the arm as shown in Figure 7.11. The wet electrode pair was not buffered, but the cables were shielded up to

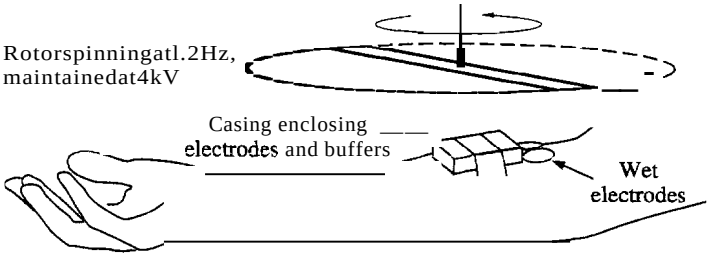

Figure 7.11: Experimental arrangement for charge sensitivity tests. The rotor was moved along the arm in a distal direction.

the alligator clips used for attachment; this shielding arrangement is typical use for AgjAgCI electrodes in a clinical environment (Wan & Nguyen 1994). The moving charge was supplied by a metal strip (32 cm long) connected to a small gearbox, such that it acted as a rotor. The frequency of rotation was set to 1.2 Hz (the frequency of rotation was monitored by an optical gate). The rotor was maintained at a voltage of 4 kV by a high voltage supply, in series with 150 MΩ so that negligible current would flow if accidental contact occurred between rotor and arm. A value of 4 kV is not unusually high, as

walking on carpet can generate a potential of tens of kilovolts on the body with respect to ground (Elliott & Gianetti 1995). The rotor was adjusted so that it was 70 mm above the electrodes, and the wrist supported such that the electrodes sat horizontally. A period of 15 minutes was allowed to elapse before measurements were taken so that the three pairs of electrodes had time to settle to steady state contact impedance levels. This is done so that changes in interference levels may be related to differences in shielding used, and not to variations in contact impedance. The rotor was moved slowly along the arm, so that all electrode pairs experienced a point where the electrical interference due to the charged rotating strip was a maximum. Without moving the dry/insulating electrode housing from the arm, the back casing was changed from plastic to steel (electrically grounded), and the rotor arrangement was moved slowly along the arm again.

7.3.2.2 Results

The maximum interference signal observed for each electrode type for the shielded and unshielded situations was extracted from each data record and averaged. The results are shown in Figure 7.12. The insulating electrodes showed more interference than the dry pair when unshielded. For both dry and insulating electrode pairs, the use of a grounded shield reduced the interference significantly. However, it was not anticipated that the interference levels for wet electrodes would be comparable to, or higher, than that for the dry and insulated electrodes in the unshielded case. The average interference reduction achieved by using shielding was 26 dB for dry electrodes, and 32 dB for the insulating electrodes. When compared to the wet electrodes, the interference levels experienced were 40 dB and 34 dB lower for shielded dry and insulating electrodes respectively.

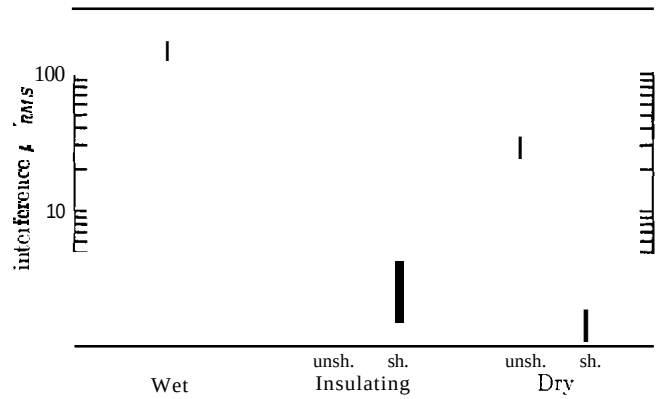

Figure 7.12: RMS interference resulting from a moving, charged rotor near three electrode types: wet, dry and insulating. The dry and insulating types were tested whilst (unsh)ielded and (sh)ielded. Bars represent standard error of the mean for the five subjects.

7.3.3 Effect of electrode movement

To enable reproducible motion of electrodes, a mechanical device which oscillates at a predictable rate was attached to the three pairs of electrodes under test.

7.3.3.1 Experiment

A solenoid with a small mass attached to its bore was encased in a metal shield and fixed to the back of the electrode case which housed the dry and insulating electrodes (described in Section 7.3.2.1). As shown in Figure 7.13, the wet electrodes (held to the arm by their self-adhesive) were connected rigidly to the housing via their snap connectors by a plastic template so that all three electrode pairs vibrate together. The total mass of the bore was 37 g, and the stroke length was 10 mm. The solenoid was set to oscillate in a direction parallel to the arm at a frequency of 5 Hz, and the RMS voltage

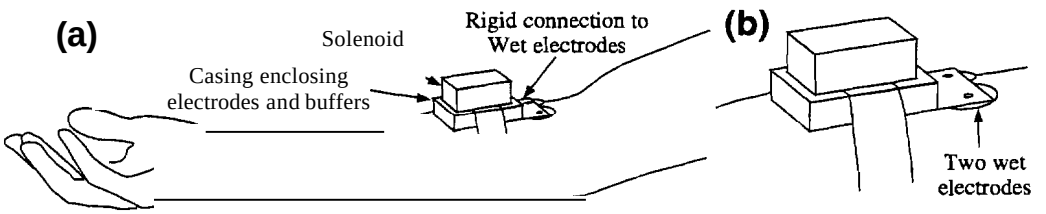

Figure 7.13: (a) Experimental arrangement for electrode movement artifact tests with (b) closeup of rigid connection to wet electrodes.

produced at this frequency was recorded over 15 minutes. Recording was done from the moment of electrode application to the forearm (posterior surface of the lower arm). A baseline recording was taken initially with the solenoid detached from, but still adjacent to, the electrode casing to ensure that signals recorded were not due to electromagnetic interference generated at the solenoid coil.

7.3.3.2 Results

Figure 7.14 shows artifact levels at the start and end of the trial. Artifact signals apparent in this test came from two sources; disruption of the electrode/skin interface and skin potential artifact. These sources are summarised below.

The mechanism for electrode/skin interface disruption differs depending on whether the signal path is ohmic or not. For wet and dry electrodes disturbance of the double layer region at the electrode/skin (or more precisely the electrode/electrolyte) interface causes unwanted signals, as described in Section 5.2.4. For insulating electrodes, bioelectric signals are capacitively coupled from the hydrated tissue beneath dry layers of skin (this effectively forms the other 'plate' of the capacitor). Variation in the separation of the

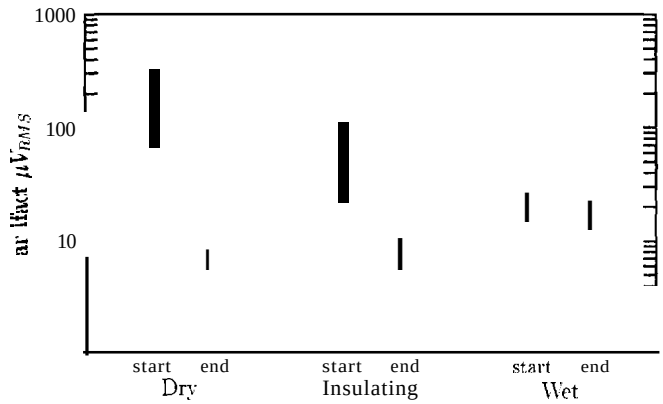

Figure 7.14: 5 Hz RMS artifact caused by vibration of three electrodes types: wet, dry and insulating. The artifact levels are shown for the start and end of the 15 minute recording interval. Chart shows averages and standard error of the mean for 5 subjects.

two plates of this capacitor causes an artifact signal, as outlined in Section 5.4.3.

The skin potential artifact (also known as the skin-stretch artifact or skin-motion artifact) arises from the change in voltage between the inner and outer layers of the skin under deformation. Skin movement can produce a change in potential at the skin surface of several millivolts (refer Section 1.3).

Figure 7.14 indicates that dry and insulating electrodes show a significant drop in the artifact suffered over the length of the trial, whereas the RMS voltage from the wet electrodes was relatively unchanged. The final artifact values for all electrode types are a combination of electrode/skin interface disturbance and skin potentials, whereas the decrease apparent in the dry and insulating electrodes is due principally to a reduction in skin/electrode interface effects. Though it has been shown that there is a slight reduction in skin potential artifact in repetitive tests (de Talhouet & Webster 1996), the large reduction in artifact with time for dry and insulating electrodes is more

likely to be due to the accumulation of perspiration under the electrodes. As perspiration builds up and hydrates the dry skin layer, the effective dielectric thickness in the insulating electrode 'capacitor' reduces. Accordingly, the effect of the change in this distance is also reduced which in turn lowers artifact levels (Geddes & Baker 1989). For dry electrodes, artifacts arise from the disturbance of the double layer region at the electrode surface. The effect of perspiration buildup is to act as a physical "shock absorber". This is similar to, but less effective than, the action of gel used in wet electrode types. Artifact for dry and insulating types also reduces over time because the electrodes and their housing will tend to adhere to the skin as perspiration accumulates, reducing the relative movement between skin and electrode surfaces in the local area.

Higher initial artifact levels shown in Figure 7.14 for dry electrodes compared to insulating types indicates that the disruption of the double layer region at the stainless steel/skin interface generates a greater signal from electrochemical means than arises from changes in the effective dielectric thickness in the insulating electrodes. Artifact levels for wet electrode types vary little, as would be expected, over the recording period. A more interesting and unexpected result is that this wet artifact level was higher than that for the final artifact levels for dry and insulating electrode types (final dry and insulating values are lower compared to final wet values with significance levels of $p = 0.09$ and $p = 0.13$ respectively). While initial RMS artifact values for dry and insulating electrodes were 20 dB and 11 dB higher than wet electrodes respectively, final values were 8.2 dB and 6.8 dB lower. This outcome may be attributed to the larger contact area of the case which houses the dry and insulating electrodes compared to the wet types. The dry and insulating electrode pairs are mounted flush on a plastic plate which, coupled

with adhesion due to perspiration, distributes the skin disturbance further from the sensing sites, lessening the artifact experienced. The contact area[4] for a wet electrode (including adhesive skirt) is less by a factor of 4 than the dry and insulating electrode housing, thus the skin potential artifact occurs closer to the sensing site for the wet electrodes. This suggestion that electrode geometry has an effect on the amount of skin potential artifact experienced has been explored previously by Odman (1982).

7.3.4 Discussion

In the study described in this chapter all three electrode types showed variable performance with no one type consistently performing 'best' in all circumstances. In summary,

Wet electrodes suffered from moving charge artifact more than the dry and insulating electrodes types (RMS interference was up to 100 times more for wet electrodes than for the other two electrode types when shielding was used). In movement tests the artifact experienced by wet electrodes varied little over the 15 minute trial period, and proved superior to dry and insulating pairs at the commencement of the trials. Notably, in the latter stages of the trials, the wet electrodes experienced more artifact than dry and insulating types, though this may be dependent on the geometry of the dry/insulating electrode housing. The contact impedance of wet electrodes was consistently half that of the metals tested.

4This is not the electrical contact area, but rather the total area of the electrode which contacts the skin. This includes the adhesive skirt (for wet electrodes) and plastic mounting plate (for dry and insulating electrodes).

Dry electrodes were least affected by moving electric charge when shielding was not employed, and showed a large reduction when shielding was in place, with the RMS interference falling by 26 dB. **In** movement artifact tests the dry type initially fared worst compared to wet and insulating types, but after this settling time they performed marginally better than the insulating and wet types. Again, this will change with electrode geometry. Contact impedances of the three metals tested for dry electrode use (stainless steel, titanium and aluminium) showed a decrease over time of a reproducible shape. The average difference between the performance of the three metals was not significant when the deviation between different subjects (or between consecutive tests on a single subject) was considered. After settling, all three metal electrodes displayed approximately the same average contact impedance values, being double that of wet electrode types. For future studies, stainless steel (which is more commonly available than titanium) is preferable to aluminium, which has been shown to have problems due to the chemical response of its oxide to perspiration (Taheri et al. 1994, Luca et al. 1979, Potter & Menke 1970).

Insulating electrodes used without shielding were influenced by moving electric charge more than the dry electrode type, but not to the same degree as wet electrodes. As with the dry electrodes, this interference was reduced effectively by the use of a shield (RMS interference decreasing by 32 dB). Tests for movement artifact with insulating electrodes showed high initial RMS levels (still comparable to dry types) which reduced with time. The RMS artifact experienced fell between that for dry and wet electrode types after some initial time had past, and this contrasts with several reports in the literature (Bergey

et al. 1971, Richardson et al. 1968) which indicate more severe movement artifact problems with insulating electrodes.

Concerns that movement artifact and charge induced interference would effectively disable dry and insulating electrodes have not been supported by the experiments conducted for this thesis. The dry and insulating types generally performed in a manner comparable to, or better than wet electrodes. Movement artifact for dry and insulating electrodes was initially higher than that for wet types, but reduced over time to levels less than that for wet electrodes. Such a result may be dependent on the geometry and size of the dry/insulating electrodes. The use of shielding for dry and insulating electrode types dramatically reduces the interference from moving electric charge to levels far below that experienced by wet types.

7.4 Example data for bioelectric recording

Some illustrative examples of bioelectric data obtained using dry, insulating and wet electrodes are shown in Figure 7.15. The electrodes used were

one pair Red Dot^{TM} Ag/AgCI electrodes.

one pair dry stainless steel electrodes. These were constructed using Bpring-Ioaded probes with a rounded stainless steel tip of diameter 1.3 mm. The probes were mounted on (but insulated from) a grounded metal casing such that the tip of the probe retracted flush with the case when force was applied. OPA132 op-amps were used inside the casing to buffer the signal.

one pair of insulating electrodes constructed from a high purity silicon wafer, with a 150 nm layer of silicon dioxide grown thermally (lOOODC in air for 1 hour, as described in Section 7.2).

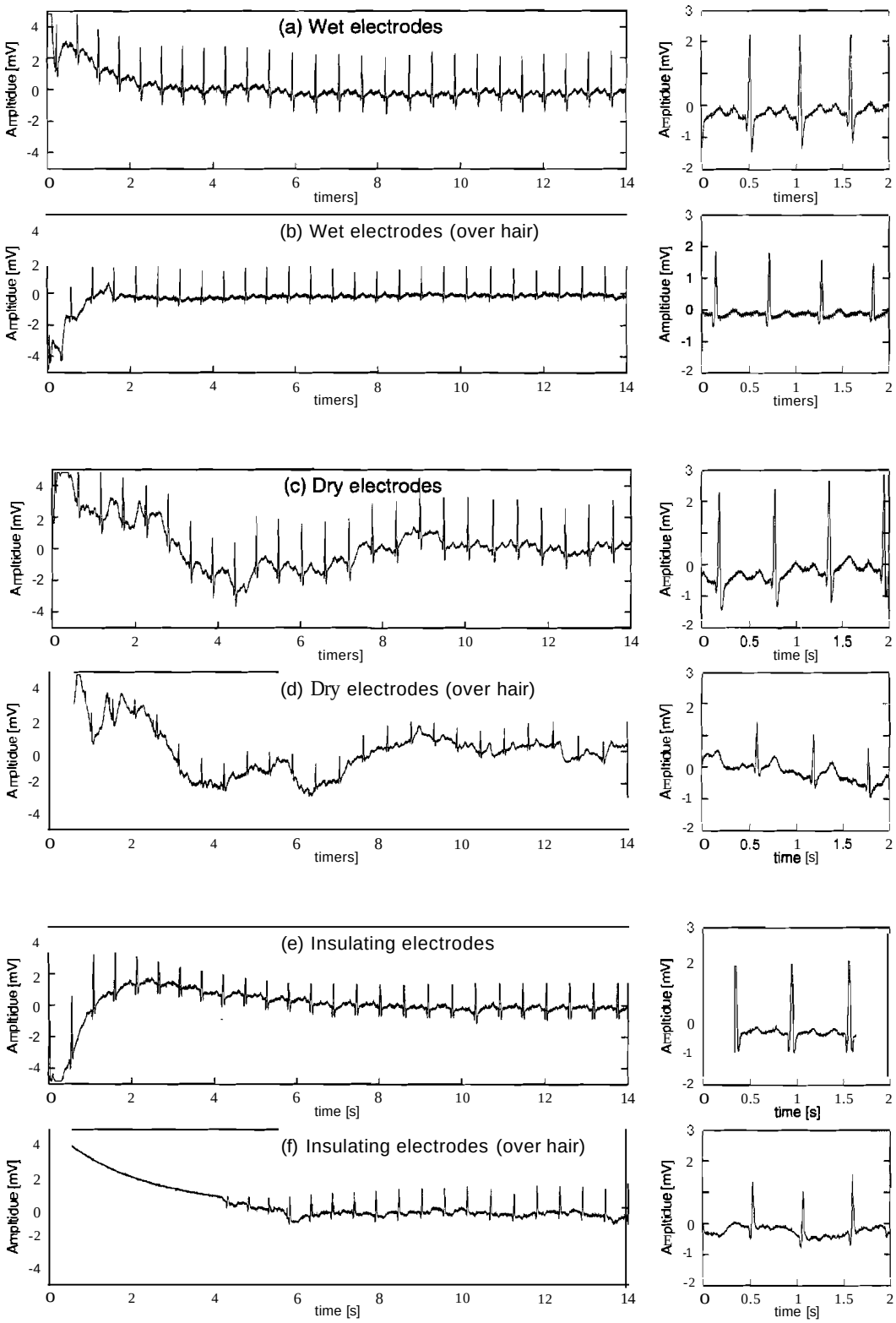

Figure 7.15: ECG recordings for wet (a,b), dry (c,d) and insulating (d,e) electrodes from one subject. Recordings were done on the chest in areas with and without hair for comparison of performance. 2 s of detail for each

As with the dry electrodes, the silicon wafer was held on (but insulated from) a grounded metal casing. OPA132 op-amps were used inside the casing to buffer the signal. The sensing area for each insulating electrode was 9 mmx8 mm.

ECG signals were recorded using the three sets of electrodes held firmly on the chest. Each pair of electrodes were applied to the same subject (male, age 27) in two different positions on the chest, such that both electrodes were placed over hair, then in positions where no hair was present. The same sets of positions were repeated for wet, dry and insulating electrodes. A ground electrode (AgjAgCl) was placed on the wrist, no shielding of cables or 'driven right leg' circuitry were used. The metal casing of the electrodes were covered in plastic, so that the grounded shields would not make ohmic contact with the skin, in accordance with shielding guidelines described in Section 5.4.1. The signals were recorded the moment of application to the chest, as shown in Figure 7.15. Two seconds of detail for each recording are also displayed in Figure 7.15. The signals obtained are not intended for ECG analysis, but rather to indicate the characteristics of the electrode types. The baseline for the signals from the wet electrode pair settles quickly for the positions over hair (Figure 7.15(b)) and without hair (Figure 7.15(a)). The ECG characteristics are visible almost immediately. The signals from dry electrodes shown in Figure 7.15(c-d) display a variable baseline which does not settle after 14 s, although the features of the EeG trace are discernible. The signals recorded from positions over hair, and in the region without hair do not differ greatly. This variability in the baseline is due the the very small surface area of the electrodes. Comparisons with dry electrodes of larger contact area has shown that the spring-loaded electrodes are more susceptible to movement than electrodes with a large, flat surface area.

Insulating electrodes produced satisfactory recordings, though the baseline takes longer to settle when compared to wet electrodes. When the electrodes are placed over hair (Figure 7.15(f)) the ECG trace takes some time to become visible while the instrumentation amplifier is saturated. Additionally, the baseline for the insulating electrodes over hair is more variable than for electrode positions where no hair is present.

Experiments with EEG signals using dry and insulating electrodes have shown results with characteristics resembling those displayed in Figure 7.15, but the problems experienced with EEG recordings were more severe. The EEG signals were severely affected by presence of hair in the recording area, especially for insulating electrodes. The signals for dry electrodes showed extreme variability in baselines, such that useable signals could not be obtained. This reveals a problematic tradeoff with dry and insulating electrodes: in order to obtain bioelectric signals free from movement artifact, electrodes with sufficient contact area are required (to avoid signals such as those from the dry electrodes used for Figure 7.15(c-d)). However, larger contact area means that hair in the recording area becomes a problem, as experienced by the insulating electrodes (and in experiments by Taheri et al. (1994)). At the conclusion of these studies the dry and insulating electrodes did not enable reliable, high fidelity recordings with EEG signals. The examples of ECG signals show that these electrode are capable of detecting bioelectric signals with good characteristics, however more work on the mechanical design for such electrodes is required before their continued use in the EEG recording field.

7.5 Conclusion

This chapter examined the performance of three electrode types simultaneously and in a controlled test environment, so that meaningful quantitative comparisons could be made for the first time. The design and manufacture of insulating electrodes by thermal growth of silicon dioxide (as outlined in Section 7.2), along with methods to create an ohmic contact with the silicon substrate, provide useable electrodes with comparable performance to dry and wet electrodes. The details of a procedure which was developed to determine the oxide film thickness was described in Section 7.2.2.

The study of the comparative performance of wet, dry and insulating electrodes in Section 7.3 revealed that no single electrode consistently gave the best result on tests conducted to study contact impedance, artifacts from electrode movement and the effects of electric fields. **In** contrast to some previously published reports, dry and insulating electrodes showed better performance compared to wet types in some circumstances. Work for this comparative study can be found in the literature (Searle & Kirkup 2000). Finally, Section 7.4 showed illustrative examples of bioelectric signals obtained using wet, dry and insulating electrodes, which indicates that all three electrode types are a viable option for ECG recording.

The work conducted for this thesis involving wet, dry and insulating electrodes has shown that all electrode types can offer good signal fidelity for biosignal use. When dry and insulating electrode contact areas are of reasonable size, good signals are obtained, thus all electrodes are suitable for use with ECG and EMG signals. The use of electrodes with smaller contact area can lead to baseline variability.

Although their performance is comparable to dry electrodes, insulating electrodes require extra fabrication, whereas dry electrodes are mechanically

simple. This means that dry electrode types are preferable for biosensing applications, as demonstrated by the number of recent ECG studies using dry electrodes (Burke & Gleeson 2000, Griss et al. 2000, MettingVanRijn et al. 1996). By contrast, reports of studies using capacitive electrodes are now rare (the last literature found is by Taheri et al. (1995)). For dry and insulating electrode use with EEG, the presence of hair leads to signal degradation. This is especially apparent with insulating electrode types, making them less suitable for EEG use. The small electrode size required to avoid hair-related problems can lead to artifacts from electrode movement. For EEG applications using dry electrodes, the physical stability of electrodes is of concern, and further work on dry electrodes for EEG use will need to give this aspect serious consideration.

The dominance of wet electrodes in clinical settings will most likely remain unchallenged by dry and insulating types for a number of reasons: wet electrodes are simple and lightweight, and each requires only one lead. Dry and insulating types require circuitry for buffers, and extra cables for power, which adds bulk and weight (although surface mount and VLSI technology (Padmadinata et al. 1990) means that this consideration is becoming less important). Additionally, the availability, relative cheapness and disposability of wet electrodes overcomes hygiene concerns, and initial contact impedances are sufficiently low to allow good recordings. However, in specialist domains such as long-term, unsupervised monitoring and spatially dense recordings, insulating and dry (especially) electrodes can offer benefits over wet electrode technology. There remains problems when applying such electrodes to EEG signals, such as the tradeoff between sensor contact area and obstruction by the presence of hair, as described in Section 7.4. Because of this, the physical construction details of an EEG electrode will be as important as the type

(wet dry or insulating) utilised.

Chapter 8

Summary, conclusions and suggestions for further work

The research presented in this thesis has investigated issues which involve the detection of alpha EEG synchronisation that occurs following eye closure for purposes of environmental control. The research has focused on aspects crucial to the utilisation of the alpha rhythm in an environmental control system which could be used by, for example, disabled persons. These were (i) the effectiveness of signal processing algorithms, and (ii) the utilisation of surface electrodes for biosignal sensing. Conclusions follow relevant to each research based chapter in this thesis.

Chapter 2

The application of alpha waves to assistive technology has been the focus of many research projects. To date there has been little attention directed to the choice and optimisation of detection algorithms for use in an unconstrained operating environment, Le. an environment in which subjects are allowed freedom of movement. Additionally, there is a lack of data concerning

the performance of alpha EEG detection methods in the presence of artifact signals.

Chapter 2 considered conventional methods of alpha EEG monitoring. These methods were reviewed, adapted and enhanced for use as detectors of alpha EEG increase associated with eye closure. An original method for comparing the alpha EEG detection methods was described and implemented using the $\overline{\chi}$ statistic which is consistently used in this thesis as a 'figure of merit'. This statistic parameterises a technique's performance with regard to detection time and false positive errors. To the author's knowledge this is the first time that such a parameter has been defined and utilised which incorporates both detection time and error rates. To enable a qualitative comparison between alpha detection methods, EEG data were recorded from 10 subjects using an electrode headband constructed for this thesis by the author. Data were recorded during activities which included eye closure, and a number of tasks designed to generate artifact signals (such as EMG from jaw clenching). The algorithms researched were intended for use in real time systems, however in order that the same EEG data be used on all alpha detection methods, the processing was performed offline. All techniques were shown to be successful in detecting the increase in alpha activity following eye closure. The use of the $\overline{\chi}$ parameter allows the different detection methods to be ranked against an appointed 'standard' method reported in past literature, namely the integration method. None of the conventional or enhanced detection techniques showed a statistically significant improvement over the integration method. From this work we concluded that further research into such conventional methods of alpha detection should be given much less emphasis as it is unlikely that this research will yield a practical improvement in activation times or error rates.

Chapter 3

New methods for preprocessing EEG signals in preparation for alpha EEG detection were developed and implemented, including spatial filters, Independent Component Analysis, adaptive filters and a head model using dipolar sources. This is the first time that such preprocessing techniques have been applied to the problem of alpha EEG detection. Of these, preprocessing using ICA showed the best performance. However, the visual inspection required for ICA as well as its computational complexity, reduces its suitability for inclusion in BCI real time systems which require minimal user intervention. The improvement shown after preprocessing by adaptive and spatial filters can be regarded as marginal; when computational requirements of these techniques are considered these techniques are regarded of limited value.

Chapter 4

Novel location-based alpha EEG detection methods were researched, developed, implemented and evaluated. To the author's knowledge, the use of source location has not been used as a method for alpha EEG parameterisation in previous studies. The techniques compared included source localisation using beamformers and the dipolar head model, the MUSIC algorithm and source power localisation. All methods were successful in detecting the increase in alpha EEG activity following eye closure, with the exception of the MUSIC technique which gave unsatisfactory results (showing that $\overline{\chi}$ values were statistically significantly worse when compared to the integration method). Based on data gathered, the source power, Bartlett beamformer and dipolar head model localisation techniques were shown to be improvements over the conventional integration method. More specifically, the source

power localisation technique was shown to be significantly better than the integration method, with p<.OOl. From a practical viewpoint, the $\overline{\chi}$ parameter showed a reduction by 37% compared to the conventional method. Of all the methods researched and utilised the source power method is the most promising. This location-based technique is convenient to implement and, although it performed best with 19 electrode sites, it is usable with only 2 sites (and still shows good performance). Further investigations into the use of alpha EEG detection methods for BCl's should focus upon the source power method. Still to be established is the performance of the algorithm using small numbers of electrodes, and the effect of the position of such electrodes. Further optimisation of the algorithm will enable its real time use in microcontrollers. Possible further work on other alpha detection methods includes the investigation of parametric source location methods (Krim & Viberg 1996, Valaee et al. 1995), and MUSIC-related methods which are able to deal with the presence of coherent signals. It remains to be established whether the performance of these techniques will exceed that of the source power method. We conclude that future investigations into alpha detection techniques should use a direct comparison parameter, in the manner described in this thesis. In particular, the power source detection method should be compared, using a larger sample of subjects and in the presence of an increased number of artifact sources, using the conventional integration detection method as a 'benchmark'.

Chapter 5

It is recognised that the signal processing task is eased considerably when the signal of interest is of high fidelity, and corruption of the signal is minimised. Arguably, the most critical component for ensuring signal fidelity is

the electrical contact between the body and sensing bioelectrode. Electrode types were extensively reviewed and relative merits considered, with particular reference to long-term monitoring of biosignals. The main varieties of bioelectric recording electrodes were grouped into three types: wet, dry and insulating. Basic electrode operating principals were discussed with special regard to electrode impedance, and factors which effect these impedances.

Chapter 6

In order to critically and quantitatively evaluate the performance of electrodes the impedance characteristics of the skin/electrode combination must be established. This chapter dealt with the contribution of skin impedance and the effect of contact impedance on signal fidelity. As part of this work it was essential to devise, implement and evaluate a new system capable of real time monitoring of impedance spectra. Additionally, such a system was required to be fast and flexible in its operation. The system designed had several advantages over other techniques, such as consistent accuracy across all selected frequency components, and prevention of 'smearing' of impedance loci for samples which have impedance characteristics which change over time. This system will be useful for any experiment in which fast impedance measurements are required, and where characteristics of the sample are nonstationary. The system was used to demonstrate the shapes of skin/electrode impedance loci (which qualitatively match theoretical models) and their changes over time. The variation of powerline noise with contact impedance was demonstrated using dry electrodes, along with the advantages of using active electrodes. Data were acquired relating to the polyexponential decay in contact impedance with time (not a simple exponential decay, as reported in previous literature). This data introduces many new questions,

and would benefit from a comprehensive and quantitative study on the mechanisms that affect skin impedance, using the impedance spectroscopy system.

Chapter 7

In order to make a balanced judgement on the merits of bioelectrodes, a direct and quantitative comparison of the three electrode types was required. Such quantitative data, to the knowledge of the author, do not exist in the literature. Therefore, experiments were conducted to determine the characteristics of wet, dry and insulating electrodes applied to skin. This chapter considered the construction and relative performance of bioelectrodes. In particular, wet, dry and insulating electrode were compared. regard to dry and insulating electrodes, these and the ancillary electronics were designed and constructed by the author. The insulating electrodes were based on silicon dioxide, thermally on a silicon substrate. For these films to be produced, a film thickness determination system had to be custom-developed, incorporating a photospectrometer, which involved fitting of theoretical curves to reflectance data. The susceptibility of the three electrode types to various artifact sources was considered and evaluated simultaneously in a controlled test environment for the first time. These artifacts had been identified as problems in previous reports on dry and insulating electrodes, but results from experiments in this thesis revealed that such artifacts were not a significant problem when precautions were taken (such as the shielding of electrodes and active buffering). We conclude that all electrodes used in this research are viable alternatives as surface electrodes for sensing of biosignals, and all were shown to be successful in detecting ECG signals. For ECG use, the application of dry electrodes is recommended, as active buffering enables useable signals to be obtained within seconds. Although insulating

electrodes also showed equally good performance, they require more fabrication than dry electrodes without added performance benefits. It was seen that the presence of hair caused some problems with electrodes of large contact surface area, but conversely electrodes with very small contact area have stability problems. A possibility for further research is to design dry electrodes for EEG applications (which would require a reduction in electrode contact area while retaining physical stability), to compare with wet and insulating electrodes.

The research presented in this thesis has found new and successful methods for the reliable detection of the increase in alpha EEG activity associated with eye closure. These techniques will enable the more robust use of Bel systems in an unconstrained operating environment, such as those currently being developed to assist persons with high level impairments. Investigations into alternative bioelectric sensing electrodes and methods of characterisation have yielded profitable results, however more work is required to enable their efficient use for EEG signals.

Appendix A

Published or presented work based on research described in this thesis

[1]Kirkup, L., Searle, A., Craig, A., McIsaac, P. & Larsen, G. (1998), 'Three methods compared for detecting the onset of alpha wave synchronization following eye closure', *Physiological Measurement* 19(2), 213-224.

Searle, A., Kirkup, L. & Craig, A. (1998), 'Novel impedance spectroscopy for medical applications', *XVth Annual Scientific Research Meeting: Royal Shore Hospital and University of Technology, Sydney.*

Searle, A., Kirkup, L. & Craig, A. (1998), 'Real time impedance plots for EEG applications', *13th National Congress of the Australian Institute of Physics, Fremantle.*

Searle, A. & Kirkup, L. (1999), 'Real time impedance plots with arbitrary frequency components', *Physiological Measurement* 20,103-114.

Ipreliminary study

Searle, A. & Kirkup, L. (1999), 'Steerable electrode arrays for reliable alpha wave detection', *XVIth Annual Scientific Research Meeting: Royal North Shore Hospital and University of Technology, Sydney.*

Searle, A. & Kirkup, L. (2000), 'A direct comparison of wet, dry and insulating bioelectric recording electrodes.', *Physiological Measurement* 21(2),271-283.

Searle, A. & Kirkup, L. (2000), 'A comparison of multi-electrode based alpha wave discrimination techniques for EEG control' *CD-ROM, Proceedings of the World Congress on Medical Physics and Biomedical Engineering, Chicago.* July 23-28.

Searle, A. & Kirkup, L. (2001), 'Detection of alpha EEG onset following eye closure using four location-based techniques', *Medical & Biological Engineering & Computing* 39, 1-7.

Appendix B

The International 10-20 System of EEG Electrode Placement

Figure B.1 shows the International 10-20 system for EEG electrode placement. The name refers to the 10% and 20% interelectrode distance used in the convention. The preceding letters denote Frontal, Temporal, Central, Parietal and Occipital regions of the brain (although there is no 'central lobe', the convention is used for identification purposes). Odd numbers refer to the left hemisphere of the brain, while even numbers denote the right hemisphere. Smaller numbers are closer to the midline, with *z* being on the midline.

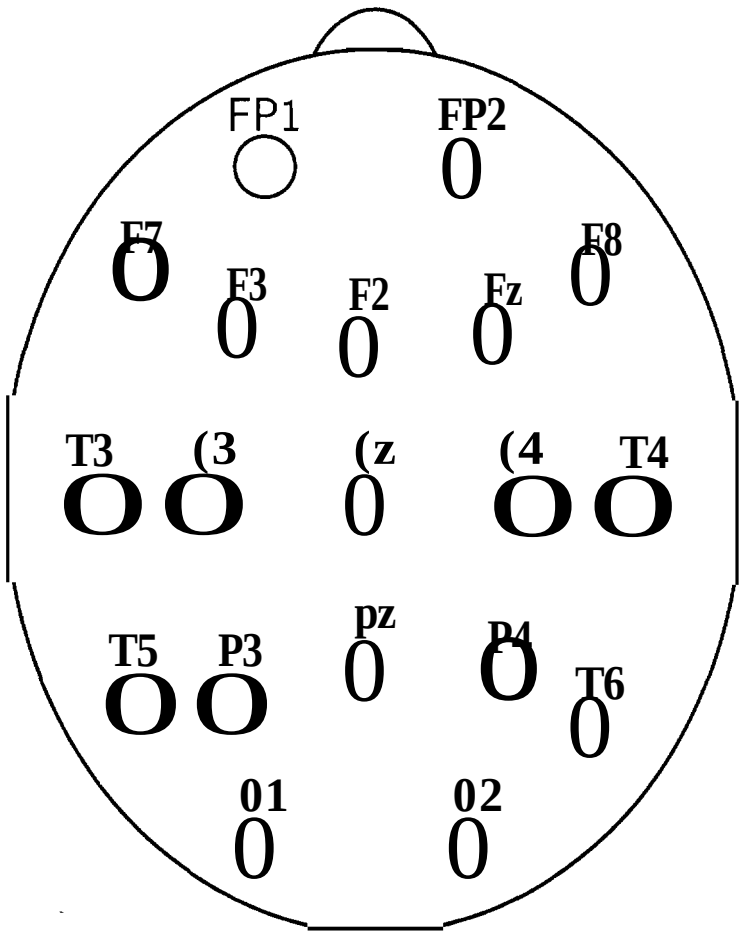

Figure B.1: The International 10-20 System of EEG Electrode Placement

Appendix C

Calculation of electrode positions on headband

The results of a survey of head dimensions from 14 randomly sampled people (mean age 29.1 yr, standard deviation 9.1 yr) is shown **in** Table C.l. For

	Mean	std. dev.
Width	78.8 mm	3.8 mm
Depth	98.0 mm	4.9mm

Table *C.1:* Mean and standard deviation of head sizes surveyed

many algorithms-used **in** this thesis the cartesian coordinates of the electrodes (which are evenly spaced around the headband) are required. To compute these coordinates a parametric description of the headband shape is used, which is assumed to be an ellipse.

$$x(O) = a\cos(O) \qquad \text{(C.l)}$$

$$y(O) = b\sin(O) \qquad \text{(C.2)}$$

where *a* is the head width and *b* is the head depth. In order for the electrodes to be placed evenly, an accurate calculation of the circumference derived from *a* and *b* is required. Two approximations for the circumference of an ellipse are shown below, however these proved to be inaccurate for the purposes of this study.

$$C \qquad 2\pi\sqrt{\frac{a^2}{2} + \frac{b^2}{2}} \tag{C.3}$$

$$C \qquad \pi(a + b)\left[1 + \frac{4(a+b)}{(a+b)2} + \frac{64(a+b)]}{(a+b)4}\right. \tag{C.4}$$

One can more accurately compute the circumference by finding the arc length, using

$$C \qquad \int_0^{2\pi} \sqrt{[x'(\theta)]^2 + [y'(\theta)]^2}\,d\theta \tag{C.5}$$

$$\int_0^{2\pi} \sqrt{[-a\sin(\theta)]^2 + [b\cos(\theta)]^2}\,d\theta \tag{C.6}$$

Equation *C.6* results in an *elliptic integral,* which is non-analytic. In order to evaluate such integrals it is necessary to use lookup tables, numerical integration or approximations methods (e.g. Walter & Fournier (1996)).

The simpler method adopted here was to sum the length of many linear segments (the start and end points determined by Equations *C.1* at Band $\theta + \Delta\theta$). A sufficiently small $\Delta\theta$ gave an answer comparable to that given by Equation *C.6* to four decimal places. The same method was used to determine the locations of electrodes, placed every $\frac{\text{circumference}}{19}$ cm. The resulting coordinates are shown **in** Figure C.l. Using the average values for *a* and *b* shown in Table *C.1,* the circumference calculated is 557.6 mm

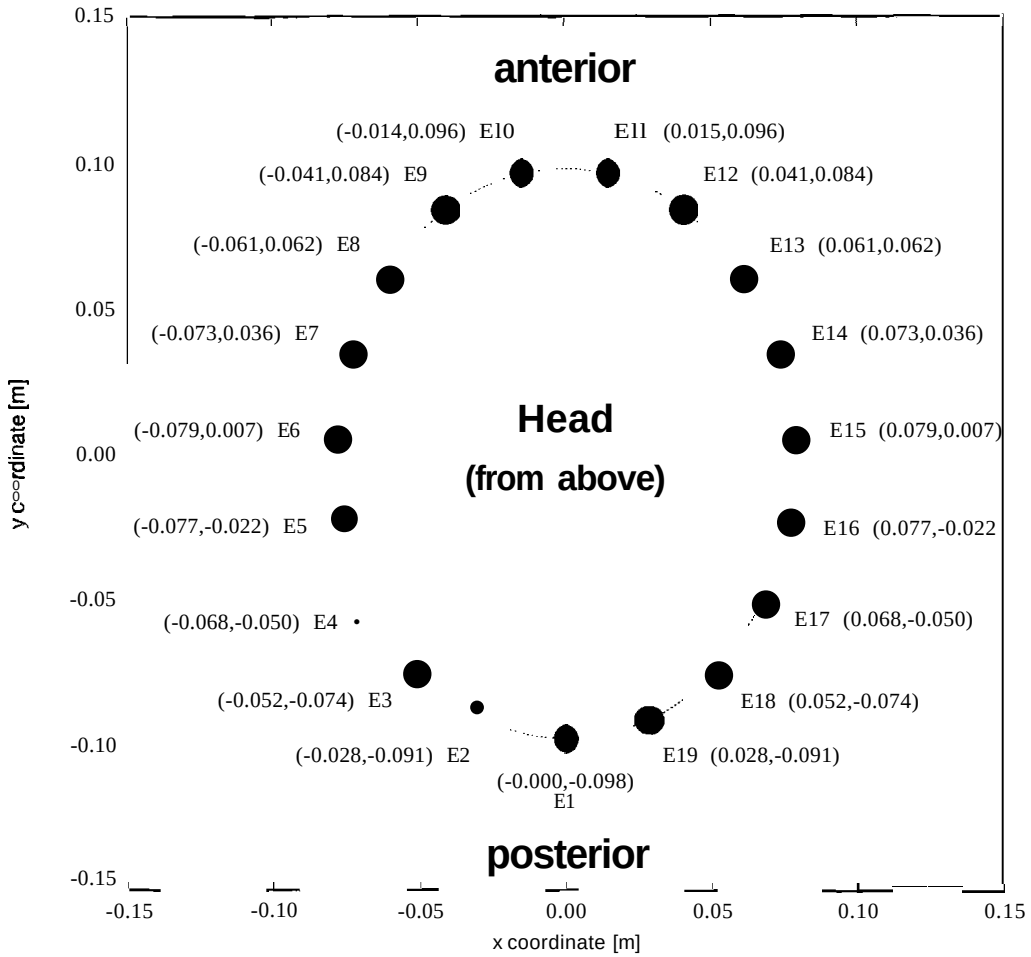

Figure C.1: Positions of the 19 electrodes on the head band. Coordinates are in m.

Appendix D

Mathematical definitions

D.I Matrix rank

The rank of a matrix is a measure of the linear independence of its rows and columns. The row rank of a matrix of order M by N is the number of linearly independent rows in the matrix, while the column rank is the number of linearly independent columns. The row rank will be between 0 and M, the column rank between 0 and N. If the row rank is equal to M, the matrix is said to have maximal or **full** row rank; there are corresponding terms for column rank.

For a square matrix, of order N, the row and column ranks will be equal. A square matrix is nonsingular if and only if it has maximal row rank; in other words, if no row is a linear combination of the other rows, and similarly for columns. A square matrix with **full** rank has an inverse, a nonzero determinant, and Gauss elimination with pivoting can be used to solve linear systems involving the matrix.

If the rank of a matrix is actually desired, a reasonable method is to compute the QR factorisation. Very small diagonal terms in the R factor

may indicate linear dependence of the corresponding columns of the matrix. The singular value decomposition (Appendix D.2) will also give this sort of information.

D.2 Singular Value Decomposition (SVD)

The SVD of a matrix A is a factorisation of the form

$$A = \mathbf{USy}^{T} \tag{D.l}$$

where S is a diagonal matrix containing the singular values of A, and U and Yare orthogonal matrices.

D.3 The pseudoinverse

The pseudoinverse is a generalisation of the idea of the inverse matrix, for cases where the standard inverse matrix cannot be applied. Such cases **in**clude matrices A which are singular, or rectangular.

The inverse of a matrix A can be defined as the unique matrix B such that:

$$\mathbf{AB} \quad \mathbf{BA=I} \tag{D.2}$$

$$\mathbf{ABA} \quad A \tag{D.3}$$

$$\mathbf{BAB} \quad B \tag{D.4}$$

The pseudoinverse can be used **in** a way similar to the wayan inverse is used. For instance, given the rectangular set of linear equations $\mathbf{Ax} = y$ a solution can be computed as $x = Cy$. **If** the equations are consistent, then x will actually satisfy the equations. Otherwise, x will be a best possible

solution, in the sense that it minimises the Euclidean norm of the square residual error.

The pseudoinverse can be computed from the information contained in the singular value decomposition, as

$$\mathbf{C} = \mathbf{V}\mathbf{S}^{\dagger}\mathbf{U}^{\mathsf{T}} \tag{D.5}$$

where $\mathbf{S}^{\dagger}$ is the matrix S with all nonzero values on the diagonal inverted.

D.3.1 Example 1: A non-singular matrix

$$\mathbf{A} = \begin{bmatrix} 1 & 3 \\ -4 & 3 \end{bmatrix} \tag{D.6}$$

using the SVT we get

$$\begin{aligned} \mathbf{U} &= \begin{bmatrix} -0.2897 & -0.9571 \\ -0.9571 & 0.2898 \end{bmatrix} \\ \mathbf{S} &= \begin{bmatrix} 5.1492 & 0 \\ 0 & 2.9131 \end{bmatrix} \\ \mathbf{V} &= \begin{bmatrix} 0.6872 & -0.7265 \\ -0.7265 & -0.6872 \end{bmatrix} \end{aligned} \tag{D.7}$$

because the matrix is nonsingular the pseudoinverse is the same as the inverse

$$\mathbf{C} = \begin{bmatrix} 0.2 & -0.2 \\ 0.2667 & 0.0667 \end{bmatrix} \tag{D.8}$$

D.3.2 Example 2: A singular matrix

$$\mathbf{A} = \begin{bmatrix} 1 & 2 \\ 1 & 2 \end{bmatrix} \tag{D.9}$$

using the SVT we get

$$u = \begin{bmatrix} -0.7071 & 00 \\ -0.7071 & \end{bmatrix}$$

$$s = \begin{bmatrix} 3.1623 & 0 \\ 0 & 0 \end{bmatrix} \qquad \text{(D.lO)}$$

$$v = \begin{bmatrix} -0.4472 & 0 \\ -0.8944 & 0 \end{bmatrix}$$

because the matrix is singular (note only one value in the diagonal for S) inverse does not exist. The pseudo inverse is

$$C = \begin{bmatrix} 0.1 & 0.1 \\ 0.2 & 0.2 \end{bmatrix} \qquad \text{(D.ll)}$$

D.4 Cholesky decomposition

Every positive definite square matrix A can be factorised in the form $A = RR^T$ with R being a lower triangular matrix with positive definite elements. Cholesky decomposition finds the matrix R; this is similar to LU decomposition except that the upper triangular part is in fact formed by the transpose ofthe lower triangular matrix, RT. Using this we can solve a matrix equation

$$Ax = b \qquad \text{(D.12)}$$

by first solving

$$Ry = b \qquad \text{(D.13)}$$

by forward substitution and then

$$R^T x = y \qquad \text{(D.14)}$$

by backward substitution. R is found via the Cholesky decomposition of A.

D.5 Numerical evaluation of Legendre and Associated Legendre polynomials

The value of an associated Legendre polynomial *F1m(x)* can be found using the following relations (Press et al. 1997). Starting with

$$P_m^m(x) = (-1)^m(2m-1)!!(1-x^2)^{m/2} \tag{D.15}$$

$$P_{m+1}^m(x) = x(2m+1)P_m^m \tag{D.16}$$

If we set $P_{m-1}^m(x) = 0$, then using Equations D.15 and D.16 the value of any associated Legendre polynomial can be found with

$$(l-m)P_l^m = x(2l-1)P_{l-1}^m - (l+m-1)P_{l-2}^m \tag{D.17}$$

The Legendre polynomial can then be found using

$$P_l(x) = P_l^0(x) \tag{D.18}$$

D.6 The Hilbert transformer

The Hilbert Transformer can be used to create an *analytic signal*, that is a signal with real and imaginary components (Reilly et al. 1994). The method works in the frequency domain as shown in this example.

$$y = \mathcal{F}^{-1}(b \times \mathcal{F}(x)) \tag{D.19}$$

where *x[k]* is the input array of size *N*, and *b[k]* is given by

$$b[k] = \begin{cases} 2 & 1 < k < \frac{N}{2} \\ 0 & \frac{N}{2}+1 < k < N \end{cases} \tag{D.20}$$

The example in Figure D.1 shows an input signal which contains only a real part. The signal is made of two sinusoidal components, at 2 Hz and 20 Hz,

with the signal sampled at 256 Hz. Figure D.2 shows *F(x)* and *b[k]* for the same signal. Figure D.3 is the output signal after Hilbert transformation,

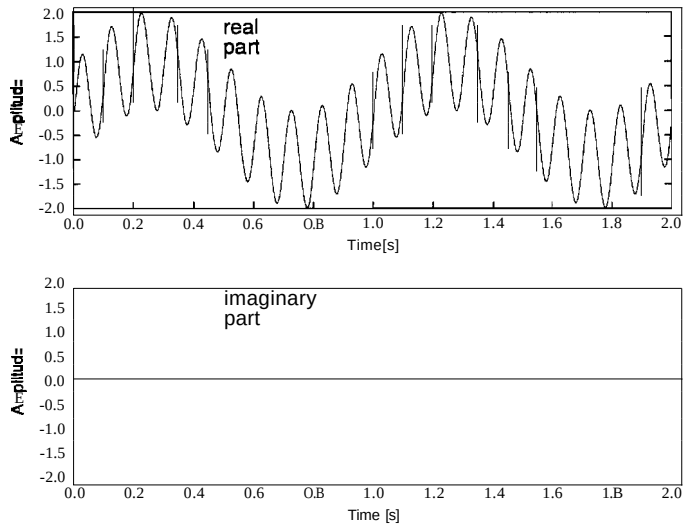

Figure D.1: Real and imaginary parts of original signal, with 2 Hz and 20 Hz components.

the signal now has an imaginary part, with the phase of each frequency component offset by $\frac{\pi}{2}$ relative to the real part.

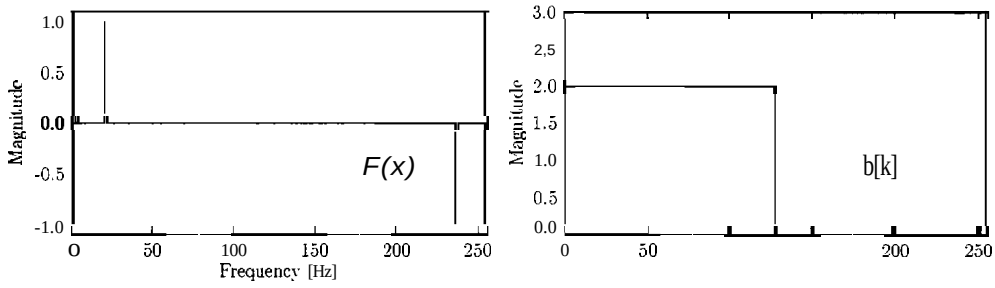

Figure D.2: Imaginary part of FFT for the input signal, and the vector *b[k].*

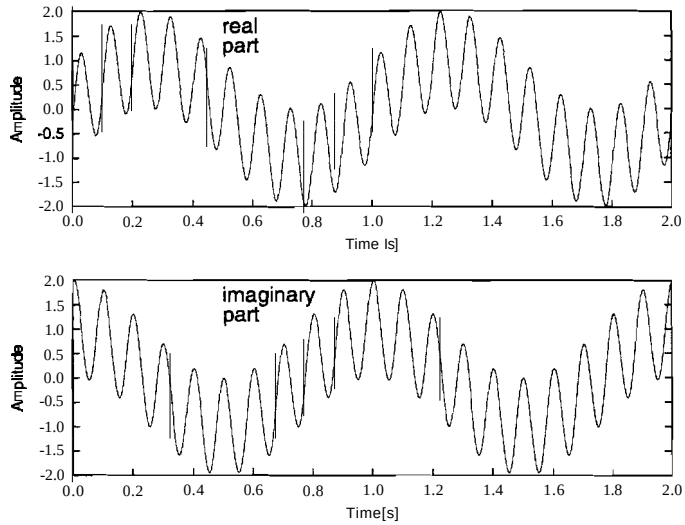

Figure D.3: Real and imaginary parts of signal after Hilbert transform.

D.7 Equivalence of constant phase element model and empirical formula

The following shows that the use of a constant phase element in parallel with a resistor, R_p, is equivalent to the empirical formula for the impedance locus **in** Equation 6.3. Here $Rp = R_o -$ Roo and $K = R_p/\tau^{\alpha}$.

$$
\begin{aligned}
Z \quad & R_\infty + R_p \parallel K(j\omega)^{-\alpha} \qquad \text{(D.21)} \\
& R_\infty + \frac{1}{\frac{1}{R_p} + \frac{1}{K(j\omega)^{-\alpha}}} \\
& R_\infty + \frac{K + R_p(j\omega)^{\alpha}}{R_p K} \\
& R_\infty + \frac{R_p}{1 + \frac{R_p}{K}(j\omega)^{\alpha}} \\
Z \quad = \quad & R_\infty + \frac{R_0 - R_\infty}{1 + (j\omega\tau)^{\alpha}} \qquad \text{(D.22)}
\end{aligned}
$$

Equation D.22 is equivalent to Equation 6.3 on p. 183.

D.8 Equivalence of frequency dependent component model and constant phase element model

Referring to Figure 6.5(a) the total impedance for the model is

$$Z = 1/\left(\frac{1}{R_2} + \frac{1}{CO/w1\text{-}f3} + \frac{1}{R_O/w^{(\beta)}}\right) \tag{D.23}$$

where

$$\frac{1}{R_2}\tau^{\beta}\sin\frac{\beta\pi}{2} \tag{D.24}$$

$$R_O = R_2 \Big/ \left(\tau^{\beta}\cos\frac{\beta\pi}{2}\right) \tag{D.25}$$

Therefore the impedance becomes

$$Z = \frac{1}{\frac{1}{R_2} + \frac{\tau^{\beta}\omega^{\beta}\cos\left(\frac{\beta\pi}{2}\right)}{R_2} + \frac{j\tau^{\beta}\omega^{\beta}\sin\left(\frac{\beta\pi}{2}\right)}{R_2}} \tag{D.26}$$

$$\frac{R_2}{1 + (TW)f3\left(\cos\left(\frac{\beta\pi}{2}\right) + j\sin\left(\frac{\beta\pi}{2}\right)\right)} \tag{D.27}$$

$$\frac{R_2}{1 + (jwT)f3} \tag{D.28}$$

This is equivalent to the empirical depressed-locus Equation 6.3 (p. 183) when $R_{OO} = 0$ and $i = 1$, which has been previously shown (see Equations D.21-D.22) to be equivalent to a model comprising of a $ZCPA$ in parallel with a frequency independent resistor.

D.9 Derivation of equations used for equal frequency spacing in impedance measurements

The frequency components used in impedance spectroscopy can be calculated so that the data points are evenly spaced around the locus, if an approximate 'three component' model is used. The three component model is shown in Figure D.4. Measurements using this model will result is a locus such as the

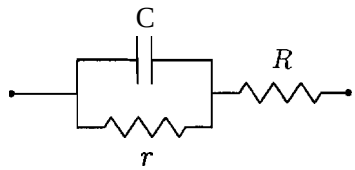

Figure D.4: Simple 'three component' skin electrical model

one in Figure D.5. The impedance of the three component model can be

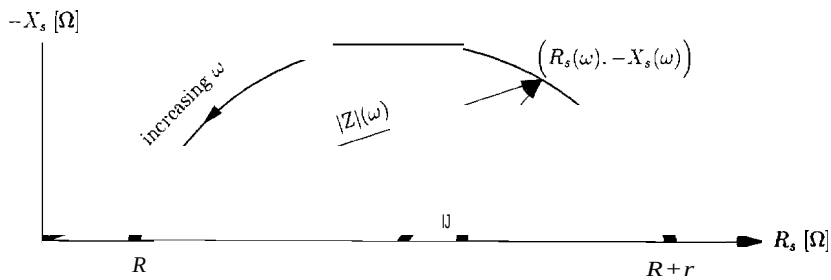

Figure D.5: Impedance locus for skin

expressed as

$$Z = R + 1/\left(\frac{1}{r} + j\omega C\right) \tag{D.29}$$

The real component of Z is

$$\text{Re[Z]} \qquad R + 1/\left(r\omega^2 C^2 + \frac{1}{r}\right) \tag{D.30}$$

If the centre of the locus is shifted to the origin by defining

$$Z2 = Z - \boldsymbol{R} - \frac{r}{2} \tag{D.31}$$

then the angle θ in Figure D.5 for a given excitation frequency can be puted using

$$\theta = \cos^{-1}\left(\frac{\mathrm{Re}[Z_2]}{|Z_2|}\right) \tag{D.32}$$

Equations D.29 - D.32 can then be combined to get the desired angle in terms of excitation frequency (where $w = 2\pi \mathbf{j}$), or required frequency in terms of angle (θ).

$$\theta(f) = \cos^{-1}\left[\frac{2}{(2\pi f r C)^2} + 1 - 1\right] \tag{D.33}$$

$$f(\theta) = 1/2\pi \left[\frac{2/(\cos\theta + 1)}{r^2 C^2}\right] \tag{D.34}$$

Appendix E

FET devices

E.l Introduction to FET types

A FET (field effect transistor) is similar to the more common BJT (bipolar junction transistor) type, in that both are three terminal devices where the current flowing between two terminals is controlled by the third "control" terminal. The FET family consists of two major devices, that is, the JFET (junction field effect transistor) and the MOSFET (metal oxide semiconductor field effect transistor). Whereas a BJT transistor requires a current flow through the control terminal (or base) to achieve this effect, conduction in the FET channel is controlled an electric field, produced by voltage applied at the control terminal (or gate). Thus no current flows through the gate, and this is the advantage of FET devices; resulting in input impedances up to 10^{14} Ω.

In a MOSFET (see Figure E.1) the gate is separated from the current channel by a layer of (most commonly) $Si0_2$, an electrical insulator. In an n-channel MOSFET current flows from the drain to source (assuming the drain is positive relative to the source terminal) when the gate voltage is

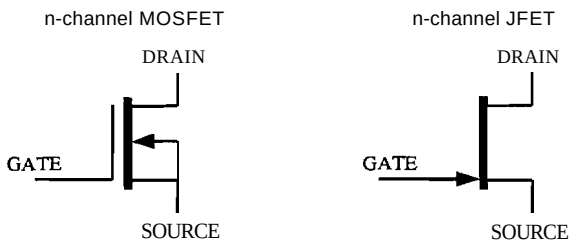

Figure E.l: n-type FETS

positive relative to the source. The oxide layer is extremely thin and makes the devices susceptible to dielectric breakdown damage by static electricity. Handling a MOSFET incorrectly can easily destroy the device.

In JFET devices the gate is separated from the current channel by a semiconductor channel. Operation is based on reverse biasing the junction between the gate semiconductor material and the bulk of the channel; this is called a *pn* juncLioll amI is equivalent tu reverse biasing diode. Even though the junction is reverse-biased a leakage current still flows (as in common diodes) to the order of 10^{-9} A. Thus the gate impedance is orders of magnitude less than that for MOSFETS, and small currents may flow if the gate is forward biased with respect to the channel. In circuit design this leakage current is often assumed to be zero.

E.l.1 Simple follower

A simple follower circuit using a JFET is shown in Figure E.2. The circuit can be described (Horowitz & Hill 1989, p. 133) with the equations E.l and E.2.

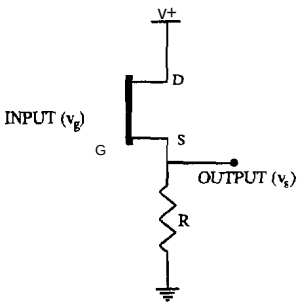

Figure E.2: JFET Source Follower

$$Vs \tag{E.1}$$

$$g_m(v_g - v_s) \tag{E.2}$$

where 9m is the transconductance

$$\therefore v_s = \left[1 + \frac{R9m}{Rg_m}\right] v^g \tag{E.3}$$

So with $R \gg 1/9m$ the gain of the follower approaches (but is always less than) one. For most operating situations 9m is less than 10.

E.1.2 Active loads

By replacing the resistor in Figure E.2 with a current source the performance can be improved. The source acts like a very high value resistance and the constant current reduces nonlinearities by keeping v_{gs} constant. A constant current source may be made from BJT transistors or simply a JFET with its gate tied to the source terminal.

Appendix F

Reflectance measurement using a spectrophotonleter

The spectrophotometer obtains the reflectance spectrum of a sample by stepping over a range of wavelengths, measuring the intensity at the detector for each wavelength value. To enable an absolute reading, the spectrophotometer stage uses three mirrors, configured as shown (not to scale) in Figure F.1. As this figure shows, the light beams are not incident at exactly 90° to the sample surfaces. It is sufficient in this case, however, to assume that the light beams are normal to the sample surfaces, and this assumption is used in all calculations for this method. The initial measurement is a baseline calibration, to determine a 100% reflectance level across the spectrum. To achieve this the central mirror is placed (referring to Figure F.1) at the bottom (baseline) position; no samples are in the stage at this time. The central mirror is then replaced in its top position, and a spectrum of the reference film is measured. In this study a thick aluminium film is used for the reference, and to obtain this spectrum the reference film is placed so that it occupies both the 'sample' and 'reference' positions (denote this spectrum as

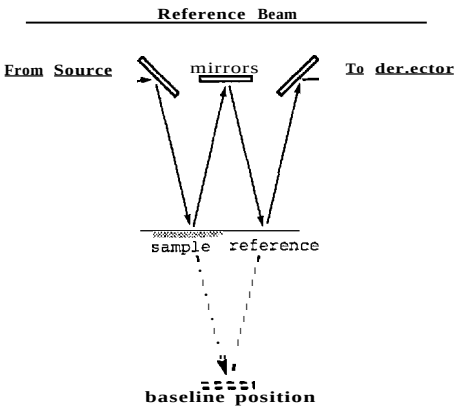

Figure F.I: stage of the spectrophotometer

$R_{al,al}(\lambda)$). Finally the sample is introduced to one half of the stage, with the aluminium reference in the other half, and a spectrum taken. (denote this spectrum as $R_{s,al}(\lambda)$). The measurements remain absolute (referred to the baseline measurement taken) owing to the fact that all measurements involve the same three mirrors. The reflectance of the sample can be calculated by dividing the values for $R_{s,al}(\lambda)$ by the reflectance for aluminium. Since the aluminium spectrum measurement, $R_{al,al}(\lambda)$, involved two reflections from the film, the square root of these values must be used. Thus the reflectance for the sample is

$$Rsample(\lambda) \qquad \frac{Rs,al(\lambda)}{\sqrt{Ral,al(\lambda)}} \qquad \text{(F.I)}$$

Appendix G

Short derivation of reflectance for a single layer film

The representation shown in Figure 7.1 can be shown in detail to illustrate E and B electromagnetic fields near the interfaces, shown in Figure G.1. The electric fields, E, point out of the page, whilst the magnetic fields, B, (not shown) have a direction determined by the direction of propagation of the electromagnetic wave, given by E x B. The magnitudes of magnetic and

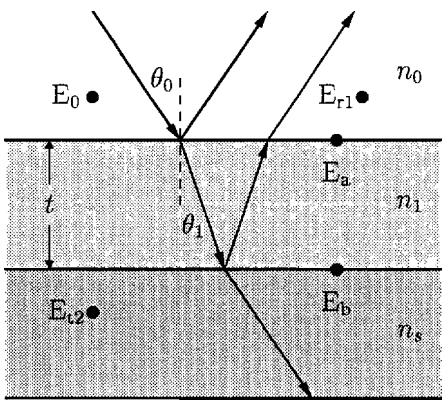

Figure G.1: Reflectance for a single layer film on substrate

electric fields can be related by

$$B = n\sqrt{\epsilon_0\mu_0}E \qquad (G.1)$$

where ϵ_0 is the permittivity, and μ_0 is the permeability, of free space. In all equations considered here, the light beam is considered to be normal to the film, thus all angles $(0_0, \theta_1)$ are equal to zero. The relationship between the net fields at the boundaries is

$$\begin{bmatrix} E_a \\ B_a \end{bmatrix} \quad \begin{bmatrix} \cos(\delta) & \frac{i\sin(\delta)}{\gamma_1} \\ i\gamma_1\sin(\delta) & \cos(\delta) \end{bmatrix} \begin{bmatrix} E_b \\ B_b \end{bmatrix} \qquad (G.2)$$

where $\gamma_x = \tilde{n}_x\sqrt{\epsilon_0\mu_0}$ (G.3)

The 2x2 matrix in equation *G.2* is termed the *transfer matrix* for the film, and can be used to extend this procedure to multilayer films. Equation *G.2* is written more simply as

$$\begin{bmatrix} E_a \\ B_a \end{bmatrix} \quad \begin{bmatrix} m_{11} & m_{12} \\ m_{21} & m_{22} \end{bmatrix} \begin{bmatrix} E_b \\ B_b \end{bmatrix} \qquad (G.4)$$

The boundary conditions for the interfaces (Pedrotti & Pedrotti 1993) require that the magnitudes of E and B fields are equal on either sides of the interfaces. Thus, using equation *G.1*

$$E_0 + E_{r1} \qquad (G.5)$$

(G.6)

$$\gamma_0(E_0 - E_{r1}) \qquad (G.7)$$

(G.8)

Now equation *G.2* may be written as

$$\begin{bmatrix} E_0 + E_{r1} \\ \gamma_0(E_0 - E_{r1}) \end{bmatrix} \quad \begin{bmatrix} m_{11} & m_{12} \\ m_{21} & m_{22} \end{bmatrix} \begin{bmatrix} E_{t2} \\ \gamma_s E_{t2} \end{bmatrix} \qquad (G.9)$$

where is as defined in Equation G.3. We now introduce the reflection coefficient

$$r \quad = \qquad \text{(G.I0)}$$

Equations G.g and G.I0 can be combined to give

$$r \quad = \quad \frac{\gamma_0 m_{11} \pm \gamma_0\gamma_s m_{12} \mp \underline{\text{m21}} \mp \gamma_s m_{22}}{\gamma_0 m_{11} + \gamma_0\gamma_s m_{12} + m21 + \gamma_s m_{22}} \qquad \text{(G.ll)}$$

Finally, expanding terms and including the transfer matrix elements

$$r \quad = \quad \frac{\tilde{n}_1(\tilde{n}_0 \mp \tilde{n}_s)\,\underline{\cos}\,\underline{\delta} \pm \underline{\text{i}}\,(\tilde{n}_0\tilde{n}_s \mp \tilde{n}_1^2)\,\underline{\sin}\,\underline{\delta}}{\tilde{n}_1(\tilde{n}_0 + \tilde{n}_s)\cos\delta + \text{i}\,(\tilde{n}_0\tilde{n}_s + \tilde{n}_1^2)\sin\delta} \qquad \text{(G.12)}$$

R is then given by

$$R \qquad \text{(G.13)}$$

Bibliography

Ackmann, J. J. (1993). Complex bioelectric impedance measurement system for the frequency range from 5 Hz to 1 MHz. *Annals of Biomedical Engineering,* 21(2) 135-146.

Adli & Yamamoto, Y. (1998). Impedance balancing analysis for power-line interference elimination in ECG signal. *Conference Record - IEEE Instrumentation and Measurement Technology Conference,* 1 235-238.

Adrian, E. D. & Matthews, B. H. C. (1934). The Berger rhythm: Potenital changes from the occipital lobes in man. *Brain,* **57** 355-385.

Anderson, C., Devulapalli, S. & Stolz, E. *(1995a).* Determining mental state from EEG using neural networks. *Scientific Programming, Special Issue on Applications Analysis,* 4 171-183.

Anderson, C. & Sijercic, Z. (1996). Classification of EEG signals from four subjects during five mental tasks. *Proceedings of the Conference on Engineering Applications in Neural Networks, Special Session on Biomedical Systems, 407-414.*

Anderson, C. W., Stoltz, E. A. & Shamsunder, S. C. *(1995b).* EEG signal classification with different signal representations. *Neural Networks for Signal Processing,* 475-483.

Armstrong, R. D., Bell, M. F. & Metcalfe, A. A. (1977). A method for automatic impedance measurement and analysis. *Journal of Electroanalytical Chemistry,* **77** 287-298.

Armstrong, R. D., Race, W. P. & Thirsk, H. R. (1968). The determination of electrode impedances over an extended frequency range by AC-bridge methods. *Electrochimica Acta,* **13** 215-239.

Arthur, R. M. & Geselowitz, D. B. (1970). Effect of inhomogeneities on the apparent location and magnitude of a cardiac current dipole source. *IEEE Transactions on Biomedical Engineering,* 17(2) 141-146.

Aston, R (1990). *Principles of Biomedical Instrumentation and Measurement.* Toronto: Merrill.

Awada, K. A., Jackson, D. R, Baumann, S. B., Williams, J. T., Wilton, D. R, Fink, P. W. & Prasky, B. (199S). Effect of conductivity uncertainties and modeling errors on EEG source localization using a 2-d model. *IEEE Transactions on Biomedical Engineering,* 45(9) 1135-1145.

Awada, K. A., Jackson, D. R, Williams, J. T., Wilton, D. R & Baumann, S. B. (1997). Computational aspects of finite element modeling in EEG source localization. *IEEE Transactions on Biomedical Engineering,* 44(S) 736-752.

Azizi, S., Ogmen, H. & Jansen, B. (1996). A unified analysis of alpha rhythm, fast synchronized oscillations, and flash visual evoked potentials. *Neural Networks,* 9(2) 223-42.

Babiloni, F., Cincotti, F., Lazzarini, L., Millan, J., Mourino, J., Varsta, M., Heikkonen, J., Bianchi, L. & Marciani, M. G. (2000). Linear classification of low-resolution EEG patterns produced by imagined hand movements. *IEEE Transactions on Rehabilitation Engineering, 8(2)* 186–188.

Back, A. D. & Weigend, A. S. (1997). A first application of independent component analysis to extracting structure from stock returns. *International Journal of Neural Systems,* 8(4) 473-4S4.

Baker, L. E. (19S9). Principles of the impedance technique. *IEEE Engineering in Medicine and Biology,* 11.

Barnett, A. (1935). Certain factors affecting the constancy of impedance angle. *Endocrinology,* **19** 66S-672.

Barnett, A. (193S). The phase angle of normal human skin. *Journal of Physiology,* **93** 349-366.

Barreto, A. B., Taberner, A. M. & Vicente, L. M. (1996). Classification of spatio-temporal EEG readiness potentials towards the development of a brain-computer interface. *Proceedings of the IEEE Southeastcon,* 99-102.

Basar, E. & Schurmann, M. (1997). Functional correlates of alpha: Panel discussion ofthe conference 'alpha processes in the brain'. *International Journal of Psychophysiology,* 26(1-3)

Basmajian, J. V. (1983). *Biofeedback: Principles and Practice for Clinicians.* Baltimore: Williams & Wilkins.

Bayliss, J. D. & Ballard, D. H. (2000). A virtual reality testbed for brain-computer interface research. *IEEE Transactions on Rehabilitation Engineering,* 8(2) 188-190.

Bell, A. J. & Sejnowski, T. J. (1995). An information-maximization approach to blind separation and blind deconvolution. *Neural Computation, 7(6)* 1129-1159.

Benetazzo, L., Narduzzi, *C.,* Offelli, C. & Petri, D. (1992). *AID* converter performance analysis by a frequency-domain approach. *IEEE Transactions on Instrumentation & Measurement,* 41(6) 834-839.

Bergey, G. E., Squires, R. D. & Sipple, W. C. (1971). Electrocardiogram recording with pasteless electrodes. *IEEE Transactions on Biomedical Engineering,* 18(3) 206-211.

Bhattacharya, J., Kanjilal, P. P. & Nizamie, S. H. (2000). Decomposition of posterior alpha rhythm. *IEEE Transactions on Biomedical Engineering,* 47(6) 738-747.

Birbaumer, N., Kubler, A., Ghanayim, N., Hinterberger, T., Perelmouter, J., Kaiser, J., Iversen, 1., Kotchoubey, B., Neumann, N. & Flor, H. (2000). The thought translation device (TTD) for completely paralyzed patients. *IEEE Transactions on Rehabilitation Engineering,* 8(2) 190-193.

Birch, G. E. & Mason, S. G. (2000). Brain-computer interface research at the Neil Squire foundation. *IEEE Transactions on Rehabilitation Engineering,* 8(2) 193-195.

Bohdanecky, Z., Indra, M., Lansky, P. & RadiI-Weiss, T. (1984.). Alternation of EEG alpha and non-alpha periods does not differ in open and closed eye condition in darkness. *Acta Neurobiologiae Experimentalis, 44(5)* 229-232.

Bohdanecky, Z., Lansky, P., Indra, M. & RadiI, T. *(1978a).* To the methodological problems of alpha activity detection. *Activitas Nervosa Superior,* 20(1) 21-2.

Bohdanecky, Z., Lansky, P., Indra, M. & RadiI-Weiss, T. *(1978b).* EEG alpha and non-alpha intervals alternation. *Biological Cybernetics,* 30(2) 109-13.

Boudrot, R. (1972). An alpha detection and feedback control system. *Psychophysiology,* 9(4) 461-6.

Boudrot, R., Goodman, D. & Mulholland, T. (1978). An EEG alpha-detection, feedback stimulation, and data analysis system. *Behavior Research Methods & Instrumentation,* 10(5) 646-651.

Bozinovski, S. (1990). Mobile robot trajectory control from fixed rails to direct bioelectric control. *Intelligent Motion Control. Proceedings of the IEEE International Workshop,* 2 463-467.

Bozinovski, S., Sestakov, M. & Bozinovska, L. (1988). Using EEG alpha rhythm to control a mobile robot. *IEEE Engineering in Medicine and Biology Society Annual Conference,* 3 1515-1516.

Burbank, D. P. & Webster, J. G. (1978). Reducing skin potential motion artefact by skin abrasion. *Medical & Biological Engineering & Computing,* **16** 31-37.

Burke,M. J. & Gleeson, D. T. (2000). A micropower dry-electrode ECG preamplifier. *IEEE transactions on biomedical engineering,* 47(2) 155-162.

Burkitt, G. R., Silberstein, R. B., Cadusch, P. J. & Wood, A. \V. (2000). Steady-state visual evoked potentials and travelling waves. *Clinical Neurophysiology,* ▮▮▮ 246-258.

Burton, C. E., David, R. M., Portnoy, W. M. & Akers, 1. A. (1974). The application of bode analysis to skin impedance. *Psychophysiology,* **11** (4) 517-25.

Cadzow, **J.** A. (1990). Multiple source location-the signal subspace approach. *IEEE Transactions on Acoustics, Speech, & Signal Processing, 38(7)* 1110-1125.

Calhoun, G. L. & McMillan, G. R. (1996). EEG-based control for human-computer interaction. *Proceedings Third Annual Symposium on Human Interaction with Complex Systems, 4-9.*

Calhoun, G. L. & McMillan, G. R. (1998). Hands-free input devices for wearable computers. *Proceedings, Fourth Annual Symposium on Human Interaction with Complex Systems, 118-123.*

Chen, D., Silberstein, R. B., Seagar, A. D., Cadush, P. J. & Murphy, D. (1998). A realistically shaped finite element model of the human head for electric field simulation. *Proceedings of the 2nd International Conference on Bioelectromagnetism, 29-30.*

Chimene, M. F. & Pallas-Areny, R. (2000). A comprehensive model for power line interference in biopotential measurements. *IEEE Transactions on Instrumentation and Measurement,* 49(3) 535-540.

Cilliers, P. J. & der Kouwe, A. J. W. V. (1996). System for YEP detection and stimulus phase discrimination. *Proceedings, Southern Biomedical Engineering Conference, 77-80.*

Clarkson, P. M. (1993). *Optimal and Adaptive Signal Processing.* London: CRC Press.

Cochran, R. J. & Rosen, T. (1980). Contact dermatitis caused by ECG electrode paste. *Southern Medical Journal,* 73(12) 1667-1668.

Cole, K. S. & Cole, R. H. (1941). Dispersion and absorption in dielectrics: 1. Alternating current characteristics. *Journal of Chemical Physics, 9* 341–351.

Cook, R. D., Saulnier, G. J., Gisser, D. G., Goble, J. C., Newell, J. C. & Isaacson, D. (1994). ACT3: A high-speed, high-precision electrical impedance tomograph. *IEEE Transactions on Biomedical Engineering,* 41(8) 713-722.

Coombs, C. F., editor (1995). *Electronic Instrument Handbook.* McGraw-Hill, 2nd edition.

Coskey, R. J. (1977). Contact dermatitis caused by ECG electrode jelly. *Archives of Dermatology,* 113(6) 839-840.

Craig, A., McIsaac, P., Tran, Y., Kirkup, L. & Searle, A. (1999). Alpha wave reactivity following eye closure: A potential method of remote hands free control for the disabled. *Technology and Disability,* **10** 187-194.

Craig, A., Tran, Y, McIsaac, P., Moses, P., Kirkup, L. & Searle, A. (2000). The effectiveness of activating electrical devices using alpha wave synchronisation contingent with eye closure. *Applied Ergonomics,* **31** 377-382.

Cram, J., Kohlenberg, R. & Singer, M. (1977). Operant control of alpha EEG and the effects of illumination and eye closure. *Psychosomatic Medicine,* 39(1) 11-18.

Creason, S. C., Hayes, J. W. & Smith, D. E. (1973). Fourier transform faradic admittance measurements: III. *Journal of Electroanalytical Chemistry,* **47** 9-46.

Cuffin, B. N. (1990). Effects of head shape on EEGs and MEGs. *IEEE Transactions on Biomedical Engineering,* 37(1) 44-52.

Cuffin, B. N. (1996). EEG localization accuracy improvements using realistically shaped head models. *IEEE Transactions on Biomedical Engineering,* 43(3) 299-303.

Cuffin, B. N. & Cohen, D. (1979). Comparison of the magnetoencephalogram and electroencephalogram. *Electroencephalography & Clinical Neurophysiology,* 47(2) 132-146.

David, R. M. & Portnoy, W. M. (1972). Insulated electrocardiogram electrodes. *Medical and Biological Engineering,* 10 742-751.

de Boer, R. W. & Oosterom, A. V. (1978). Electrical properties of platinum electrodes: Impedance measurements and time-domain analysis. *Medical & Biological Engineering & Computing.,* 16(1) 1-10.

de Munch, J. C., Vijn, P. C. M. & Silva, F. H. L. D. (1992). A random dipole model for spontaneous brain activity. *IEEE Transactions on Biomedical Engineering,* 39(8) 791-804.

de Rooij, C. & Smeyers, D. (1974). Alpha rhythm detection. In *Conference Digest.* volume 6-6.

de Talhouet, H. & Webster, J. G. (1996). The origin of skin-stretch-caused motion artifacts under electrodes. *Physiological Measurement,* **17** 81-93.

Deal, B. E. & Grove, A. S. (1965). General relationship for the thermal oxidation of silicon. *Journal of Applied Physics,* 36(12) 3770-3778.

Dewan, M. (1967). Occipital alpha rhythm eye position and lens accomodation. *Nature,* **214** 975.

Dick, D. & Vaughn, A. (1970). Mathematical description and computer detection of alpha waves *Mathematical Biosciences,* 7(1/2) 81-95.

Diniz, P. S. R. (1997). *Adaptive Filtering: Algorithms and Practical mentation*. Boston: Kluwer Academic.

Donchin, K, Spencer, K. M. & Wijesinghe, R. (2000). The mental prosthesis: Assessing the speed of a P300-based brain-computer interface. *IEEE Transactions on Rehabilitation Engineering,* 8(2) 174-179.

Douglas, S. C. (1998). Introduction to adaptive filters. In Madisetti, V. K. & Williams, D. editors, *The Digital Signal Processing Handbook,* CRC Press, chapter 18, 1-18.

Douglas, S. C. & Rupp, M. (1998). Convergence issue in the LMS adaptive filter. In Madisetti, V. K. & Williams, D. B., editors, *The Digital Signal Processing Handbook,* CRC Press, chapter 19, 1-20.

Druckman, D. & Bjork, R. A., editors (1992). *In The Minds Eye: Enhancing Human Performance.* NY: Academy Press. (Committee on Techniques for the Enhancement of Human Performance).

Dunseath, W. J. R. & Kelly, E. F. (1995). Multichannel PC-based data-acquisition system for high-resolution EEG. *IEEE Transactions on Biomedical Engineering,* **42** 1212-1217.

Dwyer, C. M., Chapman, R. S. & Forsyth, A. (1994). Allergic contact dermatitis from TENS gel. *Contact Dermatitis,* **30** 305.

Elliott, W. R. & Gianetti, G. (1995). Electrostatic discharge interference in the clinical environment. *Biomedical Instrumentation & Technology,* 29(6) 495-499.

Fernandez, M. & Pallas-Areny, R. (1996). Simple active electrode for power line interference reduction in high resolution biopotential measurements. *Annual International Conference of the IEEE Engineering in Medicine and Biology Society - Proceedings,* **1.2.3** 97-98.

Ferris, C. D. (1974). *Introduction to Bioelectrodes.* New York: Plenum Press.

Fletcher, D. J., Amir, A., Jewett, D. L. & Fein, G. (1995). Improved method for computation of potentials in a realistic head shape model. *IEEE Transactions on Biomedical Engineering,* 42(11)

Funase, A., Yagi, T., Kuno, Y. & uchikawa, Y. (1999). Prediction of eye movements from EEG. *Proceedings, 6th International Conference on Neural Information Processing,* 3 1127-1131.

Gatchel, R. J. & Price, K. P. (1979). *Clinical Applications of Biofeedback: Appraisal & Status.* N.Y.: Pergamon Press.

Geddes, 1. A. *(1973a).* Bioelectrodes. *American Journal of EEG Technology,* 13(4) 195-203.

Geddes, 1. A. *(1973b).* Measurement of electrolytic resistivity and electrode-electrolyte impedance with a variable-length conductivity cell. *Chemical Instrumentation,* 4(3) 157-168.

Geddes, 1. A. & Baker, 1. E. (1989). *Principles of Applied Biomedical Instrumentation. NY:* Wiley, 3rd edition.

Geddes, L. A., Steinberg, R. & Wise, G. (1973). Dry electrodes and holder for electro-oculography. *Medical & Biological Engineering,* 11(1)

Geddes, L. A. & Valentinuzzi, M. E. (1973). Temporal changes in electrode impedance while recording the electrocardiogram with "dry" electrodes. *Annals of Biomedical Engineering,* 1 356-367.

Gevins, A. Durousseau, D. & Libove, J. (1990). Dry electrode brain wave recording system. *US Patent #4967038.*

Ghiyasvand, M. S., Guha, S. K., Anand, S. & Deepak, K. K. (1994). Preliminary study of eye movement-induced EEG changes: A potential candidate for controlling artificial arm. *Proceedings of International Conference on Recent advances in BME, 241-244.*

Ghiyasvand, M. S., Guha, S. *K.,* Anand, S. & Deepak, K. K. (1995). New EEG signal processing technique for discrimination of eyes close and eyes open. *Proceedings of the 1st* 1995 *Regional Conference IEEE Engineering in Medicine & Biology Society and 14th Conference of the Biomedical Engineering Society of India, 3.61-3.62.*

Godin, D. T., Parker, P. A. & Scott, R. N. (1990). Noise characteristics of stainless - steel surface electrodes. *Medical & Biological Engineering & Computing,* **29** 585-590.

Gondran, *C.,* Siebert, E., Fabry, P., Novakov, E. & Gumery, P. Y. (1992). NASICON based electrodes for bioelectric signal measurements. *14th Annual International Conference on IEEE Engineering in Medicine & Biology SOCiety, 2706-2708.*

Gondran, C., Siebert, E., Fabry, P., Novakov, E. & Gumery, P. Y. (1995). Non-polarisable dry electrode based on NASICON ceramic. *Medical & Biological Engineering & Computing,* **33** 452-457.

Gondran, C., Siebert, E., Yacoub, S. & Novakov, E. (1996). Noise of surface bio-potential electrodes based on nasicon ceramic and Ag-AgCl. *Medical & Biological Engineering & Computing,* 34(6) 460-466.

Gonen, E. & Mendel, J. M. (1998). Subspace-based direction finding methods. **In** Madisetti, V. K. & Williams, D. B., editors, *The Digital Signal Processing Handbook,* CRC Press, chapter 62, 1-23.

Greef, R. (1978). Instruments for use in electrode process research. *Journal of Physics* E., 111-12.

Greenberg, J. E. & Zurek, P. M. (1992). Evaluation of an adaptive beamforming method for hearing aids. *Journal of the Acoustical Society of America,* **91** (3) 1662-76.

Griffith, M. E., Portnoy, W. M., Stotts, 1. J. & Day, J. L. (1979). Improved capacitive electrocardiogram electrodes for burn applications. *Medical & Biological Engineering & Computing,* 17(5) 641-646.

Griffiths, H. (1992). Multifrequency EIT systems. *lEE Colloquium on Impedance Tomography/Applied Potential Tomography, 3/1-3/3.*

Griss, P., Enoksson, P., Tolvanen-Laakso, H., Merilainen, P., Ollmar, S. & Stemme, G. (2000). Spiked biopotential electrodes. *The Thirteenth Annual International Conference on Micro Electro Mechanical Systems,* 323 -328.

Grovenor, C. R. M. (1989). *Microelectronic Materials.* Bristol: Adam Hilger.

Gudivaka, R., Schoeller, D. & Kushner, R. F. (1996). Effect of skin temperature on multifrequency bioelectrical impedance analysis. *Journal of Applied Physiology,* 81(2) 838-845.

Hagemann, B. & Luczak, G. 1. H. (1985). Improved "active" electrodes for recording bioelectric signals in work physiology. *European Journal of Applied Physiology and Occupational Physiology,* 54(1) 95-8.

Hague, B. & Foard, T. R. (1971). *Alternating Current Bridge Methods.* Bath: Pitman Press.

HardIe, W., Gasser, T. & Bacher, P. (1984). EEG-responsiveness to eye opening and closing in mildly retarded children compared to a control group. *Biological Psychology,* **18** 185-99.

Hardt, J. & Kamiya, J. (1976). Conflicting results in EEG alpha feedback studies: amplitude integration should replace percent time. *Biofeedback & Self Regulation,* 1(1) 63-75.

Hare, J. F., Timmons, B. H., Roberts, J. R. & Burman, A. S. (1982). EEG alpha-biofeedback training: An experimental technique for the management of anxiety. *Journal of Medical Engineering and Technology, 6* 19-24.

Harrick, N. J. (1971). Determination of refractive index and film thickness from interference fringes. *Applied Optics,* 10(10) 2344-2349.

Hawley, M. S., Cudd, P. A., \Vells, J. H., Wilson, A. J. & Judd, P. L. (1992). Wheelchair-mounted integrated control systems for multiply handicapped people. *Journal of Biomedical Engineering,* 14(3) 193-198.

He, B., Ye, W. & Musha, T. (1989). Equivalent dipole tracing of human alpha activities. *Proceedings of the Annual International Conference of the IEEE Engineering in Medicine and Biology Society,* 4 1217-1218.

Hoogerwerf, H. C. & Wise, K. D. (1994). A three-dimensional microelectrode array for chronic neural recording. *IEEE Transactions on Biomedical Engineering,* 41(12) 1136-46.

Horn, G. W. (1972). Electro-control: An EMG-controlled A-K prosthesis. *Medical & Biological Engineering,* **10** 61-73.

Horowitz, P. & W. (1989). *The Art of Electronics.* Cambridge: Cambridge University Press, 2nd edition.

Hutchison, J. M. S. & Kulkarni, V. (1995). Novel 16-electrode impedance imaging system. *IEE Colloquium (Digest),* **99** 9/1-9/3.

Hyviirinen, A. (1999). Fast and robust fixed-point algorithms for independent component analysis. *IEEE Transactions on Neural Networks, 10(3)* 626-6344.

Hyvärinen, A. & Erkki, O. (1999). Independent component analysis: A tutorial.
URL: *http://www.cis.hut.fi/aapo/papers/IJCNN99_tutorialweb/*

Hyviirinen, A. & Oja, E. (1997). A fast fixed-point algorithm for independent component analysis. *Neural Computation,* 9(7) 1483-1492.

Iguchi, H., Watanabe, K., Kozato, A. & Ishii, N. (1994). Wearable electroencephalograph system with preamplified electrodes. *Medical & Biological Engineering & Computing,* **32** 459-461.

nJackson, W. F. & Duling, B. R. (1983). Toxic effects of silver-silver chloride electrodes 011 vascular smooth muscle. *Circulation Research,* 53(1) 105-8.

Johnson, R. A. (1998). *Applied Multivariate Statistical Analysis.* NJ: Prentice Hall, 4th edition.

Jung, T.-P., Humphries, *C.,* Lee, T.-W., Makeig, S., McKeown, M. J., Iragui, V. & Sejnowski, T. J. (1998). Removing electroencephalographic artifacts: Comparison between ICA and PCA. *Neural Networks for Signal Processing VIII. Proceedings of the* 1998 *IEEE Signal Processing Society Workshop, 63-72.*

Jung, T.-P., Makeig, S., Humphries, *C.,* Lee, T.-W., McKeown, M. J., Iragui, V. & Sejnowski, T. J. (2000). Removing electroencephalographic artifacts by blind source separation. *Psychophysiology,* **37** 163-78.

Keirn, Z. A. & AUllon, J. 1. (1990). A new mode of communication between man and his surroundings. *IEEE Trans Biomed Eng,* **37** 1209-1214.

Kemp, B. & Blom, H. (1981). Optimal detection of the alpha state in a model of the human electroencephalogram. *Electroencephalography & Clinical Neurophysiology,* 52(2) 222-225.

Khalafalla, A. S., Turner, L. & Spyker, D. (1971). An electrical model to simulate skin dielectric dispersion. *Computers & Biomedical Research,* 4359-73.

Khan, A. & Greatbatch, W. (1974). Physiologic electrodes. In Ray, C. D., editor, *Medical Engineering,* Chigaco: Year Book Medical Publishers, chapter 79, 1073-1082.

Kinouchi, Y, Iritani, T., Morimoto, T. & Ohyama, S. (1997). Fast in vivo measurements of local tissue impedances using needle electrodes. *Medical & Biological Engineering & Computing,* **35** 486-492.

Kirkup, L., Searle, A., Craig, A. & McIsaac, P. *(1997a).* EEG based activation system. Australian Patent #722772.

Kirkup, L., Searle, A., Craig, McIsaac, P. & Larsen, G. (1998). Three methods compared for detecting the onset of alpha wave synchronization following eye closure. *Physiological Measurement,* 19(2) 213-224.

Kirkup, L., Searle, A., Craig, A., McIsaac, P. & Moses., P. *(1997b).* EEG based system for rapid on-off switching without prior learning. *Medical & Biological Engineering & Computing,* **35** 504-9.

Knox, S. S. (1980). Distribution of 'criterion' alpha in the resting EEG: Further argument against the use of an amplitude threshold in alpha biofeedback training. *Biological Psychology,* **11** 1-6.

Ko, W. H. (1998). Active electrodes for EEG and evoked potential. *Proceedings of the 20th Annual Conference of the IEEE Engineering in Medicine and Biology Society,* 20(4) 2221-2224.

Ko, W. H. & Hynecek, J. (1974). Dry electrodes and electrode amplifiers. In Miller, H. A. & Harrison, D. C.., editors, *Biomedical Electrode Technology: Theory and Practice,* New York: Academic Press, 169-181.

Kontturi, K. & Murtomaki, L. (1994). Impedance spectroscopy in human skin: A refined model. *Pharmaceutical Resear'ch,* 11(9) 1355-7.

Kontturi, K., Murtomaki, 1., Hirvonen, J., Paronen, P. & Urtti, A. (1993). Electrochemical characterization of human skin by impedance spectroscopy: the effect of penetration enhancers. *Pharmaceutical Research,* 10(3) 381-5.

Kostov, A. & Polak, M. (2000). Parallel man-machine training in development of EEG-based cursor control. *IEEE Transactions on tion Engineering,* 8(2) 203-205.

Krim, H. & Viberg, M. (1996). Two decades of array signal processing research: The parametric approach. *IEEE Signal Processing Magazine,* 13(4) 67-94.

Kuo, B. C. (1991). *Automatic Control Systems.* New Jersey: Prentice-Hall, 6th edition.

Lagow, C. H., Sladek, K. J. & Richardson, P. C. (1971). Anodic insulated tantalum oxide electrocardiograph electrodes. *IEEE Transactions on Biomedical Engineering,* 18(2) 162-4.

Lansky, P., Bohdanecky, Z., Indra, M. & Radil-\Veiss, T. *(1979a).* Alpha detection. Some comments on Hardt and Kamiya; 'Conflicting results in EEG alpha feedback studies'. *Biofeedback & Self Regulation, 4(2)* 127-131.

Lansky, P., Bohdanecky, Z., Indra, M. & Radil-\Veiss, T. *(1979b).* Comparison of two alpha activity detection methods. *Activitas Nervosa Superior,* 21(1) 26-27.

Lee, K. H., Liu, W. H., Campbell, S. A. & Banerjee, 1. (1993). Growth kinetics and electrical characteristics of thermal silicon dioxide grown at low temperatures. *Journal of the Electrochemical Society, 140(2)* 501-505.

Lee, T.-W., Girolami, M. & Sejnowski, T. (1999). Independent component analysis using an extended infomax algorithm for mixed sub-gaussian and super-gaussian sources. *Neural Computation,* 11(2) 417-441.

Lewes, D. (1965). Electrode jelly in electrocardiography. *British Heart Journal,* 27 105-115.

Lippold, O. (1970). The origin of the alpha rhythm. *Nature,* 226 616-618.

Lopes Da Silva, F. (1991). Neural mechanisms underlying brain waves: from neural membranes to networks. *Electroencephalography & Clinical Neurophysiology,* 79 81-93.

Lopez, A. & Richardson, P. C. (1969). Capacitive electrocardiographic and bioelectric electrodes. *IEEE Transactions on Biomedical Engineering,* 16(1) 99.

Lozano, A., Rosell, J. & Pallas-Areny, R. (1990). Two-frequency impedance plethysmograph: real and imaginary parts. *Medical & Biological Engineering & Computing,* 28(1) 38-42.

Lu, Y. Z. & Cheng, Y. C. (1984). A new model for the growth of silicon dioxide layers. *Journal of Applied Physics,* 56(6) 1608-1612.

Luca, C. J. D., Fever, R. S. L. & Stulen, F. B. (1979). Pasteless electrode for clinical use. *Medical & Biological Engineering & Computing, 17* 387-390.

Lykken, D. T. (1970). Square-wave analysis of skin impedance. *Psychophysiology,* 7(2) 262-75.

Makeig, S. (1998). Frequently asked questions about ICA applied to EEG and MEG data.
URL: *http://www. cnl.salk. edu/ scott/icafaq.html*

Makeig, 5., Bell, A. J., Jung, T.-P. & Sejnowski, T. J. (1995). Independent component analysis of electroencephalographic data. *Advances in Neural Information Processing* 8. *Proceedings of the* 1995 *Conference.,* 145-151.

Makeig, S., Enghoff, 5., Jung, T. P. & Sejnowski, T. J. (2000). A natural basis for efficient brain-actuated control. *IEEE Transactions on Rehabilitation Engineering,* 8(2) 208-211.

Malmstadt, H. Y., Enke, C. G. & Toren, E. C. (1963). *Electronics for Scientists.* New York: W.A. Benjamin, Inc.

Maras, L., Indra, M., Bohdanecky, Z. & RadiI, T. (1979). Threshold controlled detection of EEG alpha activity. *Activitas Nervosa Superior,* 21(1) 10-11.

Marshall, 1. & Neilson, J. M. (1984). Mains interference in EeG recording. *Journal of Medical Engineering & Technology,* 8(4) 177-180.

Masuda, T. & Sadoyama, T. (1988). Topographical map of innervation zones within single motor units measured with a grid surface electrode. *IEEE Transactions on Biomedical Engineering,* 35(8) 623-628.

Matsuo, T., Iinuma, K. & Esashi, M. (1973). A barium-titanate-ceramics capacitive-type EEG electrode. *IEEE Transactions on Biomedical Engineer.ing,* **188** 299-300.

McAdams, E. T. & Jossinet, J. *(1994a).* Detection of the onset of electrode-electrolyte interface impedance nonlinearity: A theoretical study. *IEEE Transactions on Biomedical Engineering.,* 41(5) 498-500.

McAdams, E. T. & Jossinet, J. *(1994b).* Physical interpretation of Schwan's limit voltage of linearity. *Medical & Biological Engineering & Computing.,* 32(2) 126-30.

McAdams, E. T. & Jossinet, J. (1995). Tissue impedance: a historical overview. *Physiological Measurement Buppl A,* 16(3) A1-13.

McAdams, E. T. & Jossinet, J. (1998). Non-linear transient response of electrode-electrolyte interfaces. *Proceedings of the 20th Annual International Conference of the IEEE Engineering in Medicine and Biology Society,* 4 1789 -1790.

McAdams, E. T., Jossinet, J., Lackermaier, A., Woolfson, D., McCafferty, D. & Anderson, J. (1993). Epidermal A.C. impedance: Low frequency distortions. *15th Annual Conference of the IEEE Engineering in Medicine and Biology Society,* 3 1497-1498.

McAdams, E. T., Lackermeier, A. & Jossinet, J. (1994). AC impedance of the hydrogel-skin interface. *Annual International Conference of the IEEE Engineering in Medicine and Biology Society - Proceedings,* 16(2) 870.

McAdams, E. T., Lackermeier, A., Mclaughlin, J. A., Macken, D. & Jossinet, J. (1995). The linear and non-linear electrical properties of the electrode-electrolyte interface. *Biosensors & Bioelectronics,* 10(1) 67-74.

Mcfarland, D. J., Neat, G. W., Read, R. F. & Wolpaw, J. R. (1993). An EEG-based method for graded cursor control. *Psychobiology,* **21** 77-81.

McLaughlin, J. A., McAdams, E. T. & Anderson, J. M. (1994). Novel dry electrode ECG sensor system. *Annual International Conference of the IEEE Engineering in Medicine and Biology Society - Proceedings, 16(2)* 804.

MettingVanRijn, A., Peper, A. & Grimbergen, C. (1994). Amplifiers for bioelectric events: a design with a minimal number of parts. *Medical and Biological Engineering and Computing,* **32** 305-310.

MettingVanRijn, A. C., Kuiper, A. P., Dankers, T. E. & Grimbergen, C. A. (1996). Low-cost active electrode improves the resolution in biopotential recordings. *Proceedings of the 18th Annual ConfeTence of the IEEE Engineering in Medicine and Biology Society, 101-102.*

Ming, C. & Shangkai, G. (1999). An EEG-based cursor control system. *Proceedings of the First Joint BMES/EMBS Conference,* 1 669.

Montagu, J. D. & Coles, E. M. (1966). Mechanism and measurement of the galvanic skin response. *Psychological Bulletin,* 65(5) 261-279.

Monzingo, R. A. & Miller, T. W. (1980). *Introduction to Adaptive Arrays.* NY:

Morrow, T. & Casey, K. (1986). A microprocessor device for the real-time detection of synchronized alpha and spindle activity in the EEG. *Brain Research Bulletin,* 16(3) 439-42.

Mosher, J. C., Spencer, M. E., Leahy, R. M. & Lewis, P. S. (1993). Error bounds for EEG and MEG dipole source localization. *Electroencephalography & Clinical Neurophysiology,* 86(5) 303-321.

Mulholland, T. (1971). Feedback electroencephalography. In Kamiya, J., Barber, T. X., DiCara, L. V., Miller, N. E., Shapiro, D. & Stoyva, J., editors, *Biofeedback and Self-Control,* N.Y.: Aldine Atherton, chapter 39, 305.

Mulholland, T. & Evans, C. (1965). An unexpected artefact in the human electroencephalogram concerning the alpha rhythm and the orientation of the eyes. *Nature,* **207** 36.

Mulholland, T. B. (1972). Occipital alpha revisited. *Psychological Bulletin,* 78(3) 176-182.

Naito, M., Homma, H. & Momma., N. (1986). Practical model for growth kinetics of thermal $Si0_2$ on silicon applicable to a wide range of oxide thickness. *Solid-State Electronics,* 29(9) 885-891.

Nathan, R. D. & Hanley, J. (1975). Spectral analysis of the EEG recorded during stimulation of the human fovea. *Research.* 91(1) 65-77.

Neamen, D. A. (1997). *Semiconductor Physics and Devices.* Chicago: Irwin, 2nd edition.

Nikookar, H. & Hashemi, H. (1993). Statistical modeling of signal amplitude fading of indoor radio propagation channels. *International Conference on Universal Personal Communications,* 1 84-88.

Nishimura, S., Tomita, Y. & Horiuchi, T. (1992). Clinical application of an active electrode using an operational amplifier. *IEEE Transactions on Biomedical Engineering,* 39(10) 1096-1099.

Norris, M. D. (1983). *Electromyography With A Dry Electrode System.*. Master's thesis, N.S.W.I.T.

Nowotny, R. & Nowotny, C. (1980). Determination of electrode impedance with an F.F.T. spectrum analyser. *Medical & Biological Engineering & Computing,* 18(6) 779-82

Nunez, P. L., editor (1995). *Neocortical Dynamics and Human EEG Rhythms*. New York: Oxford University Press.

Odman, S. (1982). On the spread of deformation potentials in the skin. *Medical & Biological Engineering & Computing,* **20** 451-456.

O'Donnell, R. D., Berkhout, J. & Adey, W. R. (1974). Contamination of scalp EEG spectrum during contraction of cranio-facial muscles. *Electroencephalography & Clinical Neurophysiology,* 37(2) 145-51.

Olson, W. H., Schmincke, D. R. & Henley, B. L. (1979). Time and frequency dependence of disposable ECG electrode-skin impedance. *Medical Instrumentation,* 13(5) 269-272.

Onaral, B. & Schwan, H. P. (1982). Linear and nonlinear properties of platinum electrode polarisation. Part 1: Frequency dependence at very low frequencies. *Medical & Biological Engineering & Computing, 20(3)* 299-306.

Oosterom, A. V. & Strackee, J. (1983). Computing the lead field of electrodes with axial symmetry. *Medical & Biological Engineering & Computing,* 21(4) 473-481.

Overton, D. A. (1974). Methods for reducing line frequency interference in EEG recordings. *Psychophysiology,* 11(3) 398-399.

Padmadinata, F. Z., Veerhoek, J. J., Dijk, G. J. A. V. & Huijsing, J. H. (1990). Microelectronic skin electrode. *Sensors & Actuators B-Chemical,* **B1** 491-494.

Palik, E. D., editor (1985). *Handbook of Optical Constants of Solids*. N.Y.: Academic Press.

Palko, T., Bialokoz, F. & Weglarz, J. (1995). Multifrequency device for measurement of the complex electrical bio-impedance - design and application. *Proceedings, Regional Conference on IEEE Engineering in Medicine and Biology Society & 14th Conference of Biomedical Engineering Society, India, 1.45-1.46.*

Pasquali, E. (1969). Alpha envelope detection and distortion. a polyphase rectifier circuit. *Electroencephalography & Clinical Neurophysiology,* 26(1) 106-9.

Pathmore, D. W., Putnam, W. L. & Knapp, R. B. (1994). Assistive cursor control for a PC window environment:electromyogram and electroencephalogram based control. *Proceedings of the Virtual Reality and Persons With Disabilities Conference.*

Patterson, R. P. & Latterell, T. (1995). Evaluations of a commercial impedance spectroscopy instrument: Inaccuracies and their corrections. 1995 *IEEE Engineering in Medicine & Biology Annual Conference & 21st Canadian Medical and Biological Engineering Conference, 651.*

Pedrotti, F. L. & Pedrotti, L. S. (1993). *Introduction to Optics.* NJ: Prentice-Hall, 2nd edition.

Penny, W. D., Roberts, S. J., Curran, E. A. & Stokes, M. J. (2000). EEG-based communication: A pattern recognition approach. *IEEE Transactions on Rehabilitation Engineering,* 8(2) 214-215.

Perrault, J. J. (1998). Electrically conductive adhesive hydrogels. US Patent #5800685.

Pfurtscheller, G., Flotzinger, D. & Neuper, C. (1994). Differentiation between finger, toe and tongue movement in man based on 40hz EEG. *Electroencephalography & Clinical Neumphys'iology,* **90** 456-460.

Pfurtscheller, G., Neuper, C., Guger, C., Harkam, W., Ramoser, H., SchlogL A., Obermaier, B. & Pregenzer, M. (2000). Current trends in Graz brain-computer interface (BCI) research. *IEEE Transactions on Rehabilitation Engineering,* 8(2) 216-219.

Pineda, J. A., Allison, B. Z. & Vankov, A. (2000). The effects of self-movement, observation, and imagination on mu rhythms and readiness potentials (RP's): Toward a brain-computer interface (BCI). *IEEE Transactions on Rehabilitation Engineering,* 8(2) 219-222.

Plutchik, R. & Hirsch, H. R. (1963). Skin impedance and phase angle as a function of frequency and current. *Science,* **141** 927-8.

Potter, A. & Menke, L. (1970). Capacitive type of biomedical electrode. *IEEE Transactions on Biomedical Engineering,* **17** 350-351.

Pregenzer, M. & Pfurtscheller, G. (1999). Frequency component selection for an EEG-based brain to computer interface. *IEEE Transactions on Engineering,* 7(4) 413-419.

Press, W. H., Teukolsky, S. A., Vetterling, W. T. Flannery, B. P. (1997). *Numerical Recipes in C : The Art of Scientific Computing*. New York: Cambridge University Press, 2 edition.

Qiao, Z. G. & Morkrid, L. (1995). Relationships between parameters describing low-frequency electrical admittance locus plot of human palmar skin. *Medical & Biological Engineering & Computing*, 33(3) 464-70.

Ramirez, R. W. (1985). *The FFT, fundamentals and concepts*. NJ: Prentice Hall.

Ray, W. J. & Cole, H. W. (1985). EEG alpha activity reflects attentional demands, and beta activity reflects emotional and cognitive processes. *Science*, **228** 750-752.

Reilly, A., Frazer, G. & Boashash, B. (1994). Analytic signal generation-tips and traps. *IEEE Transactions on Signal Processing*, 42(11) 3241-3245.

Reiser, S. J. (1978). *Medicine and the Reign of Technology*. Cambridge: Cambridge university Press.

Reizman, F. (1965). Optical thickness measurement of thin transparent films on silicon. *Journal of Applied Physics*. 36(12) 3804-3807.

Richardson, P. C. (1967). The insulated electrode: A pasteless electrocardiographic technique. *Conference on Engineering in Medicine and Biology, 15.7.*

Richardson, P. C., Coombs, F. K. & Adams, R. M. (1968). Some new electrode techniques for long-term physiologic monitoring. *Aerospace Medicine*, 39(7) 745-50.

Ristic, B., Kun, S. & Peura, R. A. (1995). Development of an impedance spectrometer for tissue ischemia monitoring: Instrument realization and performance. *Annual International Conference of the IEEE Engineering in Medicine and Biology*, 17(2) 1643-1644.

Robinson, P. A., Rennie, C. J., Wright, J. J. & Bourke, P. D. (1998). Steady states and global dynamics of electrical activity in the cerebral cortex. *Physical Review E. Statistical Physics, Plasmas, Fluids, & Related Interdisciplinary Topics*, 58(3) 3557-3571.

Roth, B. J., Balish, Gorbach, A. & Sato, S. (1993). How well does a three-sphere model predict positions of dipoles in a realistically shaped

head? *Electroencephalography & Clinical Neurophysiology,* 87(4) 175-184.

Ryu, C. S., Song, Y, Yoo, D. S., Choi, S., Moon, S. S. & Sohn, J. H. (1999). EEG-based discrimination between yes and no. *Proceedings of the First Joint BMESjEMBS Conference,* 1 444.

Sadasivan, P. K. & Dutt, D. N. (1994). Minimization of EOG artefacts from corrupted EEG signals using a neural network approach. *Computers in Biology & Medicine,* **24** 441-449.

Salu, Y, Cohen, L. G., Rose, D., Sxato, S., Kufta, C. & Hallett, M. (1990). An improved method for localizing electric brain dipoles. *IEEE Transactions on Biomedical Engineering,* 37(7) 699-705.

Sammur, N. & Hutchens, C. (1987). A proposed VLSI implementation of a digital beamformer used in ultrasonic medical imaging. *Biomedical Sciences Instrumentation,* **23** 223-230.

Schloegl, A., Lugger, K. & Pfurtscheller, G. (1997). Using adaptive autoregressive parameters for a brain-computer-interface experiment. *Proceedings of the 19th Annual International Conference of the IEEE Engineering in Medicine and Biology Society,* 4

Schwan, H. P. (1968). Electrode polarization impedance and measurements in biological materials. *Annals New York Academy of Sciences,* ***148*** 191-209.

Searle, A. & Kirkup, L. (1999). Real time impedance plots with arbitrary frequency components. *Physiological Measurement,* **20** 103-114.

Searle, A. & Kirkup, L. (2000). A direct comparison of wet, dry and insulating bioelectric recording electrodes. *Physiological Measurement, 21(2)* 271-283.

Searle, A. & Kirkup, L. (2001). Detection of alpha EEG onset following eye closure using four location-based techniques. *Medical & Biological Engineering & Computing,* **39** 1–7.

Shaw, J. C. (1992). The ubiquitous alpha rhythm - a selective review. *Journal of Electrophysiological Technology,* **18** 5-27.

Shimada, T., Shiina, T. & Saito, Y (2000). Detection of characteristic waves of sleep EEG by neural network analysis. *IEEE Transactions on Biomedical Engineering,* 47(3)

Simpson, R. W., Berberian, J. G. & Schwan, H. P. (1980). Nonlinear AC and DC polarization of platinum electrodes. *IEEE Transactions on Biomedical Engineering.,* 27(3) 166-71.

Skidmore, T. A. & Hill., H. W. (1990). Analyzing thought-related electroencephalographic data using nonlinear techniques. *Proceedings of the Annual Conference on Engineering in Medicine and Biology,* 2 853–854.

Smith, P. J. (1994). *Into Statistics.* Melbourne: Nelson.

Spencer, M. E., Leahy, R. Mosher, J. C. & Lewis, P. S. (1992). Adaptive filters for monitoring localized brain activity from surface potential time series. *Conference Record of The Twenty-Sixth Asilomar Conference on Signals, Systems and Computers,* 1 156-161.

Srikureja, W., Darbar, D. & Reeder, G. S. (2000). Tremor-induced ECG artifact mimicking ventricular tachycardia. *Circulation,* 102(11) 1337-1338.

Stoica, P. & Nehorai, A. (1989). MUSIC, maximum likelihood, and Cramer-Rao bound. *IEEE Transactions on Acoustics, Speech, & Signal Processing,* 37(5) 720-741.

Sutter, E. (1992). The brian response interface: Communication through visually-induced electrical brain responses. *Journal of Microcomputer Applications,* **14** 31-45.

Swindlehurst, A. L. & Kailath, T. (1992). A performance analysis of subspace-based methods in the presence of model errors. 1. The MUSIC algorithm. *IEEE on Signal Processing,* 40(7) 1758-74.

Sze, S. M. (198J). *Physics of Semiconductor Devices.* NY: Wiley, 2 edition.

Taheri, B., Knight, R. & Smith, R. (1994). A dry electrode for EEG recording. *Electroencephalography and Clinical Neurophysiology,* **90** 376-383.

Taheri, B. A., Smith, R. L. & Knight, R. T. (1995). An active, microfabricated, scalp electrode array for EEG recording. *Transducers* 95, *session 9-Al Implantable Devices, Telemetry,* 1 67-70.

Tassinary, L. G., Geen, T. R., Cacioppo, J. T. & Edelberg, R. (1990). Issues in biometrics: Offset potentials and the electrical stability of Agj AgCl electrodes. *Psychophysiology,* 27(2) 236-42.

Teorell, T. (1947). Applications of square wave analysis to bioelectric studies. *Acta. Physiol. Scand.,* **12** 235-254.

Thatcher, R. W., Krause, P. J. & Hrybyk, M. (1986). Cortico-cortical associations and EEG coherence: A two-compartmental model. *Electroencephalography & Clinical Neurophysiology,* 64(2) 123-143.

Thornett, C. E. (1990). Designing special switches and control systems for multiply handicapped young people-a problem-led approach. *Journal of Medical Engineering & Technology,* 14(3) 87-91.

Toole, A. M. (1977). A new highly stable silver/silver-chloride electrode. *Medical & Biological Engineering & Computing,* 15(6) 707-9.

Townsend, R. E., Lubin, A. & Naitoh. P. (1975). Stabilization of alpha frequency by sinusoidally modulated light. *Electroencephalography & Clinical Neurophysiology,* **39** 515-8.

Tregear, R. T. (1974). The skin. In Ray, C. D., editor, *Medical Engineering,* Chicago: Year Book Medical Publishers, chapter 50, 586.

Uter, W. & Schwanitz, H. J. (1996). Contact dermatitis from propylene glycol in ECG gel. *Contact Dermatitis,* **34** 230-231.

Valaee, S., Champagne, B. & Kabal, P. (1995). Parametric localization of distributed sources. *IEEE Transactions on Signal 43(9)* 2144-2153.

Valle, R. & Levine, J. (1975). Expectation effects in alpha wave control. *Psychophysiology,* 12(3) 306-9.

Veen, B., Joseph, J. & Hecox, K. (1992). Localization of intra-cerebral sources of electrical activity via linearly constrained minimum variance spatial filtering. *IEEE Sixth SP Workshop on Statistical Signal and Array Processing Conference Proceedings, 526-529.*

Veen, B. D. V. & Buckley, K. M. (1988). Beamforming: A versatile approach to spatial filtering. *IEEE Acoustics, Speech, & Signal Processing Magazine,* 5(2) 4-24.

Veen, B. D. V., Drongelen, W. V., Yuchtman, M. & Suzuki, A. (1997). Localization of brain electrical activity via linearly constrained minimum variance spatial filtering. *IEEE Transactions on Biomedical Engineering,* 44(9) 867-880.

Vigario, R, Jousmaki, V., M., Hari, R & Oja, E. (1997). Independent component analysis for identification of artifacts in magnetoencephalographic recordings. *Advances in Neural Information Processing Systems, 229-235.*

Walter, M. & Fournier, A. (1996). Approximate arc length parametrization. *Proceedings of the 9th Brazilian Symposium on Computer Graphics and Image Processing,* 143–150.

\Van, S. W. & Nguyen, H. T. (1994). 50 hz interference and noise in ECG recordings-a review. *Australasian Physical & Engineering Sciences in Medicine,* 17(3) 108-115.

Warburg, E. (1899). Uber das verhalten sogenannter unpolarisierbarer electroden gegen wechselstrom. *Annalen der Physik und Chemie, 67(3)* 493-499.

vVard, D.-M., Jones, R D., Bones, P. J. & Carroll, G. J. (1998). Enhancement of epileptiform activity in the EEG by 3-d adaptive spatial filtering: Simulations and real data. *Annual International Conference of the IEEE Engineering* in *Medicine and Biology,* 4 2116-2119.

Webster, J. G. (1984). Reducing motion artifacts and interference in biopotential recording. *IEEE Transactions on Biomedical Engineering,* 31(12) 823-826.

\Veinman, J. & Mahler, J. (1964). An analysis of electrical properties of metal electrodes. *Medical Electronics and Biological Engineering,* 2 299-310.

Wen, P., He, F. & Sammut, K. (1999). The inhomogeneous conductivity property of cranial tissues and its representation in numerical head models. *Australasian Physical & Engineering Sciences in Medicine,* 22(3) 92-98.

Williams, D. F., (1981). *Fundamental Aspects of Biocompatibility,* volume II. Boca Raton, Fla: CRC Press.

Wilson, F. N. & Bayley, R H. (1950). The electric field of an eccentric dipole in a homogeneous conducting medium. *Circulation,* 1 84-92.

Wolfson, R N. & Neuman, M. R. (1969). Miniature SijSi0_2, insulated electrodes based on semiconductor technology. *Proceedings of the 8th International Conference on Medical and Biological Engineering and the 22nd Annual Conference on Engineering in Medicine and Biology,* 14-6.

Wolpaw, J. R. & Mcfarland. D. J. (1994). Multichannel EEG-based brain-computer communication. *Electroencephalography & Clinical physiology,* **90** 444-449.

Wright, J. J. & Liley, D. T. J. (1996). Dynamics of the brain at global and microscopic scales: Neural networks and the EEG. *Behavioral & Brain Sciences,* 19(2) 285-320.

Yacoub, S., Novakov, E. P., Gumry, P. Y., Gondran, C. & Siebert, E. Noise analysis of NASICON ceramic dry electrodes. 1995 *IEEE Engineering in Medicine & Biology 17th Annual Conference & 21st Canadian Medical and Biological Engineering Conference,* **7.1.2.3** 1.5.5.3.

Yamabe. K. & Taniguchi, K. (1985). Time-dependent dielectric breakdown of thin thermally grown Si02 films. *IEEE Journal of Solid-State Circuits,* 20(1) 343-348.

Yamamoto, T. & Yamamoto, Y. (1977). Analysis for the change of skin impedance. *Medical & Biological Engineering & Computing, 15(3)* 219--27.

Yamamoto, T. & Yamamoto, Y (1981). electrical properties of skin in the low frequency range. *Medical & Biological Engineering & Computing,* 19(3) 302-310.

Yamamoto, Y, Isshiki, H. & Nakamura, T. (1996). Instantaneous measurement of electrical parameters in a palm during electrodermal activity. *IEEE Transactions on Instrumentation & Measurement,* 45(2) 483–487.

Yamamoto, Y & Yamamoto, T. (1978). Dispersion and correlation of the parameters for skin impedance. *Medical & Biological Engineering & Computing,* 16(5) 592-4.

Yamamoto, Y, Yamamoto, T. & Ozawa, T. (1986). Characteristics of skin admittance for dry electrodes and the measurement of skin moisturisation. *Medical & Biological Engineering & Computing,* 24(1) 71-7.

Yvert, B., Bertrand, 0., Echallier, J. F. & Pernier, J. (1995). Improved forward EEG calculations using local mesh refinement of realistic head geometries. *Electroencephalography & Clinical Neurophysiology,* **95** 381-392.

Zhang, Z. & Chen, W. (1988). Development of EEG biofeedback system and research of the biofeedback in the alpha frequency band. *Proceedings of the Annual International Conference of the IEEE Engineering in Medicine and Biology Society, 1482-1483.*

Zhou, D. McAdams, E. T., Lackerrneier, A. & Jones, J. G. (1994). AC impedance of Ag/AgCI reference electrodes for use in disposable biosensors. *Proceedings, Annual International Conference of the IEEE Engineering in and Biology Society,* 16(2) 832-833.